

Faculty of Engineering
Department of Mechanical Engineering

**Design and Shape Optimization of Blade Profile and support-arms
for Small Scale Vertical Axis Wind Turbine**

Gavin Scott Manggai Van Stratan

000000019885321X


This thesis is presented for the degree of
Doctor of Philosophy (Mechanical Engineering)
of
Curtin University

December 2023

Declaration

To the best of my knowledge and belief, in completing this thesis, no material contained herein has been previously published by any other person except where referenced or due acknowledgement was made.

This thesis contains no material which has been accepted for the award of any other degree or diploma in any university.

Signature : 

Name : Gavin Scott Manggai van Stratan

Date : 4th NOVEMBER 2023

This thesis is dedicated to
John Alexzander van Stratan, Siah anak Umul, and Ruster Trida Sumbang,
whose unwavering support and encouragement
helped me overcome the challenges and obstacles I faced
during my educational journey

Acknowledgement

In preparation of this thesis, I received multiple support from various persons in. As such, I acknowledge and would like to thank my supervisor, Dr. Sukanta Roy for the guidance and support I have had up to this point in my journey to obtaining a PhD. His invaluable experience in the field of Computational Fluid Dynamics and fluid mechanics has helped me immensely and I look forward to the continuing support up to the completion of this thesis. I would like to extend my gratitude and appreciation to Dr Vincent Lee for his excellent guidance and extreme patience in leading me towards the completion of this thesis. The numerous advice and feedback were immeasurable in helping to complete this thesis. As co-supervisor to this research project, I would also like to extend my gratitude to Dr. Yam Ke San for his support in writing this thesis, building fundamental understanding in Computational Fluid Dynamics and numerous advice and guidance in paper writing. His help in these areas of my study has been gratefully received. As the guidance and a personal mentor, I express the utmost gratitude to Dr. Mahmood Anwar, my final year degree supervisor who encouraged and put me on this path to continue on towards a doctorate degree.

I would also like to extend my gratitude towards the Curtin University Sarawak Graduate School for allowing me to take up my PhD as well as providing funds and monetary support. To Mr Sheikh, who has helped and supported me through multiple ICT related issues and computer related problems. To Mr. Michael and Mr Hidayat, for their help and assistance during laboratory work.

And lastly, I would like to extend much gratitude to my parents, John Alexzander van Stratan and Siah anak Umul, and fiancé Ruster Trida Sumbang, all of whom has provided innumerable support and encouragement to continue this academic path from my undergraduate days up to now. Without their continued support, this journey would not have been possible.

List of Publications

JOURNAL

GSM van Stratan, Sukanta Roy, Yam Ke San, Vincent CC Lee. “**A Novel Aerodynamic Shape Optimization Scheme on a NACA0018 VAWT for Improved Turbine Performance Using the Adjoint Method Part 1: Feasibility and 2D Optimization Study**”, in preparation.

GSM van Stratan, Sukanta Roy, Yam Ke San, Vincent CC Lee. “**Shape Optimization Application of the Adjoint Method on a cambered S1046 VAWT blade**”, in preparation.

GSM van Stratan, Sukanta Roy, Yam Ke San, Vincent CC Lee. “**A Novel Aerodynamic Shape Optimization Scheme on a NACA0018 VAWT for Improved Turbine Performance Using the Adjoint Method Part 2: 3D Blade Analysis**”, in preparation.

GSM van Stratan, Sukanta Roy, Yam Ke San, Vincent CC Lee. “**A Novel Aerodynamic Shape Optimization Scheme on a NACA0018 VAWT for Improved Turbine Performance Using the Adjoint Method Part 3: Full Turbine Characterization**”, in preparation

BOOK CHAPTER

GSM van Stratan, Sukanta Roy, Yam Ke San, Vincent CC Lee. “**Numerical Simulations on the Aerodynamic effects of turbine arms for vertical axis wind turbines**”, Accepted, - to be published in book titled "Modelling and Analysis of Sustainable Renewable Energy System", Springer.

CONFERENCE

GSM van Stratan, Sukanta Roy, Yam Ke San, Vincent CC Lee. “**The Influence of support-arms on the Performance of Vertical Axis Wind Turbines**”, International Conference on Novel Materials and Technologies for Energy and Environment Applications (NMTEEA), 18th -19th February 2022, Hyderabad, India, Materials Today: Proceedings (Elsevier).

GSM van Stratan, Sukanta Roy, Yam ke San, “**Aerodynamic Shape Optimization of a NACA0018 Airfoil Using Adjoint Method and Gradient-Based Optimizer**”, MATEC Web of Conferences 377, 01016, 2023.

Abstract

In this thesis, a comparisons study was conducted of two separate turbines to understand its performance in different turbine configurations. The first two studies were conducted on a NACA0018 turbine and a NACA0021 turbine in blade only and full turbine configuration with support structures. The results proved the implementation of the support structures reduces the performance coefficients significantly. This was due to the support-arms affecting turbine flow and reduces the aerodynamic efficiencies of the turbine blade. Hence, an optimization procedure utilizing the adjoint method together with the gradient-based optimizer to increase turbine blade moment coefficient was conducted. The turbine operating TSR, azimuth angles, and starting shapes were selected as the main parameters of the optimization. The 2D study showed optimizing at a higher operating TSR yielded the best results. Varying the azimuth angle yielded starkly different turbine blade geometry due to the varying flow field affecting the adjoint solver. When the starting shape was varied between a cambered and uncambered blade, the uncambered NACA0018 produced a larger increase in performance when compared against the optimization results of the cambered S1046 blade. The largest increase in moment coefficient was found at 120° azimuth angle at TSR 2 with an increase of 30.48% in moment coefficient over the baseline NACA0018 blade. The candidate blade was named 120D. Further 3D studies were conducted to quantify the performance of the 120D blade against the NACA0018 and S1046. The 120D turbine yielded an average increase of 20.42% in power coefficient over the NACA0018 turbine and 15.18% against the S1046 turbine. Expanding further, a second 3D numerical analysis was conducted but this time, with the 120D blade geometry applied to the turbine blade and the turbine support-arm. The 120D full turbine configuration again outperformed the NACA0018 full turbine by 12.5% with the 120D blade performing better in the downwind region compared to the NACA0018 blade. An analysis of the performance coefficient of the support-arms indicates that the 120D blade geometry led to enhanced turbine performance and decreased power coefficient losses. Lastly, a wind tunnel experimental study was conducted and the results verified the numerical findings of improved performance and power production of the 120D turbine blade over the baseline NACA0018 blade. A characterization study was also conducted to see the effects of the 120D blade geometry when turbine solidity and

aspect ratio was varied. Overall, the research questions and objectives of this thesis were answered, with the result being an original and novel turbine blade design developed from an optimization scheme utilizing the adjoint method and the gradient-based optimizer. The recommended turbine parameter for the 120D turbine blade is a 3-bladed configuration and a solidity value of 0.28, with an aspect ratio of 1 for optimal turbine performance.

Table of Contents

Chapter No.	Title	Page
	DECLARATION	I
	ACKNOWLEDGEMENT	III
	LIST OF PUBLICATIONS	IV
	ABSTRACT	V
	TABLE OF CONTENTS	VII
	LIST OF FIGURES	XIII
	LIST OF TABLES	XXII
1	INTRODUCTION	1
	1.1 Preface	1
	1.2 Wind Turbine	4
	1.3 Types of Wind Turbine	5
	1.4 Problem Statement	7
	1.5 Research Question	8
	1.6 Objective	8
	1.7 Hypothesis	9
	1.8 Scope of Study	9
	1.9 Significance of Study	10
	1.10 Thesis Structure	11
2	LITERATURE REVIEW	13
	2.1 Introduction	13
	2.2 Experiments and Numerical Models	14
	2.2.1 Wind tunnel setups and dimensions	14
	2.2.2 Turbulence intensity and modelling	15
	2.3 VAWT numerical simulation	18
	2.3.1 Mesh independency test and validation	18
	2.3.2 Reported turbulence models in literature	19
	2.4 Design of the vertical axis wind turbine	25
	2.4.1 Aerofoil Types and Modifications	25
	2.4.1.1 Symmetrical NACA blades	25
		VII

	2.4.1.2 Cambered and unsymmetrical blades	31
	2.4.1.3 Turbine blade modifications	34
	2.4.1.4 Turbine blade optimization	41
	2.4.2 Turbine Solidity and Aspect Ratio	45
	2.4.3 Vertical axis wind turbine support-arm	52
	2.4.3.1 Reported turbine support-arm geometry	52
	2.4.3.2 Turbine support-arm configurations	56
	2.4.3.3 support-arm effects in numerical studies	59
	2.5 Discussion	64
	2.6 Research Gap	68
	2.7 Summary	69
3	RESEARCH METHODOLOGY	70
	3.1 Overview	70
	3.2 Methodology Breakdown	71
	3.3 General numerical presentation of studies	74
	3.3.1 Effect of turbine support-arms on a two-bladed NACA0018 turbine	74
	3.3.2 Effect of turbine support-arms on a three bladed NACA0021 turbine	76
	3.3.3 2D aerodynamic shape optimization of the VAWT turbine blade	78
	3.3.4 3D characterization and comparison of the optimized blades against the baseline NACA0018	80
	3.3.5 3D study and characterization of the optimized blade in full turbine configuration	81
	3.4 Computational Fluid Dynamics Approach	82
	3.5 Adjoint Solver	84
	3.5.1 Discrete Adjoint Method	86
	3.5.2 Fluent Adjoint Solver	87
	3.5.3 Adjoint Optimization Procedure	90
	3.6 Theory and Governing Equations	92
	3.6.1 Continuity Equation	92
	3.6.2 Momentum Equation	95

	3.6.3 Navier-Stokes Equation	98
	3.6.4 Governing Equations for an Incompressible Flow	102
	3.6.5 K – omega SST Turbulence Model	102
	3.6.6 Other Numerical Simulation Parameters	105
	3.6.7 Performance Coefficients	105
	3.7 Experimental Setup	107
	3.7.1 Experimental Methodology	107
	3.7.2 Wind Tunnel	109
	3.7.3 Sensors and Equipment	113
	3.8 Summary	113
4	RESULTS AND DISCUSSION	114
	4.1 Overview	115
	4.2 Grid Independence Test	115
	4.3 Performance Analysis and Characterization of the Two Bladed NACA0018	116
	4.3.1 Effect of support-arms on Turbine Performance Coefficient	118
	4.3.2 Effects of support-arm on Turbine Lift and Drag Coefficient	120
	4.3.3 Velocity Flow Physics Comparisons	122
	4.3.4 Pressure Contour Comparisons	125
	4.3.5 NACA0018 - Summary	127
	4.4 Performance Analysis and Characterization of the Two Three Bladed NACA0021 With Dual support-arms	128
	4.4.1 Effect of support-arms on Turbine Performance Coefficients	129
	4.4.2 Analysis of the Lift and Drag Contribution During Turbine Operation	130
	4.4.3 Velocity Flow Physics Comparisons	131
	4.4.4 Pressure Contour and Streamlines Analysis	134
	4.4.5 NACA0021 – Summary	136
	4.5 A Novel Aerodynamic Shape Optimization Scheme on a NACA0018 VAWT for Improved Turbine Performance	138

Using the Adjoint Method	
4.5.1 Moment Optimization at TSR 1	138
4.5.1.1 TSR 1 single blade analysis	138
4.5.1.2 Full turbine performance analysis and comparison	140
4.5.1.3 20D – TSR 1 Blade profile	141
4.5.1.4 Velocity Flow Contour	142
4.5.1.5 Streamline and Pressure Contour	143
4.5.2 Moment Optimization at TSR 2	145
4.5.2.1 TSR 2 single blade analysis	145
4.5.2.2 TSR 2 full turbine performance analysis and comparison	147
4.5.2.3 120D - TSR 2 blade profile	148
4.5.2.4 Velocity flow contour analysis	149
4.5.2.5 Streamline and pressure contour	151
4.5.3 Lift Coefficient	153
4.5.4 Blade Surface Pressure Distribution	154
4.5.5 Adjoint Observables	156
4.5.6 2D Aerodynamic Optimization – Summary	157
4.6 Adjoint Method Shape Optimization of a Vertical Axis	159
Wind turbine blade: Cambered Blade Starting Shape	
4.6.1 Single Blade Optimization Analysis	160
4.6.2 Turbine Performance Analysis	161
4.6.3 Velocity Contour Comparison – S1046 Optimization	164
4.6.4 Pressure and Streamline Contour Analysis – S1046 Optimization	165
4.6.5 Lift Coefficient Analysis – S1046 Optimization	169
4.6.6 Blade Surface Pressure Comparison - S1046 Optimization	170
4.6.7 Adjoint Observables – S1046 Optimization	171
4.6.8 S1046 Optimization - Summary	172
4.7 Adjoint Method Shape Optimization of a Vertical Axis	173
Wind Turbine: 3D Analysis and Characterization of the	

Candidate 120D Blade	
4.7.1 3D Blade Comparisons	174
4.7.2 Lift Comparison – 3D Analysis	176
4.7.3 Flow Contour Comparisons	177
4.7.3.1 Pressure contour comparisons – NACA0018	177
and 120D	
4.7.3.2 Streamline comparisons – S1046 and 120D	179
4.7.3.3 Velocity flow contour comparisons – S1046 vs	182
120D	
4.7.3.4 Velocity flow contour comparisons – NACA0018	183
vs 120D	
4.7.4 Vortex Q-Criterion Comparison – S1046 vs 120D	185
4.7.5 Blade surface comparison	188
4.7.6 3D Turbine Blade Analysis - Summary	189
4.8 Adjoint Method Shape Optimization of a Vertical Axis	190
Wind Turbine: 3D Analysis and Characterization of the	
Full Turbine Configuration with Turbine support-arms	
4.8.1 3D Full Turbine Comparisons	191
4.8.2 Lift and Drag Coefficient Comparisons of Main	193
Turbine Blade	
4.8.3 Turbine support-arm Performance	195
4.8.3.1 Support-arm performance comparisons	195
4.8.3.2 Support-arm aerodynamic characteristics	200
4.8.4 Velocity Flow Contour – Full Turbine Configuration	202
4.8.5 Pressure Contour – Full Turbine Configuration	204
4.8.6 Further support-arm Analysis	206
4.8.7 Q – Criterion Flow Visualization	210
4.8.8 3D Full Turbine Configuration – Summary	212
4.9 Experimental Performance Analysis, Characterization,	215
and Validation	
4.9.1 Rotational Speed	214
4.9.2 Power Performance Analysis	215
4.9.3 Effect of Optimized Blade on Turbine Solidity	216

	4.9.4 Effect of Optimized Blade on Turbine Aspect Ratio	218
	4.9.5 Experimental Summary	219
	4.10 Chapter 4 - Summary	219
5	CONCLUSION	221
	5.1 Concluding Remarks	221
	5.2 Future Works	224
	REFERENCES	225
	Appendix	224
	Appendix A – Wind Tunnel Drawings	237
	Appendix B – Experimental sensors and equipment	241

List of Figures

Fig No.	Title	Page
Fig 1.1	Increasing trend of wind energy reproduced from annual report from REN21	2
Fig 1.2	Comparison of different energy sources in Europe	2
Fig 1.3	Structural differences between the HAWT and VAWT	5
Fig 1.4	The world's largest egg-beater shaped VAWT named Éole	7
Fig 1.5	Three-bladed helical VAWT with serrated blade design by Wang et. al.	7
Fig 2.1	Data of publications related VAWT taken from Scopus. (Hand and Cashman 2020)	14
Fig 2.2	Wind tunnel by Li et al. (Li, Maeda, et al. 2016a, b)	15
Fig 2.3	Centrifugal blower style experimental setup by Sengupta et al. (Sengupta, Biswas, and Gupta 2016)	15
Fig 2.4	Velocity contour by Naseem et al. (Naseem et al. 2020) showing high turbulent region due to bluff bodies and ideal locations for turbine placement	17
Fig 2.5	Reported predicted torque comparison between the Transition SST model and the SST $k-\omega$ model reported by Almohammadi et al. (Almohammadi et al. 2015)	20
Fig 2.6	Visualizations of Q-criterion for (a) 2.5D SST $k-\omega$, (b) 2.5D LES, (c) 3D SST $k-\omega$, (d) 3D LES by He et al. (He et al. 2020)	21
Fig 2.7	Comparisons of iso vorticity contours of (a) 2.5D URANS using the SST $k-\omega$ model and (b) 2.5D LES model by Li et al. (Li et al. 2013)	22
Fig 2.8	Comparisons of different numerical studies with different CFD codes on the NACA0021 airfoil blade.	24
Fig 2.9	Geometries of different NACA symmetrical blades.	26
Fig 2.10	Comparisons of reported (a) NACA0015 and (b) NACA0018 power coefficient predictions based on CFD of the NACA0015 by various authors. Note that the differences may be due to factors such as wind speed or numerical model used. Presented are best reported results	27

Fig 2.11	Vorticity comparisons of different turbine blades (Parakkal et al. 2019)	32
Fig 2.12	Printed blade in the experimental study comparing different blades by Sengupta et al. (Sengupta, Biswas, and Gupta 2016)	33
Fig 2.13	Vorticity streamline by Tahani et al (Tahani et al. 2016) showing larger vorticity extending throughout the inner surface of the NACA4412 against a smaller vorticity	34
Fig 2.14	Airfoil showing leading edge serration by Yan et al. (Yan et al. 2021)	36
Fig 2.15	Bionic airfoil design suggested by Zhang et al (Zhang et al. 2022)	37
Fig 2.16	Flow vorticity contour with and without trailing edge flap by Yang et al. (Yang et al. 2017)	38
Fig 2.17	Winglet blade design suggested by Lain et al. (Lain, Taborda, and López 2018).	41
Fig 2.18	Definition of the aspect ratio	45
Fig 2.19	Comparisons of solidity ratio of the VAWT by Ahmadi-Baloutaki et al. (Ahmadi-Baloutaki, Carriveau, and Ting 2014)	47
Fig 2.20	Single support-arm design utilizing airfoil blade NACA0020 by Bianchini et al (Bianchini et al. 2017)	53
Fig 2.21	Inclined support-arm arrangement by De Marco et al. (De Marco et al. 2014)	53
Fig 2.22	Effects of arm geometry on power coefficient losses by Ahmadi-Baloutaki et al. (Ahmadi-Baloutaki, Carriveau, and Ting 2014)	55
Fig 2.23	Comparisons of power coefficient of different geometry by Hara et al. (Hara et al. 2019). Experimental results were referred from another study	55
Fig 2.24	Cross section of the support-arms along its span length (Hand and Cashman 2017)	56
Fig 2.25	support-arm cross section showing different blade profile along its span length (Hand and Cashman 2017)	56
Fig 2.26	Dual support-arm configuration by Hashem and Mohamed (Hashem and Mohamed 2018)	58
Fig 2.27	Frame type configuration with support-arms at each turbine blade ends by Lee and Lim (Lee and Lim 2015)	58

Fig 2.28	Effect of turbine arm chord length on power coefficient by De Marco et al. (De Marco et al. 2014)	59
Fig 2.29	Two support-arm arrangement from He et al. (He et al. 2020)	59
Fig 2.30	V shape support-arm configuration by Vergaerde et al. (Vergaerde et al. 2020)	59
Fig 2.31	Iso vorticity contour showing vortex shedding around the turbine blades and support-arm by Bachant et al. (Bachant and Wosnik 2016b)	61
Fig 2.32	Comparison by Siddiqui et al. (Siddiqui, Durrani, and Imran 2013) showing the effects of support-arm and turbine hub on the power coefficient against the baseline turbine with no support structure	62
Fig 2.33	Vortex structures shown around the support-arm area by Qin et al. (Qin et al. 2011)	63
Fig 2.34	Comparisons showing (a) tip vortex induced by armless blades and (b) loop-like vortex generated by the rectangular arm. (Hara et al. 2019)	64
Fig 3.1	Structure of the proposed research methodology of this study	73
Fig 3.2	(a) NACA0018 dual arm turbine sketch and (b) mesh around the turbine inside the rotating region.	75
Fig 3.3	Definitions for (a) single arm, (b) dual arm and (c) sum of arms in the two-blade NACA0018 dual arm analysis	76
Fig 3.4	Definitions for (a) single arm, (b) dual arm and (c) sum of arms in the analysis three-bladed NACA0021 dual arm	78
Fig 3.5	Shown above is the (a) 2D simulation rotating domain of the NACA0018 blade and (b) mesh resolution at blade near wall	80
Fig 3.6	Shown here is the NACA0018 simulation domain of the (a) mesh of rotating region and (b) isometric view of the rotating domain	81
Fig 3.7	NACA0018 full turbine configuration showing the (a) mesh of rotating region and (b) isometric view of the rotating region	82
Fig 3.8	Visualization of the full 3D domain mesh resolution	83
Fig 3.9	Mesh resolution of the rotating domain	84
Fig 3.10	Flow chart of the adjoint solver optimization	85
Fig 3.11	(a) Adjoint observables tab with the defined parameters and (b) adjoint	88

	calculation tab	
Fig 3.12	Design tool tab where objective function and bounding region were defined	88
Fig 3.13	Bounding region and control points around the S1046 airfoil geometry set to 20 points each in the X and Y direction	89
Fig 3.14	Gradient-based optimizer tab	89
Fig 3.15	Bounding region around the single blade geometry with 20 control points in both X and Y direction	90
Fig 3.16	A representation of the single blade optimization with θ in the Fig denoted the azimuthal angle at which the optimization scheme was conducted	91
Fig 3.17	Vector visualization at the tested cases coloured by shape sensitivity magnitude	92
Fig 3.18	Visualization of a control volume of infinitesimal size	93
Fig 3.19	Sketch of the control volume showing the inflow and outflow through each face in for the x – component	96
Fig 3.20	Sketch showing the surface forces acting in the x – direction	97
Fig 3.21	(a) cross section of the turbine blade and (b) span length of the blade	108
Fig 3.22	3D CAD design of the proposed wind tunnel	109
Fig 3.23	Line diagram showing the components of the fabricated wind tunnel	109
Fig 3.24	Wind tunnel used for experiments	110
Fig 3.25	Test section area of the wind tunnel. Shown at back are the honeycomb design to straighten the flow	110
Fig 3.26	Inverter for wind speed control. Varies from 0 Hz to 50 Hz achieving wind speeds of up to 13 m/s at the outlet	111
Fig 3.27	Graph showing the relationship between the velocity inlet and the frequency	112
Fig 3.28	Graph showing the relationship between the outlet velocity and the inverter frequency	113
Fig 4.1	(a) Grid independency and (b) mesh validation against Castelli et al (Castelli et al 2012)	116

Fig 4.2	(a) Grid independence study and the (b) mesh validation of the current CFD against a published experimental study	118
Fig 4.3	Power coefficient comparisons of the baseline turbine against the full turbine comparison	119
Fig 4.4	Comparisons between baseline and full turbine configuration for (a) power coefficient and (b) moment coefficient	119
Fig 4.5	Comparisons between baseline and full turbine configuration of instantaneous (a) power coefficient and (b) moment coefficient for a single turbine blade.	120
Fig 4.6	Comparisons between different support-arm configurations in terms of (a) lift coefficient and (b) drag coefficient of the VAWT at TSR 1.5	121
Fig 4.7	Velocity contour of the flow physics for TSR 1.5 of the baseline turbine with no support-arms at azimuthal angles (a) 30°, (b) 60°, (c) 90° and (d) 120°.	123
Fig 4.8	Velocity contour of the flow physics for TSR 1.5 of the full turbine configuration at azimuthal angles (a) 30°, (b) 60°, (c) 90° and (d) 120°.	124
Fig 4.9	Pressure contour of the flow physics for TSR 1.5 of the baseline turbine with no support-arms at azimuthal angles (a) 30°, (b) 60°, (c) 90° and (d) 120°.	126
Fig 4.10	Pressure contour of the flow physics for TSR 1.5 of the full turbine configuration at azimuthal angles (a) 30°, (b) 60°, (c) 90° and (d) 120°.	127
Fig 4.11	(a) power coefficient and (b) moment coefficient comparisons of the baseline turbine	129
Fig 4.12	Comparisons between different support-arm configurations in terms of (a) lift coefficient and (b) drag coefficient of the VAWT at TSR 2.5	131
Fig 4.13	Velocity contour of the flow physics for TSR 2.5 of the baseline turbine with no support-arms at azimuthal angles (a) 30°, (b) 60°, (c) 90° and (d) 120°.	132
Fig 4.14	Velocity contour of the flow physics for TSR 2.5 of the full turbine with no support-arms at azimuthal angles (a) 30°, (b) 60°, (c) 90° and (d) 120°	134
Fig 4.15	Pressure contour of the flow physics with streamlines for the TSR 2.5 of the baseline turbine at azimuthal angles (a) 30°, (b) 60°, (c) 90° and (d) 120°.	135

Fig 4.16	Pressure contour of the flow physics with streamlines for the TSR 2.5 of the full turbine configuration at azimuthal angles (a) 30°, (b) 60°, (c) 90° and (d) 120°	136
Fig 4.17	Power coefficient comparison between candidate blades optimized at the selected angles with respect to moment and NACA0018 at TSR	140
Fig 4.18	Power coefficient comparison between VAWT turbines of candidate blades 20D – TSR 1 and NACA90D – TSR 1 against the baseline NACA0018	141
Fig 4.19	Geometric comparison between the selected candidate blade 20D and NACA0018	142
Fig 4.20	Velocity flow contour comparison in full turbine configuration between the (a) candidate torque optimized blade at 20° and the (b) NACA0018 blade at TSR 2	143
Fig 4.21	Velocity flow contour comparison in full turbine configuration between the (a) candidate torque optimized blade at 20° and the (b) NACA0018 blade at TSR 2	145
Fig 4.22	Single blade moment coefficient comparison of the selected candidate blades with respect	147
Fig 4.23	Power coefficient comparison between candidate blades optimized at the selected angles with respect to torque and NACA0018	148
Fig 4.24	Geometric comparison between the selected candidate blade optimized at 120° 120D and NACA0018	149
Fig 4.25	Velocity flow contour comparison between the (a) candidate blade 120D optimized at 120° and the (b) NACA0018 blade at TSR 2.	151
Fig 4.26	Streamline contour comparison between the (a) candidate torque optimized blade at 120° and the (b) NACA0018 blade at TSR 2. Streamline contour imposed onto pressure contour	153
Fig 4.27	Lift coefficient comparison between (a) 20D at TSR 1 and the (b) 120D at TSR 2 against the baseline NACA0018 blade. Analysis conducted at TSR 2	154
Fig 4.28	Pressure distribution comparison between (a) 20D and the (b) 120D at TSR 2 0° azimuth angle	156
Fig 4.29	(a) TSR 1 20D and (b) TSR 2 120D	157

Fig 4.30	Summary of the two selected candidate blades against the baseline NACA0018 blade	158
Fig 4.31	Instantaneous of moment coefficient comparison in single blade configuration	161
Fig 4.32	Power coefficient comparison of the cambered candidate turbines against the baseline S1046	162
Fig 4.33	Instantaneous power coefficient comparisons of single turbine blades of the candidate turbines during turbine operation at TSR 1.5	163
Fig 4.34	Shape comparison of the candidate blade S1046 – 30D and the S1046 baseline blade	163
Fig 4.35	Velocity contour comparison for (a) S1046 and (b) S1046 – 30D taken at TSR 1.5	165
Fig 4.36	Pressure contour comparison between (a) S1046 and (b) S1046 – 30D. Data taken at TSR 1.5	168
Fig 4.37	Streamline contour comparisons coloured by velocity of the baseline (a) S1046 against the (b) S1046 – 30D taken at TSR 1.5. Streamline imposed on the pressure contour from previous Fig	169
Fig 4.38	Lift coefficient comparison between (a) 20D at TSR 1 and the (b) 120D at TSR 2 against the baseline NACA0018 blade. Analysis conducted at TSR 1.5	170
Fig 4.39	Pressure distribution analysis and comparisons at 30° and 90° azimuthal angles. Data taken at TSR 1.5	171
Fig 4.40	Changes in observables for (a) S1046 – 30D and (b) S1046 - 40D	172
Fig 4.41	Power coefficient comparison between the candidate turbine against the NACA0018 and S1046 and (b) power coefficient curve at low wind speed of 3m/s.	174
Fig 4.42	Instantaneous coefficient comparison single blade between baseline NACA0018 and candidate turbine 120D at TSR 1	175
Fig 4.43	Polar plot of the instantaneous power coefficient comparison between the candidate 120D blade against the common symmetrical blades. Data taken at TSR 1	176
Fig 4.44	Lift coefficient comparison. Data taken at TSR 1.5	177
Fig 4.45	Instantaneous coefficient comparison single blade between (a) S1046 and	179

	(b) candidate turbine 120D at TSR 1.5	
Fig 4.46	Streamline and pressure contour comparison between the (a) NACA0018 blade and the (b)120D blade at TSR 1.5	181
Fig 4.47	Velocity flow comparisons between the (a) S1046 and (b) candidate turbine 120D at TSR 1.5	183
Fig 4.48	Velocity flow comparisons between the (a) NACA0018 and (b) candidate turbine 120D at TSR 1.5	185
Fig 4.49	Q-criterion comparisons between the (a) S1046 and (b) candidate turbine 120D at TSR 1.5	188
Fig 4.50	Pressure distribution analysis and comparisons at 40° and 320° azimuthal angles. Data taken at TSR 1.5.	189
Fig 4.51	Power coefficient comparison between baseline NACA0018 and candidate turbine 120D	191
Fig 4.52	Instantaneous coefficient comparison single blade and support-arm between baseline NACA0018 and candidate turbine 120D at TSR 1	193
Fig 4.53	(a) Lift coefficient vs angle of attack, (b) drag coefficient vs angle of attack, (c) lift to drag ratio vs angle of attack, and (d) lift coefficient vs drag coefficient	194
Fig 4.54	Power coefficient losses comparisons at (a) 6m/s, (b) 7m/s, and (c) 8m/s	196
Fig 4.55	Percentage power coefficient loss comparison between baseline NACA0018 arm and candidate turbine 120D	196
Fig 4.56	Instantaneous moment coefficient comparison single arm between baseline NACA0018 and candidate turbine 120D at (a) TSR 1, (b) TSR 1.25, (c) TSR1.5, and (d) TSR1.75	198
Fig 4.57	Power coefficient curve comparison between the NACA0018 support-arm and 120D support-arm over a single turbine rotation	199
Fig 4.58	Polar plot of power coefficient curve comparison over a single turbine rotation taken at TSR 1.5	200
Fig 4.59	Lift coefficient curve comparison (a) algebraic sum of arms (b) single support-arm over a single turbine rotation taken at TSR 1.5	201
Fig 4.60	Drag coefficient curve comparison (a) algebraic sum of arms (b) single support-arm over a single turbine rotation taken at TSR 1.5	202

Fig 4.61	Velocity flow contour between the (a) NACA0018 and (b) 120D	204
Fig 4.62	Pressure contour between the (a) NACA0018 and (b) 120D	206
Fig 4.63	Upper surface arm pressure contour comparison between the (a) NACA0018 and (b) 120D	208
Fig 4.64	Lower arm pressure contour comparison between the (a) NACA0018 and (b) 120D	210
Fig 4.65	Q criterion visualization contour of (a) NACA0018 turbine and (b) 120D turbine	212
Fig 4.66	Turbine rotational speed comparisons at (a) 5m/s, (b) 5.6m/s, (c) 6m/s and (d) 6.5m/s	214
Fig 4.67	Power performance comparison between the candidate 120D turbine and baseline NACA0018 turbine at (a) 5m/s, (b) 5.6m/s, (c) 6m/s and (d) 6.5m/s	216
Fig 4.68	Power performance comparison of the different turbine solidity at (a) 5m/s, and (b) 5.6m/s inlet velocity	217
Fig 4.69	Comparisons of different turbine aspect ratio at (a) 6m/s, and (b) 6.5m/s inlet velocity	219

List of Tables

Table No.	Title	Page
Table 2.1	Various reported VAWT parameters from literature	29
Table 2.2	Summary of reported optimal solidity from literature	50
Table 2.3	Reported optimal aspect ratios from literature	52
Table 2.4	Summary of the main findings and studies in this literature review	67
Table 3.1	Turbine dimensions for NACA0018 turbine	75
Table 3.2	Turbine dimensions for NACA0021 turbine	77
Table 3.3	Turbine dimensions for 2D optimization	79
Table 3.4	Turbine dimensions for 3D characterization study	80
Table 3.5	Turbine dimensions for optimization	82
Table 3.6	Velocity at the inlet relative to the frequency of the fan inverter	112
Table 3.7	Outlet velocity relative to the inverter frequency	112
Table 3.8	Summary of experimental equipment and its function	113
Table 4.1	Summary of lift and drag coefficients	121
Table 4.2	Summary of output parameters at TSR 2.5	130
Table 4.3	Average lift and drag coefficients of the wind turbine support-arms	130
Table 4.4	Summary of the torque optimization at TSR 1 at various incremental azimuth angle	139
Table 4.5	Summary of the moment optimization at TSR 2 at various incremental azimuth angle	146
Table 4.6	Summary of the moment optimization at TSR 2 at various incremental azimuth angle	161
Table 4.7	Parameters of the turbine solidity study.	217
Table 4.8	Parameters of the aspect ratio study.	218
Table 4.9	Recommended parameter for the 120D turbine.	220

Chapter 1

Introduction

1.1 Preface

Recently, the growing environmental awareness and concern over the detrimental effects of fossil fuels on climate change have fueled a surge in the global adoption of alternative renewable energy sources. This is partly due to the rapid decline of finite resources such as fossil fuels and coal, which are unsustainable for the ever-increasing energy demand worldwide. A popular source of green, renewable, and sustainable energy is wind energy. The growth of wind energy usage and production has been increasing almost exponentially in the last 10 years as shown in Fig 1.1. In 2018, China emerged as the largest wind energy consumer in both Asia and the world, boasting a capacity of 184.655 GW, accounting for 32.8% of the global wind energy capacity at that time (IRENA 2019). This was a significant advancement of wind energy adoption from 2011 when the country displayed a wind energy capacity of 62.733 GW (Islam, Mekhilef, and Saidur 2013). Along with Asia, Europe is also big wind power adopters. In 2018, Europe installed 11.3 GW of new wind energy; taking the total capacity up to 178.8 GW within the EU (WindEurope 2019). In 2019, this total grew up to 205 GW which accounted for 15% of electricity consumption among the EU-28 nations (WindEurope 2020b). Onshore infrastructures currently dominate with a capacity of 183 GW and 22 GW offshore (WindEurope 2020b). While the statistics considered both onshore and offshore wind energy sources, a trend seen in recent literature and published reports indicate new offshore installations as well as the overall cumulative capacity of offshore wind energy has been on a dramatic rise since 2009 (WindEurope 2020a). Fig 1.2 compares the wind energy adoption rate by year compared to other sources of energy. Offshore wind energy extraction has been reported to harvest wind energy better due to higher wind speeds which in turn allows turbines to produce more electrical energy (Bilgili, Yasar, and Simsek 2011). The much smoother and uniform surface of the sea also means turbines are exposed to more uniform wind speeds and less likely to experience turbulence compared to onshore turbines (Bilgili, Yasar, and Simsek 2011, Shen et al.

2018). Also, offshore wind turbines have the added advantage of being far from populated areas which means less noise pollution to humans (Shen et al. 2018). Hence, coupled with the finite amount of land use for turbine farms, means it is expected that future investment in power generation using wind energy should be more focused on offshore turbines.

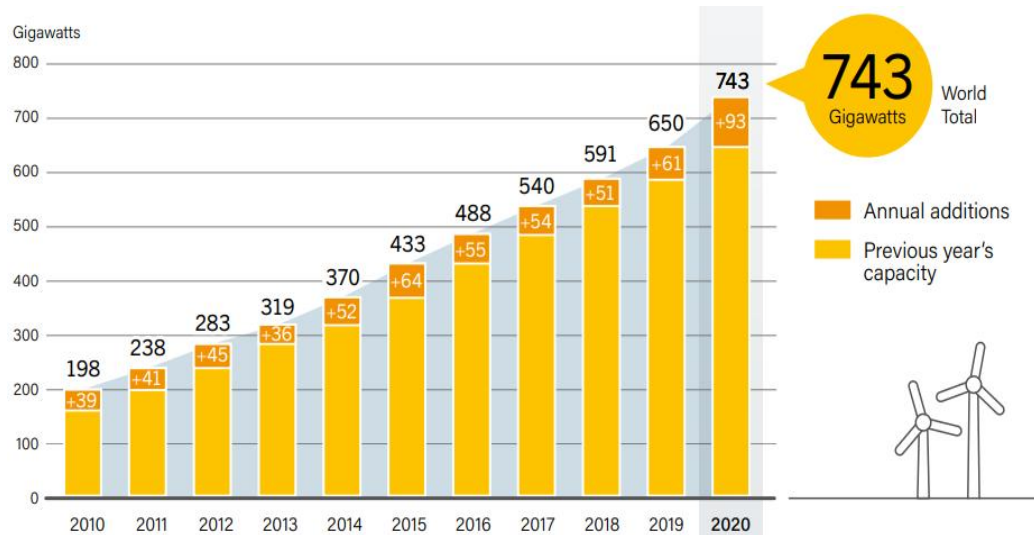


Fig 1.1 Global increasing trend of wind energy [Source; REN 21, 2021 (REN 21 2021)].

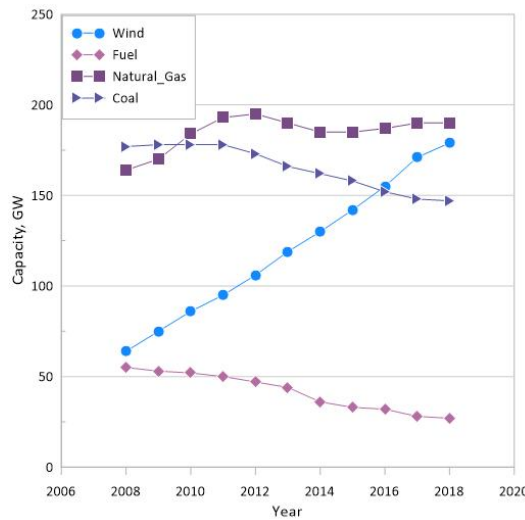


Fig 1.2: Comparison of different energy sources in Europe (WindEurope 2019).

Wind turbines can be described into two types based on their orientation: the horizontal axis wind turbine (HAWT) and the vertical axis wind turbine (VAWT). Although the horizontal axis wind turbine (HAWT) is typically considered to have higher performance efficiency compared to the vertical axis wind turbine (VAWT),

the VAWT has recently gained popularity due to its numerous advantages over its horizontal counterpart. One of its most notable advantage is that unlike the HAWT, the VAWT is omnidirectional and therefore can harvest energy at any direction without the use of a yaw mechanism (Rezaeiha, Kalkman, and Blocken 2017b). It's been known that the VAWT is less efficient with respect to power generation when compared to the HAWT whereby most large-scale power generation tend to favour the later (Islam, Mekhilef, and Saidur 2013, Wang, Wang, and Zhuang 2018, Wang, Zeng, et al. 2018, Ismail and Vijayaraghavan 2015). However, VAWTs are insensitive to wind direction which enables multiple turbines to be packed closer together at wind turbine farms. In fact, research have shown packing VAWTs together at an optimal distance can have a beneficial effect (Jin et al. 2020, Youngblood and Roy 2021). This means that on average a VAWT farm is capable of producing more energy compared to its horizontal counterpart given the same amount of land space (Islam, Mekhilef, and Saidur 2013) and coupled with the fact that VAWT have lower centre of gravity makes it ideal for offshore power generation (Delafin et al. 2016, Chen et al. 2016). Its low manufacturing cost is also attractive for small scale power generation such as in urban areas (Jacob and Chatterjee 2019, Nini et al. 2014, Li, Maeda, Kamada, Murata, Shimizu, et al. 2016). But unlike the HAWT, the viability of VAWT used in urban areas is further highlighted by the fact that VAWT tend to have lower rotational speed or operate at lower TSRs which translate to lower noise emissions (Howell et al. 2010, Lei et al. 2017). In terms of energy generation, compared to HAWT, VAWT have better scalability to generate electricity beyond 10 MW due to the orientation of the blade that does not undergo stress cycles caused by gravity (Chen et al. 2016, Chen et al. 2015, Howell et al. 2010). Also, unlike the HAWT, the VAWT turbine blades are arranged vertically around the centre shaft with the generator and gearbox located at the bottom rotor base (Islam et al. 2018). This would allow ease of maintenance of the wind turbine. Hence, with all the significant advantages of the VAWT due to its vertical design, Ismail et al (Islam, Mekhilef, and Saidur 2013) predicted that within the next 20 to 30 years VAWT type turbines will have increased prominence.

1.2 Wind turbine

In this chapter, the differences between the HAWT and VAWT were discussed. Fig 1.3 shows the structural differences between the two wind turbine types. Although it is generally known that the HAWT tend to have higher performance efficiency of the two wind turbine types, the VAWT from this point onwards, has seen a recent surge in popularity due to many advantages over its horizontal cousin. One of its most notable advantage is that unlike the HAWT, the VAWT is omnidirectional and therefore can harvest energy at any direction without the use of a yaw mechanism (Rezaeiha, Kalkman, and Blocken 2017b). It's been known that the VAWT is less efficient with respect to power generation when compared to the HAWT whereby most large-scale power generation tend to favour the later (Islam, Mekhilef, and Saidur 2013, Wang, Wang, and Zhuang 2018, Wang, Zeng, et al. 2018, Ismail and Vijayaraghavan 2015). However, VAWTs are insensitive to wind direction which enables multiple turbines to be packed closer together at wind turbine farms. This means that on average a VAWT farm is capable of producing more energy compared to its horizontal counterpart given the same amount of land space (Islam, Mekhilef, and Saidur 2013) and coupled with the fact that VAWT have lower centre of gravity makes it ideal for offshore power generation (Delafin et al. 2016, Chen et al. 2016). Its low manufacturing cost is also attractive for small scale power generation such as in urban areas (Jacob and Chatterjee 2019, Nini et al. 2014, Li, Maeda, Kamada, Murata, Shimizu, et al. 2016). The viability of VAWT used in urban areas is further highlighted by the fact that VAWT tend to have lower rotational speed or operate at lower TSRs which translate to lower noise emissions (Howell et al. 2010, Lei et al. 2017). In terms of energy generation, VAWT has better scalability to generate electricity beyond 10 MW due to the orientation of the blade that does not undergo stress cycles caused by gravity (Chen et al. 2016, Chen et al. 2015, Howell et al. 2010). Hence, with all the significant advantages of the VAWT due to its vertical design, Ismail et al predicted that within the next 20 to 30 years VAWT type turbines will have increased prominence (Islam, Mekhilef, and Saidur 2013).

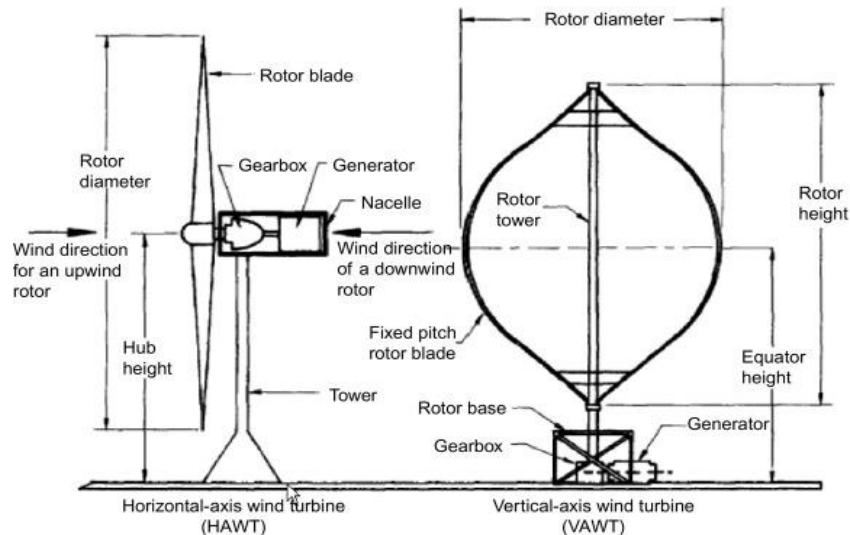


Fig 1.3. Structural differences between the HAWT and VAWT (Islam et al. 2018).

1.3 Types of VAWT

The VAWT can be divided into two types: the lift type Darrieus turbine and the drag type Savonius turbine. Several studies have demonstrated the performance differences between Savonius and Darrieus turbines, with lift-type Darrieus turbines consistently outperforming Savonius turbines in terms of power efficiency across all TSR ranges, despite the latter's strong self-starting ability (Wekesa, Saoke, and Kamau 2020). A comprehensive review of on various topics pertaining to numerical and experimental investigations of Savonius turbines have been done by Roy and Saha (Roy and Saha 2013a, Roy and Saha 2013b).

Multiple variations of the Darrieus-type VAWT exist. There have been design studies that incorporated both Darrieus and Savonius type VAWT (Chen et al. 2015) which was shown to improve turbine self-starting ability. The troposkein or egg-beater shaped VAWT is one of the earliest VAWT design first developed and described by Georges Darrieus (Marie 1931). A troposkien or egg beater shape wind turbine (Gipe 1995) typically has a tall slender tower with a narrower base and wider top, resembling an inverted egg beater. The turbine blades are usually curved or spiral-shaped, resembling the shape of an egg beater as shown in Fig 1.4. This simple configuration allows the blades to generate torque around the main rotor shaft without the need for additional support structures. One of the main problems with the egg-beater shape VAWT is the torque ripple generated by a common two bladed configurations but this can usually be improved by increasing the number of blades

(El Bassam, Maegaard, and Schlichting 2013). Although this arrangement usually generate best power and torque coefficient especially at high TSR, increasing the number of blades would also improve other aspects such as thrust and lateral force ripples therefore enhancing the turbine lifespan (Delafin et al. 2016). However, when compared to other lift types arrangement, the curved blades of the egg-beater shaped turbine was more susceptible to local dynamic stall compared to the straight bladed H-type turbine (Scheurich, Fletcher, and Brown 2010, Scheurich, Fletcher, and Brown 2011). Lastly, the egg-beater shape has poor starting torque, hampering its self-starting ability and would therefore require a starting mechanism to operate (El Bassam, Maegaard, and Schlichting 2013).

The H-type or Giromill is the most common wind turbine shape. The general configuration is an airfoil connected to the main shaft by support-arms of varying shapes and cross sections. The overall structure however may not be as aesthetically pleasing as the egg-beater shape. A key advantage of the H-type turbine over the egg-beater shape is its ability to self-start without the need for any external mechanism (El Bassam, Maegaard, and Schlichting 2013). A variation of the H-type turbine is the helical shape, shown in Fig 1.5. The main distinguishable difference between the two is that the helical turbine has each blade twisted at an angle. This structural difference was reported to have a positive effect on the torque oscillation (Wang, Wang, and Zhuang 2018, Marsh et al. 2015) and overall torque coefficient (Scheurich, Fletcher, and Brown 2010). The incline of the blade promotes a higher angle of attack which in turn increases the tangential forces acting on the blades during the blade rotations (Scheurich, Fletcher, and Brown 2010).

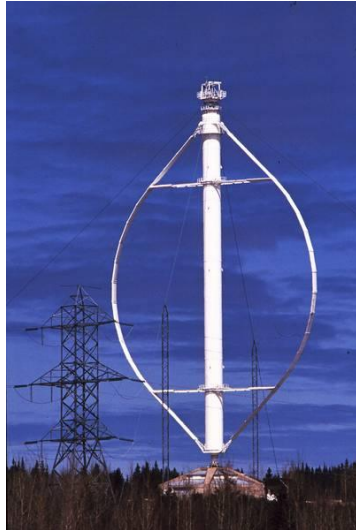


Fig 1.4. The world's largest egg-beater shaped VAWT named Éole (Gipe 1995).

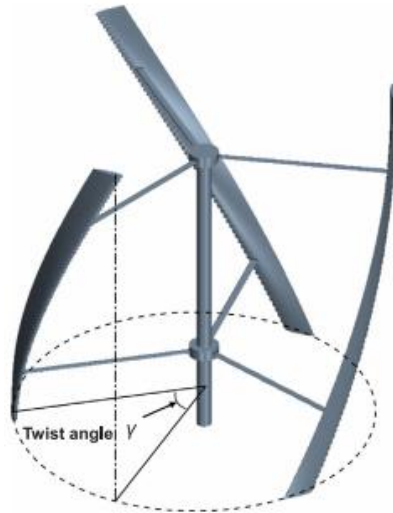


Fig 1.5. Three-bladed helical VAWT with serrated blade design by Wang et al (Wang, Wang, and Zhuang 2018).

1.4 Problem Statement

A thorough analysis of existing literature was conducted to review VAWT designs and their performance, seeking to pinpoint any possible research gaps or issues. From the current literature, various studies have described and investigated numerous ways to improve the design of VAWT. Many design considerations were made towards the turbine blade for improved turbine performance. However, the aerodynamic geometrical optimization of the turbine blade and support-arm structure of the VAWT has not been fully explored. Therefore, the following problem statement has been devised:

- Minimal design considerations as well as justifications for turbine support-arm geometry choices have been given. Several investigations on the effects of support-arms on the VAWT with respect to aerodynamic performances have been conducted but have not been fully understood especially with regards to the support-arms lift contributions.
- Although various studies have demonstrated optimization schemes to improve the VAWT, an in-depth and conclusive study on the adjoint method

and its effectiveness and efficacy to optimize the turbine blade and support-arms has not been adequately addressed in literature.

- To the author's knowledge, an optimization scheme or procedure on the aerodynamic structures of the turbine blade such as the turbine blades and support-arms has not been fully explored.
- Hence, implementing an adjoint method optimization on turbine blades to enhance aerodynamic performance and boost turbine efficiency could greatly benefit the renewable energy industry. Additionally, this optimization scheme could serve as a blueprint for applying similar improvements in the vertical axis wind turbine (VAWT) sector.

This study was conducted to address the problem statements developed above. To that end, several research questions were developed and objectives to answer these questions were then derived.

1.5 Research Question

From the literature review, the following research questions were developed:

- What are the aerodynamic force contributions of the wind turbine blade and support-arm during turbine operations?
- What are the flow physics around wind turbine blades and support arms, and how do they impact the aerodynamics of turbine operation?
- Can a shape optimization scheme be applied to a transient wind turbine problem to enhance the turbine blade and support-arm performance?
- What is the best design for the turbine blade and support arm for optimal performance?
- How does the flow physics around the new turbine blade and support-arm compare to current symmetrical and unsymmetrical blade designs?

1.6 Objectives

To address the problem statements and research questions, the following are the objectives proposed for this PhD thesis:

1. To identify the aerodynamic forces of the turbine blade and support-arms during wind turbine operations using the ANSYS Fluent software.
2. To describe and characterize the flow physics around current turbine blade and support-arm geometries with respect to the velocity and pressure flow field as well as the Q-criterion visualization.
3. To describe a shape optimization scheme based on the adjoint method and gradient based optimizer, both available in the ANSYS Fluent software, for improved turbine power production.
4. To study and quantify various possible candidate blades obtained from the optimization scheme and establish an improved turbine geometry.
5. To investigate the effect of the new optimized full turbine blade and support-arm on the turbine flow characteristics, with specific interest on velocity and pressure flow fields, and Q-criterion vortex visualization.

1.7 Hypothesis

From the literature review conducted thus far, several research questions have been proposed and a problem statement was formed. To address the various research questions, a hypothesis, with respect to the shape optimization of the VAWT, was made. It was expected that a shape optimized turbine blade as well as turbine support-arms, based on the adjoint method optimization together with the gradient based optimizer, will contribute to better flow physics that is conducive towards the turbine performance with respect to power production during turbine operation. A numerical-based procedure was developed and proposed for the shape optimization of the main aerodynamic structures of the turbine and was expected to contribute to clearer knowledge of the flow physics around the wind turbines, as well as establish an optimization procedure based on the adjoint method that enhances the turbine performance. This hypothesis was then tested and validated in numerical and experimental analyses.

1.8 Scope of Study

As was introduced in the previous chapter of this thesis, the study of wind turbines, such as the VAWT, encompasses many different areas or fields of study and

contributed significantly to the popularity and increased interest in VAWT. Hence, to ensure a thorough research and investigation into the wind turbine, particularly in relation to the VAWT support-arm design, the scope and limits of this study are:

1. Only H-type VAWT turbines will be studied and compared. Other VAWT types and HAWT were not considered.
2. The design improvement and optimization only focuses on the aerodynamic aspects of the H-type VAWT. Hence, major design changes incorporating other shapes or combinations of different turbine configurations were not considered.
3. The current study is limited to exploring the aerodynamics of the design. Other important areas of analysis such as noise, vibration, mechanical stresses, and failure analysis will not be included in this research
4. Only technical fluid dynamics with respect to wind turbine design will be considered in this study. Other studies related to wind turbines such as social policies, environmental impact and applications will not be considered.

1.9 Significance of Study

One significant benefit of implementing a new and optimized supporting arm design is the enhanced wind capture ability, resulting in improved overall performance of wind turbines. While previous research has primarily focused on refining the design of the aerofoil itself, little attention has been given to the selection of blade shapes beyond established designs or semi-parametric optimization techniques. By utilizing shape optimization through mesh morphing, it is possible to maximize the aerodynamic efficiency of the turbine blade in relation to specific boundary and initial conditions. Introducing a novel blade geometry based on desired initial conditions can greatly enhance the flow physics of the turbine, leading to increased performance. This study proposed an innovative optimization approach using the adjoint method together with a gradient-based optimizer to enhance the turbine performance. By applying this method to both the turbine blade and supporting arm design, significant improvements in overall turbine efficiency can be achieved.

With respect to the real-world application of an optimized turbine blade, this study contributes in many ways. An improved VAWT could pave the way more applications of wind energy worldwide as an alternative to fossil fuels. In 2013, it was reported that wind energy was responsible for 2.5% of the global electricity demand (Chen et al. 2016). Unlike fossil fuels, wind energy is an abundant, solar-based clean energy, that can be sourced with minimal negative impact towards the environment with an optimized VAWT (Jacob and Chatterjee 2019). It has been established that, due to various factors, VAWT is much cheaper to maintain due to lesser essential parts than a HAWT ((IRENA) 2021).

1.10 Thesis Structure

This thesis was divided into 5 chapters, each subdivided into different sections. An introduction to this research study was given in the first chapter. Chapter 2 presented a literature review on VAWT design. Chapter 3 outlines the research methodology. The results and discussions of this thesis was presented in Chapter 4. The last chapter, Chapter 5, summarized the findings of this research endeavour and addressed how the research questions and objectives were addressed. These chapters were structured to form a cohesive and persuasive dissertation, showcasing the in-depth exploration and analysis of the design of H-type Darrieus turbine.

Chapter 1 has established the foundations of PhD work by introducing the main focus of this study, the VAWT, as well as outlining important information such as the problem statement, research questions, and objectives.

Chapter 2 showcased the in-depth and meticulous analysis of the current turbine blade design in literature as well as identifying a gap with which this thesis laid its foundation on. The comprehensive critical review and discussion of the current reported literature formed the basis of research questions and research gap this thesis aims to address.

Chapter 3 discussed the research methodology and essential theoretical background on CFD and the adjoint method. The chapter introduced the overall methodology with respect to general numerical simulation parameters of each study

in this thesis, optimization method, experimental setup and instruments, as well as the theoretical background and governing equations relating to CFD.

Chapter 4, the arguably the most important chapter in this thesis, presents a comprehensive overview of all the results, findings, and discussions that were made throughout this PhD work. First, mesh analysis will be presented. Mesh independence result and validation against current published literature will be discussed. Next, two research studies, were presented to establish a baseline for current VAWT turbine performance in various configuration. Then, two 2D aerodynamic optimization procedure was proposed. The first study was done to investigate and establish an optimum set of parameters that yields an optimal turbine blade. A second study was conducted on the effects of starting blade shape. A 3D study was then conducted based on the 2D optimization results and compared, with 3D blade and tip effects added for consideration, against a symmetrical and unsymmetrical blade. Later, a full 3D analysis with the optimized blade was pitched against the baseline symmetrical blade in full turbine configuration together with the turbine support-arms, showing the optimal turbine against a current baseline turbine. Finally, the results of the optimization and numerical simulations were then validated in an experimental study. This was done by comparing the candidate turbine and the baseline turbine as well as varying the effects of other parameters to characterize the performance of the candidate turbine.

The fifth and final chapter of this thesis concluded and summarized all the research work that has been done and suggestions for future research derived from this study. The chapter was structured in point form and was crafted to highlight how the findings in the Chapter 4 successfully addressed the research questions and research objectives of this study.

Chapter 2

Literature Review

2.1 Overview

Research into VAWT has seen a significant rise in interest over the years. The surge in popularity can be attributed to multiple factors, such as a rise in renewable energy studies due to more environmentally conscious societies, or the need for a more sustainable alternative as current energy sources have dwindled significantly. The reduction in fossil fuel or finite natural resources and therefore increasing cost of such sources also leads to more research on alternatives.

The data from Scopus presented in Fig 2.1 illustrates the number of research papers published on the topic of VAWT over the years. The figure illustrates a significant increase in research output, especially from 2005 onwards, suggesting that, unlike the HAWT with its more established design, there is still ample opportunity for study and refinement of VAWT design. The abrupt increase in research output pertaining to the VAWT means there is still a lot of research gap that has not been addressed in the current literature. Due to the VAWT having a more flexible design compared to the HAWT, evidenced by its many different variations, this means the VAWT has a wider field of study and significant interest in its design. Although the power coefficient of the VAWT generally tends to be lower than that of the HAWT, which is closer to the Betz limit of 59% (De Lellis et al. 2018, Vennell 2013), the aim of literature, nevertheless, has been to improve the VAWTs efficiency towards this theoretical limit. In this chapter, various reports were made with respect to improving turbine performance. Discussions were made on the many theoretical and experimental power coefficients of the VAWT.

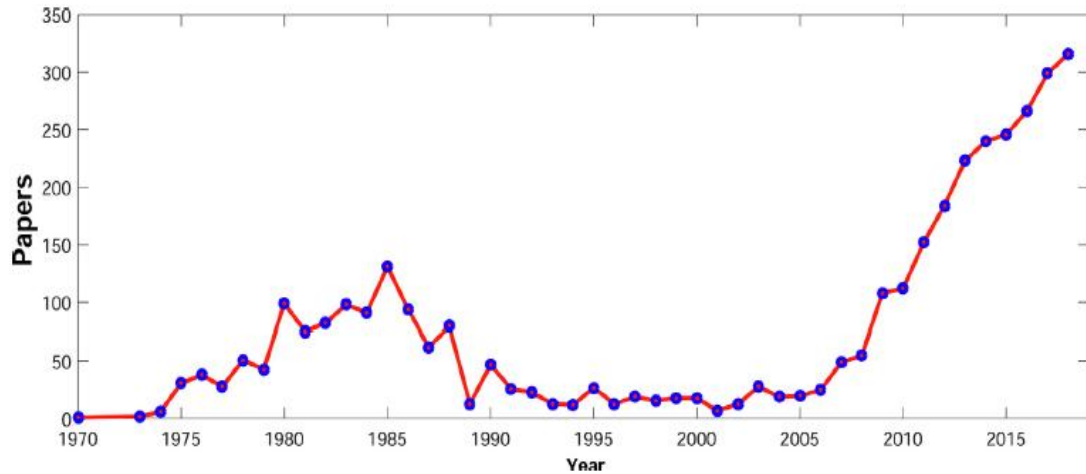


Fig 2.1. Data of publications related VAWT taken from Scopus (Hand and Cashman 2020).

2.2 Experiments and wind tunnel studies

2.2.1 Wind tunnel setups and dimensions

Experiments are designed to collect empirical data either as reference for further numerical analysis or to verify a design proposed by the study. Various VAWT studies have been conducted together with wind tunnel experiments. Multiple experimental setups have been described by various studies. An experiment was conducted by Lee and Lim (Lee and Lim 2015) using an open large-scale boundary layer wind tunnel with dimensions of 2.0 m x 2.1 m x 20.0m and maximum wind speed of 23 m/s. Wind speed was measure by means of a pitot tube at 5 m in front of the turbine at a height of 1 m. He et al. (He et al. 2020) conducted an experiment using a wind tunnel with a length of 6m and cross section of 4.5m x 4.5m consisting nine 80 kW fans. Wind speed for the experiment was varied between 2.0 and 12.5 m/s. The fans were covered by a honeycomb frame of diameter 0.9 cm and thickness of 2.7 cm to reduce flow fluctuations. Li et al. (Li et al. 2015, Li, Maeda, et al. 2016a, b, Li, Maeda, Kamada, Ogasawara, et al. 2017) conducted experiments using an open test section of circular type wind tunnel. The wind tunnel, shown in Fig 2.2, has an outlet diameter of 3.6m with a test section length of 4.5m as shown in the Fig. The wind speed was configurable between 0-30 m/s with the experiment performed at a wind speed of 8 m/s. One of the studies conducted found power coefficient in the field experiment and wind tunnel results were similar at TSR values of less than 2.0 but deviate at higher TSR (Li, Maeda, Kamada, Ogasawara, et al. 2017). Worasinchai et al. (Worasinchai, Ingram, and Dominy 2011) reported a wind tunnel experiment conducted using a 0.5 m Plinth wind tunnel with an open circuit design.

The cross section of the wind tunnel was set to a square cross section of 0.457 m x 0.457 m. Some authors have experimented with different setups other than the traditional wind turbine. A performance testing by Bravo et al. (Bravo, Tullis, and Ziada 2007, Kanyako and Janajreh 2014) utilized a 9m x 9m to determine power efficiency of a VAWT turbine at different wind speed. Sengupta et al. (Sengupta, Biswas, and Gupta 2016) Singh et al. (Singh, Biswas, and Misra 2015) conducted the experiment using a centrifugal blower test rig with wind velocities set at 4 m/s, 6 m/s and 8 m/s. The electric motor used in the centrifugal blower has a 10 HP and rated at 2800 rpm. The turbine was placed at the exit of the centrifugal blower in the free stream zone to ensure uniform wind speed shown in Fig 2.3. An experiment was conducted by Molina et al (Molina et al. 2018) using a wind turbine with a total length of 22m, a rectangular cross section measuring 2.42m x 1.6m, and powered by an inverter with variable wind speed up to 30m/s.



Fig 2.2. Wind tunnel by Li et al. (Li, Maeda, et al. 2016a, b)

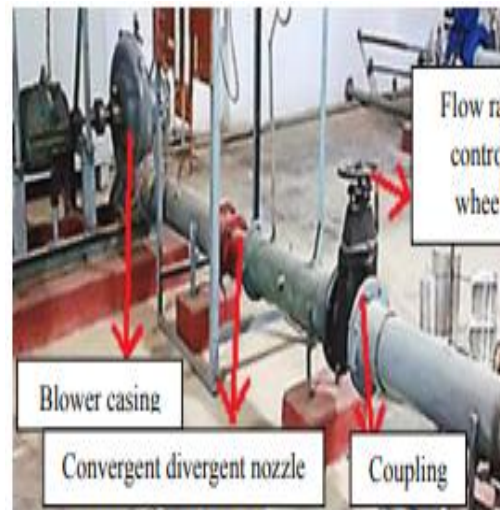


Fig 2.3. Centrifugal blower style experimental setup by Sengupta et al. (Sengupta, Biswas, and Gupta 2016)

2.2.2 Turbulence intensity and modelling

Most experimental wind tunnel studies discussed above have very low turbulence intensity of less than 1% and this is usually an ideal condition not reflective of real-world conditions. Vergaerde et al. (Vergaerde et al. 2020) used four low speed wind tunnel set ups used in their experiments. The blow-down type wind tunnel with a rectangular cross section and turbulence intensity of 0.5% was used to optimize the

experimental set up. Two open-jet type wind tunnels with octagonal and circular cross section at a turbulence intensity of 0.3% were used to measure and compare the power coefficient of the experimental set up. The last closed-circuit rectangular cross section wind tunnel was used to compare different configurations of turbine distance and direction of rotation. The wind tunnel setup mentioned earlier by Li et al. (Li, Maeda, et al. 2016a, b) were set to turbulence intensity of less than 0.5%.

While aerodynamic studies conducted in a controlled environment, such as a wind tunnel as shown above implement low turbulence intensity in their studies, this often does not represent a real-world condition in which VAWT are used in. In an analysis of urban area wind data, Janajreh et al. (su and Janajreh 2012) published a wind study and found an urban area has a turbulence intensity often ranging between 12% to 19% which varies at different heights. This study shows that urban areas do generate a lot of turbulent wind flows which would affect the power efficiency of a wind turbine. And on the effects of an urban environment, Naseem et al. (Naseem et al. 2020) published a study of a simulated urban landscape with VAWT turbines located at certain points behind bluff bodies acting as buildings in the downwind region and found the increased velocity of the wind was achieved between 12% and 25% compared to the free stream velocity which saw significant performance increase of the turbine torque coefficient of up to 56% depending on the number of bluff bodies. The velocity flow contour is shown in Fig 2.4. Although not explicitly stated in their report, it was worth noting that the study emphasised an increase in downstream velocity with contours showing large regions of vortex formations and turbulent wake flow in the immediate vicinity of the downstream region of the turbine as a direct cause of the buildings. Hence, it was suggested that these locations would see an increase in turbulence and its intensity. The turbines placed at various within this turbulent region with high velocity showed a markedly increased performance compared to the baseline turbine.

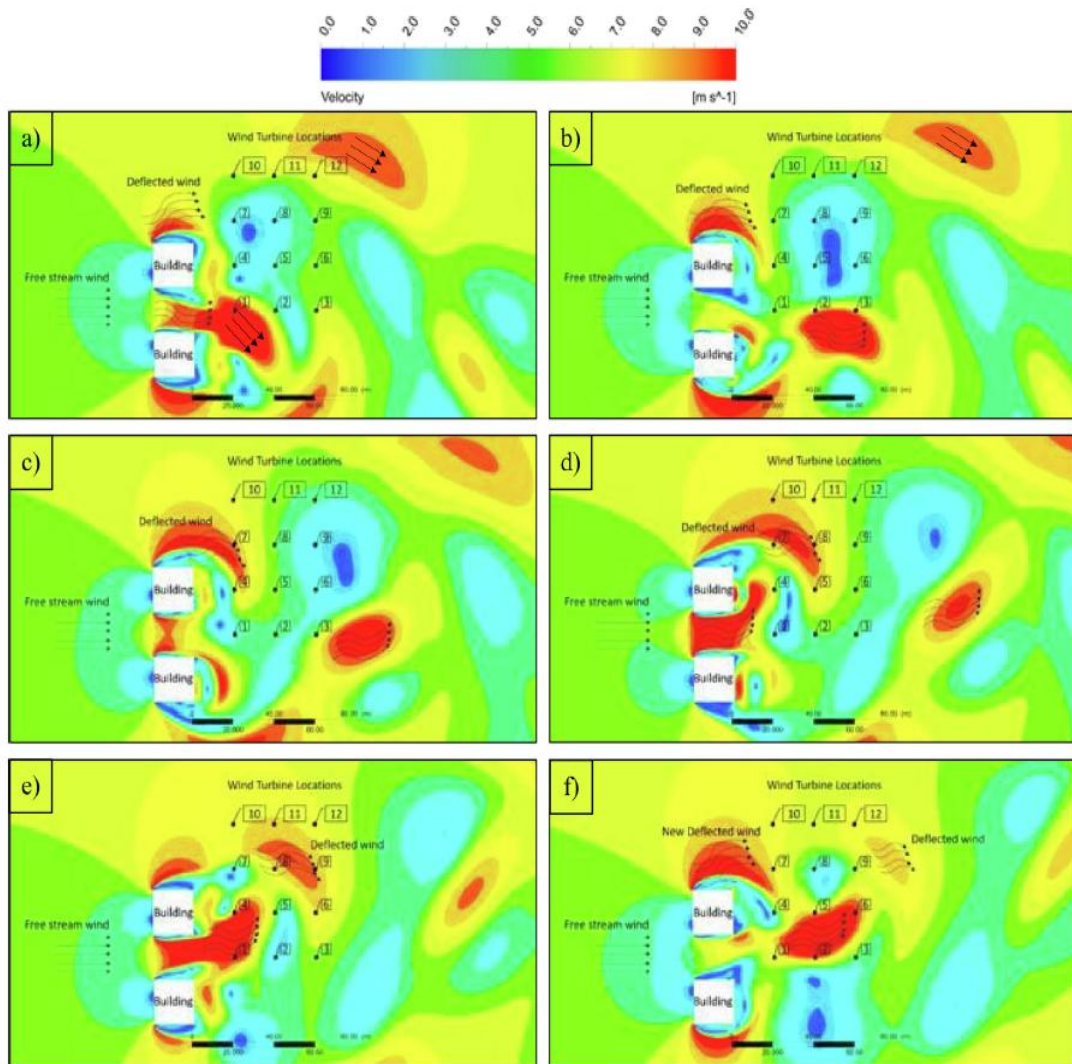


Fig 2.4 Velocity contour by Naseem et al. (Naseem et al. 2020) showing high turbulent region due to bluff bodies and ideal locations for turbine placement.

Studies pertaining to higher turbulent intensity has also been reported. Using wooden grids with varying mesh cross section of differing density to simulate increased turbulence intensity, Molina et al. (Carbó Molina et al. 2019, Molina et al. 2018), found higher turbulence intensity, when varying between 0.5% up to 14.8%, extracted a much larger power efficiency at a range of Reynolds number. A performance increased of up to 20% was seen when increasing from 0.5% up to 9.4% (Molina et al. 2018) and when increased up to 14.8%, the power coefficient increased further (Carbó Molina et al. 2019). The wake study showed more turbulent conditions results in faster wake recovery as well as reduced wake effects due to turbine shaft. These findings were also corroborated and reproduced in a 3D numerical analysis by Belabes and Paraschivoiu (Belabes and Paraschivoiu 2021),

who also found higher turbulence intensity of 14.8% extracted at better efficiency. Wekesa et al. (Wekesa, Saoke, and Kamau 2020) showed turbulent flow regimes not only supports the notion of increased efficiency, but also significantly increases self-starting ability of a small scale VAWT. The study showed that in an urban or utility-orientated usage, a turbulent condition can extract wind energy more efficiently.

2.3 VAWT numerical simulation

In the numerical studies relating to the VAWT, both 2D and 3D approach has been used for different purposes as well as justifications. Although many studies have justified the use of 2D simulation, many have shown that the 2D approach is insufficient when compared with real world data. For example, Howell et al. (Howell et al. 2010) found 2D and 3D simulation to differ by a significant margin with 3D simulation was found to be much more aligned to the experimental data. The difference was especially large at higher TSR values. This is due to 2D simulation hence most data or results predict coefficient values much larger compared to 3D and experimental results. Siddiqui et al. (Siddiqui, Durrani, and Imran 2013) showed 2D simulation tends to over predict by a significant margin due to effects such as wake, tip vorticity and other 3D effects which almost all 2D simulations do tend to omit.

2.3.1 Mesh Independency Test and Validation

A grid or mesh independency test is usually carried out to determine the optimal grid size that balances prediction accuracy as well as computational resource and simulation time. Multiple studies have reported varying optimal grid sizes based on comparisons to experimental data or convergences after multiple refinements of the mesh density. Lain et al. (Laín, Taborda, and López 2018) conducted a grid independence study by comparing a range of coarse (2×10^6 elements) to fine mesh (11×10^6 elements) to determine a suitable grid size of the flow around the turbine. The mesh density was compared to the torque coefficient produced by the turbine. Ultimately, to save computational resources, an intermediate solution was chosen with a grid density of 4.3×10^6 elements. Similar strategy was used by Yang et al. (Yang et al. 2017) whereby the total grid size was varied up to a point whereby the momentum coefficient flat lines at larger grid size showing mesh convergence. The point starting point of where the curve flattens (5.5×10^7 cells) was chosen. Other studies have shown an easier and reliable way to conduct a mesh dependency test is to compare results against experimental data. Chen et al. (Chen et al. 2015) reported

a convergence based on the torque coefficient and the results compared against an experiment which fits quite well at lower TSR but diverges slightly at TSR values of 1.5 and higher. Other studies such as those by Joo et al. (Joo, Choi, and Lee 2015), Mohamed (Mohamed 2012) and Song et al. (Song et al. 2019) also verified their numerical results against experiments data.

2.3.2 Reported Turbulence Models in Literature

With each having its own variations, the two most used models for turbulent flow simulation reported in literature are the $k-\omega$ and $k-\epsilon$. Both models uses two partial differential equations to solve for the turbulence kinetic energy (k) and rate of dissipation of the kinetic energy (ω or ϵ) (Wilcox 2008a, Launder and Spalding 1974). $k-\epsilon$ model predicts in the far field whereas the $k-\omega$ predicts turbulence better near wall. Menter (Menter 1994) described a combination of both turbulence equation which is also widely used called the shear-stress transport model or SST $k-\omega$. An important criterion in the selection of turbulence model is the y^+ factor or distance from the first grid point to the wall. For far field predictions this value is usually > 30 whereas near wall the value is usually around 1 for near wall region (Gosselin, Dumas, and Boudreau 2013). Although a study found that the standard $k-\epsilon$ model did not agree well when applied to HAWT analysis (Wolfe et al. 1997), said model is usually more appropriate for VAWT simulation. Howell et al. (Howell et al. 2010) showed that the RNG $k-\epsilon$ model used in the 3D simulation compared favourably to wind tunnel results. Almohammadi et al. (Almohammadi et al. 2015) compared the Transition SST and the SST k -omega. Shown in Fig 2.5, in the predicted torque comparison, the transitional SST model was found to predict the dynamic stall earlier by 11° than the SST k -omega model. The reason for this, according to the authors, is that the SST k -omega model does not predict transitional flow formations such as separation bubbles and vortex formation. In a study by Durraini et al. (Durraini et al. 2011), they found the RNG $k-\epsilon$ model predicted much larger vortices magnitude in the trailing edge section of the airfoil compared the standard $k-\epsilon$ model. The standard $k-\epsilon$ model produced higher turbulence intensity as well as kinetic energy which results in a lower power output. This was proven when, compared to the RNG and Realizable models, the standard model significantly under predict the performance coefficient by almost a 100% margin. The result was corroborated by another study in which again they found the standard $k-\epsilon$ under

predicts the various aerodynamic coefficients (Wolfe et al. 1997). The Realizable and RNG $k-\epsilon$ models however showed comparable results between the two. Hence, the authors used the RNG $k-\epsilon$ turbulence model as a baseline in their simulation.

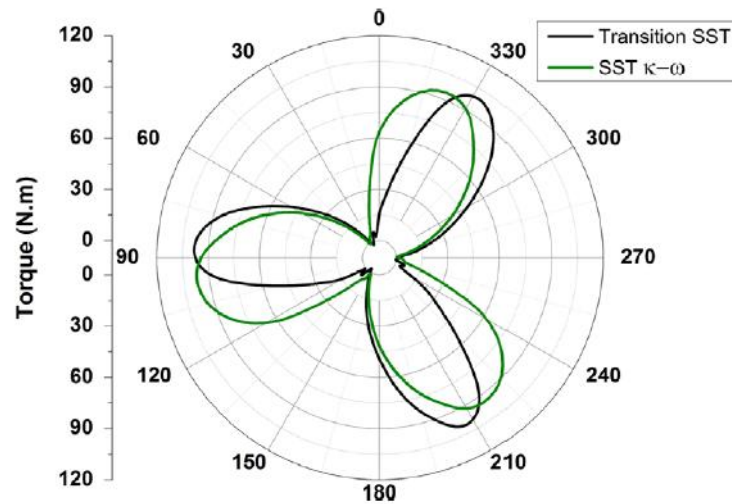


Fig 2.5 Reported predicted torque comparison between the Transition SST model and the SST $k-\omega$ model reported by Almohammadi et al. (Almohammadi et al. 2015)

He et al. (He et al. 2020) compared Unsteady Reynolds-Averaged Navier-Stokes (URANS) method using the SST $k-\omega$ model against the Large Eddy Simulation (LES) method in 2D, 2.5D and 3D model for the URANS method and 2.5D and 3D for the LES method. They found the LES method predicted the performance of the VAWT more accurately in both 2.5D and 3D compared to the URANS method at low and high TSR values. The URANS model was found to over predict the power coefficient significantly compared to the LES method and 3D URANS model. The 2.5D LES results also indicated that neglecting the tip vortices effects in the simulation does not affect the outcome of the prediction, hence implying that other factors may be more significant. 2D and 2.5D simulations in the URANS method did not consider effects of tip vortices. In the 3D simulation, due to the more detailed flow separation in the vortices the 3D LES showed better accuracy compared to the 3D URANS at low TSR but was considered much more complex to simulate compared to the 2.5D LES. They concluded that the 2.5D LES model is more suitable compared to the URANS model due to the improved accuracy between the two at the initial start-up stage of the turbine, but the trade-off is that the 2.5D method requires significantly more computational time compared to the URANS method. Visualizations of the Q-criterion comparisons are shown in Fig 2.6. Another

study by Li et al. (Li et al. 2013) also compared a 2.5D LES model against a 2D and 2.5D URANS using SST $k-\omega$ model. The 2D URANS suffered from significant overprediction due to overestimation of tangential forces and delay in predicting the dynamic stall. The 2.5D LES simulation model was deemed to be more accurate with better agreement against experimental study. The flow field visualization showed more realistic vortex diffusion right after flow separation which leads to more accurate results. The authors however did not compare the simulation time between the two models used. Fig 2.7 shows the iso-surface comparison between the two models. It can be observed that the 2.5D LES model predicted much more developed flow separation and formation of vortex in each case compared to the 2.5D URANS. Large eddies shedding from the blade can be clearly seen in the 2.5D LES whereas the 2.5D URANS model showed lesser developed wake.

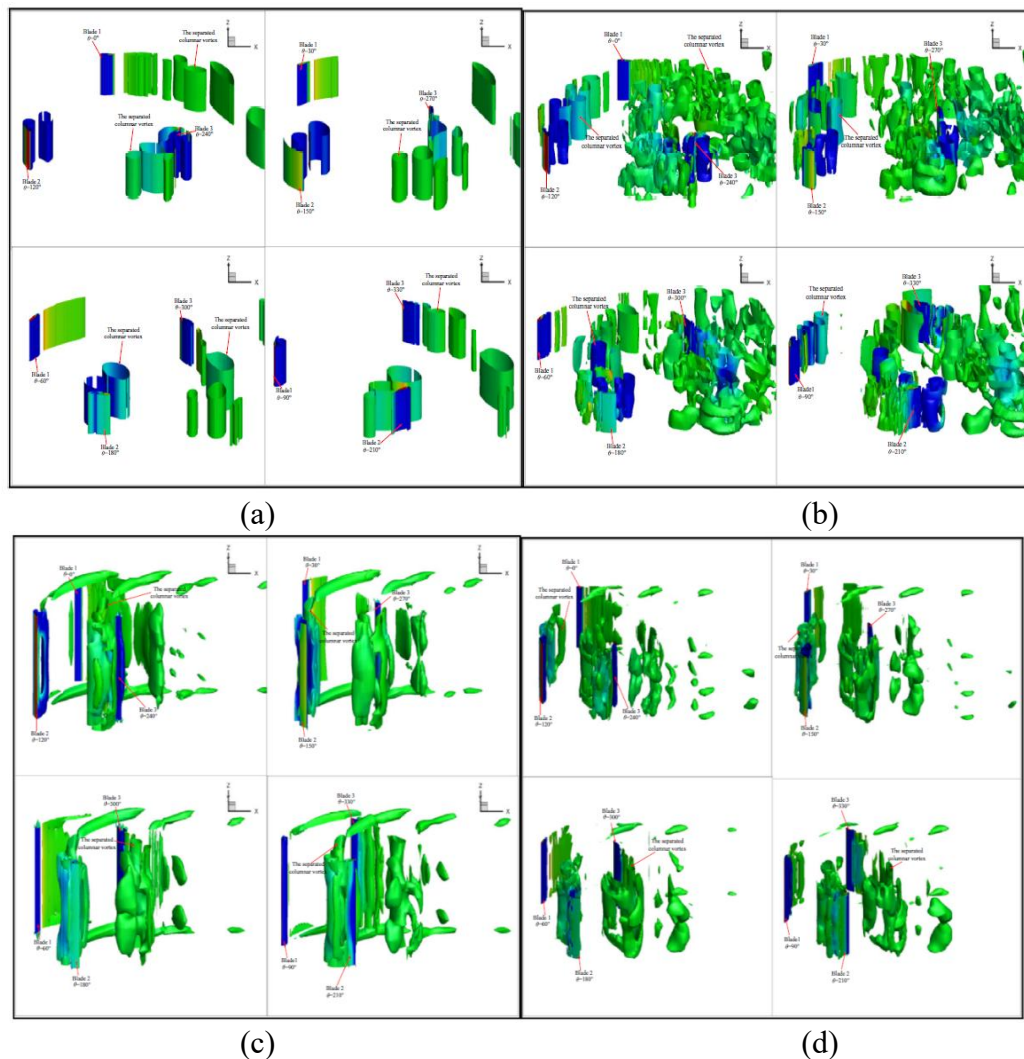


Fig 2.6 Visualizations of Q-criterion for (a) 2.5D SST $k-\omega$, (b) 2.5D LES, (c) 3D SST $k-\omega$, (d) 3D LES by He et al. (He et al. 2020)

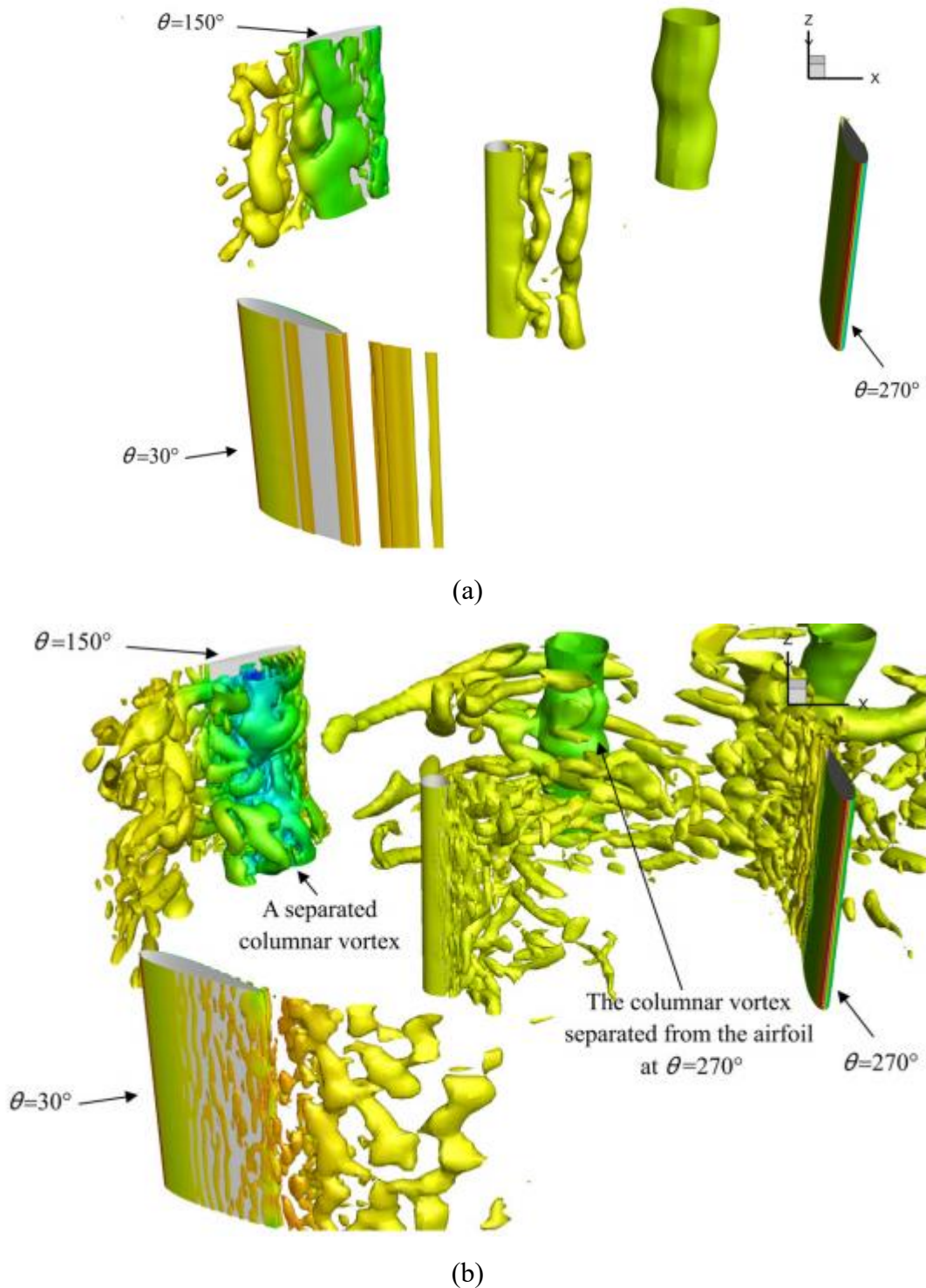


Fig 2.7 Comparisons of iso vorticity contours of (a) 2.5D URANS using the SST $k-\omega$ model and (b) 2.5D LES model by Li et al. (Li et al. 2013)

Daroczy et al. (Daroczy et al. 2015) compared different turbulence models at different sets of TSR and turbulence intensity and found the Realizable $k-\epsilon$ model compared favourably at both low and high turbulence intensities. SST $k-\omega$ model with a cubic correction was able to predict the optimal TSR with distinct accuracy

for the first three simulation conditions however the 4th condition at high turbulence intensity saw values which were too unrealistic. Transitional SST and Spalart-Allmaras models were also tested with good results in the first 3 conditions but at the high turbulence intensity condition the simulation failed to converge. Sanei and Razaghi (Sanei and Razaghi 2018) found Transition SST model to agree well with experimental validation. At high Reynolds number, the Spalart-Allmaras and SST $k-\omega$ predicted results quite well similar to the Transition SST model. However, at low Reynolds number and angle of attack between 5° to 6°, the Transition SST model was the most reliable of the three. Bachant et al. (Bachant and Wosnik 2016b) compared the $k-\omega$ SST and Spalart-Allmaras Reynolds-averaged Navier Stokes models in 2D and 3D simulation and found the $k-\omega$ SST model predicted the turbulence kinetic energy more accurately whereas the Spalart-Allmaras model predicted the momentum transport near wake better. The SST model was also found to predict turbine performance as well as near wake quite well but over predict the power output by 30%. Wu and Cao (Wu and Cao 2018) also reported significant over prediction beyond the blades stall region at higher angles of attack. Another study, by Campobasso et al. (Campobasso et al. 2009), highlighted the difference between RANS models using the Integrated Solution Algorithm for Arbitrary Configurations or ISAAC code. Using the skin friction results of an XFOIL code as a baseline, between the $k-\omega$ and $k-\varepsilon$ models in both linear or standard and ASM variant, the $k-\omega$ ASM model was found to compare most favourably to the XFOIL code. However, both linear and ASM variants of the $k-\varepsilon$ models weren't far off as well. The linear $k-\omega$ model was shown to be the most inaccurate of the four models tested. All four models showed negligible differences compared to the XFOIL code in terms of static pressure coefficient. Depending on the parameters studied, similar outcomes where no differences between turbulence models used were observed in other studies. Lain et al. (Laín, Taborda, and López 2018) found using different turbulence models sees no discernible differences and shows the results of their winglet design were unaffected by any particular type of model employed on the flow turbulence. Others have simply used multiple turbulence models in the simulation by having the SST $k-\omega$ and Enhanced Wall Treatment Realizable $k-\varepsilon$ for y^+ values of 30 and 1 respectively with acceptable results (Castelli et al. 2010). Lanzafame et al (Lanzafame, Mauro, and Messina 2014) compared several RANS turbulence models against the Transition Turbulence Model. The SST $k-\omega$ over predicted the lift

coefficient and under predicted the drag coefficient in the near stall region whereas the Transition model adequately predicted the lift and drag coefficients. Both models were compared in two separate turbine models against experimental results and in both cases, the Transitional model predicts the power coefficient performance much more accurately than the former. Barnes et al (Barnes et al. 2021) compared 5 turbulence models by conducting a wake prediction study and compared the models against experimental results. The models were SST $k-\omega$ SST, SSTI $k-\omega$, $k-\omega$ LRN, Transition SST and $k-k-\omega$. The author summarized none of the models were accurate enough to the experimental results however, the Transition SST provided the closest approximation. However, it should be noted that the numerical study and comparison were done in 2D, hence negating various 3D effects from the calculation. Fig 2.8 summarizes a selection of reported turbulence model comparisons for NACA0021.

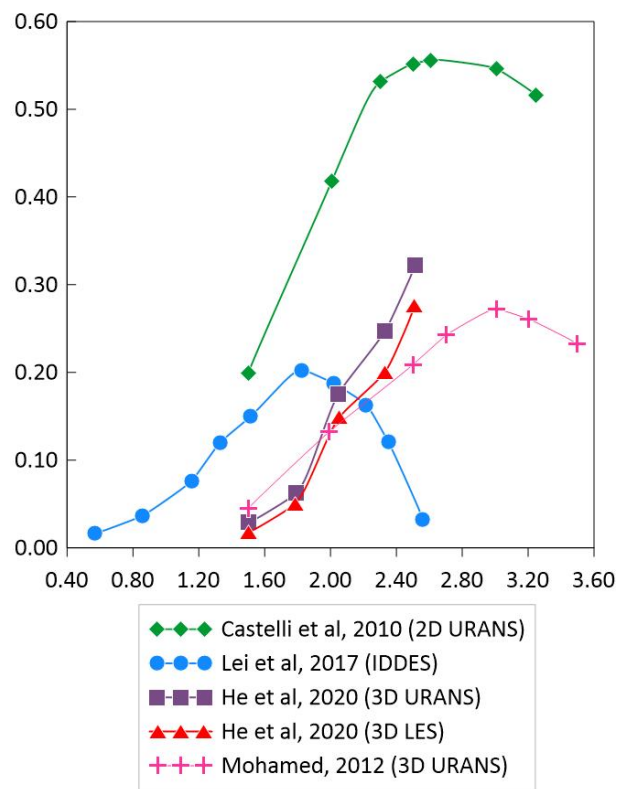


Fig 2.8. Comparisons of different numerical studies with different CFD codes on the NACA0021 airfoil blade.

2.4 Design of the vertical axis wind turbine

The VAWT involves many design parameters. Many studies have been conducted on various aspects of the VAWT to increase the turbine performance efficiencies as well

as improve turbine implementation and ease of integration into various applications such as energy extraction for urban use or large-scale offshore use. The design of a VAWT encompasses various parameters for consideration for optimal performance. However, for this review, certain design parameters of the VAWT reported throughout literature were highlighted and discussed.

2.4.1 Airfoil types, selections, and modifications

Arguably the most important design variable of the VAWT are the airfoil blades which catch wind energy to transfer torque to the gearbox and power unit. Hence, various airfoil types, selections, comparisons, and design modifications were reported in literature. This section discussed the various types of airfoils in terms of shapes, performance efficiencies, geometric modifications as well as other turbine interactions during operation.

2.4.1.1 Symmetrical NACA blades

The Darrieus type VAWT performance is heavily influenced by the type and selection of its airfoil. airfoils can generally be grouped into symmetrical or unsymmetrical blades with both having their suitable use cases. As such, both blade types have been reported in literature. Symmetrical blades the most common ones are the NACA0012 (Wang et al. 2014, Bangga et al. 2017), NACA0015 (Lee and Lim 2015, Chen et al. 2015, Wu and Cao 2018), NACA0018 (Li et al. 2019, Tsai and Colonius 2016, Zhong et al. 2019, Jacob and Chatterjee 2019), NACA0020 (Bachant and Wosnik 2015, Bachant and Wosnik 2016a, Bachant and Wosnik 2016b, Bianchini et al. 2017) and NACA0021 (He et al. 2020, Li, Maeda, et al. 2016a, Li, Maeda, Kamada, Ogasawara, et al. 2017, Li, Maeda, et al. 2016b, Lei et al. 2017). Fig 2.9 shows the turbine blade geometry of these symmetrical blades. However, non-symmetrical airfoil or cambered blades have also been reported due to their various advantages over the symmetrical blades.

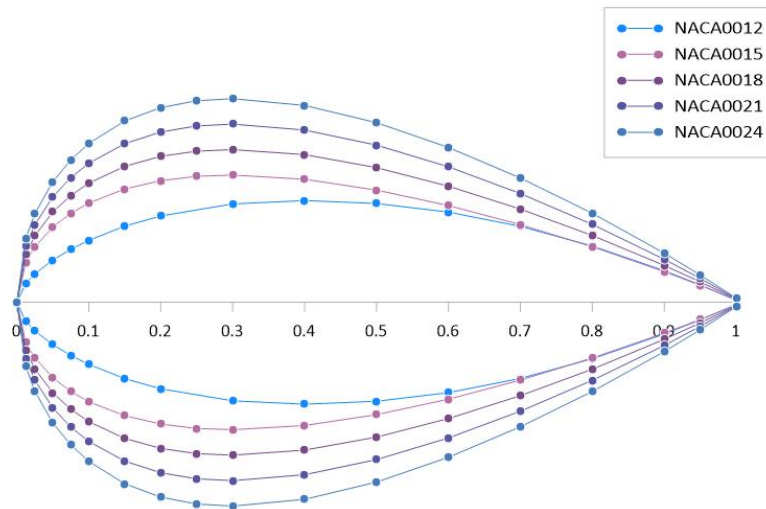


Fig 2.9. Geometries of different NACA symmetrical blades

Symmetrical blades are widely used and tends to be the blades of choice in many studies and VAWT designs. Danao et al (Danao, Qin, and Howell 2012) found at $TSR = 3.5$, the blade NACA0012 extracted the largest power coefficient of four tested blades by a significant margin of 0.50 against the next best LS0421 blade with coefficient 0.4 with the thicker NACA0022 blade slightly lower at 0.38. However, Siddiqui et al (Siddiqui, Durrani, and Imran 2013, Siddiqui, Durrani, and Akhtar 2015) preferred the NACA0022 due to the maximum power coefficient obtained compared against other symmetrical NACA blades. In a helical blade study, Alaimo et al (Alaimo et al. 2015) showed a NACA0021 performed better in a straight bladed configuration than in a twisted setup with higher power efficiency over the tested TSR range. Despite that, the instantaneous torque coefficient comparison showed higher peaks and deeper troughs by the straight bladed turbine, but the helical turbine showed smoother, more circular curves during the turbine rotation which indicates lower loading conditions. However, while acknowledging some of the advantages of the helical turbine as well as its more eye-catching design, this research study only focused on the straight blade design.

Durrani et al (Durrani et al. 2011) showed that although using thicker airfoils results in higher drag acting on the blades, it also allows for the operation at a wider rotational speed range due to the enhance structural integrity. Cambered airfoils were found to have weaker performance compared to the baseline NACA0022 with the NACA6412 extracting the weakest power efficiency. Of the four tested symmetrical airfoils tested with thickness ranging from 15-22%, over a range of wind speed

between 6-14 m/s, the NACA0015 blade had a slightly higher peak power coefficient but the NACA0022 yielded the best overall performance coefficient over a wider range of TSR, peaking at TSR value of 2.5 when wind speed was set at 14 m/s. Lee and Lim (Lee and Lim 2015) compared NACA0015 against NACA0018 and NACA0021 and found airfoil with width ratio of 0.15 has the best power coefficient at $TSR = 2$. Comparisons of the symmetrical blades NACA0015 and NACA0018 and their reported power coefficient based on studies from literature are shown in Fig 2.10.

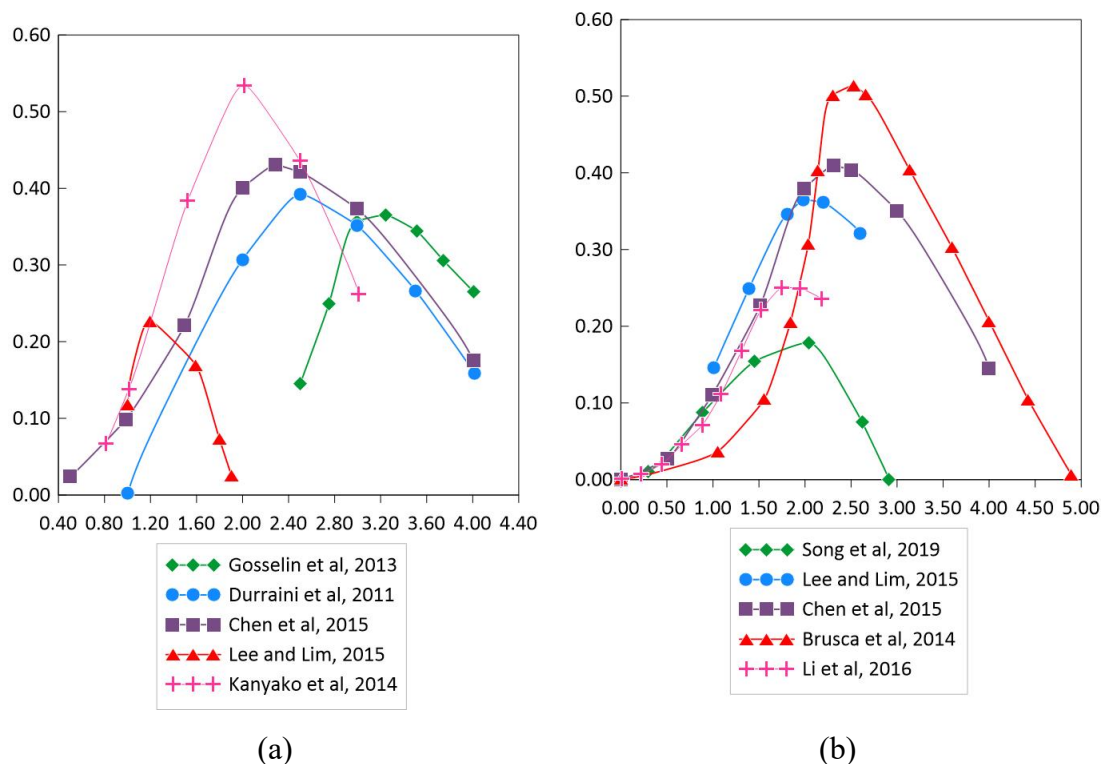


Fig 2.10. Comparisons of reported (a) NACA0015 and (b) NACA0018 power coefficient predictions based on CFD by various authors. Note that the differences may be due to factors such as wind speed, numerical model used, turbine dimensions etc. Presented are best reported results.

Gosselin et al (Gosselin, Dumas, and Boudreau 2013) found when comparing blade thickness, thicker blade thickness operate at a wider range of TSR values where energy can be extracted however at larger TSR values it reaches a point of diminishing return as drag starts to play a role. They recommended the 15% thickness as ideal, which sees the largest power efficiency between the range of thickness 12-25%. This observation was corroborated by another (Song et al. 2019) in which the authors also found similar performance uplift of blade thickness of 15% over thicker blades at a range of low TSRs. When compared to the NACA0021 blade, the vorticity of the NACA0015 was found to be significantly weaker at a TSR value

of 2.0 while in terms of pressure distribution, NACA0015 blade experienced larger pressure values compared to the NAA0021. Kanyako and Janaireh (Kanyako and Janajreh 2014) compared the symmetrical blades NACA0015 and NACA0018 against the S1046 and DU06-W-200 cambered blades, the NACA0015 blade extracted the best efficiency with a difference of 4.58% higher than the second best NACA0018 but the S1046 blade extracted a more efficiently at higher TSR and therefore has a wider operating TSR range. Yang et al (Yang et al. 2017) found thinner blades such as the NACA0009 and NACA0012 yielded larger power coefficient but the differences of the two compared to the NACA0015 is largely negligible. These studies show that thinner blades tend to extract the largest power coefficient. In a study highlighting the effects of maximum thickness locations on a NACA0018 blade, the Wang et al (Wang, Shen, et al. 2018) showed the maximum power coefficient as well as optimal TSR does not change. However, a significant performance degradation was observed when the thickness was at 50% to 60% of the chord length. It was showed that the ideal location for maximum thickness was between 20% to 35%. Tirandaz et al (Tirandaz and Rezaeiha 2021) conducted a parametric study on a single bladed turbine with varying number of thicknesses. Comparisons were made between 10% to 24% blade thickness with varying parameters varies such as leading-edge radius, blade thickness and blade thickness chord-wise location. The authors found the optimum shape of 18% thickness to 24%, location from 27.5% to 35% of the chord and a leading-edge radius index of 4.5 from 6. These two optimum shapes were named NACA0018-4.5/2.75 and NACA0024-4.5/3.5. Table 1 highlights studies relating to some of the turbine blades reported in literature.

Table 2.1. Summary of turbine blade selections in literature. Also highlighted are methodology, reported maximum power coefficient, and turbulence model used.

Author (s)	Blade Airfoil	Maximum Power Coefficient	Methodology	Turbulence Model	Corresponding TSR
Gosselin et al (Gosselin, Dumas, and Boudreau 2013)	NACA0015	0.36 (No pitch angle)	3D blades only	k- ω SST	3.0
		0.40 (Pitch angle -3°)			
Lee and Lim (Lee and Lim 2015)	NACA0015	0.23	Wind tunnel experiment	RNG k- ϵ	1.25
		0.38	2D CFD simulation		2.0
Chen et al (Chen et al. 2015)	NACA0015	0.40	2D CFD simulation	k- ω SST	2.5
		0.34	Experiment		
Li et al (Li et al. 2019)	NACA0018	0.25	Experiment	RNG k- ϵ	1.8
Siddiqui et al (Siddiqui, Durrani, and Akhtar 2015)	NACA0022	0.51	2D CFD simulation	Realizable k- ϵ	3.0
		0.36	3D with support-arms and tip effects		
Siddiqui et al (Siddiqui, Durrani, and Imran 2013)	NACA0022	0.40	3D blades only	Realizable k- ϵ	3.0
		0.35	3D with support-arms and central hub		
Durrani et al (Durrani et al. 2011)	NACA0022	0.40	2D CFD simulation	RNG k- ϵ	2.5
El Samanoudy et al (El-Samanoudy, Ghorab, and Youssef 2010)	NACA0024	0.25	Experiment	N/A	1.3
	NACA4420	0.16			
Chen and Kuo (Chen and Kuo 2013)	NACA2412	0.29	2D CFD simulation	k- ω SST	3.55
Mohamed (Mohamed 2012)	NACA0018	0.2964	2D CFD simulation	Realizable k- ϵ	6
	S-1046	0.4051			8

Danao et al (Danao, Qin, and Howell 2012)	LS0421	0.40	2D CFD simulation	k- ω SST	3.5
		0.38 (inverted)			
Parakkal et al (Parakkal et al. 2019)	Joukowski J-5	0.55	2D CFD simulation	k- ω SST	10
	Joukowski J-6	0.43			

2.4.1.2 *Cambered and unsymmetrical blades*

The symmetrical blades are characterized by their distinct proportional profile along the camber line of the blade. Hence, unlike non symmetrical blades, the camber line and chord line overlap. A cambered airfoil is denounced by the curve of the camber line. A positive camber is when the camber line curves above the chord line whereas a negative chamber is the exact opposite (Gudmundsson 2014). However, in VAWT designs, positive cambered blades are usually favoured. This is due to the positive effects on the aerodynamic lift on the blade which shifts the lift curve and increases the maximum lift coefficient of the blade (Gudmundsson 2014). A negative camber would have the opposite effect instead. In a study by Danao et al (Danao, Qin, and Howell 2012), they found inverting non-symmetrical blades NACA5522 and LS0421, hence mimicking a negative camber design, performed poorly compared to the non-inverted form. A study found non-symmetrical Joukowski airfoils yielded better performance than the symmetrical NACA0012 as well as the cambered NACA4512 and NACA4312 at very high TSR values (Parakkal et al. 2019). The blades also obtained reasonable lift coefficient over both symmetrical and non-symmetrical NACA blades. When comparing vorticity field contours at high TSR value of 9, the influence of the Joukowski rotors results in no vortex shedding unlike the NACA airfoils where two significant formation of vortex shedding was seen at each side of the rotor shown in Fig 2.11. Critically however, the authors noted that although a significant enhancement to the performance of the wind turbine - especially with respect to torque - can be made when using the Joukowski airfoils, it comes at a cost of having a poor self-starting ability for the wind turbine. Mohamed (Mohamed 2012) compared the S-series blade family and found other the S1046 and S809 to have significantly higher power efficiency then the symmetrical NACA airfoils with the S1046 airfoil in particular having a 26.83% uplift over the base NACA0021. However, at lower TSR, symmetrical NACA airfoils provide largest torque efficiency. Other observations include poor performances from unsymmetrical blades such as the NACA6312 and AG18 against symmetrical blades.

Wang et al (Wang, Shen, et al. 2018) found moving the maximum thickness of a cambered NACA630018 airfoil yielded significantly different results with shifting maximum power coefficient at different thickness locations. When varying

the camber of a NACA4415 airfoil, a camber range of between 0.61% to 4.16% peaked lower at TSR 2.51 whereas increasing the camber to between 4.75% to 5.94% shifts the maximum power coefficient forward to TSR 3.09 and continues up to TSR 3.30 for cambers between 6.53% to 7.71%. Although this means increasing the maximum camber results in increasing operational TSR, the drawback is the reduced maximum power coefficient values.

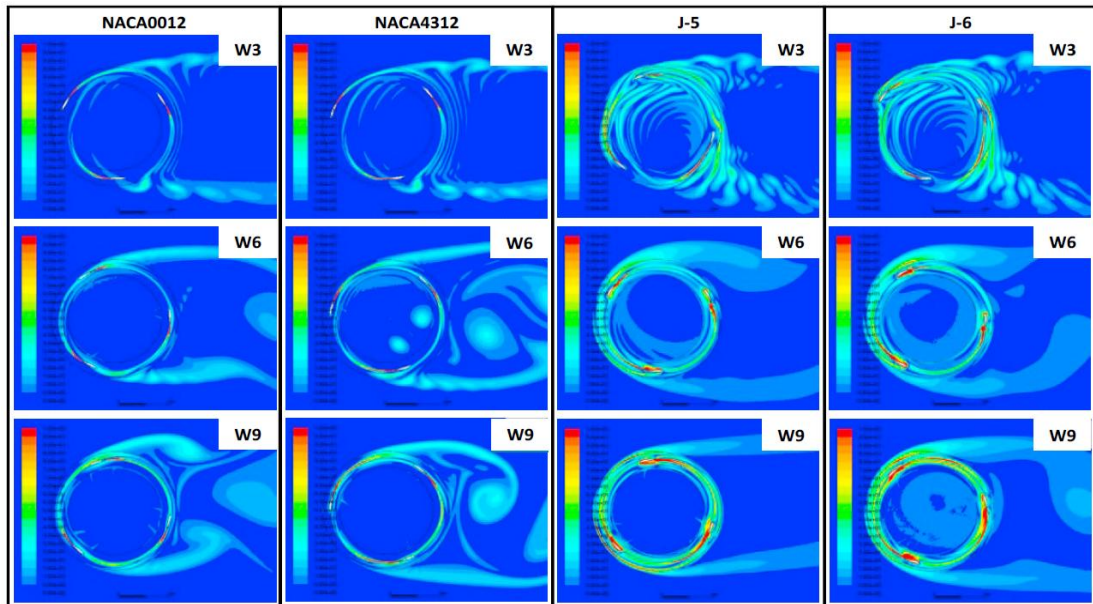


Fig 2.11 Vorticity comparisons of different turbine blades (Parakkal et al. 2019).

Sengupta et al (Sengupta, Biswas, and Gupta 2016) compared the symmetrical NACA0018 against S815 and EN005 illustrated in Fig 2.12. They found maximum performance coefficient was obtained by the S815 blade. Comparing the static pressure contour of each blade type, S815 sees static pressure drop from 55.6 Pa in the upwind zone to 13.1 Pa in the downwind zone. The EN0005 sees a static pressure drop of 47.7 Pa down to -85.6 Pa whereas NACA0018 drops from 33.2 Pa to -18.1 Pa. The difference in static pressure in the upwind and downwind region was an indication as to why the S816 blade performed better of the three tested blades due to this pressure drop resulting in higher lift force. An extension of the study by Singh et al (Singh, Biswas, and Misra 2015) found similar results when comparing a S1210 airfoil against the symmetrical NACA0012. The static torque coefficient of the S1210 airfoil at aspect ratio of 1.0 was much higher than the NACA0012 and S1046. However, the S1210 was found to have a significantly lower operational TSR range. They concluded that the S1210 turbine blade is still operational at much lower

TSR with excellent efficiency. The lower TSR also indicates lower centrifugal stress acting on the turbine and lower blade noise levels. Another study (Danao, Qin, and Howell 2012) also found unsymmetrical blade LS0421 which has a modest cambered design along its profile to extract better power coefficient of 0.40 compared to the NACA0022 with power coefficient of 0.38. Interestingly, the study also showed that inverted blades of the unsymmetrical NACA5522 and LS0421 performed worst compared to their respective non-inverted counterpart in terms power coefficients.

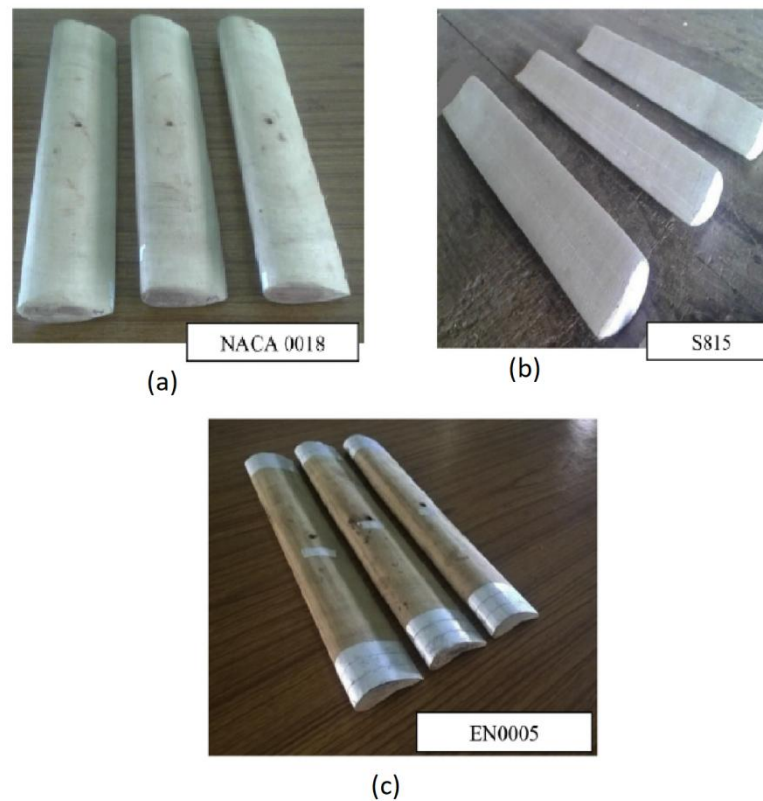


Fig 2.12. Printed blade in the experimental study comparing different blades by Sengupta et al. (Sengupta, Biswas, and Gupta 2016).

Worasinchai et al (Worasinchai, Ingram, and Dominy 2011) compared the NACA0012 symmetrical blade against cambered blades SG6043 and SD7062. They found larger lift coefficients values of 1.431 and 1.397 respectively against the much smaller value of 0.816 by the NACA0012. The maximum lift coefficients were also found to occur at larger angles of attack of 18° compared to the NACA0012 at 12° . El Samanoudy et al (El-Samanoudy, Ghorab, and Youssef 2010) published the effects of various airfoil parameters on the turbine performance. In all the performance

parameters measured, they found cambered airfoils NACA4420 and NACA4520 performed poorly compared to symmetrical profiled airfoils and increasing the airfoil chord length increases the power performance. However, in unsteady wind condition, a cambered design performed better. Chen and Kuo (Chen and Kuo 2013) found cambered designs like the NACA4412 have better self-starting ability compared to the symmetrical NACA0012 blade. Varying the pitch angle to increase lift to drag ratio saw NACA2412 cambered airfoil achieve maximized torque coefficient as well as improved self-starting characteristics compared to the symmetrical NACA0012. Bausas and Danao (Bausas and Danao 2015) found a 1.5% cambered design was able to obtain a power coefficient of 0.31 against a steady flow value of 0.34. An optimization study employing multiple continuous optimization algorithms by Tahani et al (Tahani et al. 2016), with turbine diameter and blade chord length selected as continuous decision variables and airfoil type defined as discrete decision variable, selected the NACA4412 blade as the most optimal with a power efficiency uplift of 44% against the baseline NACA0012 turbine. In Fig 2.13, the authors illustrate a comparison between the two blades showing a much higher magnitude of vorticity around the NACA4412 blade which contributed to the larger torque and power of the turbine. Lastly, a study by Souaissa et al (Souaissa et al. 2018) on the NACA4312 found the cambered blade increased self-starting ability at high solidity compared to the symmetrical blade of similar thickness.

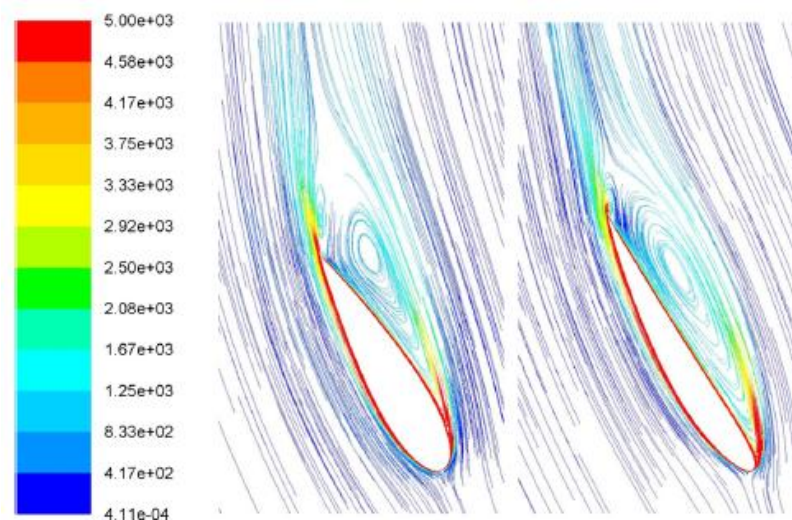


Fig 2.13 Vorticity streamline by Tahani et al (Tahani et al. 2016) showing larger vorticity extending throughout the inner surface of the NACA4412 against a smaller vorticity.

2.4.1.3 Turbine blade modifications

The previous studies showed that each blade choices have its own benefit in their design of an optimal VAWT. Beyond just choosing the right blade for optimal aerodynamic performance however, other studies have observed numerous benefits by making modifications to the airfoil itself to further enhance its performance. For example, implementing a blade taper ratio of 0.5 to a NACA0015 airfoil yielded better power efficiency of up to 2% (Coton, Galbraith, and Jiang 1996).

A study by Lositano and Danao (Lositaño and Danao 2019) compared the cambered design against a tubercle leading edge (TLE) profile modification and found the TLE cambered blades suffered from reduced lift forces as well as increased drag forces which led to much lower torque values. Significant vortices induced by the modification see flow separation along the TLE surface and trailing edge which degrades flow and reduces lift while increasing the drag. They summarized that overall performance favoured the cambered design against the TLE cambered blade modification. Chen et al (Chen et al. 2015) suggested a blade modification with an opening for improved starting characteristics on a NACA0015 airfoil. They summarized that the power coefficient of a rotor with an opening is lower compared to one without. An inner opening saw a decrease of up to 66% in power coefficient with an outer opening has a loss percentage between 18.4 to 22.65%. However, it does enhance the static torque coefficient of the rotor especially pronounced when the opening is placed on the outer side of the blade which sees close to a linear increase as the opening ratio increases. A similar leading edge modification using plasma actuators was reported by Greenblatt et al (Greenblatt, Schulman, and Ben-Harav 2012) which saw a performance enhancement in power coefficient by up to 38%.

Wang et al (Wang, Wang, and Zhuang 2018) implemented an airfoil design with leading edge serration using Taguchi method that was found to have improved power performance at low TSR of 2. Using the NACA0018 airfoil, serration pattern was implemented at the leading edge of the blade. Using Taguchi method, a 2.5% blade chord length and wavelength of $C_b/6$ coupled with a blade twist angle of 60° produced a performance increase of 18.3% over the baseline. Yan et al (Yan et al. 2021) also implemented similar modifications to a NACA0018 blade with leading

edge protuberance or serrations and saw an amplitude (g) of $1\%c$ coupled with a wavelength (W) of $2.5\%c$ of the blade chord length yielded the best power coefficient especially at lower TSR range between TSR 1 to TSR 2.5. Fig 2.14 below shows the geometry of the airfoil with this modification. Zhang et al (Zhang et al. 2022) suggested a bionic blade design featuring leading edge serrated design for VAWT application. Fig 2.15 shows the bionic blade design. At higher angles of attack, the bionic blade showed higher lift coefficient than the baseline. The power coefficient at TSR 1.38, TSR 2.19 and TSR 2.58 were increased by 7.02%, 7.35%, and 3.42% respectively. Lin et al (Lin et al. 2016) proposed a tubercles blades. Results showed that increasing the amplitude and wavelength of the tubercles led to a maximum thrust increase of up to 2.31% and a power coefficient improvement of 16.4% compared to straight blades. Additionally, blades with a modified trailing edge demonstrated superior overall and maximum thrust performance compared to blades with a wave-like leading edge. This improvement was attributed to a shift in the location of vortices caused by the induced flow.

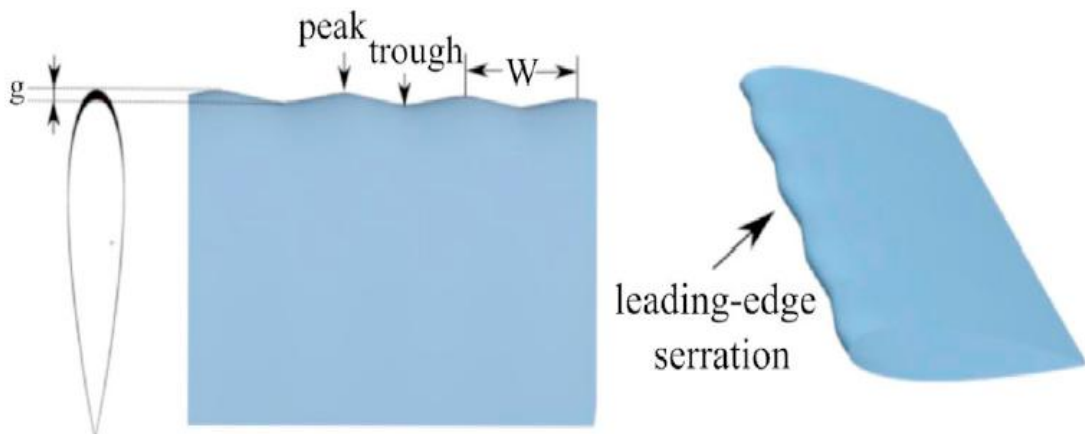
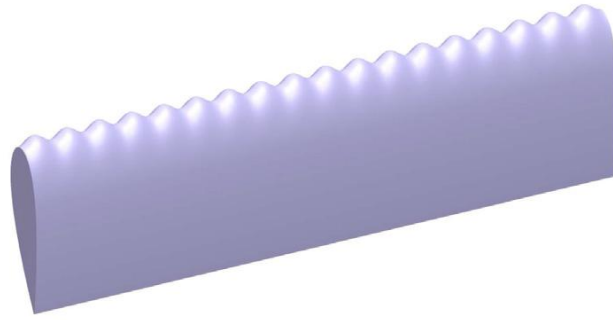


Fig 2.14. Airfoil showing leading edge serration by Yan et al. (Yan et al. 2021).



(a)



(b)

Fig 2.15. Bionic airfoil design suggested by Zhang et al (Zhang et al. 2022).

A popular flow control strategy to improve turbine performance is the application of a flap design. Multiple studies and reports have attempted to propose an optimal using this design philosophy. Ismail et al (Ismail and Vijayaraghavan 2015) suggested a design modification of an NACA-0015 airfoil involving an inward semi-circular dimple with a Gurney flap on the lower surface at the trailing edge of the blade. The profile modification was found to have increased the torque output of the generator by way of improving the aerodynamics of the blade. Yang et al (Yang et al. 2017) presented a NACA0012 turbine blade with a trailing edge flap control mechanism. Overall power coefficient of the turbine was found to increase by 10% over the baseline turbine as well as having a much wider operating TSR range. The lift coefficient was also found to increase by 0.15 and lift to drag ratio increased by 73. Comparing the flap design against the turbine blade without flap control, shown in the vorticity contour illustration in Fig 2.16, the flap control showed a stark difference between the two configurations with the flap control blade exhibiting a more streamlined flow with less turbulent flow in its wake. Zhang et al (Zhang et al. 2021) implemented a trailing edge split flap on a NACA0015 blade. The authors trialed a variety of flap dimensions and found a 22%*c* flap length at 92%*c* location, and 10° flap deflection to be the most optimal. This modification was found to increase the turbine maximum operating TSR by 25.9% and maximum power coefficient by 5.8%. The streamlines visualization showed the split flap modification was found to increase flow circulation around the turbine blade. The modification was also found to increase positive pressure difference in the upwind region and reduce negative pressure difference in the downwind region of the turbine.

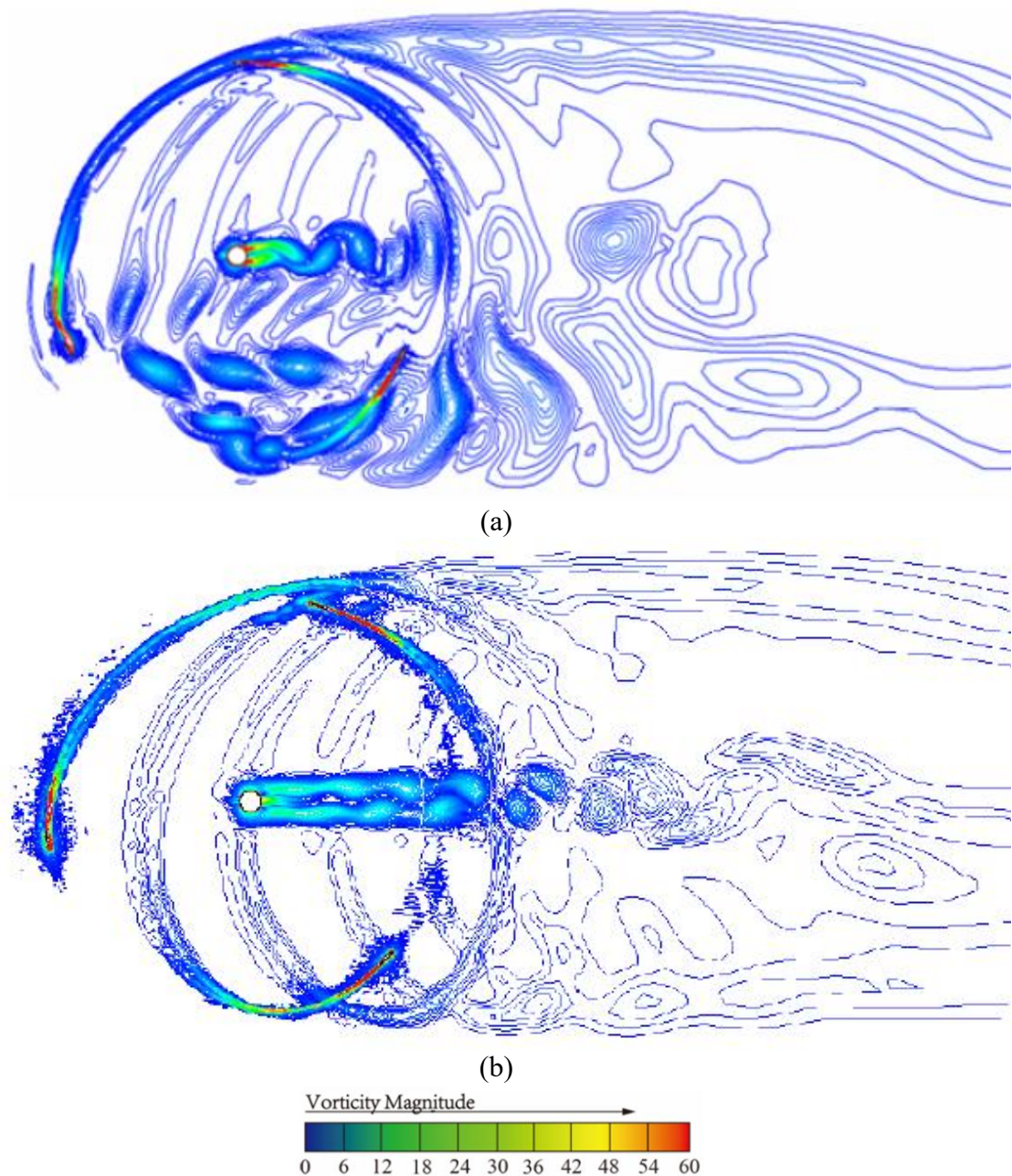


Fig 2.16. Flow vorticity contour with and without trailing edge flap by Yang et al. (Yang et al. 2017).

Chakroun and Bangga (Chakroun and Bangga 2021) employed a gurney modification on the trailing edge of a VAWT turbine blade. Studying the effects of gurney flap height, the authors found at lower TSR, a 0.5% of the blade chord, c , or $0.5\%c$ was found to be the most efficient. Increasing the gurney flap height further to $6\%c$ was found to be the most optimal in terms of turbine efficiency with peak power coefficient achieved at TSR 2.19. However, beyond that, and especially seen at TSR

3, the 6%*c* height was seen to be the least efficient with the baseline blade with no flap now being the most efficient. Liu et al (Liu et al. 2019) presented a movable flap modification located at the trailing edge of a NACA0018 airfoil. The movable flap modification was found to increase power coefficient at TSR 1.3 and 1.4 by 24.2% and 23.7% respectively compared to a baseline blade. The addition of the flap was found to have delayed stall from 14° to 16° and increases the maximum lift coefficient of the blade from 0.85 up to 1.16. The sound pressure level (SPL) analysis also showed that the movable flap was found to have an overall reduction effect on the noise generated by the turbine and is especially prominent at lower frequency band. Manickam and Roy (Manickam and Roy 2020) reported on the aerodynamics effects and performance of a modified NACA4412 airfoil with trailing edge flap and leading-edge passive surface roughness. The analysis was done by comparing two configurations of only trailing edge flap in the first configuration and leading-edge passive surface roughness with the trailing edge flap in the second and comparing both configurations against the baseline with no modifications. The first configuration was found to increase lift to drag ratio compared to the baseline. The second configuration saw a slight reduction of lift to drag ratio when compared against the first configuration. Flow separation was found to be high for the second configuration. A study by Zhu et al (Zhu et al. 2021) investigated the various effects of geometric parameters of a Gurney flap pointed outboard from the upper surface of the blade on the VAWT. In all instances of the dimensions of the Gurney Flap, the performance coefficients showed increased performance over the baseline NACA0021 airfoil. With respect to the Gurney flap dimensions, a 0.75%*c* was found to be the most optimal height of the flap, but the width was considered a non-factor. The authors found a maximum increase of 21.32% in performance with the addition of the Gurney flaps. This was due to the added structure being able to increase the blade tangential force in the upstream region which in effect increases the turbine efficiency. The shorter Gurney flap was able to reduce the effects of aerodynamic losses in the downstream area. Another study (Zhu et al. 2019) was conducted on the effects of various gurney flap variations on the turbine solidity of the NACA0021 VAWT. These are inboard, outboard, two-sided Gurney flap and dimple (also outboard, inboard and both sides). All versions of the Gurney flap were found to increase the turbine performance over the clean baseline. The outboard and dimple

GF increased the power coefficient at all instances of TSR over the clean VAWT at various solidity. Increasing the turbine solidity by means of blade number was found to reduce the blade load fluctuations which also negatively affects the aerodynamic performance of the blade. The authors stated that this may be due to the increased interaction between trailing edge vortices with the incoming blade. The outboard GF was found to be the most optimal with an increase of 17.92% albeit with a narrower operational TSR range.

Lain et al (Lain, Taborda, and López 2018) compared two variations of a winglet design modifications against the standard straight blade of NACA0025. They found the addition of the winglets improved performance over the standard blade version resulting in improved efficiency. Of the two winglet configurations, the symmetric winglet design saw the larger improvement in torque coefficient by about 20% compared to the base standard blade design. Comparing thrust coefficient also sees similar results with the symmetric design showing highest thrust but this time the minimum value was when using the standard blade. The winglet design was shown in Fig 2.17.

A study by Abdolahifar et al (Abdolahifar and Karimian 2022) suggested a slotted blade design for reduced flow separation. The blade slots were designed to transfer flow from the pressure side to the suction side to delay flow separation and improve torque generation. The best slot location was found to be at $c/3$ from the blade leading edge, which resulted in significant improvement in average torque coefficient and a delay of up to 15.5 degrees in the torque coefficient peak. At TSR values of 0.5, 1.0, and 1.5, the average torque coefficient increased by 93.4%, 66.1%, and 10.5% respectively for the slotted blade. A report by Wang et al (Wang et al. 2016) proposed a novel deformable turbine blade design which saw a significant power coefficient improvement at low turbine solidity by 14.56% as well as 7.51% and 8.07% respectively in a two bladed and four bladed setup respectively. The adaptive turbine blade design was achieved by response to the surface pressure on the blade. Vortex structure comparisons show minimal vortex shedding compared to the conventional NACA0015 turbine. In a novel turbine blade design proposal, Auyanet et al (García Auyanet et al. 2022) presented several J-shaped blade design for VAWT application. The comparisons were made against a NACA0015 blade.

The suggested J-shaped blade features a cut out of the NACA0015 blade with various comparisons made against various designs of the shape. The author found a cut out of the shape on the outer surface was found to be most optimal, with increased starting torque over the baseline NACA0015 turbine by 135%. The internal cut suffered from vortices formation. Comparisons were made and the J1 blade with outer cut was found to have a vortex forming within the inner curvature of the cut in the blade and this leads to a change in momentum which enhanced the positive drag effects and improved the turbine start up torque. The J1 blade suction side also showed increased tangential force which the author describes as mimicking the characteristics of a Savonnius turbine. Power coefficient characteristics was found to be the same as the NACA0015 but with better curve over the TSR range which the authors suggest could reduce fatigue stresses on the turbine.

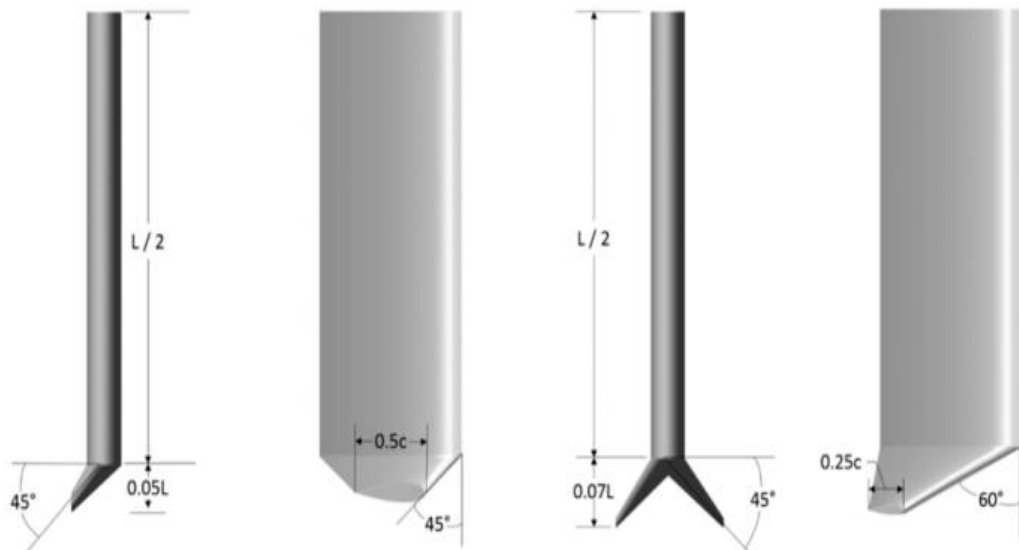


Fig 2.17. Winglet blade design suggested by Lain et al. (Lain, Taborda, and López 2018).

2.4.1.4 Turbine blade optimization

Many literatures have concentrated on semi arbitrary changes or variations of different parameters such as solidity, turbine blade thickness, pitch and twist. Studies have compared cambered and symmetrical blades with varying results and conclusions. Blade thickness between similar shapes were also compared and various conclusions were drawn. There seems to an agreement in literature with regards to turbine solidity with many identifying solidity ratios between 0.3 and 0.4 being the

most optimal for maximum turbine efficiency but there are varying findings and suggestions when it comes to blade chord length and number of blades. Ideal blade pitch and twist has also been identified. These studies show by changing certain variables or dimensions, the VAWT can be improved. However, blade optimization techniques have also been explored with varying results.

Attempts at blade optimization using optimization codes have been put forth by various authors in recent years. De Tavenier et al (De Tavernier, Ferreira, and van Bussel 2019) also used the genetic algorithm approach to optimize the VAWT by examining 2000 different airfoil shapes and found the DU17VAWT200, DU17VAWT250, and DU17VAWT300 blades performed the best and were therefore recommended as turbine blades. Santos et al (Santos, Pantaleão, and Salviano 2023) used deep generative adversarial network or Bézier-GAN to generate an optimized VAWT blade which improved 20.5% and 9.1% over the NACA0015 and NACA0021 baseline respectively. Ma et al (Ma et al. 2018) employed the multi-island genetic algorithm scheme to optimize a NACA0018 and yielded an improved design with increased power coefficient at moderate TSRs with the highest increase found at TSR 0.9 with an improvement of 26.82%. Carrigan et al (Carrigan et al. 2012) applied a differential evolution optimization scheme on a NACA0015 turbine which increased the turbine blade thickness by 58% with a solidity reduction by 40%. The candidate blade achieved maximum torque earlier in the rotation and achieved a 6% increase in power coefficient compared to the baseline NACA0015 turbine.

The adjoint method, usually used together in tandem with the gradient based optimizer, is an optimization method that focuses on nodal displacement and considering mesh sensitivity with respect to the input parameters. This mesh deformation approach is in stark contrast to other optimization codes such as the GA and EA codes whereby a large sample size of potential geometry is created and tested to obtain the most optimal geometry. This means, in terms of computational resource, the adjoint method together with mesh morphing tends to be more efficient in obtaining an optimal airfoil shape compared to other optimization codes. To highlight this, a demonstration of this observation was presented by Fleischli et al (Fleischli et al. 2021) who showed the adjoint method obtaining a significant 19.23% output improvement compared to the EA based optimization while running at 30%

computational time. In wind turbine studies, Dhert et al (Dhert, Ashuri, and Martins 2017) obtained a significant 22.4% increase in torque when applied to a NREL blade on a horizontal axis wind turbine (HAWT). This study demonstrates the potency of the adjoint solver to optimize a turbine blade for increased torque output and efficiency. A study by Day et al (Day et al. 2021) also applied the adjoint method in steady RANS on a NACA0018 blade used in a VAWT. The authors applied a 5% increase in tangential force which corresponded to an increase in turbine performance and improved airflow around the turbine blade. Although the authors demonstrated the viability of the adjoint method applied to a VAWT blade, the full turbine performance analysis of the candidate turbine blade was not presented.

Marinic-Kragic et al (Marinić-Kragić, Vučina, and Milas 2019, 2022, Marinić-Kragić, Vučina, and Milas 2018) demonstrated the optimization of a Savonius type VAWT in numerous studies. The first study (Marinić-Kragić, Vučina, and Milas 2018) was conducted using shape parameterization along with a genetic algorithm code. The developed code was able to generate a proposed VAWT turbine based on user input as opposed to an initial starting shape. A second study by the same author proposed a novel flexible shaped Savonius turbine which increases power coefficient by 8% (Marinić-Kragić, Vučina, and Milas 2019). A later study (Marinić-Kragić, Vučina, and Milas 2022) saw a 12% improvement in a 2 bladed design and almost 50% increase in performance for a 4 bladed and 6 bladed setup over the baseline. Wang et al (Wang et al. 2022) performed an aerodynamic shape optimization of a NACA0015 airfoil with the particle swarm optimization (PSO) scheme together with the RFOIL program. The optimization scheme was found to increase 8.45% over the baseline NACA0015 airfoil. Elsaka et al (Elsakka et al. 2022) employed response surface optimization (RSM) together with the multi-objective Genetic Algorithm (MOGA) to suggest an optimal turbine solidity of 0.31 and blade pitch angle of 3.6. The 2D results show minimal improvements but 3D simulation shows a significant 34.5% increase in power coefficient over the baseline which was then increased even higher when the turbine blades were fitted with winglets at the blade tips. Daroczy et al (Daróczy, Janiga, and Thévenin 2018) used the genetic algorithm to optimize a NACA0021 blade. The maximum TSR was located at TSR 3.5, and the optimization results yielded a blade thinner than the

original NACA0021 blade. The optimized blade was found to have a maximum C_p of 0.48 against the baseline NACA0021 of C_p 0.39, which is a 20.7% increase in efficiency. Interestingly, the genetic algorithm optimization process computed a large sample size and took 200,000 computational hours to complete. Baghdadi et al (Baghdadi et al. 2020) implemented a dynamic optimization scheme using a Bernstein polynomial-based code. The blade optimization was conducted at varying azimuthal angles with 60° azimuth angle yielding the best result. 3D simulation was conducted and confirmed a significant increase in performance with the largest increase found at TSR 2.5 at 98% increase in power coefficient. While the study showcased the strength of the optimization procedure, the authors concede it was proof of concept with no validation conducted.

Maalouly et al (Maalouly et al. 2022) conducted an optimization study based on the turbine chord length, airfoil shape, and angle of attack to produce a turbine for transient flow and steady state flow. The study was structured in a sequential optimization method where one parameter was studied at a time while other factors were fixed. Therefore, the authors included the Taguchi experimental method to reduce the number of simulation and streamline the amount variation from 125 simulations to just 25. The determining factor they found was the turbine solidity which has the most significant effect. The steady state turbine was found to have higher average power coefficient than the transient turbine, but the transient turbine achieves quasi static state much faster due to better start up. Drag and lift force analysis showed the drag effects to have a positive effect on the transient turbine at higher TSR. During testing at different wind conditions, at lower wind speeds, a high frequency sinusoidal flow yielded the most optimal for power production. The dynamic loading analysis shows the transient turbine to be more easily controlled. Minimizing the inertia of the steady turbine was found to improve start up.

Chen et al (Chen et al. 2016) showed that using different optimization codes could yield better efficiency for NACA0018. Using an orthogonal algorithm combined with automatic computational fluid dynamics analysis (ACFDA) and a second optimization step was a combination of one-factor at a time (OFAAT) algorithm with the ACFDA module, they found the NACA0018 had a maximum power coefficient of 0.4585 or 15.5% uplift when compared to an optimized

NACA0015. These studies generally found lower thickness blades produced worst torque efficiencies but has higher maximum performance coefficients as well as wider operational TSR range.

2.4.2 Turbine Solidity and Aspect Ratio

Numerous studies have shown considerations towards turbine solidity and aspect ratio as important factors in turbine design. Turbine solidity can be defined as the ratio of the blade swept area over the turbine radius or diameter (Ahmadi-Baloutaki, Carriveau, and Ting 2014). In equation form this is expressed as (Li, Maeda, Kamada, Shimizu, et al. 2017):

$$\sigma = \frac{Nc}{\pi D}$$

Where N describes the number of turbine blades and c denotes the chord length of the blade. Turbine aspect ratio is calculated as the ratio of blade length H to turbine diameter D. Fig 2.18 defines these parameters. In equation form, this is expressed as (Shamsoddin and Porté-Agel 2020):

$$\text{Aspect ratio} = \frac{H}{D} \text{ (Equation 2)}$$

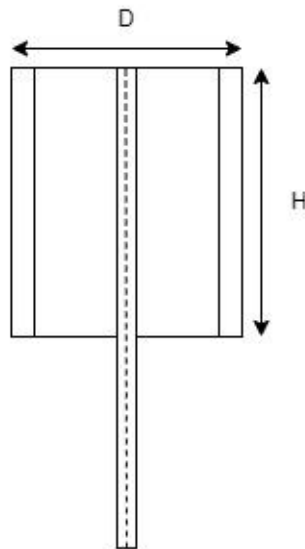


Fig 2.18. Definition of the aspect ratio

Where, H is the span length of the blade. The aspect ratio of the turbine blade is calculated similarly by replacing the turbine diameter D to the blade chord length c.

From the equations presented above, solidity value can be controlled either by changing the chord length or by varying the number of blades.

Ahmadi-Baloutaki et al (Ahmadi-Baloutaki, Carriveau, and Ting 2014) have shown a range of solidity values between 0.2 to 0.6 to be ideal based on various design considerations but a turbine solidity between 0.3 to 0.4 would yield the maximum power coefficient. The comparison was illustrated in Fig 2.19. A study on the effects of aspect ratio and turbine solidity by means of varying chord length value was given by Li et al (Li, Maeda, Kamada, Shimizu, et al. 2017). When solidity is fixed at $\sigma = 0.064$, they found maximum power to increase as the ratio of diameter to blade span length H/D increases, peaking at 0.273 when the ratio was at 1.2 with turbine diameter of 2 m. The results show that a smaller turbine diameter, determined by the length of the support-arms attached between the blades and the turbine shaft, yielded better power efficiency. When locking the aspect ratio of the turbine at $H/c = 6$, it was found that higher H/D ratio of 1.2 with larger solidity produced larger power coefficient at smaller TSR value of 2.0 but the smaller ratio with lower solidity extracts power with better efficiency at a larger range of TSR, with the optimum TSR value of 2.5. The local power coefficient study also showed that the last 10% of the blade tip along the span wise position is the least efficient location in extracting power. In a follow up study by the same authors, they found, by varying the number of NACA0021 airfoil blades to affect the solidity of the turbine, pressure difference acting on a single blade decreased as solidity, or in this case number of blades increased (Li, Maeda, Kamada, Murata, Shimizu, et al. 2016). Increasing solidity was found to reduce the lift and drag coefficients but increases the resultant flow velocity due to the increase in optimum TSR. Other factors such as aerodynamic efficiency also contribute to the performance of VAWT which affects the overall power generation capabilities of the wind turbines. They found power coefficients decreased with the increase in solidity. They noted that increasing the number of blades reduces single blade tangential and normal coefficient. Another study (Mohamed 2012) found lower solidity rotors operate better at higher TSR ratios whereas higher solidity rotors typically operate better at lower TSR ratios. At a low solidity of 0.1, the turbine was able to extract power at a wider range compared to the baseline up to TSR value of 10. These findings were corroborated by Brusca et

al (Brusca, Lanzafame, and Messina 2014) who also found maximum power coefficient to peak at around 0.51 at turbine solidity value of 0.3 with solidity 0.4 achieving almost similar efficiency. Low solidity turbines were found to have lower power coefficient with solidity of 0.1 achieving about 0.43 power coefficient but was operable at a significantly larger range of TSR values even beyond a TSR of 10. High turbine solidity saw limited operable TSR while achieving lower power coefficient. A solidity of 0.75 was found to peak at TSR of 2 at around 0.37 power coefficient. Singh et al (Singh et al. 2022) reported higher solidity of 0.45 and 0.375 predicted the maximum power coefficient but was only operational at lower TSRs. Lower solidity of 0.225 was found to be more efficient at higher TSR of 3 or more. Comparing a low solidity turbine (0.26) against a higher solidity turbine (0.34), Eboibi et al (Eboibi, Danao, and Howell 2016) reported similar results to previous findings favouring the later solidity over the former. A Particle Image Velocimetry analysis shows the formation and shedding of vortices starting earlier in the lower solidity turbine which leads to the dynamic stall happening earlier than the higher solidity turbine.

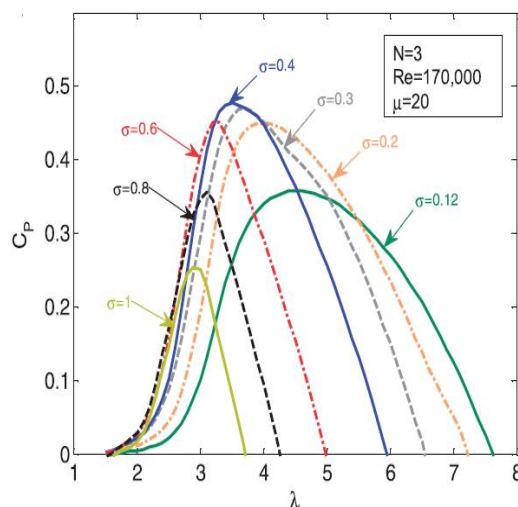


Fig 2.19 Comparisons of solidity ratio of the VAWT by Ahmadi-Baloutaki et al. (Ahmadi-Baloutaki, Carriveau, and Ting 2014)

However, some studies have shown that relatively high turbine solidity was found to have higher power coefficient. Joo et al (Joo, Choi, and Lee 2015) reported a turbine solidity of 0.5 achieved maximum power coefficient of 0.23 peaking at TSR about 2.6 which was higher than other solidity values. Lower solidity values

were seen to operate as well as peaking at a higher TSR. They also showed that high solidity turbines between 0.5 to 0.7 achieved the maximum torque by a significantly higher margin compared to the lower solidity turbines. Further analysis comparing torque per unit solidity with respect to TSR however showed that solidity between 0.3 to 0.5 achieved maximum value. Although the results indicate positive aspects of the turbine at high solidity, they also noted that increasing solidity was found to increase the effects of blockage and interactions. Reducing solidity reverses this effect but at the expense of the turbine's ability to self-start due to a reduction in the negative torque at lower TSR. However, this effect can be reversed by implementing a pitch offset to reduce the negative torque dip at lower TSR which helps enter the lift zone faster compared to the zero-offset turbine (Hill et al. 2008). Another approach to this problem was put forth by Huang et al (Huang, Luo, and Li 2023) in their novel design with varying solidity for improved turbine self-starting capability. The turbine design has a self-starting solidity of 0.83 which reduces to 0.417 during power generation. This allows for an increase in maximum power by 188%. A study by Fiedler and Tulis (Fiedler and Tullis 2009) also suggested some modifications to blade pitch and offset by applying a toe out pitch angle of $\pm 3.9^\circ$ and $\pm 7.8^\circ$ in improve a high solidity turbine which saw significant uplift of up to 29%.

Durrani et al (Durrani et al. 2011) compared varying number of blades setup and found similar to other studies a three-blade setup as the most optimal with maximum power efficiency of about 0.4. Increasing the number of blades up to six blades was found to reduce power efficiency significantly. Similar findings based on the number of blades were found by Li et al (Li et al. 2015). Increasing the number of blades which increases solidity sees a reduction in operational TSR range as well as extracting lower power coefficient with a two bladed arrangement obtaining the maximum efficiency. However, increasing the blade pitch angle to 8° improves the three or four bladed to relatively close to the two-blade set up. This adjustment to improve the turbine efficiency was significantly useful as they also showed that increasing solidity by number of blades saw increased torque coefficient which sees better starting characteristics of the VAWT. Tahani et al (Tahani et al. 2016) used an optimization campaign using various different algorithms and found a three-bladed turbine to be most optimal with a solidity ratio of 0.254. Celik et al (Celik et al. 2020)

found peak power coefficient was obtained with 3 turbine blades but increasing the number of blades up to 5 improves the turbine start up but the downside is the reduced turbine power coefficient. This was due to the increased number of blades increasing the power coefficient at the lower TSR values which is directly related to the turbine startup. The turbine startup was related to the positive drag effects which is more pronounced during the initial startup phase at lower TSR. However, when the TSR increases beyond TSR 1, lift force takes effect, hence why more turbine blades improved start up due to the better drag whereas a higher maximum power coefficient is obtained by reducing the number of blades.

Subramanian et al (Subramanian et al. 2017) found 2 bladed setup to be the most efficient over a longer range of TSR for both NACA0012 and NACA0030 turbine blades but a three bladed setup was more efficient for TSR of less than 2. Hand and Cashman (Hand and Cashman 2017, Hand, Cashman, and Kelly 2019) showed maximum power efficiency was produced at solidity values of 0.3 to 0.4 with reduced turbine radius but smaller solidity turbine operates at a much higher TSR range. They also show that increasing number of turbine blades with solidity kept constant results in higher power efficiency albeit at the cost of leaner blades. Hence, the authors recommended a two-bladed design. Gosselin et al (Gosselin, Dumas, and Boudreau 2013) also found that when turbine solidity was kept constant, increasing the number of blades up to 9 saw power efficiency increased over the three blade setup. Keeping the number of blades constant at three blades however saw significant power uplift in smaller solidity of 0.1829 over the larger solidity of 0.5486. However, similar to Li et al (Li et al. 2015), for a high solidity of 0.5486, implementing a 9° blade pitch angle was found to gain 27% efficiency. The author summarized a three-blade turbine with solidity of 0.2 to be most ideal. Difuntorum and Danao (Difuntorum and Danao 2019) found ideal turbine solidity to be 0.4 in a four-bladed turbine configuration. They showed maximum power coefficient achieved to be 0.3158 which is a slight improvement over the baseline. A two bladed set up with solidity ratio of 0.2 yielded slightly lower power coefficient of 0.283 but at a higher TSR of 4.5. Table 2.2 summarizes the reported optimal solidity and corresponding maximum reported power coefficient.

Table 2.2. Summary of reported optimal solidity from literature.

Author	Number of blades, N	Blade chord length, c (m)	Solidity Ratio	Reported maximum C_p
Ahmadi-Baloutaki et al (Ahmadi-Baloutaki, Carriveau, and Ting 2014)	3	-	0.4	0.46
Brusca et al (Brusca, Lanzafame, and Messina 2014)	2	0.303	0.3 at high Reynolds Number ($Re = 5 \times 10^6$) 0.2 at lower Reynolds number ($Re = 1 \times 10^5$)	0.51 (at ratio 0.3) 0.4 (at ratio 0.2)
Joo et al (Joo, Choi, and Lee 2015)	2	0.1 – 0.35	0.5	0.23
Hand and Cashman (Hand and Cashman 2017)	2	6.357	0.3	0.31
Gosselin et al (Gosselin, Dumas, and Boudreau 2013)	3	-	0.1372	0.50
Difuntorum and Danao (Difuntorum and Danao 2019)	4	0.15	0.4	0.3158
Subramanian et al (Subramanian et al. 2017)	2	0.420	0.33	0.34 (NACA0012) 0.35 (NACA0030)
Belabes and Paraschivoiu (Belabes and Paraschivoiu 2021)	2	1.75	0.1	0.34
Naseem et al (Naseem et al. 2020)	3	0.4	0.6	0.475
Yan et al (Yan et al. 2021)	3	0.246	0.138	0.24 (unmodified blade) 0.26 (best case serrated blade)
Tahani et al (Tahani et al. 2016)	3	0.1	0.254	0.44
Singh et al (Singh et al. 2022)	3	0.057 0.045	0.37 0.45	0.233

Table 2.3 sums up reported optimal aspect ratio from literature. For turbine aspect ratio, generally, lower aspect ratio or higher turbine radius tends to yield better efficiency. Sengupta et al (Sengupta, Biswas, and Gupta 2016) and Singh et al (Singh, Biswas, and Misra 2015) found maximum performance coefficients were obtained at an aspect ratio of 1 as well as having a much wider operational range of TSR compared to other tested ratios. Lee and Lim (Lee and Lim 2015) studied the effects of turbine solidity by varying the chord length and found by varying the chord length at a constant turbine radius, longer chord length extracted maximum power coefficient as well as being more efficient at TSR lower than 2. However, shorter chord length was found to produce higher torque and power coefficient at TSR values higher at or higher than 2.4. When increasing the rotor aspect ratio by increasing the diameter to blade span length ratio H/D , they found the effects of induced drag to be minimized, hence having a positive effect on the turbine power efficiency. A study by Tong et al (Tong et al. 2023) proposed a dimensionless ratio of airfoil chord length to rotor circumference (RCC) with the blade chord length and turbine diameter the varying parameter. They recommended an RCC value of 8% when chord length was kept constant and an RCC range of value between 9.5 to 13.4% when the rotor diameter was kept constant. Another study on the effects of aspect ratio by means of varying turbine height to diameter ratios was shown by Gupta et al (Gupta, Roy, and Biswas 2010) with a twisted blade design. The largest power coefficient was obtained at H/D ratios of 1.0 and 1.54 respectively. The results were corroborated by another study (Ahmadi-Baloutaki, Carriveau, and Ting 2014) which suggested optimal aspect ratio to be between 0.5 to 2 with maximum power coefficient obtained at $AR = 1$. When investigating the effects of aspect ratio, Brusca et al (Brusca, Lanzafame, and Messina 2014) found a low aspect ratio turbine $h/R = 0.4$ extracted a power efficiency of 0.475 whereas the higher h/R value of 2 extracted power coefficient of 0.464. The authors suggested lower aspect ratio turbines tends to be more efficient than higher aspect ratio turbines. With respect to turbine aspect ratio, a study on the effect of a VAWT aspect ratio in exhaust energy extraction, Singh et al (Singh et al. 2023) also found a lower aspect ratio of 0.44 to be the most optimal when comparing between a range of 0.3 to 0.7. This was attributed to the positive guided flow effect on the VAWT.

Table 2.3. Reported optimal aspect ratios from literature.

Author	Turbine height, H (m)	Turbine diameter, D (m)	Aspect ratio	Reported maximum C_p
Li et al [21]	1.2	3	0.4	0.25
Lee et al (Lee and Lim 2015)	0.6	1	0.6	0.46
Gupta et al (Gupta, Roy, and Biswas 2010)	-	-	1.5 and 1.54	0.51
Singh et al (Singh, Biswas, and Misra 2015)	0.3	1.2	1	0.32
Yan et al (Yan et al. 2021)	0.78	1.7	0.46	0.24 (unmodified blade) 0.26 (best case serrated blade)

2.4.3 Vertical axis wind turbine support-arm

2.4.3.1 Reported turbine support-arm geometry

In this section, the turbine support-arm geometry was discussed. Unlike the HAWT, the VAWT, particularly the H-type VAWT, requires support structures to hold and connect the turbine blades in place for torque transfer to the main shaft. The turbine support-arm is an essential part of a VAWT and can play an aerodynamic role during turbine operation. support-arm geometry generally reported tends to be either circular, rectangular or NACA blades. Circular geometry were reported by Nini et al (Nini et al. 2014) and Lei et al (Lei et al. 2017). A rectangular support-arm has also been reported by Siddiqui et al (Siddiqui, Durrani, and Akhtar 2015, Siddiqui, Durrani, and Imran 2013) as well as its significant effects as support-arm structure on the VAWT performance. Studies by Howell et al (Howell et al. 2010) and Qin et al (Qin et al. 2011) also reported using rectangular support-arms but its aerodynamics effects were not studied. A variation of the rectangular arm reported by Chen et al (Chen et al. 2015) saw a three bladed VAWT with a rectangular cross sectioned monolithic support-arms connected at two different points along the wingspan of the blade which were deemed the aerodynamic centre of the airfoil.

Some studies have also explored the viability of blade type support-arms using the NACA family airfoil of varying thickness. A study by Bianchini et al (Bianchini et al. 2017) used thicker airfoil of NACA0020, shown in Fig 2.20 in their turbine design which they suggest would reduce parasitic torque acting on the support-arms. De Marco et al (De Marco et al. 2014) used NACA0018 airfoil in an inclined arm configuration to reduce drag acting on the support-arm shown in Fig 2.21. The simulation results showed promise with respect to air flow and performance coefficients. Bachant et al (Bachant and Wosnik 2015, Bachant and Wosnik 2016a, Bachant and Wosnik 2016b) also used a single arm configuration with NACA0020 profiled support-arms. The designed 3 bladed turbine had a performance peak at TSR value approximately 1.8 with power efficiency value of 0.26 and drag coefficient of 0.96. Drag coefficient was found to increase almost linearly as the tip speed ratio increases although the support-arm effects on the drag was not mentioned (Bachant and Wosnik 2015). Vergaerde et al (Vergaerde et al. 2020) used thicker NACA0024 airfoils to support the turbine blades with NACA0018 profile. Kjellin et al (Kjellin et al. 2011) also used modified thicker blades similar to NACA0025 with a shorted trailing edge to support turbine blade arms of NACA0021.

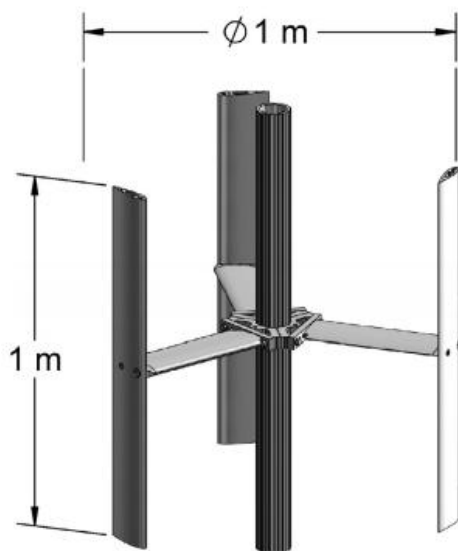


Fig 2.20. Single support-arm design utilizing airfoil blade NACA0020 by Bianchini et al (Bianchini et al. 2017).

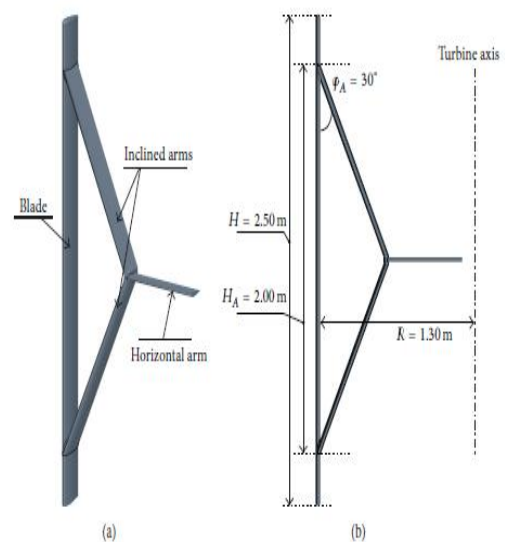


Fig 2.21. Inclined support-arm arrangement by De Marco et al. (De Marco et al. 2014).

With respect to effects of turbine support-arm geometry on turbine performance, in a short analysis, Ahmadi-Baloutaki et al (Ahmadi-Baloutaki, Carriveau, and Ting 2014) compared different support-arm geometry from literature against the authors suggested aerodynamically profiled NACA0015 blade. They found the NACA0015 arms showed the least turbine power coefficient loss with the rectangular and diamond shape geometry showing significantly larger losses especially pronounced at $TSR > 3$. The results are shown in Fig 2.22. However, the NACA0015 also experienced larger maximum stress with the hollow cylinder experiencing the least. A study by Li et al (Li and Calisal 2010) compared two arm profiles of different cross sections; a thick bullet-like profile with thickness 0.38in and length of 1.84in against the NACA0012 airfoil profile. The study showed that the former was significantly inferior with respect to power coefficient at TSR ranged between 1 and 4. The NACA0012 support-arm was found to have maximized power coefficient at TSR value between 2.6 and 2.8. Hara et al (Hara et al. 2019) compared the three different support-arm geometries namely the NACA0018 blade profile, a rectangular cross section, and a circular rod. Fig 2.23 shows the airfoil NACA0018 arm reported the best result in terms of power coefficient. The airfoil arm also yielded the least in terms of averaged pressure-based tangential force coefficients along the turbine arm with a value of 0.05 while the highest was recorded by the rectangular arms 0.415 and circular 0.376. The opposite, however, was true whereby the airfoil arms recorded the largest averaged friction-based tangential force coefficient along the arm with a value of 0.024 while the rectangular arm recorded a negative coefficient of -0.004. They found resistance caused by pressure to have more significant than resistance due to friction. The largest total resistance torque was obtained by the rectangular arm while the NACA0018 arm recorded the lowest. It was noted that the resistance torque coefficient due to friction was found the highest in the airfoil arm. Lastly, comparing the blade and arm structure together, it was found that the circular arm contributed the most to the total resistance torque coefficient at 82.1% with the turbine blade only accounting for the remaining 17.9%. The NACA0018 arm however was found to have much lower contribution at 38.7%. With respect to turbine arm optimal geometry, Miao et al (Miao et al. 2023) attempted a parametric optimization by varying the support-arm chord length, thickness, and streamline shape. The authors suggested an olivary

shape - a dual front and back sharp tip similar to the trailing edge of an airfoil, as the most optimal. However, a spanwise analysis was not presented and, hence, the olivary shape was applied across the span length of the support-arm.

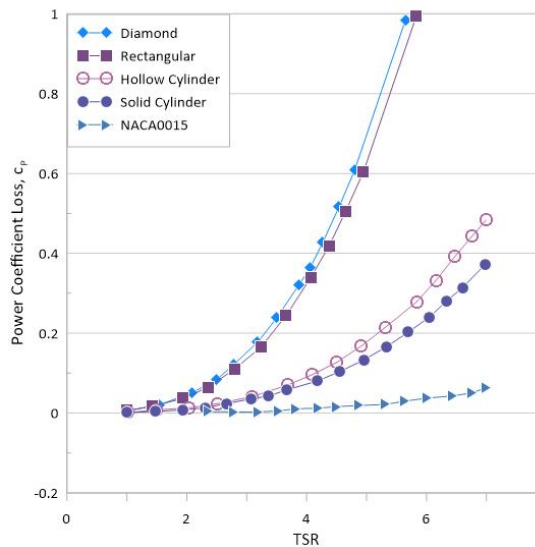


Fig 2.22. Effects of arm geometry on power coefficient losses by Ahmadi-Baloutaki et al. (Ahmadi-Baloutaki, Carriveau, and Ting 2014)

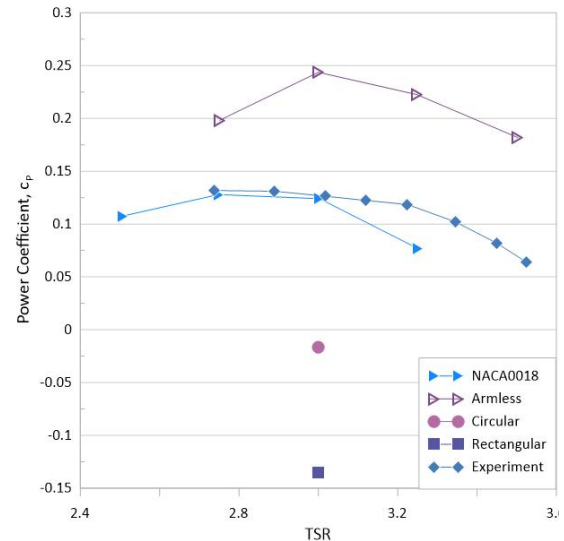


Fig 2.23. Comparisons of power coefficient of different geometry by Hara et al. (Hara et al. 2019). Experimental results were referred from another study.

In a study by Hand and Cashman (Hand and Cashman 2017, Hand, Cashman, and Kelly 2019), found lower thickness support-arms tend to produce higher maximum power coefficient as well as extract power at a longer range of TSR. Thicker support-arms however were found to suffer severely at higher TSR while producing lower maximum efficiency. This was due to thicker support-arms experiencing higher drag which leads to power losses especially at higher TSR. Considering this, they proposed a variable cross section support-arm similar to how HAWT turbine blades shown in Fig 2.24 and Fig 2.25. The support-arms were designed with a circular cross section at the root connected to the main shaft that then shapes into a thick airfoil profile and tapers down as it connects to the turbine blades. The thickest blade chord was located at r/R of just under 0.3 with minimum thickness at the support-arm tip connected to the turbine blade. However, justification for these design choices were not given.

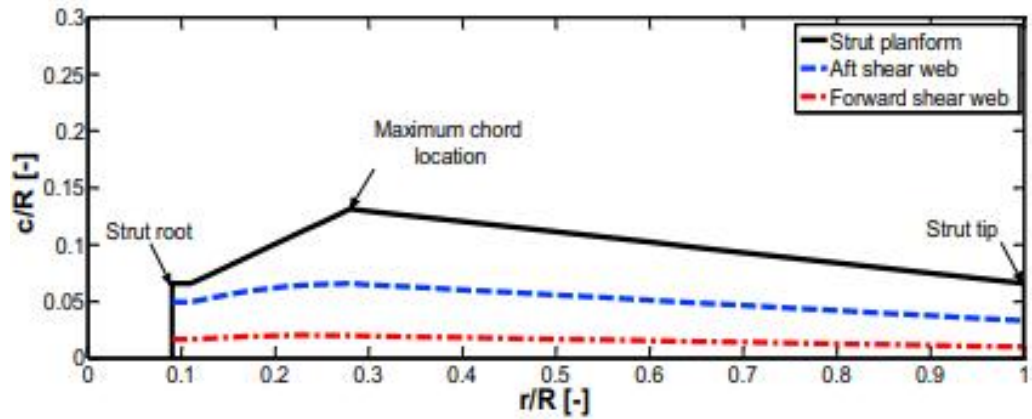


Fig 2.24. Cross section of the support-arms along its span length (Hand and Cashman 2017).

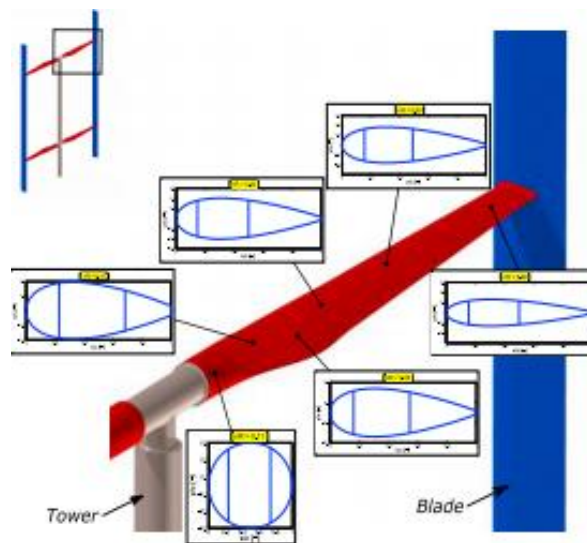


Fig 2.25. support-arm cross section showing different blade profile along its span length (Hand and Cashman 2017).

2.4.3.2 Turbine support-arm configurations

In this section, the turbine support-arm configuration or arrangement will be reviewed. Different support-arms configuration has been reported in literature. The design of a straight bladed VAWT utilizes either a one or two support-arm connected to the turbine blades. A dual support-arm arrangement is when the turbine arms are connected at two locations along the span length or at the tip of the blade. A typical dual support-arm configuration can be seen in Hashem et al. (Hashem and Mohamed 2018) study shown in Fig 2.26. When support-arms are connected at the ends of the turbine blades, this is referred to as a frame type configuration. Lee and Lim (Lee and Lim 2015) used this configuration in their design of a three bladed 500W

(VAWT) shown in Fig 2.27. Other examples were also provided Xu et al (Xu, Peng, and Zhan 2019) and Singh et al (Singh, Biswas, and Misra 2015). A single support-arm design is typically known as a H-type configuration. Bianchini et al (Bianchini et al. 2017) suggested single support-arm with an airfoil NACA0020 cross section previously shown in Fig 2.20. Siddiqui et al (Siddiqui, Durrani, and Akhtar 2015, Siddiqui, Durrani, and Imran 2013) used similar arrangement as well as other authors throughout literature (Bachant and Wosnik 2015, Bachant and Wosnik 2016a, Bachant and Wosnik 2016b). For both single and dual support-arm configuration, the locations of the support-arm relative to the span length and chord length have also been established. The mounting position of a single support-arm VAWT is usually at the midpoint of the blade span length. Chen et al (Chen et al. 2015) found the mounting ratios or mounting positions of the support-arms relative to the airfoils chord length were determined to be best at 0.25 of the turbine blade which is the aerodynamic centre of the NACA0015 airfoil used. Another study (Difuntorum and Danao 2019) observed similar findings with the ideal mounting position with respect to the leading edge of the blade is at $0.7c$. Maximum power coefficient was located at this position which was higher than the baseline $0.5c$. The least ideal mounting position was $0.15c$. With respect to the spanwise location of the support-arms, a simple stress analysis by Ahmadi-Baloutaki et al (Ahmadi-Baloutaki, Carriveau, and Ting 2014) determined that the optimal dual support-arms location to be at 0.21 from the end of the blade at each end.

A helical design is defined by the helix-like angle of the turbine blades. Some studies have discussed its benefits even though maximum power coefficient tends to be achieved with no helical angle applied with all else being equal (Lee and Lim 2015, Marsh et al. 2015). One of the helical designs main benefits is the aerodynamic forces acting on the turbine blades. Wang et al (Wang, Wang, and Zhuang 2018) showed a high twist angle of 120° was found to reduce low torque fluctuations but a more modest angle of 60° was found to produce highest power coefficient. The helical design was found to significantly reduce the force fluctuations experienced by the blades due to more even force generation per blade. This means the longevity of the turbine blades can be enhanced. Albeit a different medium and application, similar results were observed by Marsh et al (Marsh et al. 2015) a saw helical angle

blade design reduces torque oscillations and mounting force but at the cost of power coefficient. This was attributed to the reduced moment coefficient due to the shape of the curvature of the blades.

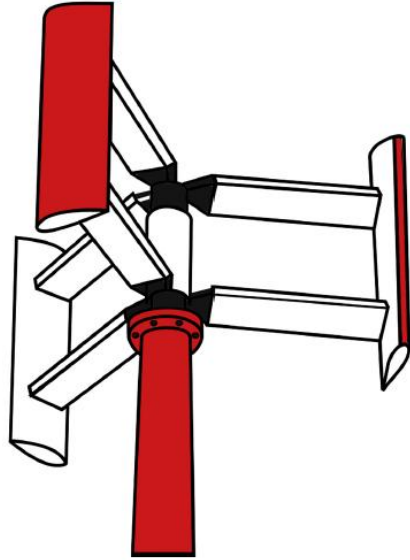


Fig 2.26. Dual support-arm configuration by Hashem and Mohamed (Hashem and Mohamed 2018).

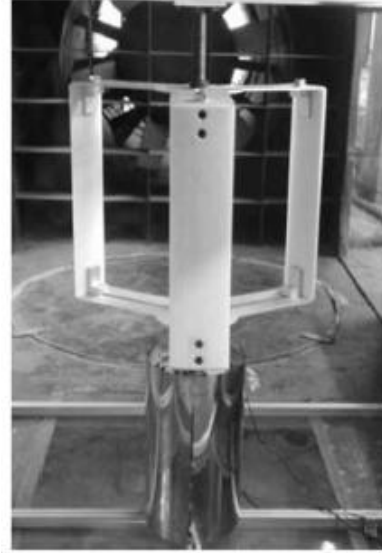


Fig 2.27. Frame type configuration with support-arms at each turbine blade ends by Lee and Lim (Lee and Lim 2015).

De Marco et al (De Marco et al. 2014) suggested a three-part inclined support-arm arrangement in their turbine design. By comparing the instantaneous total torque, they found a two bladed arrangement yielded larger torque, but a three bladed arrangement showed more frequent peaks due to the added blade. However, performance coefficient favoured the two bladed arrangements instead with higher efficiency. When taking only the three-arm arrangement into account, the multipart configuration was able to generate more wakes which enhanced turbine performance in the downwind zone. Using this three-arm configuration, they observed a turbine radius of 1.3 m was able to extract wind power at a larger TSR range but a turbine radius of 1.6 m maximized performance efficiency. Also, at a TSR range between 2 to 3, lower turbine arm chord length of 0.12 m yielded maximum power coefficient value of about 0.29 but a longer chord length of 0.20 m extracted higher power efficiency at TSR value of 2 or lower. The observations are shown in Fig 2.28. Another field study also reported similar support-arm configuration (Lin et al. 2018). Other arrangements such as the V design was also reported by He et al (He et al.

2020) connected at $\frac{1}{4}$ of the chord length to three turbine blades shown in Fig 2.29. A variation of the V arrangement with a large gap between the two support-arms was also described by Vergaerde et al (Vergaerde et al. 2020) as shown in Fig 2.30.

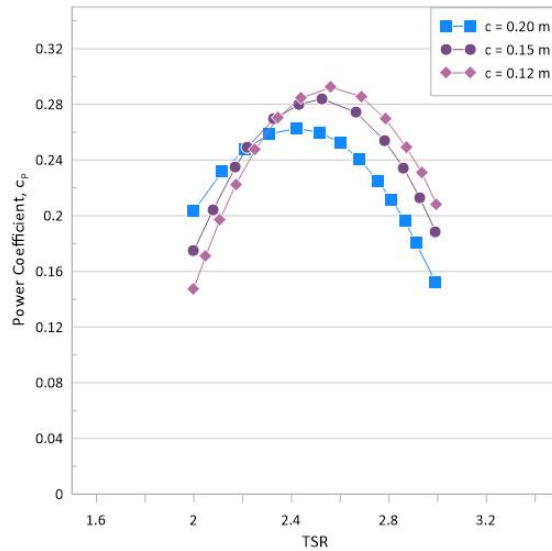


Fig 2.28. Effect of turbine arm chord length on power coefficient by De Marco et al. (De Marco et al. 2014).



Fig 2.29. Two support-arm arrangement from He et al. (Hashem and Mohamed 2018).

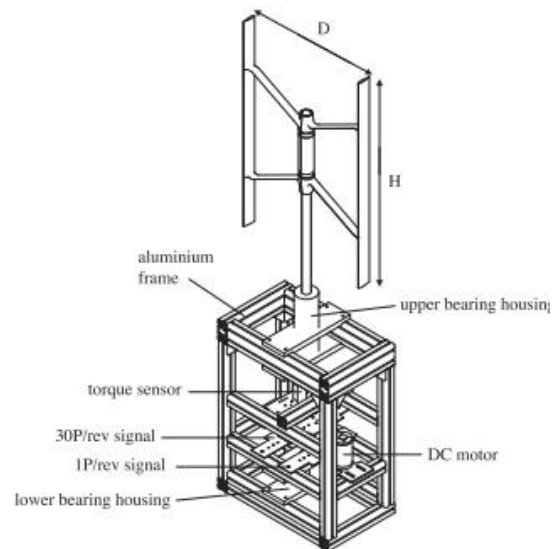


Fig 2.30 V shape support-arm configuration by Vergaerde et al. (Vergaerde et al. 2020).

2.4.3.3 Support-arm Effects in Numerical Studies

From literature, it was shown that the upstream region just after the first blade usually induces turbulent flow that induces vortex into and around the support-arm

region. This would therefore have some aerodynamic effects on the support-arms itself. Also, the rotating motion of the turbine about the main shaft means that the support-arms itself would induce wake vortices. This was observed by Li et al (Li et al. 2019) who found turbulent flow of the blade wake and vortices were most pronounced at the centre of the blade within the rotor shaft and support-arm region. Lei et al (Lei et al. 2017) showed in the instantaneous vorticity magnitude Figs the negligible effects of supporting arm design where only the turbine blade effects were pronounced during surge and non-surge motion. This minimal effect was significant as the iso-surface contours showing normalized velocity illustrates that large vortex structure can be seen around the shaft area of the VAWT especially in the downwind instance where the supporting arms are located. Bachant et al (Bachant and Wosnik 2016b) demonstrated the formation of blade tip vortices in their 3D study but also significant vortex shedding from. This led to vortex shedding from the centre of the turbine blade as shown in Fig 2.32. This observation showed a physical effect the support-arm has on the flow physics of the support-arm. Therefore, it is expected that turbine performance would be linked to the support-arms structural arrangement and geometry. Although some studies showed this effect in 2D and 3D simulations, many of them do not take the support-arm design, arrangement or geometry into consideration (Lee and Lim 2015, Mohamed 2012). Studies have shown 3D simulation with arm effects to have a significant effect with over prediction of the performance coefficient being the main one (Hara et al. 2019, Daróczy et al. 2015). Some have also reported that support-arms have been known to cause significant drag (Hand and Cashman 2017, Paraschivoiu 2002) which can be highly dependent on the operating TSR of the turbine (Howell et al. 2010).

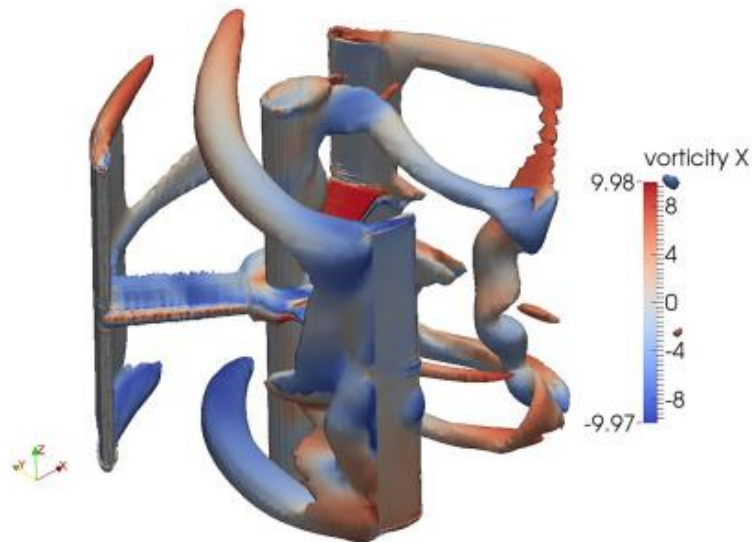


Fig 2.31. Iso vorticity contour showing vortex shedding around the turbine blades and support-arm by Bachant et al (Bachant and Wosnik 2016b).

The 3D effects of support-arms have been reported in numerous studies. When comparing the simulation data, Castelli et al. (Castelli et al. 2010) found for small aspect ratio turbines, the effects of arm losses due to drag further reduce the performance measured by 40% against the baseline 2D simulation. They concluded that for micro VAWT arm drag effects can play a significant role in the performance of the turbine. This observation was also reported by another study. Arm drag on the support-arms were also noted to directly act against torque generation. Siddiqui et al. (Siddiqui, Durrani, and Imran 2013) studied the effects of 3D support-arms with a simple 3D simulation without the added structures. In the power coefficient comparison, illustrated in Fig 2.32, it was shown that, as the TSR value increases, so does the difference between the two types of simulation with 3D results without the support-arms over predicting by over 35% at TSR value of 4 and above. A second study found, due to the presence of the support-arms and rotor shaft geometries, there was a noticeable drop in performance during the downwind portion of the flow between 220° to 360° (Siddiqui, Durrani, and Akhtar 2015).

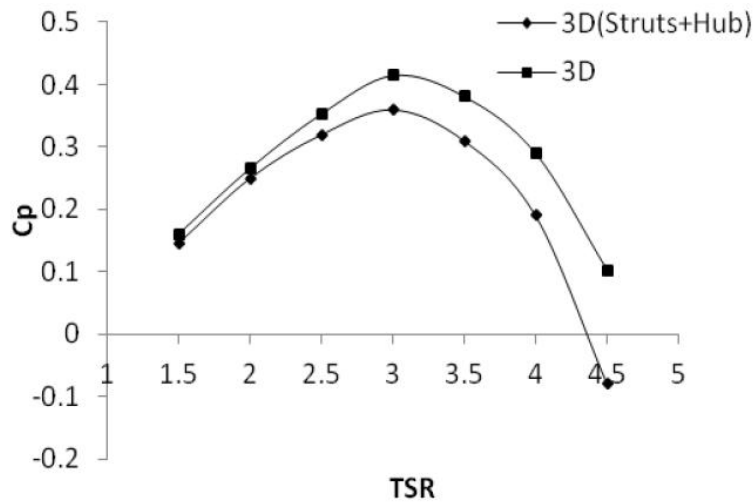


Fig 2.32. Comparison by Siddiqui et al. (Siddiqui, Durrani, and Imran 2013) showing the effects of support-arm and turbine hub on the power coefficient against the baseline turbine with no support structure.

This was attributed to the significant induced vortices from said assemblies as well as drag due to the support-arms. Comparing the full structure with support-arms and rotor shaft against 2D simulation results only considering the turbine blades, they found ignoring the support assemblies altogether results in an over 25% overestimation in turbine power. Nini et al. (Nini et al. 2014) designed a VAWT with two flat radial type turbine arms each connected to all three turbine blades. In the normal plane study, vertical structures generated by the support-arms can be observed with higher concentration on the upper arm surface compared to the lower arm surface. Also, computational studies in the symmetry plane where X velocity and Z vorticity shows that at higher tip speed ratio wake is irregular and shows significant interference between the blades and shaft region. For a small rooftop VAWT, Qin et al. (Qin et al. 2011) conducted a comparative study between a 2D simulation on just the turbine blade arms against a 3D simulation taking the whole VAWT structure including the support-arms showed significant discrepancies. A drop of almost 40% was observed which the authors attributed as blade tip and supporting arm losses. They found significant vorticity effects around the supporting arms which contribute to losses due to viscous effects shown in Fig 2.33.

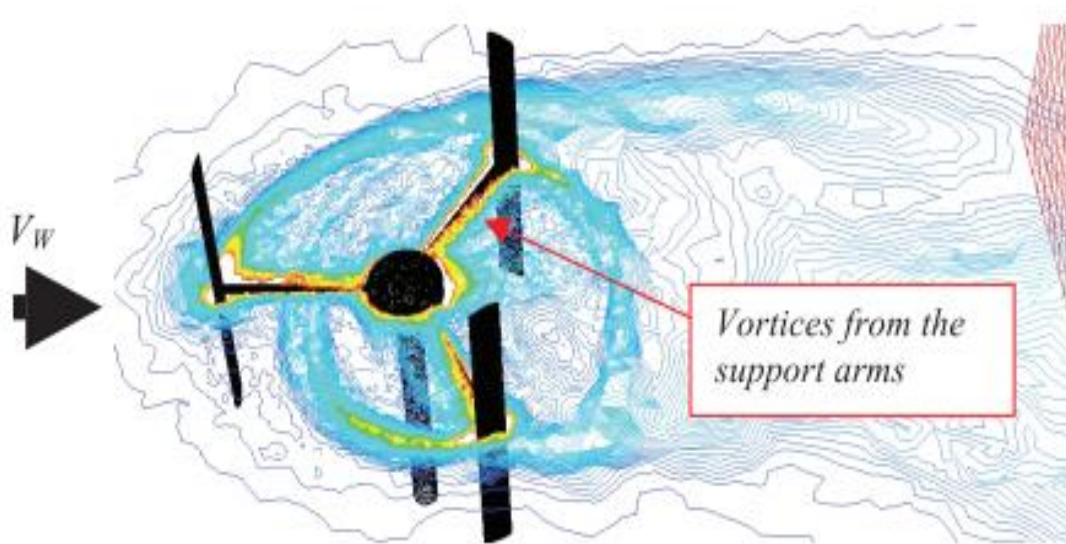


Fig 2.33. Vortex structures shown around the support-arm area by Qin et al. (Qin et al. 2011).

Studies have shown that the support-arm arrangement not only affects the turbine measurable performance but also significantly affect the flow field around the turbine. In a single support-arm arrangement, Bianchini et al (Bianchini et al. 2017) used NACA0020 airfoil as the support-arm structure. In their velocity field diagram, it was shown that generally low wind speed was observed in the rotor shaft area towards the downwind with ripples were observed at two separate locations when $TSR = 1.4$. The first high wind speed ripple was caused by the separation of strong vortices from the upwind portion. The second low wind ripple was attributed to a velocity deficit in the wake of the rotor shaft. At $TSR = 1.9$, low wind speed ripple was also observed at the downwind portion of the flow. A separate study (Bachant and Wosnik 2016b) using the same configuration found in the iso-vorticity contour significant vortex shedding on the upper side of the blades and the blade support-arms. Comparisons between different support-arm geometry by Hara et al (Hara et al. 2019) observed from the Q- criterion and vorticity diagram significant vortex shedding consistent with the von Karman vortex street in the wake of the circular arms. The vortex shedding for the airfoil arm NACA0018 was minimal and came mainly from the trailing edge of the airfoil. Both airfoil and rectangular arms displayed similar loop-like vortex generated by the support-arm geometries shown in Fig 2.34. The arm-less turbine however only produced tip vortices induced by the blades which are consistent with other reported findings. Another configuration with

a multipart support-arm arrangement proposed by De Marco et al (De Marco et al. 2014) noted that the arrangement generated significant wake vortices which were mainly generated at the 45° arm blades and the connection part between the straight section and inclined section. These findings indicate that support-arm arrangement and geometry do contribute to the development of vortex structures around the turbine.

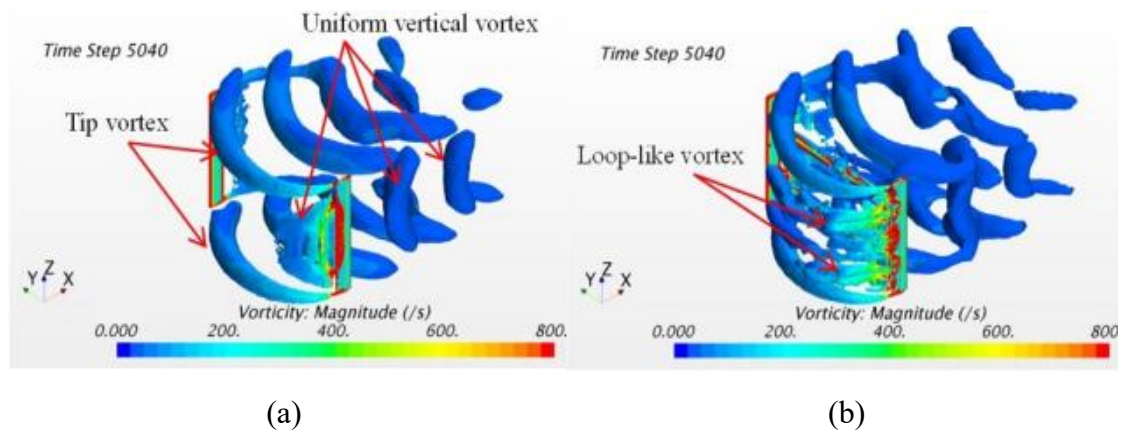


Fig 2.34. Comparisons showing (a) tip vortex induced by armless blades and (b) loop-like vortex generated by the rectangular arm. (Hara et al. 2019)

2.5 Discussion

Recent studies have covered various design aspects as well as reported many improvements made to further enhance the performance of the VAWT. An important aspect in most studies was developing a proper experimental set up in which the wind tunnel played a significant role. Although other experimental set ups were proposed, the wind tunnel set up has been very much favoured. Another important analysis method was the CFD numerical method implemented in various ways by different studies. Although many codes and models do exist and have their use cases, literature tend to favour the URANS code in CFD simulation with $k-\omega$, $k-\epsilon$ and their variants being the most popular. In these simulations, it was summarized that 2D simulation results tend to over predict the performance coefficients significantly when compared to 3D and experimental results. Studies have attributed this mainly due the absence of 3D effects such as arm drag and tip vortices in 2D simulations that are otherwise present in 3D simulation and experiments. Attempts to improve 2D results, such as applying velocity correction factor (Li et al. 2015), to bridge this

discrepancy were reported. However, the differences compared to 3D simulation and experimental results were still significant.

Various blades have been studied and its effects compared and improved by numerous authors. Symmetrical blades were especially popular with various blades used such as the NACA0015, NACA0018 and NACA0021. However, the NACA0015, with a thickness of 15%, was reported to be the most consistent in achieving maximum power coefficient as well as operate at an acceptable TSR range. This is an important factor as it is desirable for a VAWT to operate at least at 70% of its maximum power coefficient over as large of a range of TSR as possible (Ahmadi-Baloutaki, Carriveau, and Ting 2014). Other symmetrical blades, such as the NACA0018 and NACA0021, were also found to perform admirably and were used for various reasons and justifications. Non-symmetrical blades were also shown to be better at extracting wind energy compared to symmetrical blades. Extracting wind energy at lower TSR can be useful especially for urban use and densely populated areas since lower TSRs tend to favour more tolerable noise emissions. Profile modifications, the often-reported ones being the trailing edge flap design and blade-edge serrations, were also suggested which improved performance coefficients when compared the non-modified baseline. Hence, multiple reports in literature has been done either to identify and decide on optimal blade suggestion through comparisons of different blade designs by numerical or experimental means, or present profile modifications on pre-existing blade designs. Although such methods have shown varying degrees of improvement to the turbine efficiency, the inconsistent, diverse, and at times conflicting, opinions from different studies raises the question of could a different or new turbine blade geometry instead be developed entirely? Therefore, to answer this question, another method of VAWT improvement has seen a rise in interest over recent years.

The use of optimization codes to identify combinations of parameters for optimal or ideal turbine or an ideal turbine blade has been reported. Many reports were made on the use of genetic algorithm combined with other methods to optimize the VAWT. Some studies used the algorithms to generate a suitable combination of parameters in a semi-parametric optimization study that yielded good results. Other studies have shown using the optimization algorithms or codes to generate new blade

profiles which illustrates the significant possibility of yielding a plethora of novel optimized blade shapes which can be more suitable for more specific use cases based on the design requirements compared to current established blade profiles. Although these studies have shown that an optimization strategy can generate new blades, at the moment, very limited studies have actually tried to go past a proof of concept idea and into developing a proper optimization procedure showing not only the initial steps, blade parameter considerations and improvements to the turbine performance, but also other blade elements such as flow physics of the developed turbine blade, aerodynamic characteristics, and real world application of the new turbine blade.

On the effects of turbine solidity and aspect ratio, literature tends to favour a three bladed setup for optimal torque generation and power coefficient as well solidity values of between 0.3 to 0.4. This was due to the turbine being able to extract maximum power efficiency at a more modest TSR of between 2 to 4. Although lower solidity turbines tend to increase operational TSR range (Joo, Choi, and Lee 2015), it does promote other negative aspects such as increased noise levels at higher TSR values as well as poorer torque efficiency. Hence, a solidity value of 0.3 is quite optimal due to maximum power efficiency and TSR. In terms of number of blades, it was generally understood that increasing the number of blades also means increasing the number of support-arms which would contribute to increased drag (Gosselin, Dumas, and Boudreau 2013). Although the two-blade setup was also popular due to the maximum power coefficient achieved, a three-blade setup produces smoother torque generation as well as comparable performance efficiency. The three-bladed turbine also has the added advantage of having better self-starting capability compared to the two bladed turbine which has been studied to be highly dependent on its starting position (Dominy et al. 2007). However, varying the number of turbine blades or solidity ratio would also vary the turbine support-arms structure and the effect of this has not been fully understood.

In the next section, it was seen that a significant number of studies seems to neglect the design and effects of turbine support-arms in their design and analysis. However, of those that do consider support-arm design and effects in their simulation, they concluded the support structure to be a significant factor in the performance of the turbine (Hara et al. 2019). Neglecting support-arms in simulation was found to

have a profound effect on turbine performance coefficients, which indicated accuracy of simulation results could be affected (Daróczy et al. 2015). Hence, some studies have presented different support-arm geometries and arrangements to improve the turbine performance. The effects of arm drag can be significant depending on the shape of the support-arms as well as arrangement (Li and Calisal 2010, De Marco et al. 2014). Lastly, although there were some literatures showing the 3D effects of the support-arm, such as vortices structures generated on its surface as well as being an arbitrary source of parasitic drag, the lift and drag contribution as well as the characteristics of each during turbine operation has not been fully addressed and would deserve as more thorough investigation. Table 2.4 summarizes some of the important points presented in this paper.

Table 2.4. Summary of the main findings and studies in this literature review.

Authors	Studies	Main Findings
Howell et al (Howell et al. 2010)	Studies comparing 2D and 3D predictions against experimental results	2D predictions tend to over predict performance coefficients significantly due to the absences of 3D effects such as tip vortex.
De Marco et al (De Marco et al. 2014) and Hara et al (Hara et al. 2019)	Arm arrangement and its performance effects on the wind turbine	Different support-arm configuration or arrangement results in wildly different flow field around the wind turbine.
Hand and Cashman (Hand and Cashman 2017), Hara et al (Hara et al. 2019) and Ahmadi-Boulataki et al (Ahmadi-Baloutaki, Carriveau, and Ting 2014)	The effects of arm geometry on the aerodynamic performance of the wind turbine	Symmetrical NACA airfoils performed the most optimal of all other support-arm geometries. Unsymmetrical or cambered blades, however, were not considered.
Li et al (Li, Maeda, Kamada, Murata, Shimizu, et al. 2016) and	Effect of rotor aspect ratio or solidity	Maximum performance coefficients tend to favour a two bladed set up but, at a constant solidity value, efficiency favours turbines with more blades

Joo et al (Joo, Choi, and Lee 2015)		
Mohamed (Mohamed 2012) and Durrani et al (Durrani et al. 2011)	Comparisons of different blades	Many different turbine blades can be usable for optimal power extractions. Symmetrical blades are popular choices for efficient turbine performance, but some unsymmetrical blades have been shown to generate good performances with respect to turbine efficiency.
Siddiqui et al (Siddiqui, Durrani, and Imran 2013)	Effect of support-arms in 2D and 3D	Describes the effect of neglecting support-arms in simulation resulting in over prediction of performance parameters studied.
Marinic - Kragic et al (Marinić-Kragić, Vučina, and Milas 2022, Marinić-Kragić, Vučina, and Milas 2018)	Shape optimization using multi objective genetic algorithm (MOGA)	Shape optimization using the genetic algorithm MOGA yielded increased performance in Savonnius turbines.
Wang et al (Wang et al. 2022)	Blade shape optimization using particle swarm optimization algorithm and RFOIL	Shape optimization code yielded an improvement in NACA0015 performance.
Day et al (Day et al. 2021)	Adjoint based optimization	Shape optimization of a NACA0018 blade showed improvements to the turbine blade tangential force. However, this improvement was not translated into a full turbine analysis.

2.6 Research Gap

Literature has shown multiple reports on improving the VAWT with respect to its main lift structure, the turbine blade, by performing and suggesting various methods to this end. The theoretical aspects of various optimization methods were reported but a more in-depth study on an optimization scheme with respect to performance

coefficients, aerodynamic performance, flow physics analysis, and finally a real-world application and test has not been thoroughly established. Therefore, this study aimed to address this gap by applying the adjoint method paired with the gradient-based optimizer to suggest a new and novel optimized blade. This was done through numerical work and experimental investigations on the candidate VAWT turbine with optimized turbine blade and support-arm geometry.

2.7 Summary

To summarize, many studies have been done on improving the VAWT. Aspects of turbine design such as the turbine blade selection and its various efficiency ranges and operating TSR has been presented by various authors. The consensus was that the symmetrical blades were efficient but unsymmetrical and cambered blades can be considered as well. The turbine solidity ratio and aspect ratio also influenced turbine efficiency and operating TSR range but, to a certain extent, the ideal ratios of both parameters have been consistently established and agreed upon in literature. The turbine support-arm studies concerning geometrical shape, effects in numerical simulation and real-world application have been reported. Although a general understanding of its effects to turbine performance has been established, limited research was conducted to further improve the support-arm structure with regards to the turbine performance. And lastly, besides a parametric approach to turbine improvements, numerous attempts have been made to improve the turbine performance using various optimization codes. The results were positive but also showed there is room for more research to this approach as well as implementing the optimization results in real world test to validate the performance improvements.

Chapter 3

Research Methodology

3.1 Overview

To study the effects of turbine support-arms, as a basis for further design optimization in later parts of this study, a clear understanding of current turbine support-arm geometry and arrangement or configuration is necessary. The first turbine is an ideal turbine for comparison. The ideal turbine, or baseline turbine, is a turbine design with only blades and no support structures. The other two turbines are turbines in full configuration with support structures to consider during numerical calculations. The first is a two bladed NACA0018 turbine with dual circular support-arms. Numerical analysis will be done to study the predicted torque and power coefficient of the turbine as well as drag and lift coefficients of the turbine support-arms. Then, the turbine flow physics of the turbine at different azimuthal angles will be analyzed. All analysis will be compared against the baseline turbine.

The second comparative study is on a three bladed NACA0021 turbine with dual circular shaped support-arms. The thicker blade, as well as increase in one extra pair of blades – support-arm combination, was expected to generate a more pronounced wake and turbulence within the inner turbine region and this effect was be studied. Similar analysis and comparison to a baseline turbine was also conducted on this turbine.

After the baseline performance of a current VAWT understood, an optimization scheme applied on the turbine blade was then explored and established. A 2D optimization scheme was developed using the adjoint method together with the gradient-based optimizer. Several turbine parameters were objectively analyzed and their effects on the result of the adjoint optimization were presented. Then, two 3D numerical studies were conducted to further analyze the candidate blades with 3D

effects such as blade tip losses. The first study focused on the 3D performance of the candidate blade compared to the baseline blades. The second 3D study explored a full turbine configuration with the candidate blade geometry applied to both the turbine blade and the support-arm geometry.

Lastly, a wind tunnel experiment was conducted. The candidate blade was compared to the baseline NACA0018 blade performance comparisons were made between the two turbines. Then, a parametric analysis of the candidate blade, comparing turbine solidity, number of blades, and aspect ratio was conducted. At the end, a suggestion was made on the ideal turbine parameters for optimal turbine performance based on the turbine blade's optimized shape.

3.2 Methodology Breakdown

This research was divided into three different stages. The first stage involved comparisons of current turbine support-arm geometries and configuration against a baseline turbine for the numerical section. Once an understanding of current turbine support-arm geometry and configuration has been established, for the second stage, the adjoint shape optimization strategy was developed and implemented on two different types of turbine blades: the symmetrical NACA0018 and the cambered S1046. The optimization scheme involving various parameters deemed crucial to the development of the candidate blades discussed. Multiple candidate blades were presented and compared against one another and the baseline blades with the goal of determining the best candidate blade with respect to turbine power performance and efficiency. The results of the optimization, the best case from the optimization scheme yielding the most optimal candidate blades, were then extracted for stage 3.

In stage 3, further 3D numerical analysis and experimental tests were conducted to further verify the results of the 2D optimization. The candidate blade were extracted and redrawn into 3D blades. 3D numerical analysis was conducted in two configurations: blade only and full configuration with turbine support-arms. The performance coefficients were evaluated considering 3D effects such as tip losses and support-arm losses. The flow field contour, with respect to velocity contour, pressure contour, and streamline were analyzed. Lastly, an experiment was also

conducted to support and confirm the results of the optimization showing the improved turbine performance with respect to power production. A map of the stages in this study was shown in Fig 3.1.

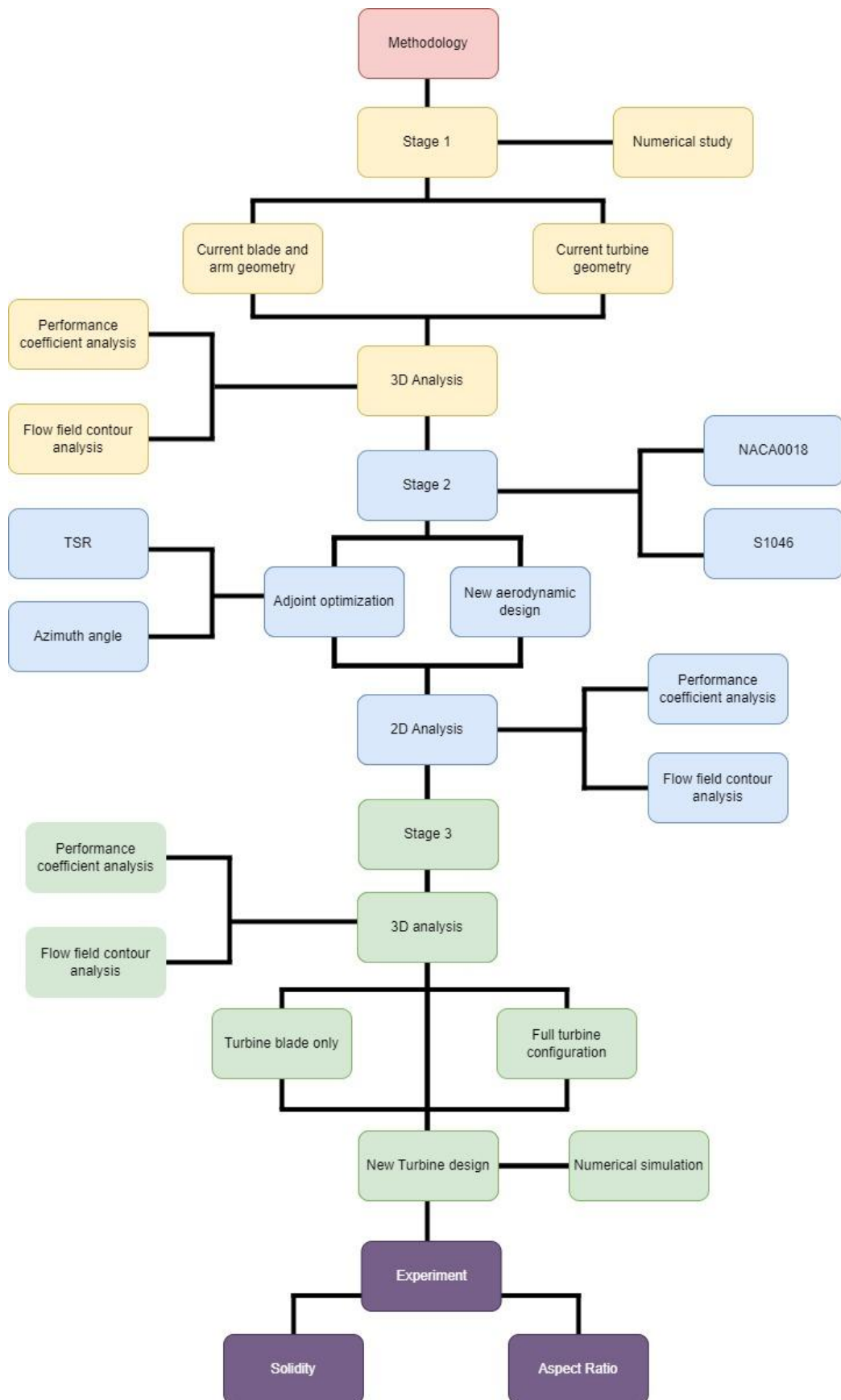


Fig 3.1. Structure of the proposed research methodology of this study.

3.3 General numerical presentation of studies

This section describes an overall glance at the numerical methodology of the various studies in this thesis. Although some numerical parameters were presented, a more thorough discussion was included in a later chapter. Five different studies were done in this thesis and therefore five subsections were presented. The first is the numerical setup of a dual blade NACA0018 turbine with single arms. The second is a numerical setup of a three bladed dual support-arms NACA0021. These two studies were conducted to establish a baseline of understanding current VAWT configuration in numerical simulation setting.

Then, the third subsection described the 2D numerical optimization of the NACA0018 and S1046 blade. The parameters for optimization were presented, justified, and discussed. The fourth subsection builds upon the results of the 2D optimization by comparing and analyzing the candidate turbine performance but with 3D effects such as blade tip losses. The last section discussed and proposed the full turbine configuration with support-arms in a 3D simulation. Finally, a novel and original turbine blade geometry with the candidate optimized blades were presented.

3.3.1 Effect of turbine support-arms on a two-bladed NACA0018 turbine

In this unsteady CFD analysis, to compare the aerodynamic effects of turbine support-arms on the performance and flow physics of the wind turbine, a two bladed NACA0018 with dual cylindrical or circular shaped solid support-arms was compared against a baseline turbine without arms. As past studies have suggested it as an ideal choice for number of blades, in addition, a two bladed setup was selected as it would simplify visualizing the flow field in the velocity and pressure contour plots. Each turbine blade was connected to the central rotor shaft at 0.25 and 0.75 of the blade span direction. The turbine parameters are described in Table 3.1. To compare the aerodynamic effects of a circular shaped turbine support-arm on the performance and flow physics of the wind turbine, two turbines were considered; the first, considered the baseline for comparison, is a turbine with only NACA018 blades to represent an ideal condition, the second is the full turbine configuration previously described. Fig 3.2(a) shows the full turbine geometry and Fig 3.2(b) shows the mesh

around the turbine in the rotating region. In the simulation analysis, it was determined that 5 rotations were deemed sufficient for the turbine to reach a quasistatic state and therefore, only the last rotation would be analyzed. Analysis on the lift and drag effects will be conducted with respect to a single arm, dual arms, and the sum of all arms. Fig 3.2 illustrates the conditions for each case.

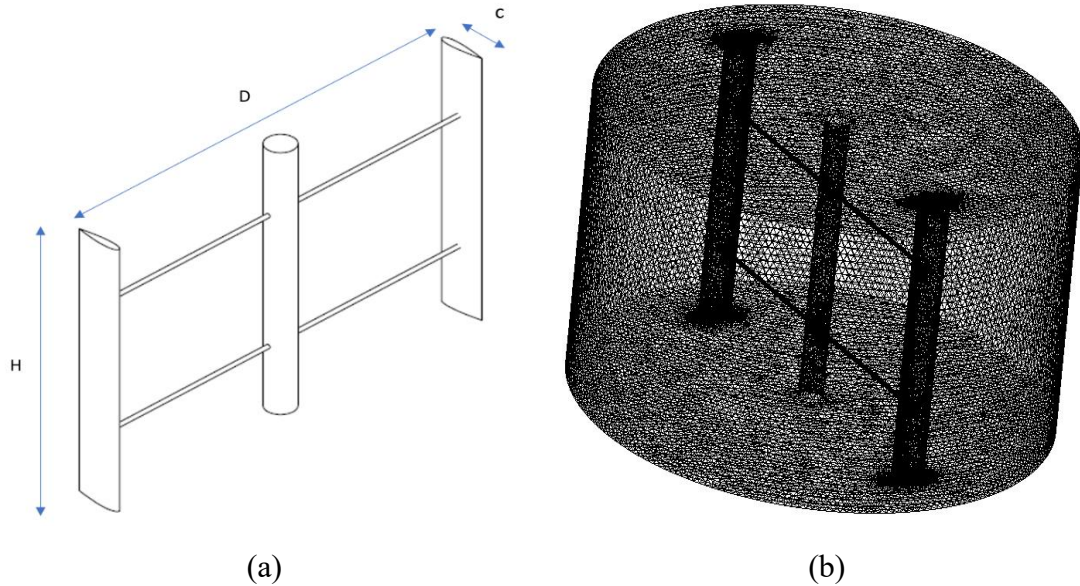


Fig 3.2. (a) NACA0018 dual arm turbine sketch and (b) mesh around the turbine inside the rotating region.

Table 3.1. Turbine dimensions for NACA0018 turbine

Parameter	Unit	Value
Chord length, C	m	0.08
Blade height, H	m	0.5
Turbine diameter, D	mm	0.75
Free stream velocity, U_0	m/s	7
Blade selection	-	NACA0018
Solidity, σ	-	0.148
Aspect Ratio	-	0.5

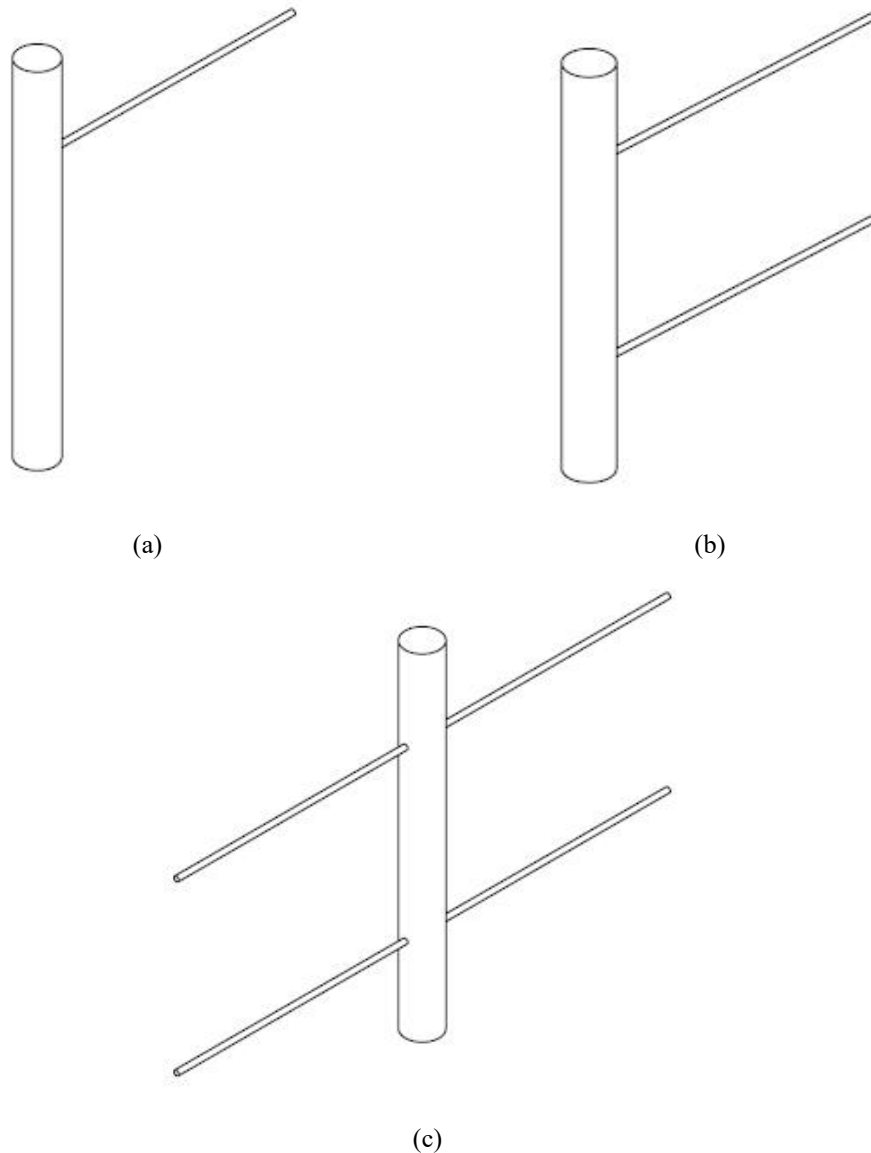


Fig 3.3. Definitions for (a) single arm, (b) dual arm and (c) sum of arms in the two-blade NACA0018 dual arm analysis.

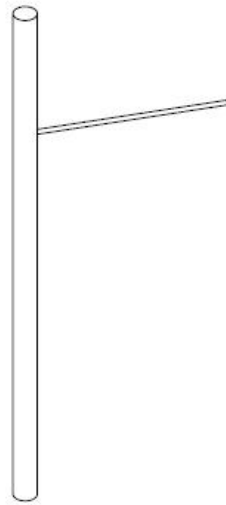
3.3.2 Effect of turbine support-arms on a three bladed NACA0021 turbine

The wind turbine described in this 3D study is a three-bladed NACA0021 turbine with a double support-arm configuration connected to each blade at located at 0.25 and 0.75 in the spanwise direction. The dimensions of the turbine used in the simulation is summarized in Table 3.2. The output parameters such as the average power coefficient and velocity flow field were compared. Two turbines will be studied; the first is the turbine with only NACA0021 blades with no support structure. The second is a full turbine with support-arms connected to each turbine blade and a

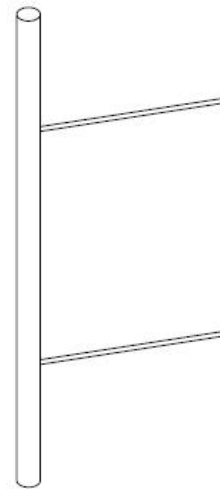
rotor shaft in the centre making a total of six support-arms. The turbine with no arms will be deemed the baseline against which the full turbine configuration will be compared to. Similar to the NACA0018 study, the analysis was conducted over 5 rotations and results of the last rotation was scrutinized. Analysis on the lift and drag effects will be conducted with respect to a single arm, dual arms, and the sum of all arms. Fig 3.3 defines these cases.

Table 3.2. Turbine dimensions for NACA0021 turbine

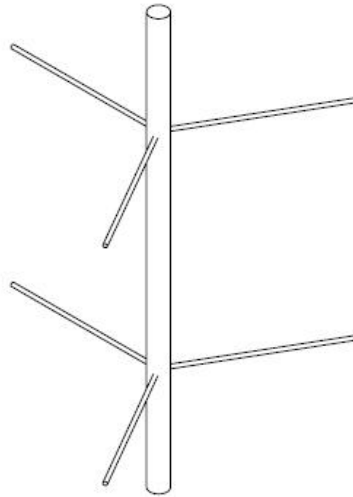
Parameter	Unit	Value
Chord length, C	m	0.08
Blade height, H	m	0.2575
Turbine diameter, D	mm	0.515
Blade Selection		NACA0021
Free stream velocity, U_0	m/s	9
Solidity, σ	-	0.148
Aspect Ratio	-	0.5



(a)



(b)



(c)

Fig 3.4. Definitions for (a) single arm, (b) dual arm and (c) sum of arms in the analysis three-bladed NACA0021 dual arm

3.3.3 2D aerodynamic shape optimization of the VAWT turbine blade

This section discussed the 2D aerodynamic adjoint based shape optimization. Two blades were selected for optimization: the symmetrical NACA0018 blade and the cambered S1046 blade. The optimization was carried out in 2D numerical simulation. Since the Darrieus turbine is a straight-bladed VAWT which shape and geometry does not vary along the blade span, simplifying the simulation to a 2D problem helps reduce computational time and minimize flow complexity and therefore improves the optimization process. The optimization was conducted on a single blade. A significant factor and input in an adjoint optimization are the initial flow field results to produce the sensitivity data and gradient to be fed into the gradient-based optimizer.

To study the effects of the flow field on the output of the optimization scheme, two parameters were varied. The first is varying the turbine blade azimuthal angle. The maximum torque or moment extraction happens within the upwind phase of the rotation and, therefore, would be an ideal region for optimization. The azimuthal angle range selected was between 0° to 120° . The turbine blade was rotated at an increment of 10° steps and the simulation ran at a steady state due to the limitations of the adjoint solver. The second factor affecting the flow field is the TSR. As was summarized in Table 2.1 from the previous chapter, a typical VAWT in an

experimental setting operates with maximum efficiency between TSR 1 to TSR 2. Hence, the optimization was run at TSR 1 and TSR 2 to generate two different flow fields for low TSR and high TSR. Hence, 3 parameters affecting the result of the adjoint solver were studied here: the effect of starting blade shape, the effect of different flow field due to the changing azimuthal angle, and the effect of TSR. This would theoretically yield different turbine blade geometries due to different flow fields yielding different sensitivity data. A more detailed discussion on the optimization scheme was presented in section 3.7.3. An increase of 5% was applied as the goal of the optimization set on the defined turbine blade moment. The resulting mesh of the candidate geometries were then extracted from the Fluent solver and imported into ICEM and then exported as an STL file to be redrawn in the 3D CAD software Solidworks.

In this 2D study, the numerical simulation consists of two domains; a rectangular, stationary domain designated as a fixed domain, and a circular domain where the blades were located designated as the rotating domain shown in Fig 3.4(a). The mesh resolution at the blade near wall was shown in Fig 3.4(b). Due to the mesh morphing of the blade, the mesh density was developed consistent with reported literature (Tzanakis 2014). The rotating domain mesh was formed using triangular mesh. Mesh independence test was presented in Chapter 4 and sliding mesh technique was used to simulate turbine rotation. Power and moment coefficients curves were compared, and other aerodynamic outputs were analyzed. Table 3.3 below summarizes the parameters in this study.

Table 3.3. Turbine dimensions for 2D optimization

Parameter	Unit	Value
Chord length, c	m	0.06
Turbine diameter, D	mm	0.2
Free stream velocity, U_0	m/s	7
Blade selection	-	NACA0018, S1046
Tip speed ratio, TSR	-	1,2
Objective function	-	5%

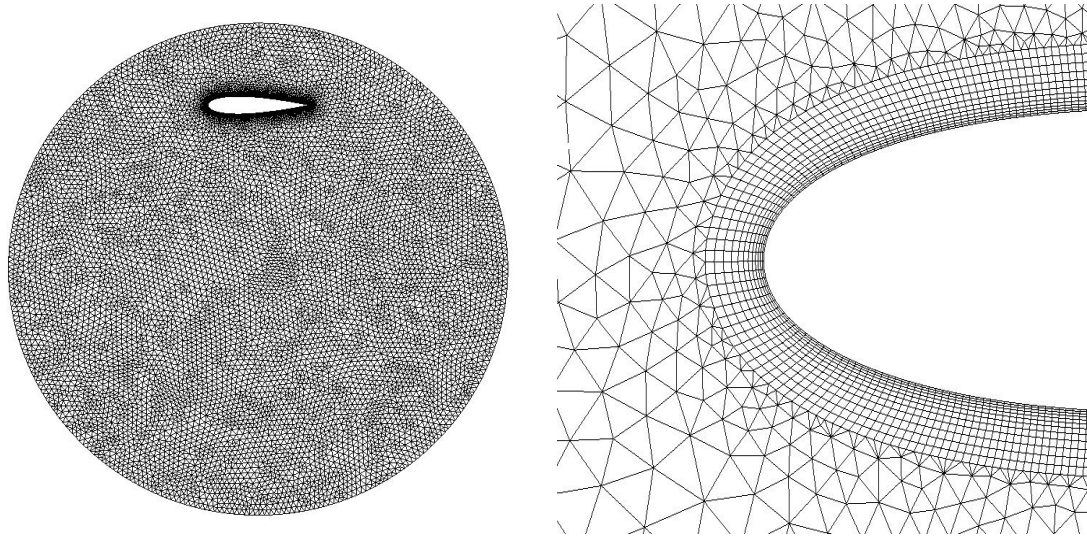


Fig 3.5. Shown above is the (a) 2D simulation rotating domain of the NACA0018 blade and (b) mesh resolution at blade near wall.

3.3.4 3D characterization and comparison of the optimized blades against the baseline NACA0018

After the optimization was conducted, a 3D study was conducted to investigate further on the candidate blades and its performance when 3D effects were applied. For consistency, the parameters in this study were kept similar to the previous 2D simulation. The turbine height was set to 0.2m making the aspect ratio 1 and the turbine solidity 0.6. The turbine blades were simulated at ideal settings where other turbine structures such as support-arms and central rotor were not considered. The sliding mesh technique was again used here to simulate turbine rotation and other turbine parameters kept constant. Second order discretization was selected for the pressure and momentum formulations and the SIMPLE scheme was used for the pressure-velocity coupling. Table 3.4 below summarizes the turbine parameters.

Table 3.4. Turbine dimensions for 3D characterization study.

Parameter	Unit	Value
Chord length, c	m	0.06
Turbine diameter, D	m	0.2
Blade height, H	m	0.2
Free stream velocity, U_0	m/s	7
Turbine solidity, σ	-	0.2
Aspect ratio	-	1

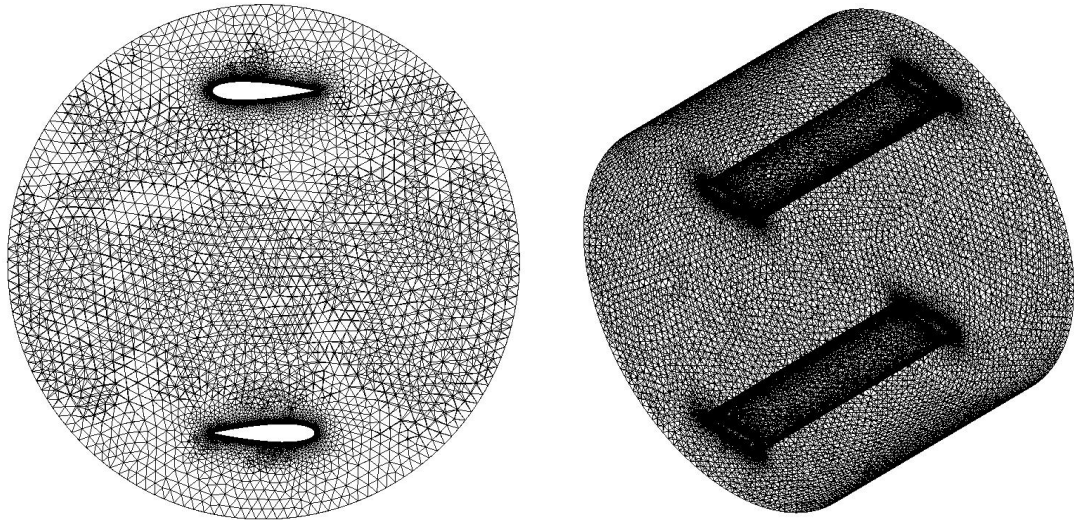


Fig 3.6. Shown here is the NACA0018 simulation domain of the (a) mesh of rotating region and (b) isometric view of the rotating domain.

3.3.5 3D study and characterization of the optimized blade in full turbine configuration

This study was conducted together with the effects of support-arms. Unlike the previous studies in section 3.2.1 and 3.2.2, however, the full turbine configuration will not feature the main rotor at the centre. This allows a more focused analysis on the differences of the developed flow field due to the difference in geometry of the turbine blade and support-arm without the added consideration and interruption of fluid flow due to the central column. The turbine dimensions were described in Table 3.5. The single support-arm blade was attached to the midpoint of the turbine blade. The performance coefficients of the blade and support-arm structures were analyzed together. A separate aerodynamic support-arm analysis was also conducted. The study was conducted similarly to the previous section. The aerodynamic characteristics such as lift and drag coefficients as well as performance efficiencies were analyzed and discussed. Flow field visualization was also presented to show the improvements made to the overall turbine by the adjoint optimization scheme. The work done here was therefore a summary of the whole study on the development of the optimization scheme, its application on the turbine blade and improvements made over the baseline turbine with enhanced power production for optimal turbine performance.

Table 3.5. Turbine dimensions for optimization

Parameter	Unit	Value
Number of blades, N	-	2
Chord length, c	-	0.06
Turbine height, H	-	0.20
Free stream velocity	m/s	7

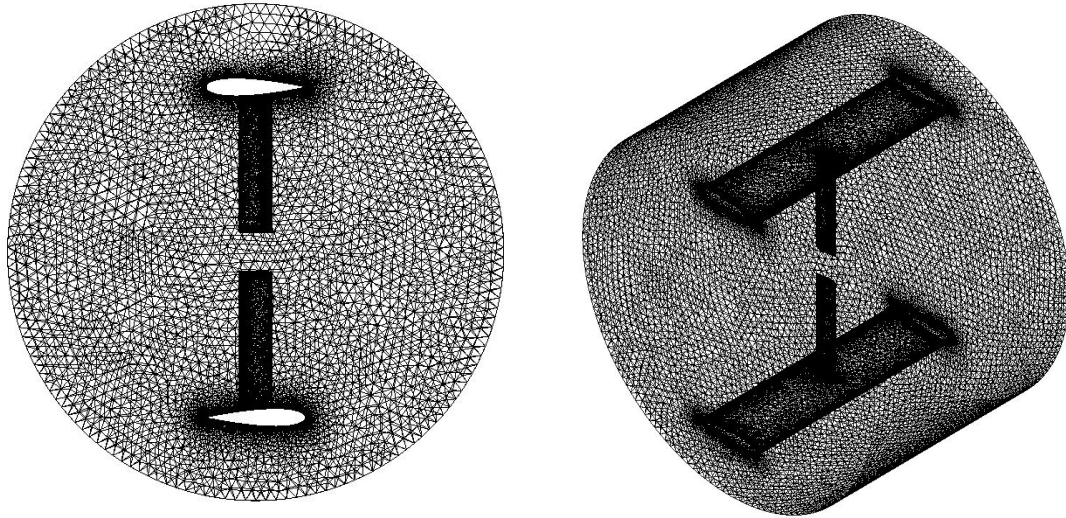


Fig 3.7. NACA0018 full turbine configuration showing the (a) mesh of rotating region and (b) isometric view of the rotating region.

3.4 Computational Fluid Dynamics Approach

This section discusses the computational fluid dynamics of this study and the methods used in the numerical simulation. The full domain with dimensions are presented in Fig 3.8 based on the suggested domain dimensions by Vergaerde et al. (Vergaerde et al. 2020). For the boundary conditions, the left side of the domain is set to inlet with varying velocity values and the outlet set to the right side. Turbulence intensity for both inlet and outlet were set to 1%. No slip conditions were applied to the walls. To simulate the rotating of the turbine, sliding mesh technique was used. The rotational angular velocity is based on the TSR and this value is calculated using Equation (53). The number of rotations was set to 10 as was recommended by previous authors (Howell et al. 2010, Rezaeiha, Kalkman, and Blocken 2017a) with the final turbine rotation taken as the average for comparisons and analysis. Studies (Rezaeiha, Kalkman, and Blocken 2017a, Elsakka et al. 2022) have suggested various time step sizes in 2D and 3D simulations for accurate

numerical predictions. This study will employ a time step size of 1° which is consistent with reported literature.

For the meshing of the turbine and the whole simulation domain, tetrahedron meshes were used. Various sizing parameters applied to the turbine blade faces and edges as well as the sliding mesh interfaces. An inflation layer was applied to all turbine blades and support-arms. The inflation layer option was set to first layer thickness, and this was calculated based on the turbine chord length or support-arm thickness, wind velocity, target y^+ set to 1.0 and 12 inflation layers. Mesh skewness was the metric used to ensure good mesh quality and skewness value ranging from 0.86 to 0.89 were obtained from this meshing technique. A mesh independency study was conducted, and, for all cases involving 3D turbines, a mesh size of about 7×10^9 cells was implemented as it was found to be the most optimal. The result of this mesh independency is discussed further in section 4.2. Fig 3.8 and Fig 3.9 illustrates the full mesh domain and rotating domain respectively.

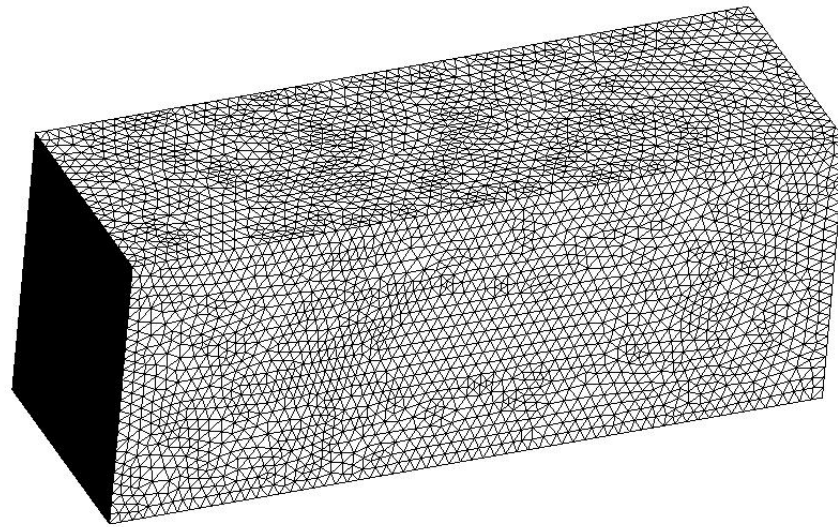


Fig 3.8. Visualization of the full 3D domain mesh resolution.

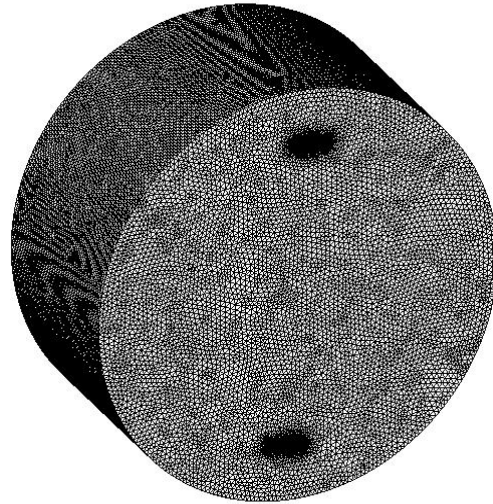


Fig 3.9. Mesh resolution of the rotating domain.

3.5 Adjoint Solver

For the optimization section, the aerodynamic optimization of the turbine blade was conducted using the adjoint solver. The adjoint solver is an included package within the ANSYS Fluent CFD code which was also paired with the gradient-based optimizer. The optimization process can be described in a multi-step process. The optimization was first conducted by initializing a CFD calculation on the starting geometry of the turbine blade. In this study, two symmetrical blades were chosen as the starting initial blade. The first blade is the uncambered NACA0018 and the second a cambered S1046 blade. The initial CFD simulation was conducted based on the desired inputs and boundary conditions. This includes the operating TSR, blade location or azimuthal angle, and the starting blade shape. The initial calculation provides a baseline data and results such as the velocity and pressure flow contour, XY plots such as the turbine performance coefficients as well as the aerodynamic coefficients like lift and drag. These results were then considered the inputs for the adjoint solver. The observables, which is the turbine moment force, were then defined. The adjoint solver was initialized and run to obtain the adjoint information such as mesh shape sensitivity data with respect to the defined observables based on the initial conditions and the flow contour results. The shape sensitivity data is a crucial step as it identifies regions or node locations near the turbine blade where nodal displacements maximize the defined observables. The bounding region, where

the control points were defined in a rectangular box, was then setup to enclose the turbine blade. Finally, the gradient-based optimizer was initialized and with the goal of increasing the defined observable based on the desired percentage increase. This is an iterative process until a suitable number of iterations was reached. Fig 3.10 below summarizes the whole optimization process.

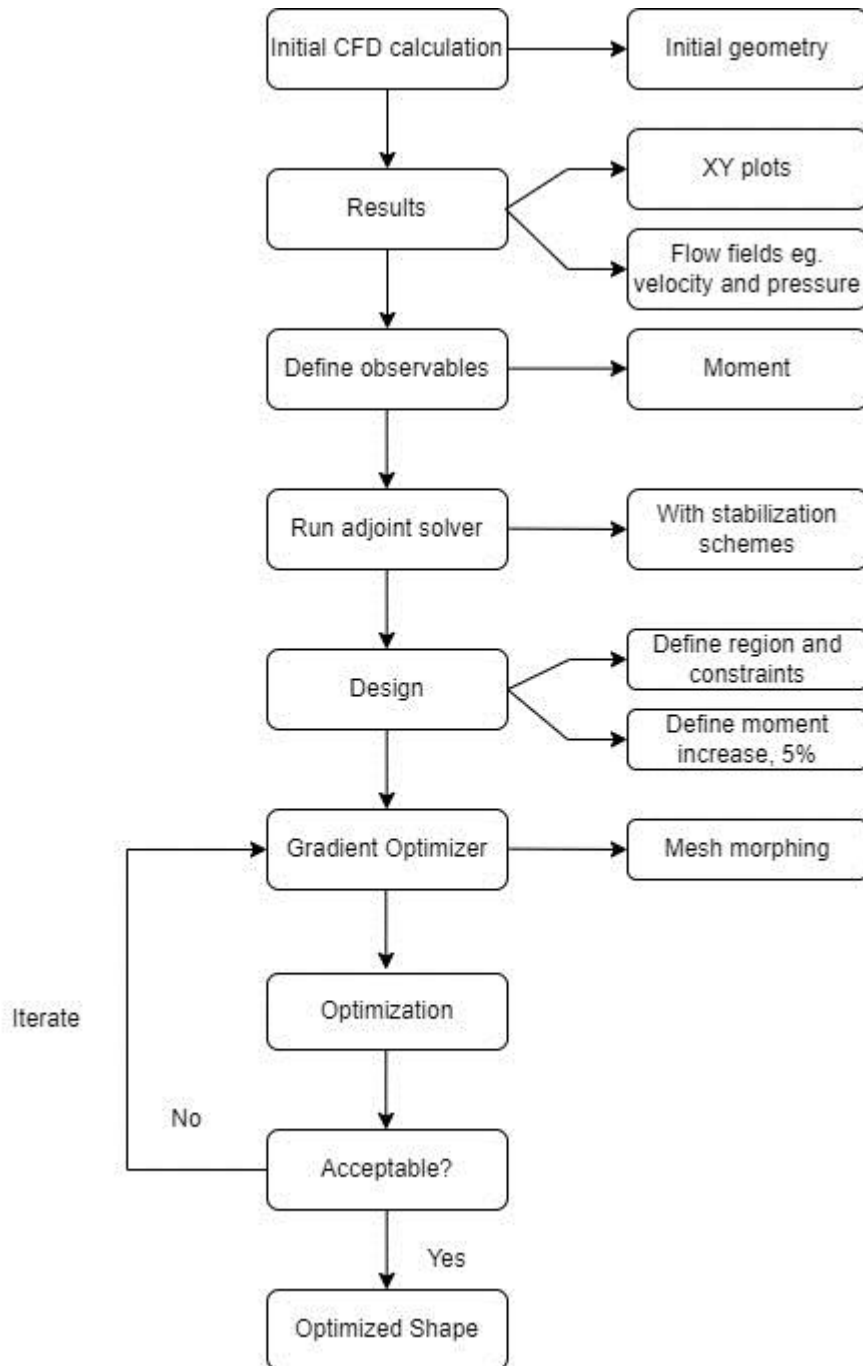


Fig 3.10. Flow chart of the adjoint solver optimization.

3.5.1 Discrete Adjoint Method

The adjoint method can be divided into two different approaches: the continuous approach and the discrete approach. The main difference between the two approach is the discretization of the adjoint equations. The continuous method derives the adjoint equation directly from the CFD governing equations and is discretized afterwards. The discrete method is the exact opposite in which the governing equation is discretized first and the discrete adjoint equation then computed afterwards. The adjoint method algorithm available in ANSYS Fluent package uses the discrete adjoint approach and this will be discussed in the following section.

The adjoint objective function is defined in terms of flow field condition and the control variables or engineering input. This can be expressed as

$$J = J(q(c), c) \quad \text{Equation (1)}$$

And the adjoint residual defined as

$$R = J(q(c), c) = 0 \quad \text{Equation (2)}$$

The goal of this optimization is to maximize the objective function defined in Equation (57) subject to the constraint of the adjoint residual, Equation (58), equals to zero.

$$\begin{cases} \text{maximize } J(q(c), c) \\ \text{Subject to } R = J(q(c), c) \text{ equals to } 0 \end{cases}$$

$$\delta J = \delta q \frac{\partial J}{\partial q} + \delta c \frac{\partial R}{\partial c} \quad \text{Equation (3)}$$

And the adjoint residual remains zero,

$$\delta R = \delta q \frac{\partial R}{\partial q} + \delta c \frac{\partial R}{\partial c} = 0 \quad \text{Equation (4)}$$

Introducing the Langragian multiplier ϕ^T is introduced. Hence, combining equation and equation and rearranging yields equation,

$$\delta J = \delta q \frac{\partial J}{\partial q} + \delta c \frac{\partial R}{\partial c} - \phi^T \left(\delta q \frac{\partial R}{\partial q} + \delta c \frac{\partial R}{\partial c} \right)$$

$$\delta J = \delta q \left(\frac{\partial J}{\partial q} - \phi^T \frac{\partial R}{\partial q} \right) + \delta c \left(\frac{\partial J}{\partial c} - \phi^T \frac{\partial R}{\partial c} \right) \quad \text{Equation (5)}$$

The value chosen for Lagrangian multiplier ϕ^T is such that it reduces the following equation to

$$\frac{\partial J}{\partial q} = \phi^T \frac{\partial R}{\partial q} \quad \text{Equation (6)}$$

And finally, the adjoint sensitivity equation is defined as,

$$dJ = \delta c \frac{\partial J}{\partial c} - \delta c \left(\phi^T \frac{\partial R}{\partial c} \right) \quad \text{Equation (7)}$$

The above equations were derived and obtained from the ANSYS Fluent Adjoint Solver manual provided from the ANSYS website.

3.5.2 Fluent Adjoint Solver

This section described the optimization procedure with examples of screenshots taken from the software after the initial CFD calculation was concluded and the output results determined. The first step is to define the adjoint observable as the blade moment force as shown in Fig 3.11(a). The adjoint simulation was then initialized and calculated as shown in Fig 3.11(b). This then provides the adjoint solution which provided the shape sensitivity data of the mesh around the turbine blade. An example with shape sensitivity visualization was given in the following chapter. With the adjoint sensitivities related to the initial flow field calculations now established, the design tool tab, in Fig 3.12, was opened and the bounding region around the airfoil geometry and control points in each X and Y direction were defined. This is the mesh morphing were controlled by the number of points defined around the airfoil geometry and this was set to 20 points each in the X and Y directions illustrated in Fig 3.13. The mesh morpher tool here also has a function that not only morphs the mesh but also applies a smoothing process to ensure good mesh quality. Lastly, the gradient-based optimizer tab, shown in Fig 3.14, set to shape optimization algorithm, was opened. The optimization settings were configured to 10 design iterations with the goal being a target increase of 5%. The adaptive value

function was unchecked to force the solver to aggressively maintain the defined target goal. To maintain a good quality mesh, the minimum orthogonal quality was kept to the default settings of 0.01. The gradient-based solver was initialized and ran until a convergence was reached and the airfoil shape satisfies the objective function target of 5% increase.

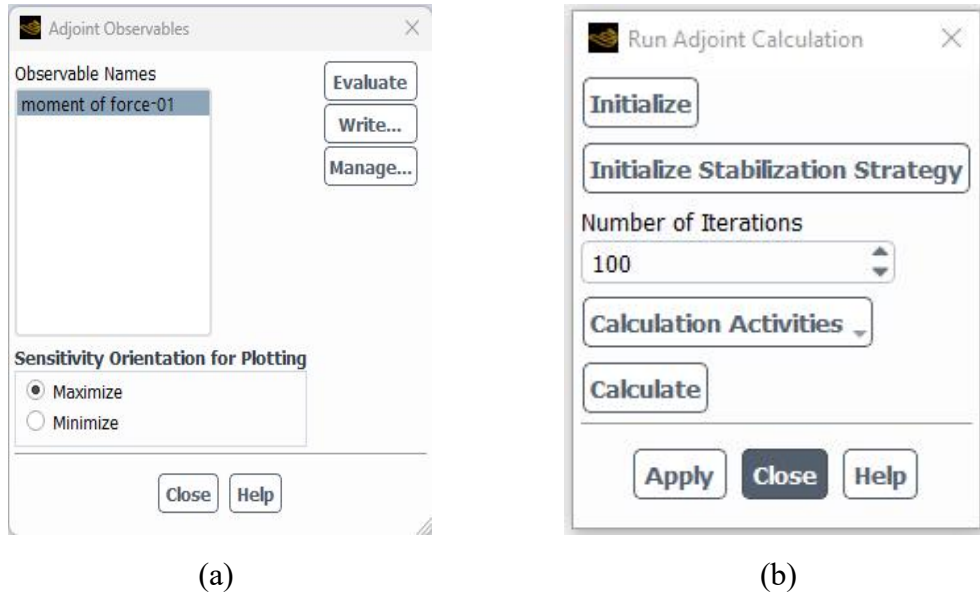


Fig 3.11. (a) Adjoint observables tab with the defined parameters and (b) adjoint calculation tab.

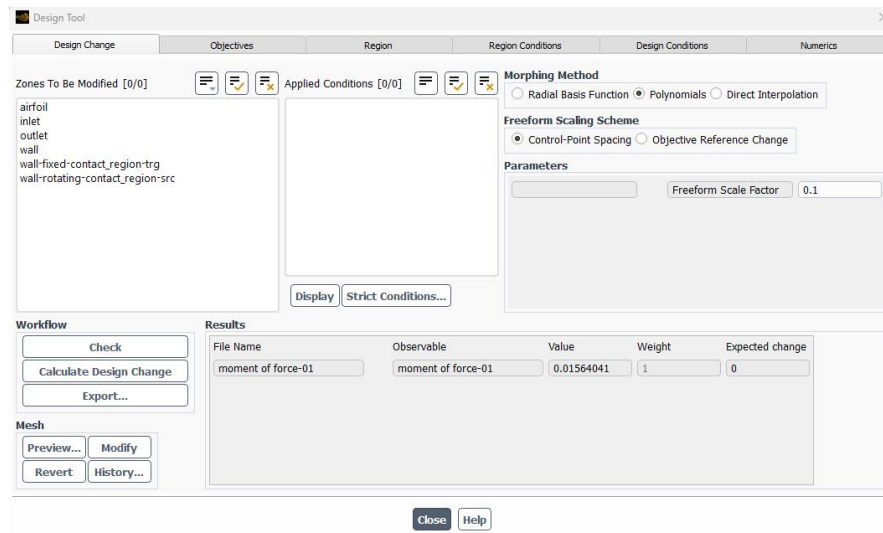


Fig 3.12. Design tool tab where objective function and bounding region were defined.



Fig 3.13. Bounding region and control points around the S1046 airfoil geometry set to 20 points each in the X and Y direction.

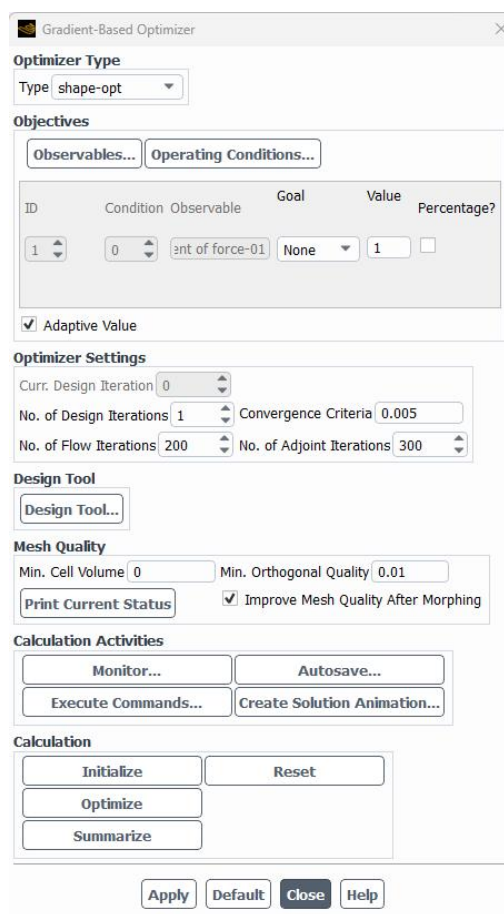


Fig 3.14. Gradient-based optimizer tab.

3.5.3 Adjoint Optimization Procedure

Fig 3.15 shows the single blade geometry with the single blade within the rectangular bounding region. As was stated in the previous section on the adjoint method, the main and unique feature of this optimization scheme is the output geometry's

dependence on the mesh sensitivity data from the initial flow field with respect to the defined observables. The optimization procedure is therefore heavily reliant and affected by the initial flow conditions from the starting CFD calculations. This means changing the initial variables, in this case the blade angle of attack or turbine azimuthal angles to simulate different flow conditions at various intervals of the turbine cycle, would produce different flow fields and therefore a different optimized candidate blade profile. This can be achieved due to different sensitivity data based on different flow fields by changing the initial conditions. Hence, a wide variety of blade profiles was expected to be produced at different angles.

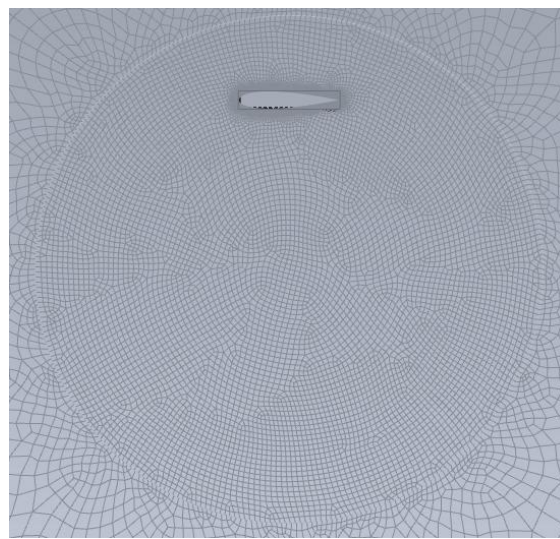


Fig 3.15. Bounding region around the single blade geometry with 20 control points in both X and Y direction.

The optimization scheme was conducted using a blend of the adjoint method and the gradient based optimizer which were available within the ANSYS Fluent CFD code. The optimization process involved a sensitivity analysis of the mesh nodes which led to mesh deformation or mesh morphing and therefore a cambering of the starting baseline geometry to yield an unsymmetrical blade geometry. The effect of this mesh morphing was investigated on two turbine blades: the symmetrical NACA0018 and the symmetrical but cambered S1046. The optimization was conducted at 12 different azimuth snapshots within the upwind region of the turbine rotation at 10° steps. The tested azimuth ranges were all within the windward and upwind region, between 0° to 120° , which are regions where maximum torque extraction occurs. This was illustrated in Fig. 3.16. The optimization was done in a

semi-transient state in that the turbine is rotated to a desired azimuthal angle and is then kept static in a steady state during optimization. This was done to simulate varying conditions such as velocity flow field and forces acting on the turbine blade at different instances of the turbine operation. As well as optimizing the turbine blade at various azimuthal angles, the optimization was also conducted at two different TSR values: TSR 1 and TSR 2 to investigate the effect of TSR on the optimization result. Hence, the effect of starting blade shape, azimuth angle, and operating TSR on the optimization scheme were investigated.

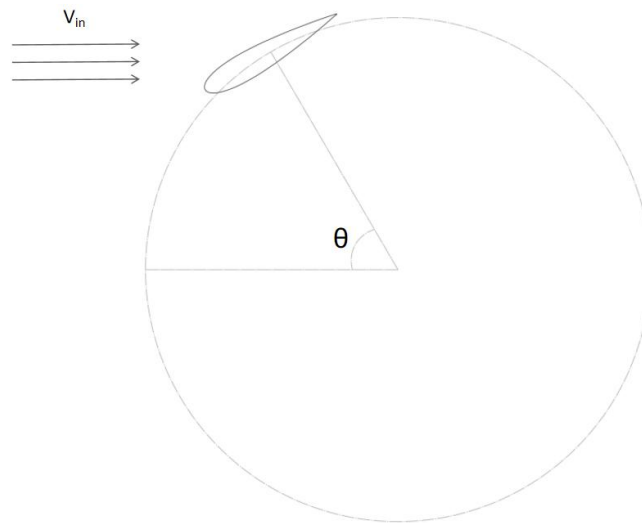


Fig 3.16. A representation of the single blade optimization with θ in the figure denotes the azimuthal angle at which the optimization scheme was conducted.

As a result of the different azimuthal angles at different rotational speed, a different initial flow condition can be developed at each test cases. This results in a different adjoint flow field in each instance of azimuthal angle. To highlight this hypothesis, Fig 3.17 shows the vector visualization at each azimuthal angle instance showing different magnitude of shape sensitivity and direction. This condition allows the turbine blade to experience the aerodynamic environment at that instance and would theoretically yield increased torque. The resulting geometry was extracted using ANSYS ICEM and redrawn in 2D and 3D using the CAD software Solidworks in further turbine analysis.

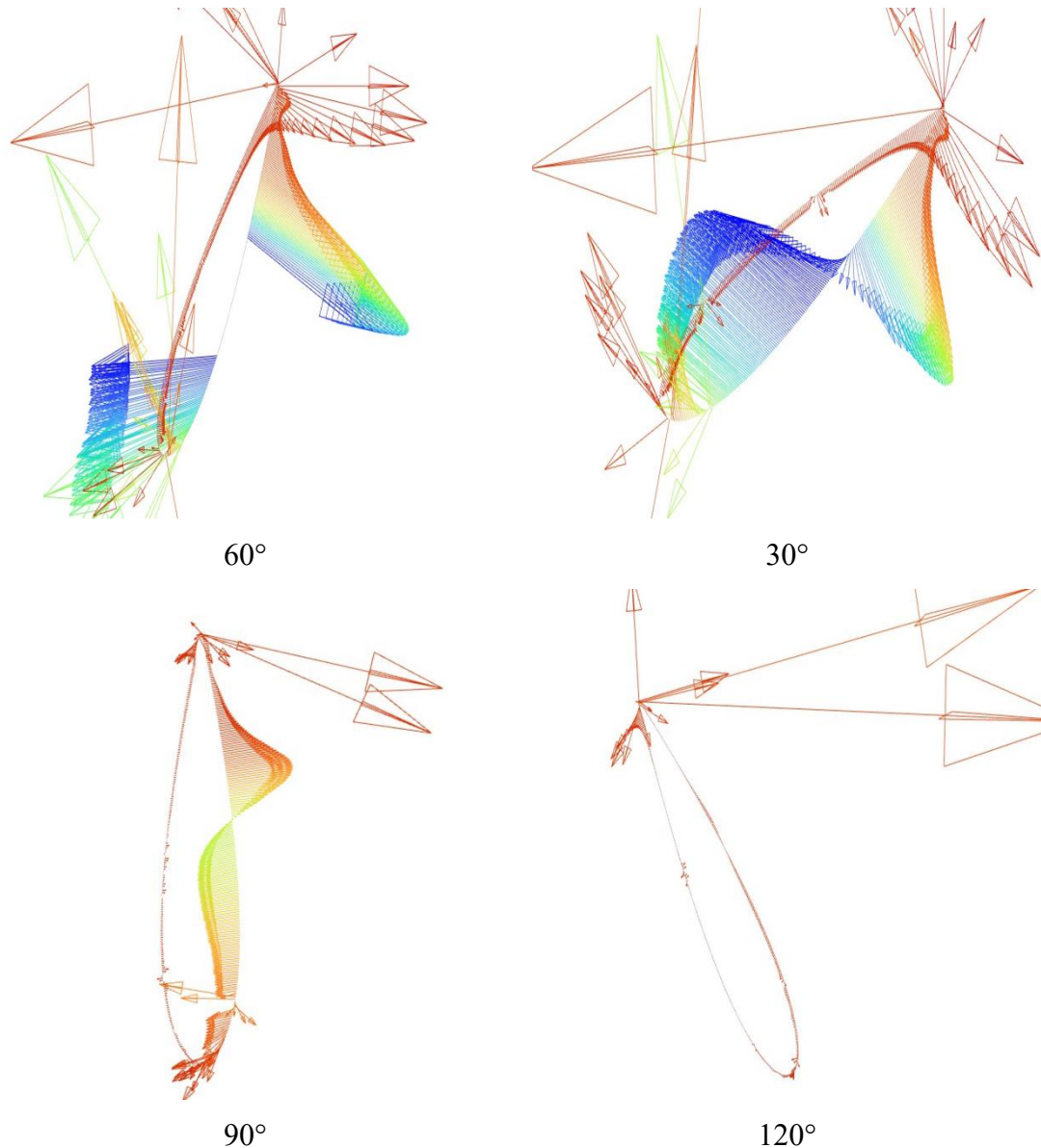


Fig 3.17. Vector visualization at the tested cases coloured by shape sensitivity magnitude.

3.6 Theory and Governing Equations

In this section, theoretical knowledge relating to CFD was presented. Various equations used and calculated during numerical simulations were derived and presented. A summary of the governing equations was presented later in the chapter.

3.6.1 Continuity Equation

The continuity equation, in relation to fluid dynamics, is one of the most important essential theories to understand in CFD. To start, a rectangular control volume was visualized in Fig 3.18. The most basic definition of continuity is as follows:

$$\dot{m}_{in} = \dot{m}_{out} \quad \text{Equation (8)}$$

$$A_1 V_1 = A_2 V_2 \quad \text{Equation (9)}$$

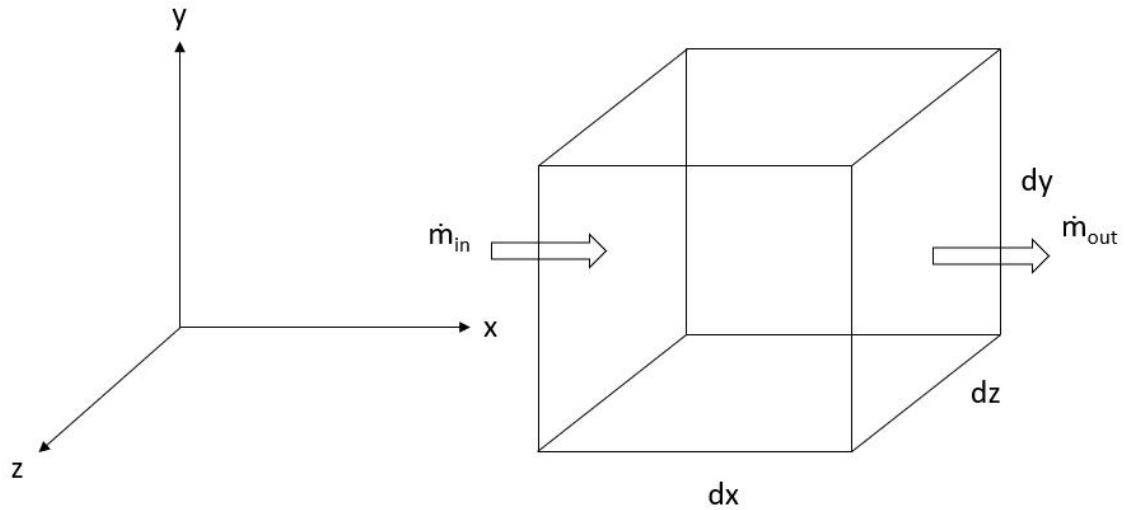


Fig 3.18. Visualization of a control volume of infinitesimal size.

As per the equations above, the continuity equation is just a statement of conservation of mass. The equation above is also only relevant for a steady state flow whereby pressure is constant and there is no change in mass flow with respect to time. For an unsteady state however, the continuity equation can be defined as:

$$\dot{m}_{in} - \dot{m}_{out} = \frac{dM}{dt} \quad \text{Equation (10)}$$

Note here that the mass and density can be related as,

$$m = \rho V \quad \text{Equation (11)}$$

From Fig 3.8, consider a mass flow from the left-hand side in the x- direction into the cube. This mass flow can be described as the area of the left-hand side surface multiplied by the fluid velocity. This can be defined as,

$$\dot{m}_{in} = \rho u \cdot dydzx$$

The equation above describes the mass flow rate going into the control volume with respect to the x-direction. Considering the other two cartesian directions in their respective positive directions, the equation for total mass flow rate in becomes,

$$m_{in} = \rho u. dydz + \rho v. dx dz + \rho w. dy dz \quad \text{Equation (12)}$$

Again, consider mass flow rate out of the control volume in the positive x – direction. As mass flows out of the right-hand side, the mass flow rate out can be expressed as,

$$m_{out} = \left[\rho u + \frac{\delta(\rho u)}{\delta x} dx \right] dy dz$$

The total mass flow rate out in all three cartesian directions become,

$$m_{out} = \left[\rho u + \frac{\delta(\rho u)}{\delta x} dx \right] dy dz + \left[\rho v + \frac{\delta(\rho v)}{\delta y} dy \right] dx dz + \left[\rho w + \frac{\delta(\rho w)}{\delta z} dz \right] dx dy \quad \text{Equation (13)}$$

The above equation is the mass flow rate out of the control volume with respect to the positive x - direction. We now have the mass flow rate into the control volume and the mass flow rate out. As mentioned before, for an unsteady state flow, the difference between the mass flow rate in and the mass flow rate out of the control volume equals to the change in mass with respect to time. In equation form, the rate of change of m, from Equation (4), with respect to time, can be defined as,

$$\frac{dM}{dt} = \frac{\delta \rho}{\delta t} dx dy dz \quad \text{Equation (14)}$$

Now, substituting equations (4), (5) and (6) into Equation (3), we get,

$$\begin{aligned} & \rho u. dy dz + \rho v. dx dz + \rho w. dy dz - \left[\rho u + \frac{\delta(\rho u)}{\delta x} dx \right] dy dz \\ & + \left[\rho v + \frac{\delta(\rho v)}{\delta y} dy \right] dx dz + \left[\rho w + \frac{\delta(\rho w)}{\delta z} dz \right] dx dy \\ & = \frac{\delta \rho}{\delta t} dx dy dz \end{aligned} \quad \text{Equation (15)}$$

Multiplying both sides by $dx dy dz$ and rearranging, we get the generalized equation of the continuity equation,

$$\frac{\delta \rho}{\delta t} + \frac{\delta(\rho u)}{\delta x} + \frac{\delta(\rho v)}{\delta y} + \frac{\delta(\rho w)}{\delta z} = 0 \quad \text{Equation (16)}$$

Or simplified further,

$$\frac{\delta\rho}{\delta t} + \nabla(\rho V) = 0 \quad \text{Equation (17)}$$

Equations (9) and (10) can be described as the continuity equation in its differential form. The continuity equation can also be stated in its integral form as,

$$\int_{cv} \frac{\delta\rho}{\delta t} dV + \sum_{i=1}^{out} (\rho_i A_i V_i) - \sum_{i=1}^{in} (\rho_i A_i V_i) = 0 \quad \text{Equation (18)}$$

In fluid mechanics, the continuity equation can be modified based on special cases. For example, in a case of steady state flow, the fluid density does not change with respect to time. This means the first pressure term becomes zero. Therefore, Equation (9) becomes,

$$\frac{\delta(\rho u)}{\delta x} + \frac{\delta(\rho v)}{\delta y} + \frac{\delta(\rho w)}{\delta z} = 0 \quad \text{Equation (19)}$$

For incompressible flow, which, for a standard air medium has been experimentally proven to have a mach number of $M < 0.3$, the fluid density is considered constant with respect to space and time. Therefore, Equation (9) now becomes,

$$\frac{\delta u}{\delta x} + \frac{\delta v}{\delta y} + \frac{\delta w}{\delta z} = 0 \quad \text{Equation (20)}$$

3.6.2 Momentum equation

The linear momentum equation is derived in this section. The momentum equation is an expression of Newton's Second Law of motion for fluid flow. This means that the equation is also a form of conservation of momentum. For this derivation, an elemental volume approach similar to the derivation of the continuity equation will be shown. Other derivation methods such as based on the divergence theorem can be found in (Cimbala 2009). The linear momentum equation can be expressed as,

$$\begin{aligned} \sum \vec{F} &= \sum \vec{F}_{body} + \sum \vec{F}_{surface} \\ &= \int_{cv} \frac{\partial}{\partial t} (\rho u) dV + \sum_{out} \beta \dot{m} u - \sum_{in} \beta \dot{m} u \end{aligned} \quad \text{Equation (21)}$$

First, we consider the left-hand side of the momentum fluxes in the x – component. The momentum flux in the x direction occurs all on 6 faces of the infinitesimal cube. This is shown in the Fig 3.19 below.

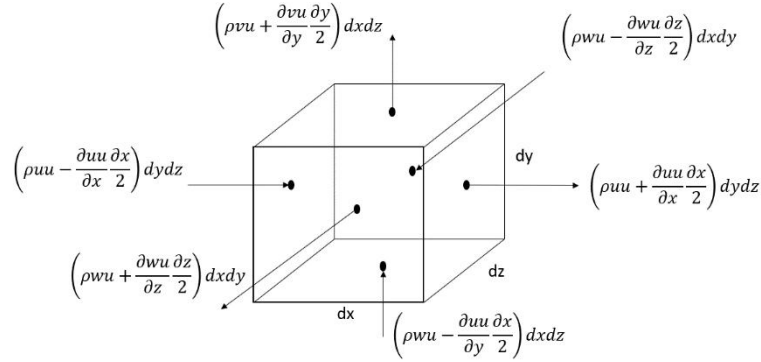


Fig 3.19. Sketch of the control volume showing the inflow and outflow through each face in for the x – component.

Hence, the equation for the rate of change of momentum in the x – component is,

$$\sum \vec{F} = \left(\frac{\partial(\rho u)}{\partial t} + \frac{\partial(\rho u u)}{\partial x} + \frac{\partial(\rho u v)}{\partial y} + \frac{\partial(\rho u w)}{\partial z} \right) dx dy dz \quad \text{Equation (22)}$$

Next, we consider the body force. The body force can in this case is the gravitational force of the fluid body. Hence, the gravitational force, in the x direction, can be expressed as,

$$F_{x, body} = m g_x$$

$$\sum F_{x, body} = \sum F_{x, gravity} = \rho g_x dx dy dz \quad \text{Equation (23)}$$

Lastly, we consider the force acting on the surfaces of the control volume. Fig 3.20 shows the forces acting on the surfaces of a control volume in the x – direction.

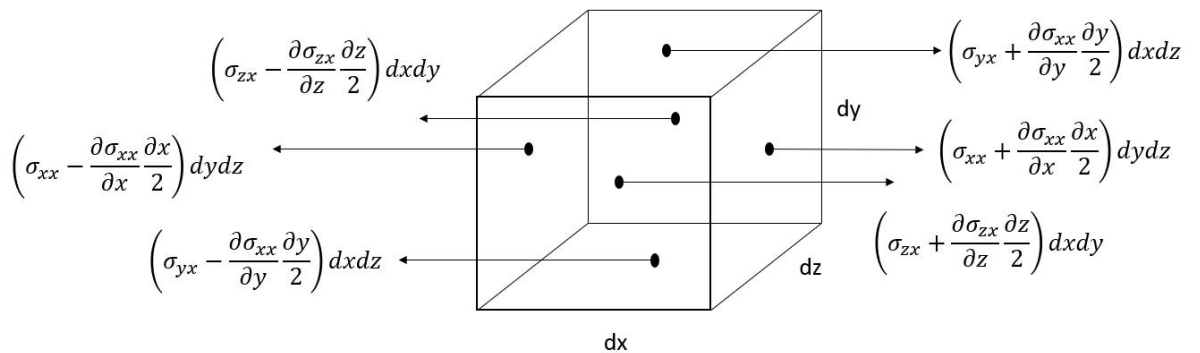


Fig 3.20. Sketch showing the surface forces acting in the x – direction.

The sigma, or σ , above denotes the stress tensor of the fluid. Therefore, summing up all the forces in the diagram and simplifying, momentum equation in the x – direction becomes,

$$\sum F_{x,surface} = \sum F_{x,out} - \sum F_{x,in}$$

$$\sum F_{x,surface} = \left(\frac{\partial \sigma_{xx}}{\partial x} + \frac{\partial \sigma_{yx}}{\partial y} + \frac{\partial \sigma_{zx}}{\partial z} \right) dx dy dz \quad \text{Equation (24)}$$

Finally, putting everything together, we get,

$$\frac{\partial(\rho u)}{\partial t} + \frac{\partial(\rho uu)}{\partial x} + \frac{\partial(\rho uv)}{\partial y} + \frac{\partial(\rho uw)}{\partial z} \quad \text{Equation (25)}$$

$$= \rho g_x + \frac{\partial \sigma_{xx}}{\partial x} + \frac{\partial \sigma_{yx}}{\partial y} + \frac{\partial \sigma_{zx}}{\partial z}$$

Which is the full form of the linear momentum equation in the x – component. Similarly, the momentum equations, in differential form, with respect to the y and z directions are,

$$y - \text{direction: } \frac{\partial(\rho v)}{\partial t} + \frac{\partial(\rho uv)}{\partial x} + \frac{\partial(\rho vv)}{\partial y} + \frac{\partial(\rho vw)}{\partial z} \quad \text{Equation (26)}$$

$$= \rho g_y + \frac{\partial \sigma_{xy}}{\partial x} + \frac{\partial \sigma_{yy}}{\partial y} + \frac{\partial \sigma_{zy}}{\partial z}$$

$$z - \text{direction: } \frac{\partial(\rho w)}{\partial t} + \frac{\partial(\rho wu)}{\partial x} + \frac{\partial(\rho wv)}{\partial y} + \frac{\partial(\rho ww)}{\partial z} \quad \text{Equation (27)}$$

$$= \rho g_z + \frac{\partial \sigma_{xz}}{\partial x} + \frac{\partial \sigma_{yz}}{\partial y} + \frac{\partial \sigma_{zz}}{\partial z}$$

The momentum equations above can, summarily, be reduced in concise form as,

$$\frac{\partial(\rho \vec{V})}{\partial t} + \vec{\nabla} \cdot (\rho \vec{V} \vec{V}) = \rho \vec{g} + \vec{\nabla} \cdot \sigma_{ij} \quad \text{Equation (28)}$$

Or,

$$\rho \frac{D\vec{V}}{Dt} = \rho \vec{g} + \vec{\nabla} \cdot \sigma_{ij} \quad \text{Equation (29)}$$

This is also known as Cauchy's linear momentum equation. This is a precursor to the important Navier-Stokes Equation in the next section.

3.6.3 Navier-Stokes Equation

In this section, a derivation of the Navier-Stokes equation was made. The Navier-Stokes equation is the most important equation in fluid mechanics and in the application of Computational Fluid Dynamics (CFD). It is considered a cornerstone in the field of fluid mechanics (Cimbala 2009). It is an essential equation in the application of 3D numerical simulation. As of this section, the continuity equation and three linear momentum equations have been derived. The total unknowns sum up to ten, which are the pressure term, the three velocity terms, and six stress tensor terms. Therefore, a total of six more equations, called the constitutive equations, to solve for the components of the stress tensor in terms of the velocity and pressure fields (Cimbala 2009).

To derive the Navier-Stokes equation, we consider an incompressible Newtonian fluid. In the previous section, the linear momentum equation was derived as,

$$\rho \frac{D\vec{V}}{Dt} = \rho \vec{g} + \vec{\nabla} \cdot \sigma_{ij} \quad \text{Equation (22)}$$

From Equation (22), we see that the furthest term in right-hand side of the equation shows the stress tensor, σ , of the fluid with respect to its spatial location. For a fluid at rest, only local hydrostatic pressure is present, which acts inward and normal to the surface of the fluid. Therefore, the fluid tensor σ_{ij} can be defined as,

$$\sigma_{ij} = \begin{pmatrix} \sigma_{xx} & \sigma_{xy} & \sigma_{xz} \\ \sigma_{yx} & \sigma_{yy} & \sigma_{yz} \\ \sigma_{zx} & \sigma_{zy} & \sigma_{zz} \end{pmatrix} = \begin{pmatrix} -P & 0 & 0 \\ 0 & -P & 0 \\ 0 & 0 & -P \end{pmatrix} \quad \text{Equation (30)}$$

The negative sign indicates the direction of pressure acting on the fluid surface. When a fluid is moving, the viscous stresses start to exist on top of the existing hydrostatic pressure. The stress tensor in Equation (23) becomes,

$$\sigma_{ij} = \begin{pmatrix} \sigma_{xx} & \sigma_{xy} & \sigma_{xz} \\ \sigma_{yx} & \sigma_{yy} & \sigma_{yz} \\ \sigma_{zx} & \sigma_{zy} & \sigma_{zz} \end{pmatrix} = \begin{pmatrix} -P & 0 & 0 \\ 0 & -P & 0 \\ 0 & 0 & -P \end{pmatrix} + \begin{pmatrix} \tau_{xx} & \tau_{xy} & \tau_{xz} \\ \tau_{yx} & \tau_{yy} & \tau_{yz} \\ \tau_{zx} & \tau_{zy} & \tau_{zz} \end{pmatrix}$$

$$\sigma_{ij} = \begin{pmatrix} \sigma_{xx} & \sigma_{xy} & \sigma_{xz} \\ \sigma_{yx} & \sigma_{yy} & \sigma_{yz} \\ \sigma_{zx} & \sigma_{zy} & \sigma_{zz} \end{pmatrix} = \begin{pmatrix} -P + \tau_{xx} & \tau_{xy} & \tau_{xz} \\ \tau_{yx} & -P + \tau_{yy} & \tau_{yz} \\ \tau_{zx} & \tau_{zy} & -P + \tau_{zz} \end{pmatrix} \quad \text{Equation (31)}$$

From Equation (24), the new term introduced is called the viscous stress tensor, τ_{ij} . For a Newtonian fluid, it can be defined as a fluid in which its shear stress is linearly proportional to the shear strain rate. This can be expressed as

$$\tau_{ij} = 2\mu\varepsilon_{ij} \quad \text{Equation (32)}$$

Whereby the new term introduced here is defined as the strain rate tensor, ε_{ij} and dynamic viscosity or viscosity coefficient μ . Therefore, expanding this further, the viscous tensor τ_{ij} now becomes,

$$\begin{aligned} \tau_{ij} &= \begin{pmatrix} \tau_{xx} & \tau_{xy} & \tau_{xz} \\ \tau_{yx} & \tau_{yy} & \tau_{yz} \\ \tau_{zx} & \tau_{zy} & \tau_{zz} \end{pmatrix} \quad \text{Equation (33)} \\ &= \begin{pmatrix} 2\mu \frac{\partial u}{\partial x} & \mu \left(\frac{\partial u}{\partial y} + \frac{\partial v}{\partial x} \right) & \mu \left(\frac{\partial u}{\partial z} + \frac{\partial w}{\partial x} \right) \\ \mu \left(\frac{\partial v}{\partial x} + \frac{\partial u}{\partial y} \right) & 2\mu \frac{\partial v}{\partial y} & \mu \left(\frac{\partial v}{\partial z} + \frac{\partial w}{\partial y} \right) \\ \mu \left(\frac{\partial w}{\partial x} + \frac{\partial u}{\partial z} \right) & \mu \left(\frac{\partial w}{\partial y} + \frac{\partial v}{\partial z} \right) & 2\mu \frac{\partial w}{\partial z} \end{pmatrix} \end{aligned}$$

Putting the above Equation (26) into the original stress tensor, σ_{ij} , in Equation (24) yields,

$$\begin{aligned} \sigma_{ij} &= \begin{pmatrix} \sigma_{xx} & \sigma_{xy} & \sigma_{xz} \\ \sigma_{yx} & \sigma_{yy} & \sigma_{yz} \\ \sigma_{zx} & \sigma_{zy} & \sigma_{zz} \end{pmatrix} \quad \text{Equation (34)} \\ &= \begin{pmatrix} -P + 2\mu \frac{\partial u}{\partial x} & \mu \left(\frac{\partial u}{\partial y} + \frac{\partial v}{\partial x} \right) & \mu \left(\frac{\partial u}{\partial z} + \frac{\partial w}{\partial x} \right) \\ \mu \left(\frac{\partial v}{\partial x} + \frac{\partial u}{\partial y} \right) & -P + 2\mu \frac{\partial v}{\partial y} & \mu \left(\frac{\partial v}{\partial z} + \frac{\partial w}{\partial y} \right) \\ \mu \left(\frac{\partial w}{\partial x} + \frac{\partial u}{\partial z} \right) & \mu \left(\frac{\partial w}{\partial y} + \frac{\partial v}{\partial z} \right) & -P + 2\mu \frac{\partial w}{\partial z} \end{pmatrix} \end{aligned}$$

The equation above now defines the stress tensor of a moving fluid in terms of the hydrostatic pressure and the stresses due to viscosity in each Cartesian coordinate. If we consider only the x -component and plugging Equation (27) into Equation (18), we get,

$$\begin{aligned} \rho \frac{Du}{Dt} &= \rho g_x + \frac{\partial}{\partial x} \left(-P + 2\mu \frac{\partial u}{\partial x} \right) + \frac{\partial}{\partial y} \left(\mu \left(\frac{\partial u}{\partial y} + \frac{\partial v}{\partial x} \right) \right) \\ &\quad + \frac{\partial}{\partial z} \left(\mu \left(\frac{\partial u}{\partial z} + \frac{\partial w}{\partial x} \right) \right) \quad \text{Equation (35)} \end{aligned}$$

or,

$$\rho \frac{Du}{Dt} = \rho g_x - \frac{\partial P}{\partial x} + 2\mu \frac{\partial^2 u}{\partial x^2} + \mu \frac{\partial^2 u}{\partial y^2} + \mu \frac{\partial}{\partial y} \left(\frac{\partial v}{\partial x} \right) + \mu \frac{\partial^2 u}{\partial z^2} + \mu \frac{\partial}{\partial z} \left(\frac{\partial w}{\partial x} \right) \quad \text{Equation (36)}$$

At this point, four terms have been derived, which are the hydrostatic pressure term, or normal stress acting inwards to the fluid surface and viscous stress tensor, which consist of both normal and shear stress. As is, Equation (29) is technically fully derived, which shows the body force or gravitational force, pressure force and stress forces all defined in the equation. However, the equation in its current state can be modified even further. Some simplifications and rearranging of the equation would yield,

$$\rho \frac{Du}{Dt} = -\frac{\partial P}{\partial x} + \rho g_x + \mu \left[\frac{\partial^2 u}{\partial x^2} + \frac{\partial^2 u}{\partial y^2} + \frac{\partial}{\partial y} \frac{\partial v}{\partial x} + \frac{\partial^2 u}{\partial z^2} + \frac{\partial}{\partial z} \frac{\partial w}{\partial x} \right]$$

$$\rho \frac{Du}{Dt} = -\frac{\partial P}{\partial x} + \rho g_x + \mu \left[\frac{\partial^2 u}{\partial x^2} + \frac{\partial^2 u}{\partial y^2} + \frac{\partial^2 u}{\partial z^2} + \frac{\partial}{\partial x} \left(\frac{\partial u}{\partial x} + \frac{\partial v}{\partial y} + \frac{\partial w}{\partial z} \right) \right] \quad \text{Equation (37)}$$

Note that the right-hand side has a term in parenthesis that is familiar. Looking back at Equation (13), for an incompressible flow, the term in the parenthesis reduces to zero. Also, the second order partial differential of the u velocity in the x – direction can be further simplified using a Laplacian operator. Therefore, taking these two points into account and applying even further reduction, Equation (30), as a statement of conservation of momentum for the x – component, can be expressed as,

$$\rho \frac{Du}{Dt} = -\frac{\partial P}{\partial x} + \rho g_x + \mu \nabla^2 u \quad \text{Equation (38)}$$

Similarly, the momentum equations for the y – component and z – component are defined as,

$$\rho \frac{Dv}{Dt} = -\frac{\partial P}{\partial y} + \rho g_y + \mu \nabla^2 v \quad \text{Equation (39)}$$

$$\rho \frac{Dw}{Dt} = -\frac{\partial P}{\partial z} + \rho g_z + \mu \nabla^2 w \quad \text{Equation (40)}$$

Finally, in a more generalized form, the Navier – Stokes equation for an incompressible flow is expressed as,

$$\rho \frac{DV}{Dt} = -\nabla p + \mu \nabla^2 V + f \quad \text{Equation (41)}$$

Or,

$$\rho \left(\frac{\delta v}{\delta t} + (u \cdot \nabla)u \right) = -\nabla p + \mu \nabla^2 u + g \quad \text{Equation (42)}$$

Another form of this equation is,

$$\rho \frac{Du}{Dt} = -\nabla p + n \nabla^2 u + f \quad \text{Equation (43)}$$

Whereby the left-hand side

$$\rho \frac{Du}{Dt}$$

Is the mass and acceleration component and the right-hand side,

$$-\nabla p + n \nabla^2 u + f$$

Is the internal forces due to the pressure gradient of the fluid, the forces due to the effects of viscosity and gravitational force. To summarize even further, the Navier-Stokes equation, in words, can be expressed as (White 2009),

$$\begin{aligned} & \text{density of a fluid} \times \text{acceleration in each spatial direction} && \text{Equation (44)} \\ & = \text{pressure force per unit volume} \\ & + \text{viscous forces per unit volume} \\ & + \text{gravitational force per unit volume} \end{aligned}$$

3.6.4 Governing Equations for an Incompressible Flow - Summary

At this point, all governing equations for a 3D incompressible fluid flow has been fully derived. The continuity equation, as a statement of mass conservation, and linear momentum equation, as a statement of conservation of momentum, has been fully defined. These equations are used to compute the fluid flow in all numerical simulation software. To summarize, the four equations of motion, for a 3D incompressible flow, are

- Continuity equation

$$\vec{\nabla} \cdot \vec{V} = 0$$

- Navier – Stokes momentum equation

$$\rho \frac{Du}{Dt} = -\frac{\partial P}{\partial x} + \rho g_x + \mu \nabla^2 u$$

$$\rho \frac{Dv}{Dt} = -\frac{\partial P}{\partial y} + \rho g_y + \mu \nabla^2 v$$

$$\rho \frac{Dw}{Dt} = -\frac{\partial P}{\partial z} + \rho g_z + \mu \nabla^2 w$$

These equations are then used to calculate the pressure field from a known velocity field. All derivations and further explanations can be found in textbooks (Cimbala 2009) and (White 2009).

3.6.5 K – omega SST Turbulence Model

The application of 3D numerical simulation and computational fluid dynamics (CFD) relies heavily on many factors such as various governing equations to solve the fluid flow problem and physical real-world resources to carry out the procedure such as computational power and storage space. Hence, modern solution to numerical simulation predictions requires a method, as accurate as possible, to help with balancing computational resource with solution accuracy at an acceptable amount of simulation time. The method that was developed is turbulence modelling; various RANs turbulence model and the Large Eddy Simulation (LES). These are considered the closure equations to the transport and momentum equations in numerical simulation.

Many studies have utilized various turbulence models, and this has been extensively discussed in Chapter 2. In this numerical study, the URANS turbulence model K – ω SST model, or K – ω Shear Stress Transport, was used. The model has been widely adopted in various CFD studies and has been known to produce excellent results as well as having a good balance with simulation time. In the case of simulating and visualizing the flow field in a location or region with an adverse pressure gradient such as near airfoil wall, the K – ω SST model is suitable due to its blending of the K – ω model in the near wall region while simultaneously solving for far field using the K – ϵ model (Menter 1994).

To better understand how this model is applied and its differences as well as advantages over the standard model, a brief overview of the standard models should be first established. For the K – ε model, the turbulence transport equation K is defined as

$$\frac{\partial(\rho k)}{\partial t} + \nabla \cdot (\rho U k) = \nabla \cdot \left(\left(\mu + \frac{\mu_t}{\sigma_k} \right) \nabla k \right) + P_k - \rho \epsilon \quad \text{Equation (45)}$$

The transport dissipation rate, ε, is defined as,

$$\frac{\partial(\rho \epsilon)}{\partial t} + \nabla \cdot (\rho U \epsilon) = \nabla \cdot \left(\left(\mu + \frac{\mu_t}{\sigma_k} \right) \nabla \epsilon \right) + C_1 P_k \frac{\epsilon}{k} - C_2 \rho \frac{\epsilon^2}{k} \quad \text{Equation (46)}$$

The relationship between ε and ω is defined as,

$$\omega = \frac{\epsilon}{C_\mu k} \quad \text{Equation (47)}$$

Whereby the turbulence model constant, C_μ , is usually taken as 0.09. Substituting Equation (47) into Equation (46),

$$\begin{aligned} \frac{\partial(\rho \omega)}{\partial t} + \nabla \cdot (\rho U \omega) &= \nabla \cdot \left(\left(\mu + \frac{\mu_t}{\sigma_k} \right) \nabla \omega \right) + \frac{Y}{v_t} P_k - \beta \rho \omega^2 \\ &+ \left(2 \frac{\rho \sigma_\omega^2}{\omega} \nabla k : \nabla \omega \right) \end{aligned} \quad \text{Equation (48)}$$

(Additional term)

Which is the ε equation but rewritten into as ω. If we ignore the additional term on the furthest right-hand side of the equation, Equation (48) is actually the transport equation for the specific turbulence dissipation rate ω. The left-hand side of the equation is the temporal derivative and convection term. The right-hand side is the diffusion, production, and dissipation or destruction term. The omega (ω) and epsilon (ε) are considered sink terms in that these terms are used to solve the turbulent kinetic energy and convert into thermal energy. To be more precise, the ω term is called the specific turbulence dissipation rate whereas the ε term is called the turbulence dissipation rate (m²/s³). The additional term at the end has role to play, however. If we add an engineering function or blending function (1-F₁), we get,

$$2(1 - F_1) \frac{\rho \sigma_\omega^2}{\omega} \nabla k : \nabla \omega \quad \text{Equation (49)}$$

Here, for cells that are far from the wall, $F_1 = 0$, the model selects the $K - \epsilon$. When the cells are close to the wall or near wall, $F_1 = 1$, the $K - \omega$ model becomes dominant. For regions in between $0 < F_1 < 1$, a hyperbolic tangent is used for smoother blend of the two models (Menter 1994). Note that both turbulence models have empirical constants β in them. The blending function also takes those into account to blend between the empirical constants, which is defined as,

$$\phi = F_1 \phi_\omega + (1 - F_1) \phi_\epsilon \quad \text{Equation (50)}$$

Hence, Equation (48) now becomes,

$$\begin{aligned} \frac{\partial(\rho\omega)}{\partial t} + \nabla \cdot (\rho U \omega) \\ = \nabla \cdot \left(\left(\mu + \frac{\mu_t}{\sigma_k} \right) \nabla \omega \right) + \frac{Y}{u_t} P_k - \beta \rho \omega^2 \\ + 2 \left((1 - F_1) \frac{\rho \sigma_\omega^2}{\omega} \nabla k : \nabla \omega \right) \end{aligned} \quad \text{Equation (51)}$$

Whereby gradient of $\nabla k : \nabla \omega$ is defined as,

$$\nabla k : \nabla \omega = \frac{\partial k}{\partial x_j} \frac{\partial \omega}{\partial x_j} = \frac{\partial k}{\partial x} \frac{\partial \omega}{\partial x} + \frac{\partial k}{\partial y} \frac{\partial \omega}{\partial y} + \frac{\partial k}{\partial z} \frac{\partial \omega}{\partial z} \quad \text{Equation (52)}$$

Which is the tensor in a product of the two transport terms. Equation (48) is known as the $K - \omega$ BST equation or Baseline Stress Transport model. The equation forms the foundation for blending of the two standard models into one based on the applied blending function. The $K - \omega$ BST equation, however, suffers from overprediction of the wall shear stress. To rectify this, the viscosity, μ_t in Equations (47) and Equation (48) were modified. The viscosity, in its original form, is defined as

$$\mu_t = \frac{\rho k}{\omega} \quad \text{Equation (53)}$$

Hence, to overcome this weakness, a limiter is introduced. This is known as the viscosity limiter and is defined as

$$\mu_t = \frac{a_1 \rho k}{\max(a_1 \omega, SF_2)} \quad \text{Equation (54)}$$

Which gives a much better accuracy in measurements of flow separation. Here, the second blending function, F_2 , is also a hyperbolic tangent which measures the

distance to the nearest wall and would determine which of the two models are selected (Menter et al. 2003). For all constants, the default values were used in the Fluent which were suggested by Wilcox (Wilcox 2008b) and has been considered optimal by Menter (Menter et al. 2003).

3.6.6 Other Numerical Simulation Parameters

The solver algorithm used is the SIMPLE scheme. The SIMPLE scheme is a pressure-based segregated algorithm to solve the pressure-velocity coupling. Other solver algorithms were tested and compared to the SIMPLE algorithm. The SIMPLER and PISO schemes were also available with mesh skewness correction factor, but this was not required as the meshing of the model was done within acceptable levels of skewness (< 0.90). The Coupled scheme was much more time intensive than the SIMPLE scheme. However, it is also much more robust and was considered for simulations where simulation stability was prioritized. Second order discretization was employed for both pressure and momentum equations.

A study by McLaren (McLaren 2011) found that for a small enough time step size of between 0.5,1 and 2.5, the power coefficient varied only by 1.5% which is negligible. For this study, to capture differences in velocity and pressure flow fields at 30° interval while maintaining a reasonable simulation time, a suitable time step size or the amount of rotation the turbine takes in degree of 5° was selected. The same author also found differences between the 5th, 6th and 7th rotation to differ negligibly. Hence, this study will only analyse data from the 5th rotation.

3.6.7 Performance Coefficients

Power extraction and calculation for various parameters with respect to the VAWT is slightly different to the HAWT. This is obviously due to the difference in geometry, blade orientation and axis of rotation. In measuring and extracting data on the various performance coefficients during turbine operations, both numerical and experimental, the following equations were used for the VAWT:

Moment coefficient, C_M

$$C_M = \frac{\tau}{\frac{1}{2} \rho A_{swept} U_0^2} \quad \text{Equation (55)}$$

Whereby the torque, τ , is defined as

$$\tau = \frac{P_{output}}{RPM} \times \frac{30}{\pi} \quad \text{Equation (56)}$$

Power coefficient, C_p

$$C_p = \frac{P_{mech}}{P_{wind}} = \frac{\tau \omega}{\frac{1}{2} \rho A_{swept} U_0^3} \quad \text{Equation (57)}$$

Whereby the wind power, P_{wind} is defined as,

$$P_{wind} = \frac{1}{2} \times \rho \times V^3 \times A_{swept} \quad \text{Equation (58)}$$

Both moment and power coefficient can easily be calculated by its relation to the tip speed ratio. This is expressed as,

$$C_p = C_T \times \lambda \quad \text{Equation (59)}$$

Whereby the tip speed ratio (TSR), λ , is calculated by the following equation.

$$\lambda = \frac{\omega r}{U_0} \quad \text{Equation (60)}$$

The lift coefficient,

$$C_L = \frac{L}{\frac{1}{2} \rho A_B V^2} \quad \text{Equation (61)}$$

The drag coefficient,

$$C_D = \frac{D}{\frac{1}{2} \rho A_B V^2} \quad \text{Equation (62)}$$

Lastly, the lift to drag ratio is defined as,

$$\text{Lift to drag ratio} = \frac{C_L}{C_D} \quad \text{Equation (63)}$$

3.7 Experimental Setup

After the numerical section was completed, experimental work to test and validate the results of the simulation and optimization was conducted. The following subsections described the workings and methodology of the wind tunnel experiment.

3.7.1 Experimental Methodology

A carbon fiber rod of 12mm diameter was used as the main rotating rotor shaft. Turbine blades and support-arms are 3D printed using a 3D printer. The wind turbine was placed in the wind tunnel within the test section area. The fabrication of the wind turbine was such that the connecting parts, especially the shaft to support-arm connection, were designed to be interchangeable with different support-arm numbers and geometry. This allowed various settings and configurations to be studied without the need to constantly print and design multiple new parts for each experiment. The result was a significantly reduced printing and experiment time which allowed for more studies to be conducted.

For the wind tunnel experiment, several steps were developed. The experimental procedure was described below:

1. The turbine blades were 3D printed and the blade surface was sanded to reduce surface roughness.
2. The turbine blades were connected to a 3D printed turbine connector and the turbine parts were assembled. The assembled turbine was then connected and secured to the carbon fibre - made shaft using grub screws. The top end of the carbon fibre shaft was then connected to a torque sensor to measure the moment and rotational speed (rpm) of the turbine.
3. The wind tunnel fan was turned on and the inverter was adjusted to a frequency value of about 34.5Hz to obtain a 7m/s wind speed (Fig 3.27).
4. Using the rope brake dynamo meter, braking force was applied on the turbine shaft to achieve different TSR values.
5. The values of torque or moment, in Nmm, were extracted using the torque sensor that was connected to a computer.

6. Steps 4 and 5 were repeated twice more and the value of torque and rotational speed were averaged. The data was then extracted and analyzed.

Multiple turbines of each baseline and the candidate optimized blade, which was discussed later in this thesis, were printed to ensure the results were consistent and repeatable. This meant multiple experimental tests were conducted on multiple days and, therefore, a large number of data was produced to ensure an accurate representation of the experimental result. This ensured that the findings of the wind tunnel experiment were conclusive and, therefore, validated the simulation results. Fig 3.21 below shows the 3D printed turbine blade with skeletal design to improve blade structure while reducing turbine blade.

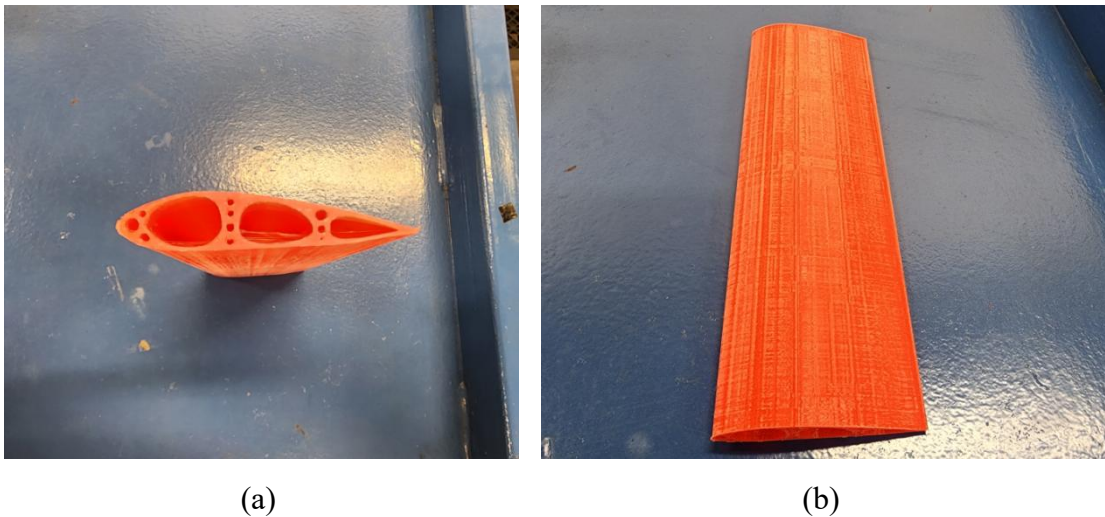


Fig 3.21. (a) cross section of the turbine blade and (b) span length of the blade.

3.7.2 Wind Tunnel

For the experimental portion of this study, a wind tunnel was designed and is currently undergoing fabrication. A blow-down configuration was designed which was deemed suitable given the restricted laboratory space as well as experimental requirements and expectations. Fig 3.22 shows the 3D CAD drawing of the proposed wind tunnel. The wind tunnel consists of the 3 main sections: the flow contractor, straightener and the test section. A line diagram of these components is shown in Fig 3.23. The engineering drawing of the wind tunnel is attached in the Appendix section showing all design specifications and dimensions. The full experimental setup was

illustrated in Fig 3.24, Fig 3.25, and Fig 3.26. The inverter controlling the wind tunnel wind speed is shown in Fig 3.26.

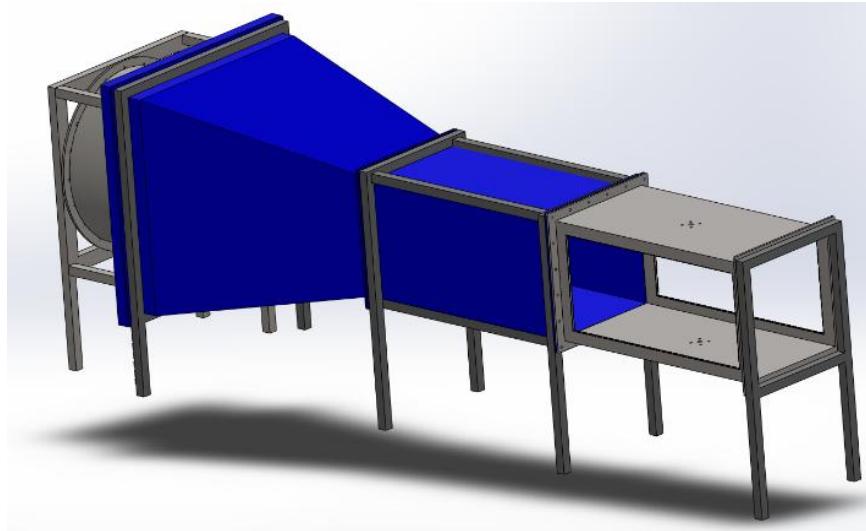


Fig 3.22 3D CAD design of the proposed wind tunnel.

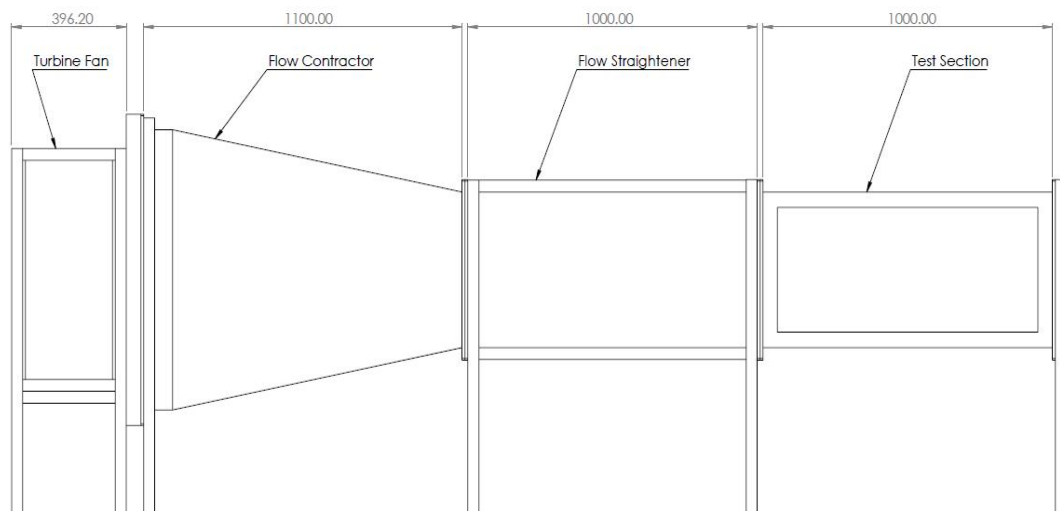


Fig 3.23 Line diagram showing the components of the fabricated wind tunnel.



Fig 3.24. Wind tunnel used for experiments.



Fig 3.25. Test section area of the wind tunnel. Shown at back are the honeycomb design to straighten the flow.



Fig 3.26. Inverter for wind speed control. Varies from 0 Hz to 50 Hz achieving wind speeds of up to 13 m/s at the outlet.

Engineering drawings with more technical details and dimensions used as reference for the fabrication of the wind tunnel can be found in the Appendix section. Preliminary wind tunnel testing was conducted to calibrate the wind speed and the fan inverter. Wind speed measurements were done at two locations in the test section. The first location is at 200mm in front of the turbine shaft and is treated as the inlet region. The result of this measurement was summarized in Table 3.6 and Fig 3.27. The second measurement is done at the end of the test section and is treated as the wind tunnel outlet shown in Table 3.7 and Fig 3.28. The dimension of the tested turbine was set as per Table 3.4. This yielded a blockage ratio of 16% which was deemed suitable according to (Al-Obaidi and Madivaanan 2022). A graph of these data was then plotted and used to obtain the desired speed by adjusting the inverter. The experiment was conducted different wind speeds. The next chapter discussed these wind speed settings and its effects on the experimental findings.

Table 3.6. Velocity at the inlet relative to the frequency of the fan inverter

Frequency, Hz	Mean Inlet Velocity (m/s)	Standard Deviation
5	0.93	0.07
10	1.9	0.13
15	2.88	0.13
20	3.88	0.21
25	4.95	0.3
30	5.98	0.41
35	7.21	0.44
40	8.54	0.43
45	9.46	0.55

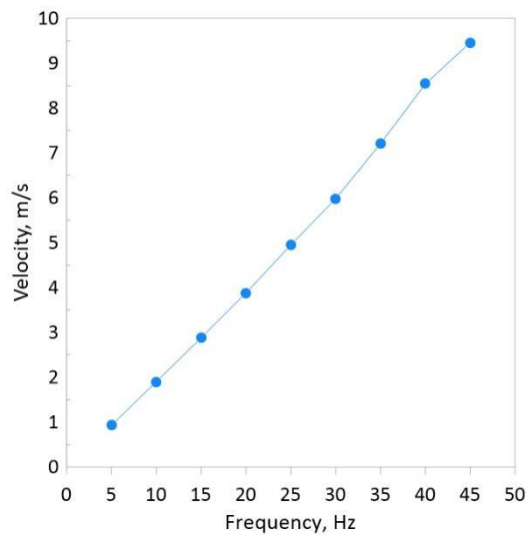


Fig 3.27. Graph showing the relationship between the velocity inlet and the inverter frequency.

Table 3.7. Outlet velocity relative to the inverter frequency.

Frequency, Hz	Trial 1	Trial 2	Trial 3	Average
5	1.13	1.1	1.12	1.12
10	2.21	2.39	2.38	2.33
15	3.66	3.69	3.68	3.68
20	5.09	5.01	5.01	5.04
25	6.51	6.55	6.51	6.52
30	7.81	7.87	7.70	7.79
35	9.14	9.03	9.07	9.08
40	10.45	10.38	10.38	10.40
45	11.65	11.82	11.64	11.70
50	12.97	12.89	12.75	12.87

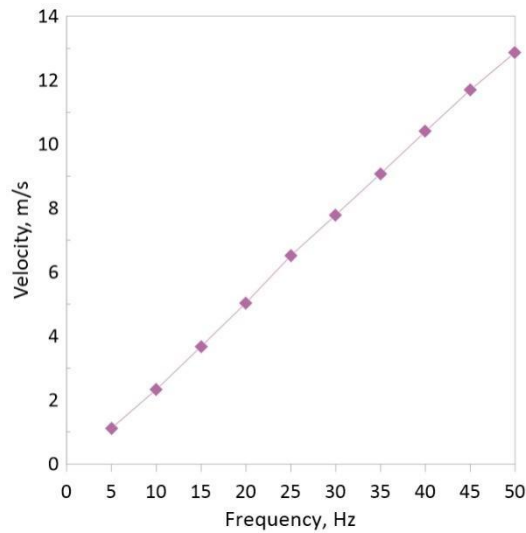


Fig 3.28. Graph showing the relationship between the outlet velocity and the inverter frequency.

3.7.3 Sensors and Equipment

This section discusses the various equipment and sensors which will be used in the planned experimental section of this study. Parameters such as power extracted from the turbine, static and dynamic pressure measurements will be measured in this study. Table 3.8 below highlights some of the sensors and equipment for the experimental study. More information and technical data can be found in the Appendix.

Table 3.8. Summary of experimental equipment and its function.

Equipment	Model	Description
Torque sensor	n.Gineric 2nm	Connects to the turbine shaft to measure torque generated by wind turbine which is used to calculate power.
Velocity sensor	Testo 420	Measures wind velocity in the wind tunnel
3D printer	Crealitiy Ender 3	Prints turbine components and other experimental instruments, attachments, fixtures etc.

3.8 Summary

In this chapter, the outline of the methodology, experimental equipment, theoretical background and governing equations, and simulation parameters were discussed. The optimization scheme using the adjoint solver together with the gradient-based

Chapter 3: Research Methodology

optimizer was also described. The results of all the planned and outlined methodology here was presented in the following chapter.

Chapter 4

Results and Discussion

4.1 Overview

In this chapter, the results of the numerical simulations that has been done so far were presented. The grid independence test and mesh validation were conducted first to verify the validity of the suggested mesh. Next, two turbine configurations were proposed and studied in a comparative analysis against a baseline turbine of each respective turbine. A 2D optimization study was then presented. The first study focuses on the feasibility of the adjoint solver together with the gradient-based optimizer on a NACA0018 airfoil. The second study will be on the various turbine parameters and its effects on the outcome of the adjoint optimization when conducted in a turbine setting. Then, the resulting candidate blade from the 2D optimization was extracted and two 3D studies were conducted. These studies will include varying turbine configuration and the result of the candidate blade measured against the baseline blade with 3D effects. Discussion for each section were also presented.

4.2 Grid Independence Test

The numerical section encompasses a 2D study in the optimization stage and 3D studies in the initial baseline studies and the optimization comparisons stage. In both 2D and 3D studies, a similar approach was taken with respect to the mesh generation.

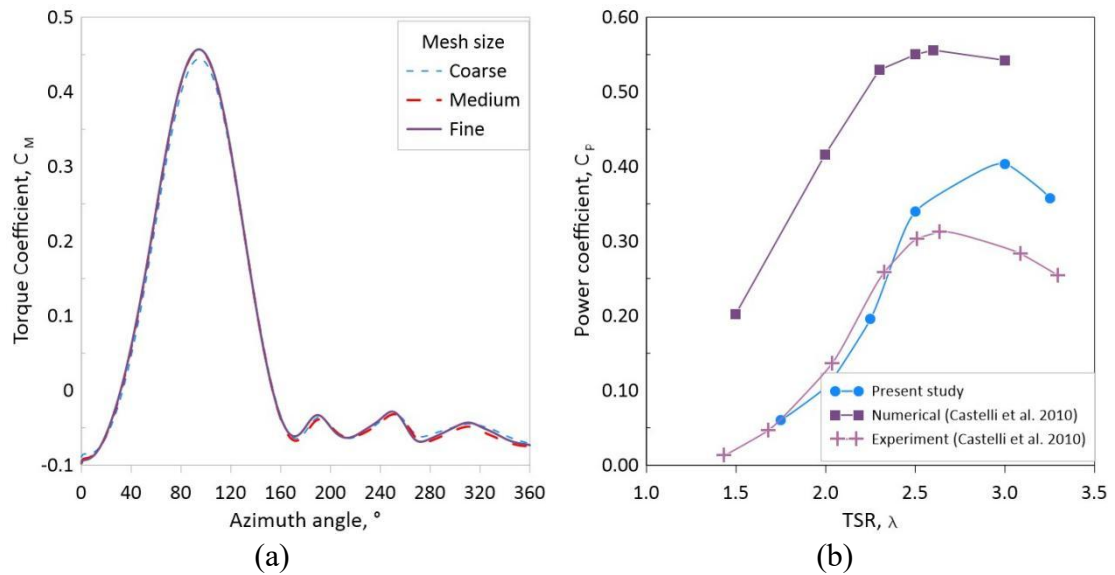


Fig 4.1. (a) Grid independency and (b) mesh validation against Castelli et al (Castelli et al. 2010).

An appropriate mesh resolution is essential to balance numerical accuracy and computational time. Therefore, a mesh independence was conducted varying mesh density from course to fine. Fig 4.1(a) above shows the domain size comparisons and grid independence test. The Fig indicates an overall negligible difference between the largest mesh (117,165 elements) and the medium mesh (54,430 elements) with the differences only observed at critical locations in the upwind and downwind phrase of the rotation. For the adjoint optimization, however, an exception was made. The meshing was done separately and a suitable mesh resolution was selected based on literature (Lång 2019, Tzanakis 2014) to enhance the optimization efficiency and reduce mesh complexity around the turbine. Therefore, a mesh size of $\sim 55,000$ was selected as the suitable mesh size to balance simulation time and computational resource. This mesh size was applied to all turbine setup in this study.

Fig 4.1(b) shows the mesh validation compared against a numerical and experimental study referenced from Castelli et al (Castelli et al. 2010). It was observed that the mesh grid agreed well especially at lower TSR values. A difference was observed at TSR 2.5, and above which can be attributed to the lack of 3D effects in 2D numerical studies such as blade tip effects, drag and vibration losses as well as the infinite depth. However, this study compared very well against the 2D numerical study from the quoted study and therefore was deemed acceptable. The number of rotations was set to 10 as was recommended by previous authors (Howell et al. 2010, Rezaeiha, Kalkman, and Blocken 2017a) with the final turbine rotation taken as the

average for comparisons and analysis. Structured 2D mesh were used in all simulations. Second order discretization was selected for the pressure and momentum formulations and SIMPLE scheme was used for the velocity-pressure coupling. Studies (Rezaeiha, Kalkman, and Blocken 2017a, Elsakka et al. 2022) have suggested various time step sizes in 2D and 3D simulations for accurate numerical predictions. This study will employ a time step size of 1° which is consistent with reported literature.

For the 3D study, the grid independence test was carried out by varying a grid size between 3×10^6 cells coarse up to a very fine mesh of 1.2×10^7 number of cells to determine a suitable grid size. From the Fig, a grid size of about 7×10^6 was chosen as a balance between result accuracy and total simulation time. The mesh validation was then carried out by comparing the performance of the turbine against known experimental study by Castelli et. al. (Castelli et al. 2010) [72]. The comparison was done by plotting power coefficients, C_p of the baseline turbine against the experimental results shown in Fig 4.2(b). Similar to the 2D study above, the mesh generated agreed well at lower TSR values of less than 2.5. The difference observed at the higher TSR values can be attributed to the absence of vibration or friction losses that usually occurs during experiments. Hence, the validation of both 2D and 3D studies can be said to agree well to the referenced experimental study at lower TSR ranges of less than TSR 2.5. Therefore, the numerical study was conducted at TSR 2.5 or lower.

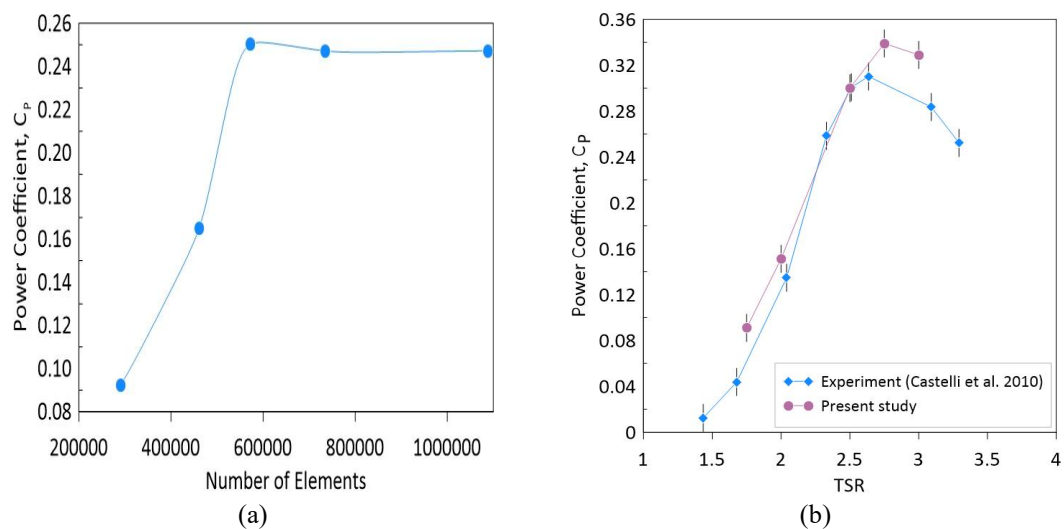


Fig 4.2. (a) Grid independence study and the (b) mesh validation of the current CFD against a published experimental (Castelli et al. 2010).

4.3 Performance analysis and characterization of the two bladed NACA0018

The following are results of the analysis on the NACA0018 turbine with single circular shaped support-arms connected to each blade. This study was conducted to investigate the performance effects of turbine support-arms in a 3D study.

4.3.1 Effect Of support-arms on Turbine Performance Coefficient

Fig 4.3 shows the power coefficient, C_p comparison between the baseline turbine and the full turbine configuration with dual support-arms. It is observed that the baseline predicted much higher than the full turbine configuration. The C_p difference at TSR 1.5 was 55.5 % and less pronounced at a higher TSR of 2 with a performance difference of around 47.2%. This observation is consistent with other findings whereby the addition of the support-arms in numerical predictions results in a significant performance coefficient over prediction Castelli and Siddiqui (Castelli et al. 2010, Siddiqui, Durrani, and Akhtar 2015, Siddiqui, Durrani, and Imran 2013).

Fig 4.4 shows a comparison of the performance of each turbine at the final rotation at TSR 1.5. Fig 4.4(a) illustrates the full turbine predicted a generally lower power coefficient compared to the baseline turbine. Higher negative torque and slightly lower peaks in the positive region lowers the average power coefficient values. This observation is supported by the lower overall torque experienced by the full turbine compared to the baseline shown in Fig 4.4(b).

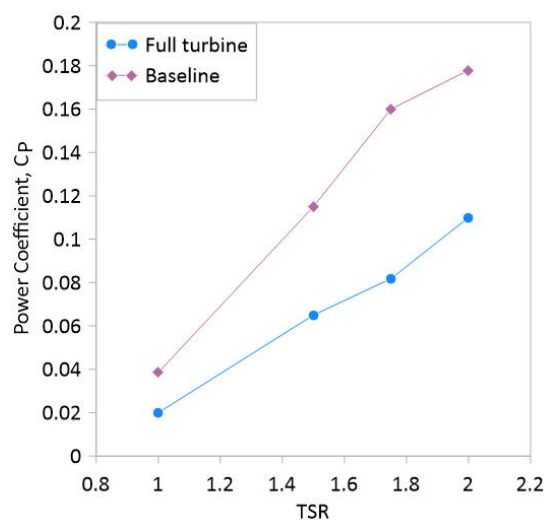


Fig 4.3. Power coefficient comparisons of the baseline turbine against the full turbine comparison

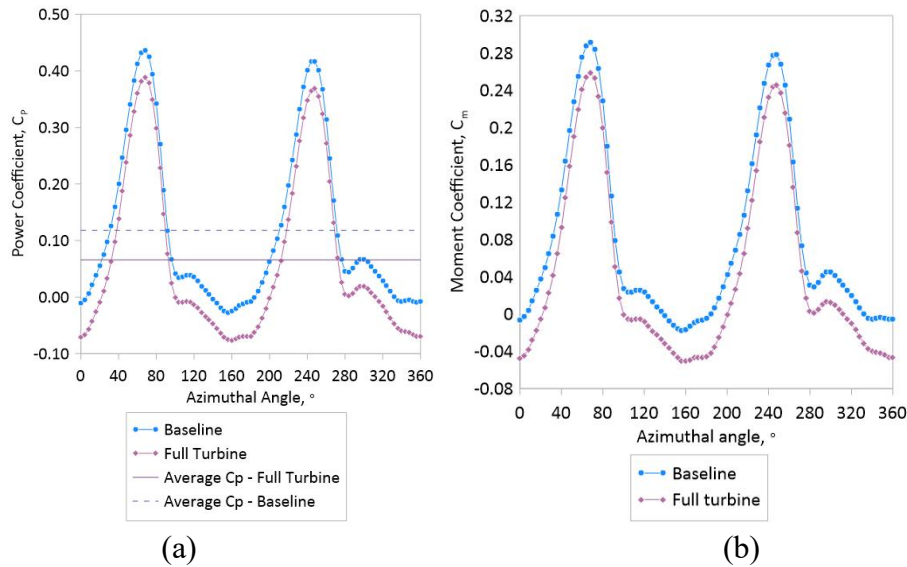


Fig 4.4. Comparisons between baseline and full turbine configuration for (a) power coefficient and (b) moment coefficient.

Fig 4.5 illustrates the instantaneous single blade coefficients comparisons between the baseline and full turbine coefficients. The full turbine configuration has a lower overall coefficient compared to the baseline turbine. This can be seen most prominently between the azimuthal angles 0° - 140° . For the data points between 0° - 80° , the lower coefficient of the full turbine seems to show a rather lagging effect with the curve slight behind the baseline. From both Fig 4.5(a) and Fig 4.5(b), both turbine turbines undergo reduced efficiency with the full turbine experiencing a pronounced oscillation. In comparison, the baseline turbine was much smoother in terms of torque and power between the 160° to 320° azimuthal angle. The full turbine peaks and dips significantly at 200° and 280° respectively, but the baseline turbine has a more gradual and linear decrease in instantaneous performance efficiency. This indicates that the presence of the support-arms has a significant effect within this region during rotation.

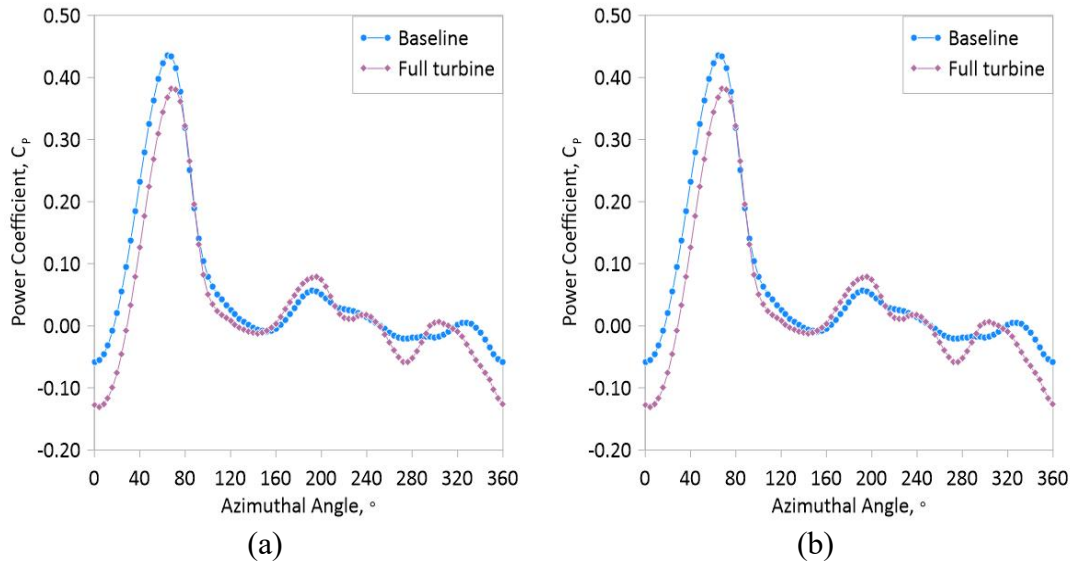


Fig 4.5. Comparisons between baseline and full turbine configuration of instantaneous (a) power coefficient and (b) moment coefficient for a single turbine blade.

4.3.2 Effects Of support-arms on Turbine Lift and Drag Coefficient

Fig 4.6 shows the lift and drag coefficient of the wind turbine circular support-arms in multiple configurations for the TSR of 1.5. The single arm in this instance refers to a single support-arm of the four support-arms. The double arm constitutes the dual support-arm on a single turbine blade at the same blade. From Fig 4.6(a), both the single arm and double arm have a peak lift coefficient, C_L value of 1.5 and 3.0 at 50° azimuthal angle with the average C_L value of 0.08 and 0.16 respectively. The incremental increase in C_L coincides with the blade moving from the windward region into the upwind region. The C_L value reduces to 0 between 140° to 200° during the leeward region and then experiences negative lift with a peak value of -1.18 at about 310° . Also shown is the average sum for all the support-arm structures which demonstrates the cycle for both blades and their pair of support-arms. The average C_L value of all four arms was found to be 0.32.

From Fig 4.6(b), we see that the drag coefficient, C_D for both the double arm single blade and the total drag for all 4 arms are almost similar with a peak value of 4.99 and 5.06 respectively at about 5° as the blade enters the upwind region. This shows that during this stage of the turbine cycle, the effect of drag predominantly affects the first blade and its support-arms with less drag acting on the second blade with an average C_D of 0.66 for single arm and 1.3 average for both arms on the first

blade. The effects of drag than reduces for both the single and double arm structures and peaks at -0.21 and -0.40 respectively at 120° while the overall sum of the support-arms increases at 90° mostly due to the second blade as it passes through the downwind region and into the windward region. Thereafter, minimal changes were observed as the first blade moves from 90° to 270° azimuthal angle. This shows the effects of drag on the support-arms are minimal during the transitional phase as the blade moves and exits the upwind region, passes through the leeward region, and then enters the downwind region. The curve of the total sum of all four support-arms underlines this observation. It is interesting here to note that, generally, the most significant effects of drag are almost concentrated between the transitional region of 270° and 360° as the blade exits the downwind and enters the windward region. Table 2 below summarizes the average coefficients for both lift and drag for each support-arm structure of interest.

Table 4.1 Summary of lift and drag coefficients.

Geometry	Average lift coefficient, CL	Average drag coefficient, CD
Single arm	0.08	0.66
Double arms	0.16	1.30
Sum of arms	0.32	2.53

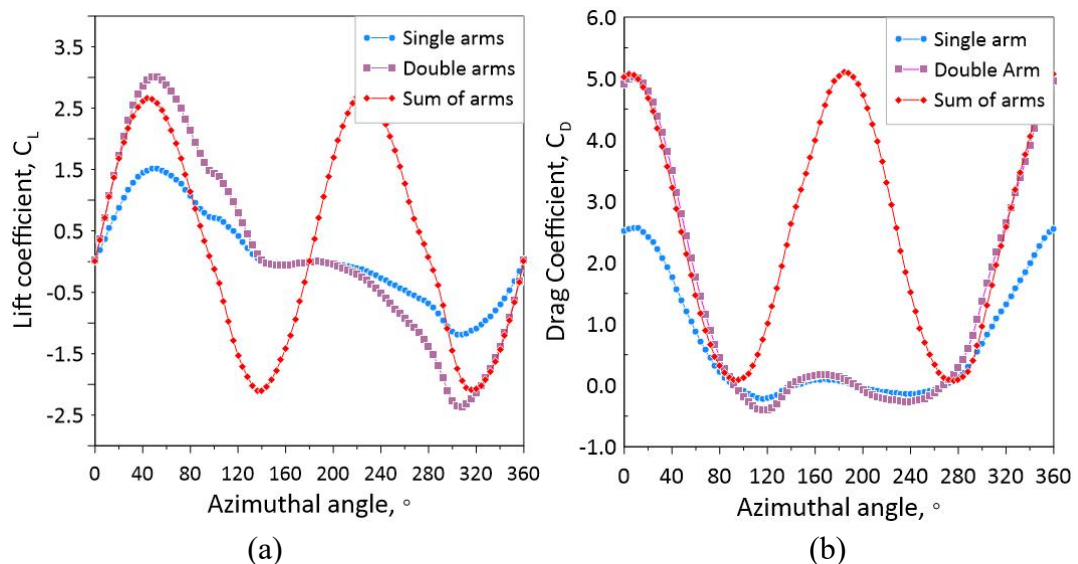
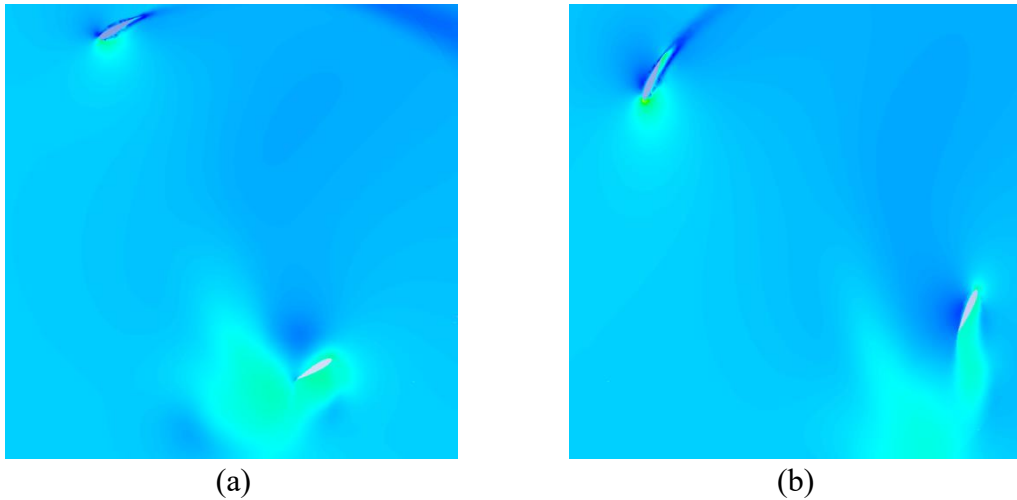


Fig 4.6. Comparisons between different support-arm configurations in terms of (a) lift coefficient and (b) drag coefficient of the VAWT at TSR 1.5.

4.3.3 Velocity Flow Physics Comparisons

For this analysis, an XY plane was created at the midplane of the first turbine support-arm. Fig 4.7 illustrates the flow velocity of the baseline turbine at azimuth angles 30°, 60°, 90°, and 120°. In Fig 4.7(a), it was observed high flow velocity concentrated at the front section of the inner surface of the first blade as it entered the upwind region. Significant flow vorticity was observed enveloping the second turbine blade as it exits the leeward region and enters the downwind region creating a significant wake as it passes. From both Fig 4.7(b) and Fig 4.7(c), as the first blade moves from 60° to 90°, high flow velocity moves along the inner surface towards the trailing end of the blade. It is also observed significant vorticity starts to form on the leading side of the blade. The second blade, within the downwind region, experiences high flow velocity at the upper surface. In Fig 4.7(d), significant circular vorticity fully was formed at the inner side of the first blade which indicates the flow is turbulent. The flow contour around the second blade starts to be more streamlined as it exits the downwind region and enters the windward region.



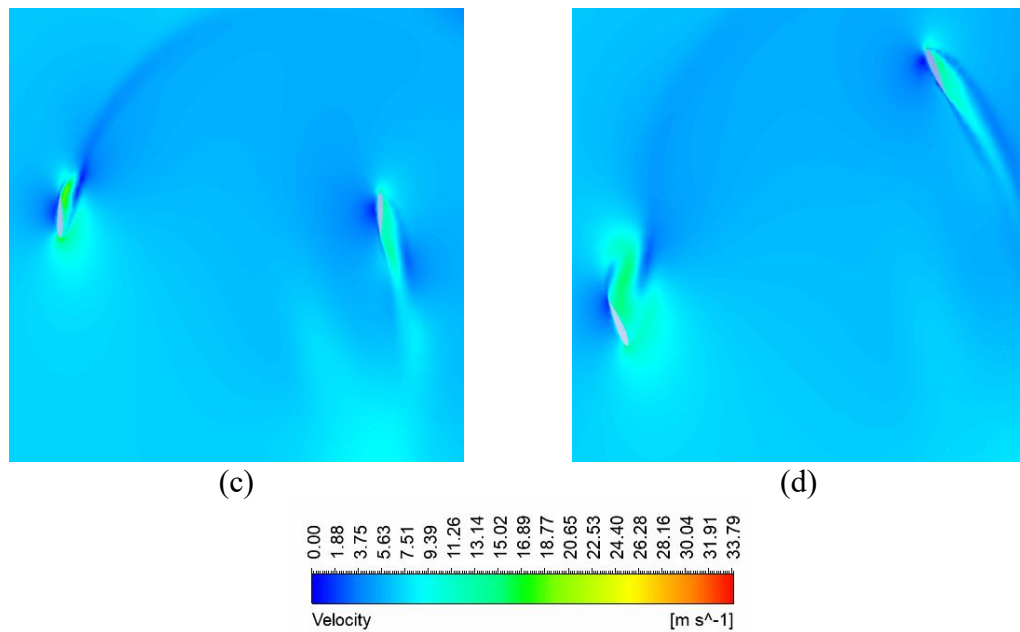


Fig 4.7. Velocity contour of the flow physics for TSR 1.5 of the baseline turbine with no support-arms at azimuthal angles (a) 30°, (b) 60°, (c) 90° and (d) 120°.

Fig 4.8 illustrates the flow velocity contour of the full turbine configuration. Here, the effects of support-arms on the flow physics of the turbine can be observed. In Fig 4.8(a), high velocity flow concentrated more at the trailing end of the blade rather than at the front of the blade as observed in Fig 4.7(a). High flow velocity also stretched along the turbine arms and concentrated more towards the arm-blade connection. The magnitude of high flow velocity within the second blade entering the leeward region was observed to be less intense and significant compared to the second blade in Fig 4.7(a). As the first blade enters the upwind region, in Fig 4.8(b), it was observed that the high flow velocity starts to concentrate more towards the arm-blade connection with lesser flow velocity within the turbine rotor region. Similar observations were made at 90°, shown in Fig 4.8(c). Both the first and second blades experienced significant high flow velocity at the upper and inner side respectively. The flow vorticity experience by the second blade was also observed to be more intense and larger compared to the more streamlined flow of the baseline in Fig 4.7(c). In Fig 4.8(d), high flow velocity concentrated more at the arm-blade connection region while the front of the blade sees a more diffused flow velocity. The flow velocity observed is more intense than the baseline turbine shown in Fig 4.7(d), possibly due to the wake generated by the support-arms. The second blade,

however, experiences a flow separation, unlike the baseline Fig 4.7(d), as it exits the downwind region and enters the windward region. High flow velocity along the turbine support-arms also starts to form. One thing to note from all the Figs is how the turbine rotor shaft at the centre affects the flow physics around the turbine area. Significant turbulent flow resembling the formation of a Von Karman vortex street is observed at every instance of the turbine rotation. This additional flow consideration in the numerical calculation affects the turbine performance prediction.

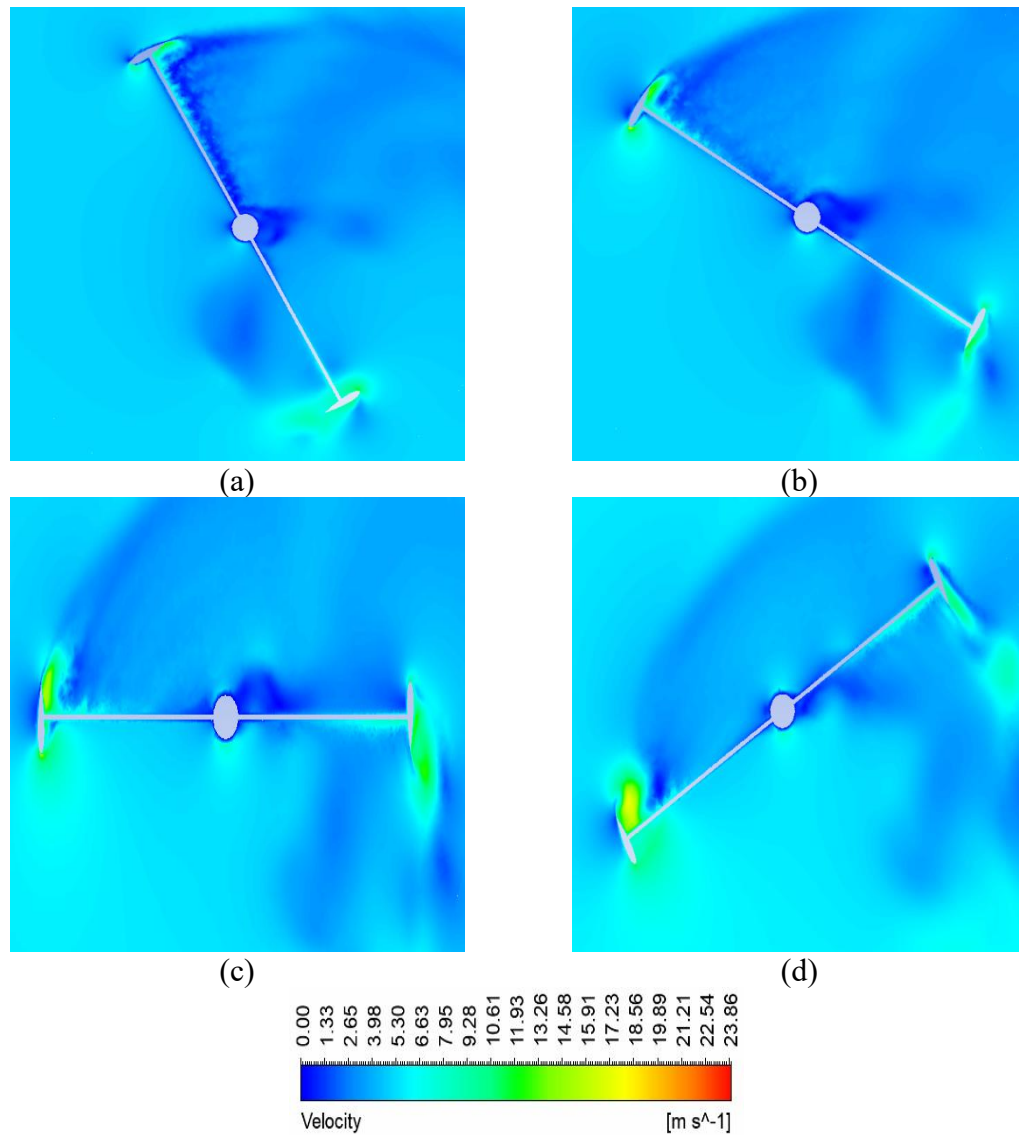


Fig 4.8. Velocity contour of the flow physics for TSR 1.5 of the full turbine configuration at azimuthal angles (a) 30°, (b) 60°, (c) 90° and (d) 120°.

4.3.4 Pressure contour comparisons

For the pressure contour analysis and comparison, similar XY plane was used from the velocity analysis. Fig 4.8 shows the pressure contour of the baseline turbine. From Fig 4.9(a), at 30° azimuthal angle, high pressure levels concentrated at the upper surface of the leading edge while large negative pressure spreads across the inner surface of the first blade. The second blade in the leeward region experienced low pressure. As the first blade advanced into the upwind region, shown in Fig 4.9(b) at 60° azimuthal angle, it experiences a higher-pressure intensity on the upper surface while negative pressure concentrated more on the inner surface of the leading edge. The second blade saw higher pressure starting to act on the inner surface of the second blade as it enters the downwind region. At 90° azimuthal angle, in Fig 4.9(c), the first blade experienced lower positive and negative pressure regions. The second blade shows similar pressure distribution as in the previous angle but with slightly higher values at the inner surface of the leading edge. Lastly, in Fig 4.9(d), the first turbine blade experiences lower pressure in general within its vicinity. However, the pressure contour shows a disconnected or separated flow as large pressure formation indicating significant vortex appears near the trailing edge of the blade. The second blade, entering the windward region, shows high pressure levels on the inner surface of the leading edge and low pressure at the upper surface.

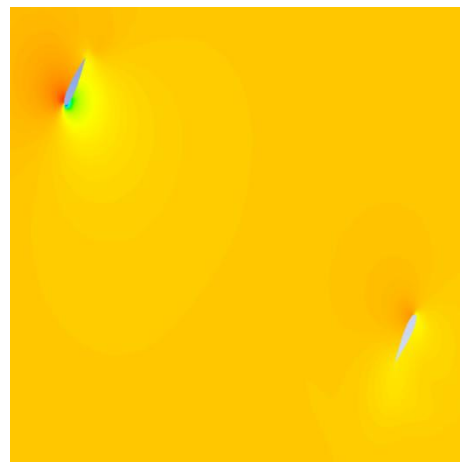
Fig 4.10 shows the pressure contour of the full turbine configuration. At azimuthal angle 30°, shown here in Fig 4.10(a), similar observations to Fig 4.9(a) were made whereby large positive pressure values concentrated on the upper surface of the leading edge while a low negative pressure accumulated along the inner surface extending slightly off the trailing edge. Negative pressure also spreads along the turbine support-arms, increasing in magnitude as it nears the arm-blade connection. From Fig 4.10(b) and Fig 4.10(c), as the turbine continues to rotate from 60° and 90° into the upwind region, both blades experienced similar pressure distribution to its baseline turbine counterparts. The first turbine support-arm, however, saw the negative pressure moving along the arm towards the arm blade region while the front side of the second support-arm experienced positive pressure along its span. In Fig 4.10(d), large negative pressure formations detached from the turbine blade and concentrated around the turbine arm. Compared to Fig 4.9(d), the

magnitude of this negative pressure region is larger and more significant, indicating a large vortex and turbulence forming near the first blade.

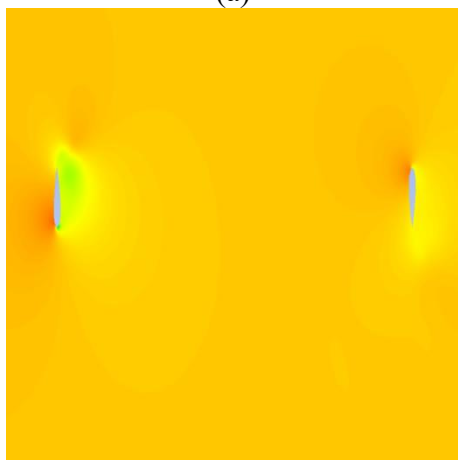
From the observations made above, while noting the pressure range of both turbines, it was found that the magnitude of both the positive and negative pressure experienced by the baseline turbine were larger compared to the full turbine configuration. The larger pressure values or magnitudes means that the blades in the baseline turbine experienced a larger pressure difference between its upper and lower surface of the leading-edge, which then generates higher lift force on the blade. The added turbine arms in the full turbine configuration reduces the overall pressure difference in the blades as well as adding drag effects during turbine rotation and would, therefore, result in lesser force in the lift direction acting on the blade. This difference in pressure profile around the blades of each turbine would suggest why the predicted power coefficient was lower in the full turbine configuration.



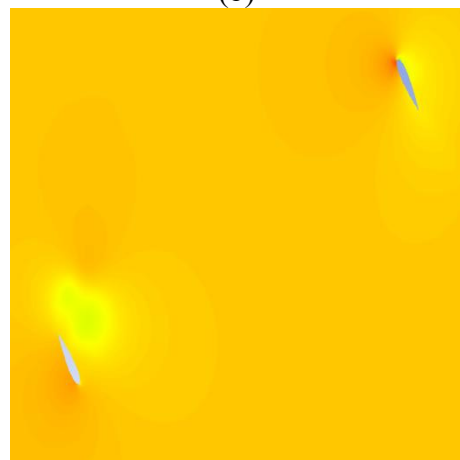
(a)



(b)



(c)



(d)

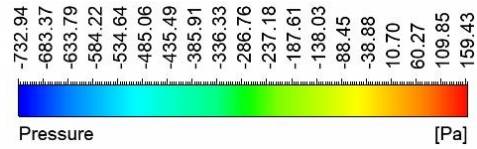


Fig 4.9. Pressure contour of the flow physics for TSR 1.5 of the baseline turbine with no support-arms at azimuthal angles (a) 30°, (b) 60°, (c) 90° and (d) 120°.

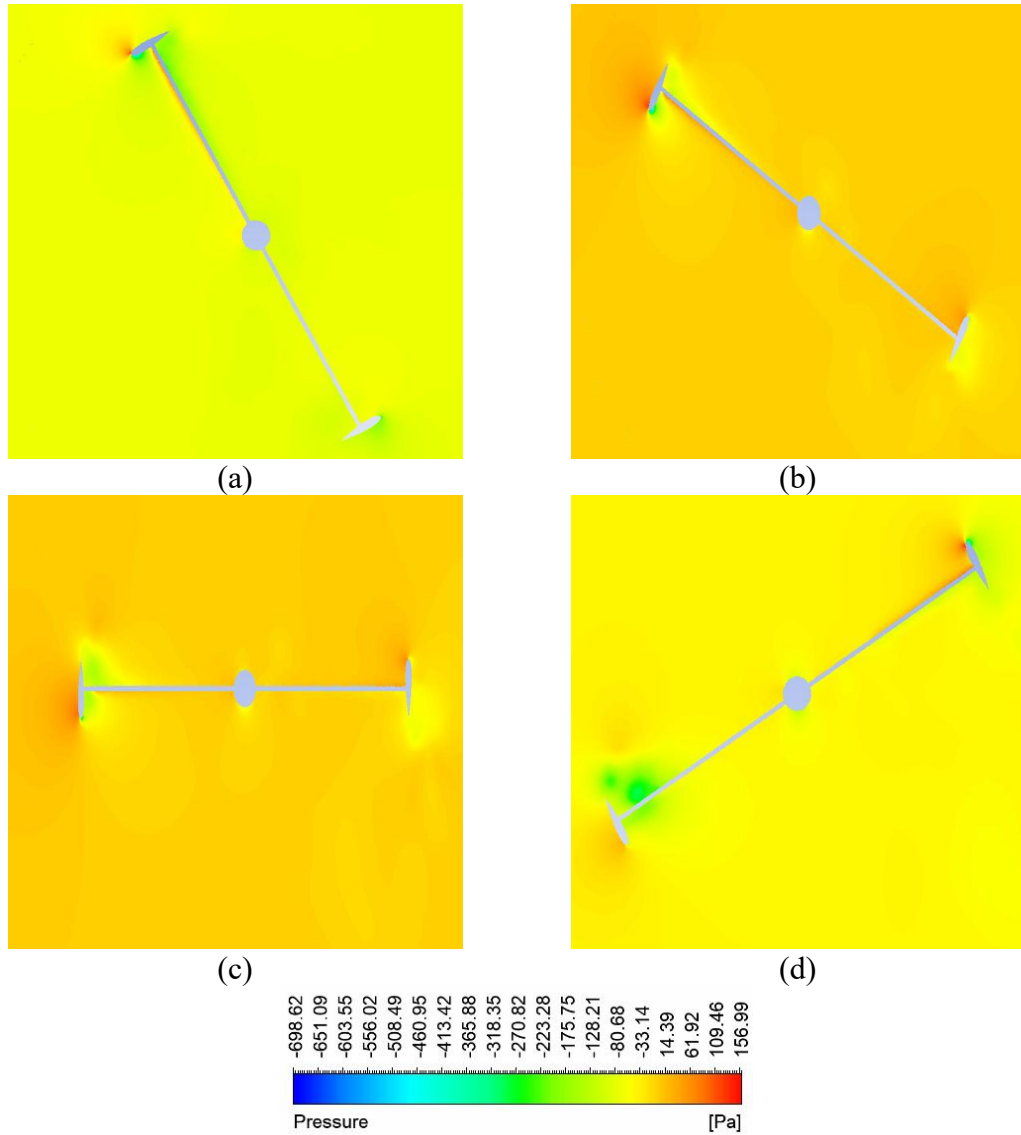


Fig 4.10. Pressure contour of the flow physics for TSR 1.5 of the full turbine configuration at azimuthal angles (a) 30°, (b) 60°, (c) 90° and (d) 120°.

4.3.5 NACA0018 - Summary

The 3D numerical studies were conducted to analyse and characterize the turbine support-arm effects using metrics such as the performance coefficients as well as lift

and drag coefficients. Visualization of the fluid flow with respect to the velocity flow physics and pressure contour plots were performed to further understand the effects of the support-arms on the overall flow field of the turbine. To summarize, the following conclusions were drawn:

- The addition of turbine support-arms saw a significant under prediction of performance coefficients when the result was compared against the baseline turbine.
- The 55.5% drop in performance was attributed to the increased drag due to the presence of the support structure. The added component would also change the fluid flow around the turbine and resulted in a reduced performance prediction.
- On the support-arms, the lift and drag analysis shows positive lift was significant only when the blade starts to exit the windward region and enters the upwind region between 0° to 140° .
- The drag coefficient on a single support-arm and the set of arms is the most significant when the blade progresses from 280° to about 80° . This observation occurs during the transitional phase of the turbine from the windward region into the upwind region.
- The velocity flow showed there are significantly more regions of high velocity within the full turbine configuration compared to the baseline turbine where velocity flow was seen to be more streamlined.
- Significant vortices were also seen generated by the flow as it passes through the turbine rotor shaft which produces wake interference that affects the second blade.
- The pressure contour plots showed similar contours between both turbines, but the added support-arms introduced higher intensity for both positive and negative pressure around the turbine blades as well as the support-arms themselves.

4.4 Performance Analysis and Characterization of The Three Bladed NACA0021 With Dual support-arms

The following study is on the three bladed turbine with NACA0021 blades. Each turbine blade was supported by dual circular support-arms.

4.4.1 Effect of support-arms on turbine performance coefficients

Fig 4.11(a) shows power coefficient, C_p , comparison between the baseline turbine and the full turbine configuration. It is observed that the full turbine has a much lower curve and overall predicted average value compared to the baseline. The same is observed in Fig 4.11(b) with respect to the moment coefficient. The reduced power coefficient curve found here is consistent with a study reported by Siddiqui et. al. (Siddiqui, Durrani, and Imran 2013), whereby the authors also showed a significant reduction in terms of power coefficient curves between the 3D case (only turbine blades considered) and a full 3D turbine configuration with support-arms and central hub. The performance coefficient prediction of the baseline is much higher than the full turbine prediction and this difference was seen to increase as the TSR increases. This indicates that the effect of drag increases as TSR increases. The performance difference between the baseline and full turbine configuration is 37.6% at TSR2.5. This observation is consistent with other findings whereby the addition of the support-arms in numerical predictions results in a significant performance coefficient loss (Castelli et al. 2010, Siddiqui, Durrani, and Imran 2013). The difference can be attributed to the presence of the support structures which introduced additional 3D effects such as drag into the numerical calculations. For further analysis, TSR 2.5 will be considered in the following effects on lift and drag section. Table 4.2 summarizes the performance coefficients between the baseline turbine and the full turbine configuration at TSR 2.5.

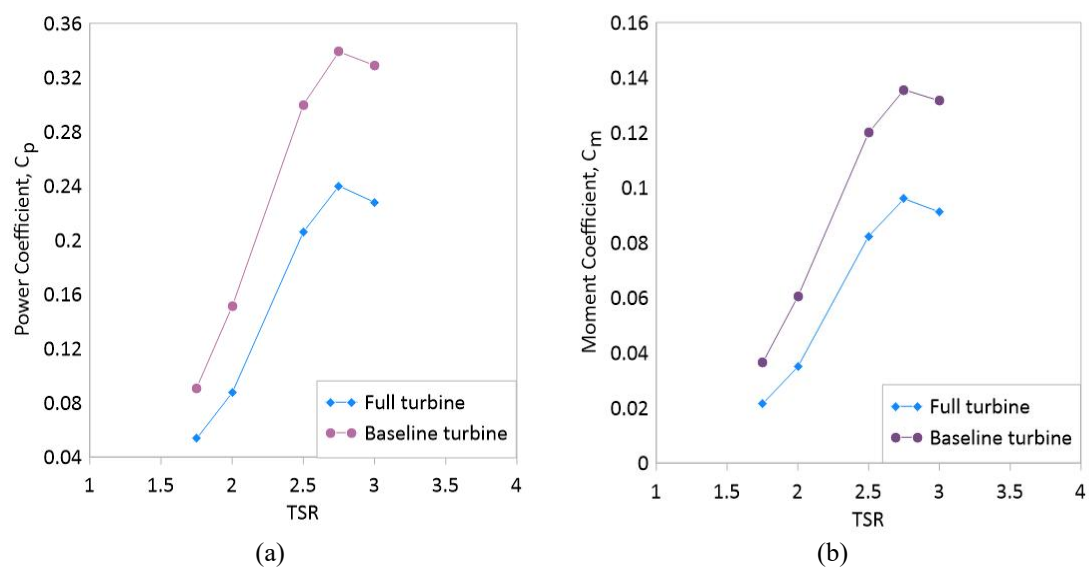


Fig 4.11. (a) power coefficient and (b) moment coefficient comparisons of the baseline turbine.

Table 4.2. Summary of output parameters at TSR 2.5

Output	Unit	Baseline Turbine	Full Turbine
Average power coefficient, C_p	-	0.30	0.21
Average moment coefficient, C_m	-	0.12	0.08
Average power	W	50.23	35.16
Average torque	Nm	0.57	0.40

4.4.2 Analysis of the Lift and Drag Contribution During Turbine Operation

Fig 4.12 illustrates the lift and drag coefficient of the wind turbine circular support-arms in multiple configurations at TSR 2.5. The single arm in this instance refers to a single support-arm of the six support-arms. The dual arm represents dual support-arm on a single turbine blade. From Fig 4.12(a), both the single arm and dual arm have a peak lift coefficient, C_L value of 2.9 and 5.5 at about 70° azimuthal angle with the average C_L value of 0.05 and 0.11 respectively. The incremental increase in C_L coincides with the blade moving from the windward region into the upwind region. The C_L value of the single and dual support-arms reduces to 0 between 140° to 200° during the leeward region and then experiences negative lift with a peak value of -4.4 and -2.1 at about 285° . Also shown is the average sum for all the support-arm structures which demonstrates the cycle for both blades and their pair of support-arms. The average C_L value of all six arms was found to be 0.27.

Table 4.3. Average lift and drag coefficients of the wind turbine support-arms.

Geometry	Average lift coefficient, C_L	Average drag coefficient, C_D
Single arm	0.05	0.78
Double arms	0.11	1.55
Sum of arms	0.27	4.27

From Fig 4.12(b), as the blade enters the upwind region, the drag coefficient, C_D for both the single arm and dual arms peak at about 10° with a peak C_D value of 3.9 and 7.5 respectively. However, the total drag for all 6 arms peaked slightly ahead at 38° with a value of 5.6. This showed that during this stage of the turbine cycle, the effect of drag predominantly affected the first blade and its support-arms with less

drag acting on the other turbine blade arms with an average C_D of 0.78 for single arm and 1.55 average for both arms on the first blade. The C_D value here for the single arm was consistent with reported values for long cylindrical geometry which was usually between 0.75 – 1.2. The effects of drag than reduced significantly as it passed through the upwind region for both the single and dual arm structures and peaked at -0.6 and -1.3 respectively at 120° . The overall sum of the support-arms reduced to a minimum value of 3.3 at 100° . Thereafter, minimal changes in C_D were observed for the single arm as the first blade moves from 120° to 240° azimuthal angle while the dual arms saw marginal fluctuations. This showed the effects of drag on the support-arms were minimal during the transitional phase as the blade moved and exited the upwind region, passed through the leeward region, and then entered the downwind region. The curve of the total sum of all four support-arms underlined this observation. It was also noted that, generally, the most significant effects of drag were concentrated between the transitional region of 270° and 360° as the blade exited the downwind and entered the windward region. Table 4.3 summarized the average coefficients for both lift and drag for each support-arm structure of interest.

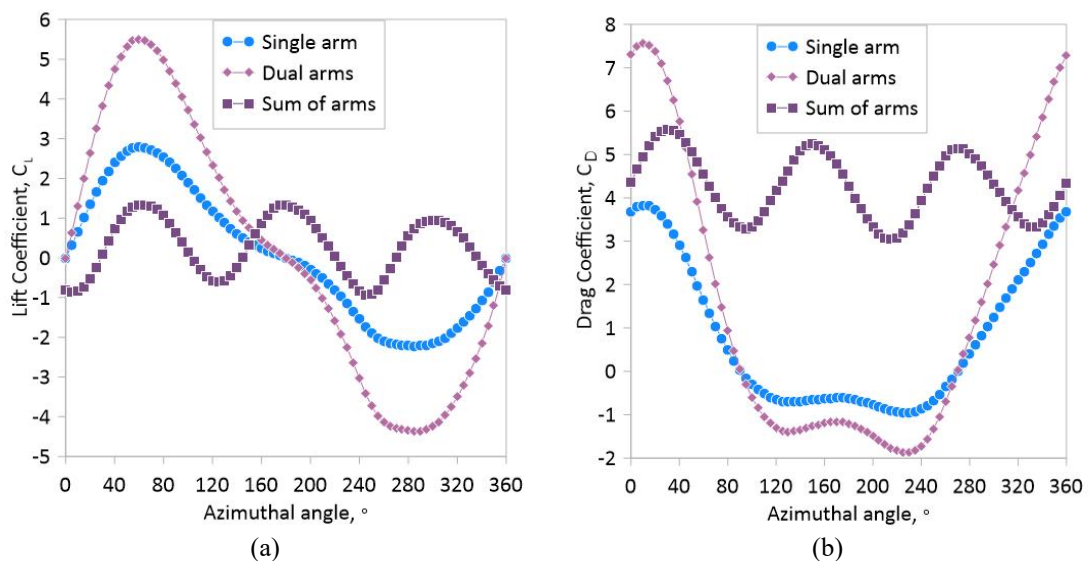


Fig 4.12. Comparisons between different support-arm configurations in terms of (a) lift coefficient and (b) drag coefficient of the VAWT at TSR 2.5

4.4.3 Velocity Flow Physics Comparisons

For the velocity flow physics comparisons section, a plane was created at the middle section of the first support-arm looking down from the XY plane. This

analysis concentrated on the flow velocity at TSR 2.5. Fig 4.13 illustrated the velocity at azimuth angles 30° , 60° , 90° , and 120° of the baseline turbines. From Fig 4.13(a), Fig 4.13(b), and Fig 4.13(c), it was observed that as the turbine moves from one azimuthal angle to the next, high velocity flow started to develop and concentrated at the inner surface of the turbine blade which propagated along the lower surface of the turbine blade. The largest flow vorticity was experienced at 90° shown in Fig 4.13(c). Fig 4.13(d) showed, at azimuthal 120° , the trailing edge experienced large vorticity as it exited the upwind region and entered the leeward region.

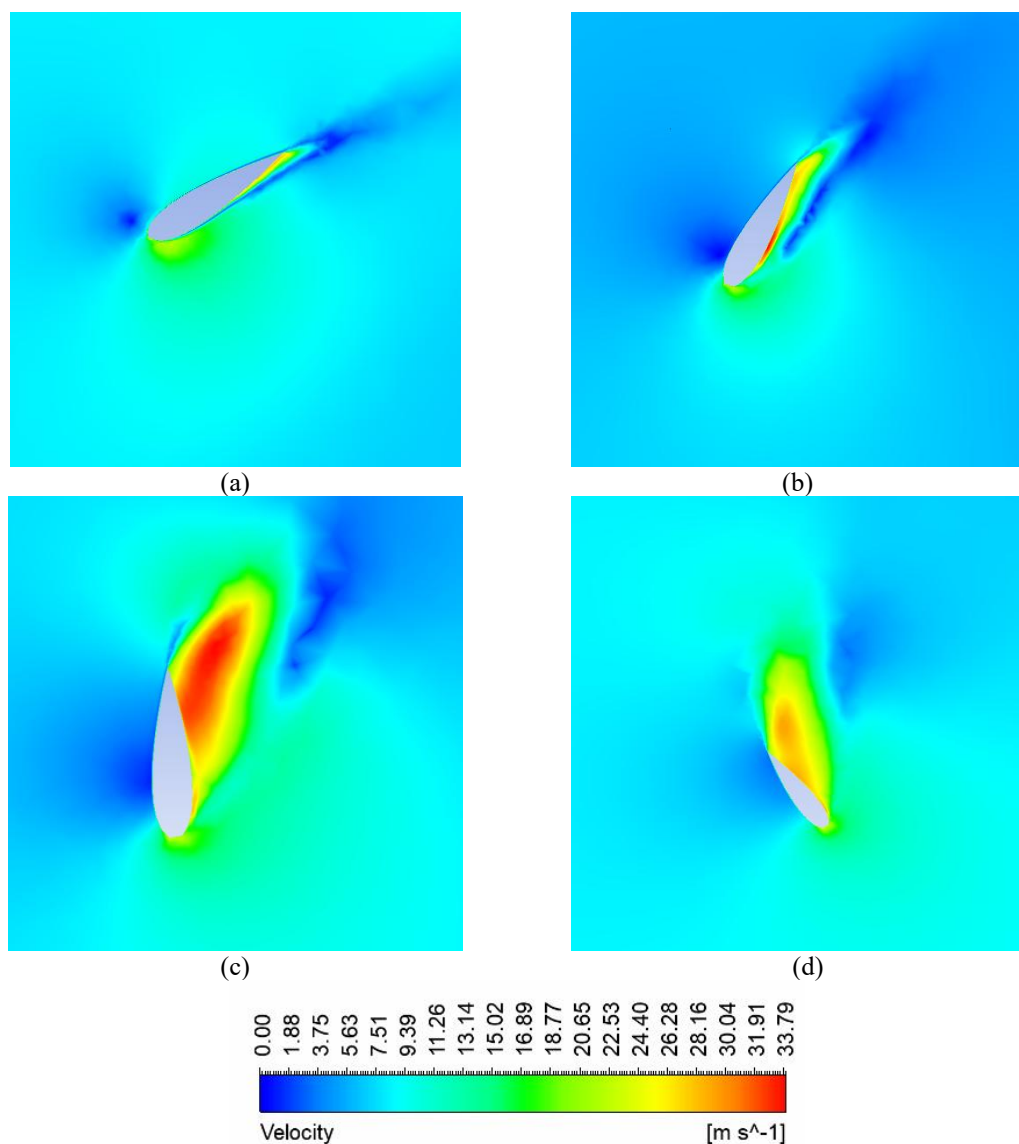
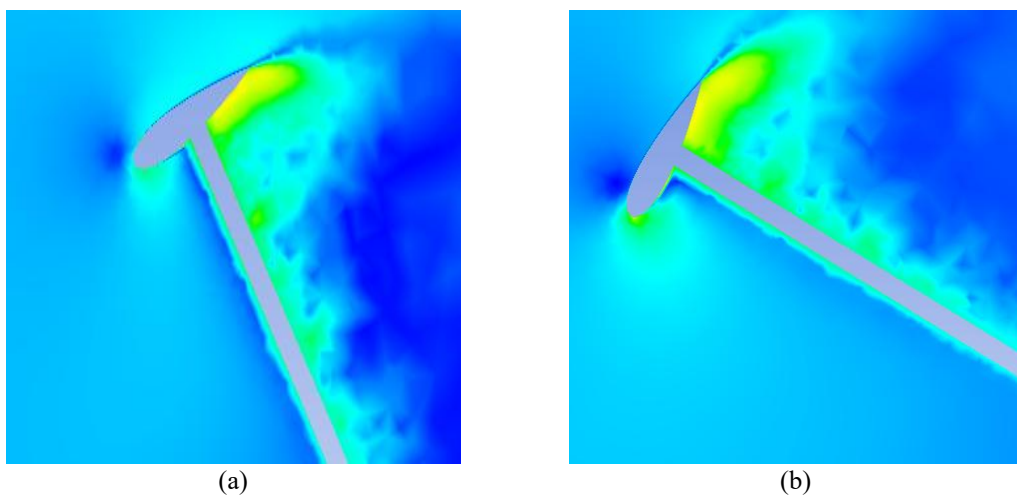


Fig 4.13. Velocity contour of the flow physics for TSR 2.5 of the baseline turbine with no support-arms at azimuthal angles (a) 30° , (b) 60° , (c) 90° and (d) 120° .

Fig 4.14 illustrated the velocity flow physics at different azimuthal angles of the full turbine with circular arm for TSR 2.5. It is observed that, in general, larger regions of high velocity flow existed around each blade and support-arm mostly in the trailing edge section compared to the baseline turbine. From Fig 4.14(a), for the first turbine blade in the upwind region, the velocity contour showed an even distribution of high velocity along the support-arm. As the turbine arm passed through, however, it generated a high concentration of low velocity at its wake as it passed into the upwind region. Fig 4.14(a) indicated large flow velocity at the trailing edge of the blade. When the turbine blade rotates along from 60° and 90° , it is observed that the concentration of high velocity moved along the support-arm towards the turbine blade. This can be observed in Fig 4.14(b) and Fig 4.14(c). In Fig 4.14(c), high velocity concentrates over a much larger region at the trailing edge compared to the baseline in Fig 4.13(c). Turbulence in the downstream region was also shown to be much more pronounced. The wake generated by the turbine blades and support-arms were much larger and more irregular compared to the blades in the baseline turbine. In Fig 4.14(d), notable areas of low flow velocity on the lower surface nearer to the leading edge can also be observed which is not seen in the baseline turbine. This extended towards the support-arm as it entered the upwind region. High velocity regions mostly concentrated around the area connecting the blade to the support-arms and tapered down towards the turbine rotor. This indicated that the maximum drag effect was concentrated in this region in particular.



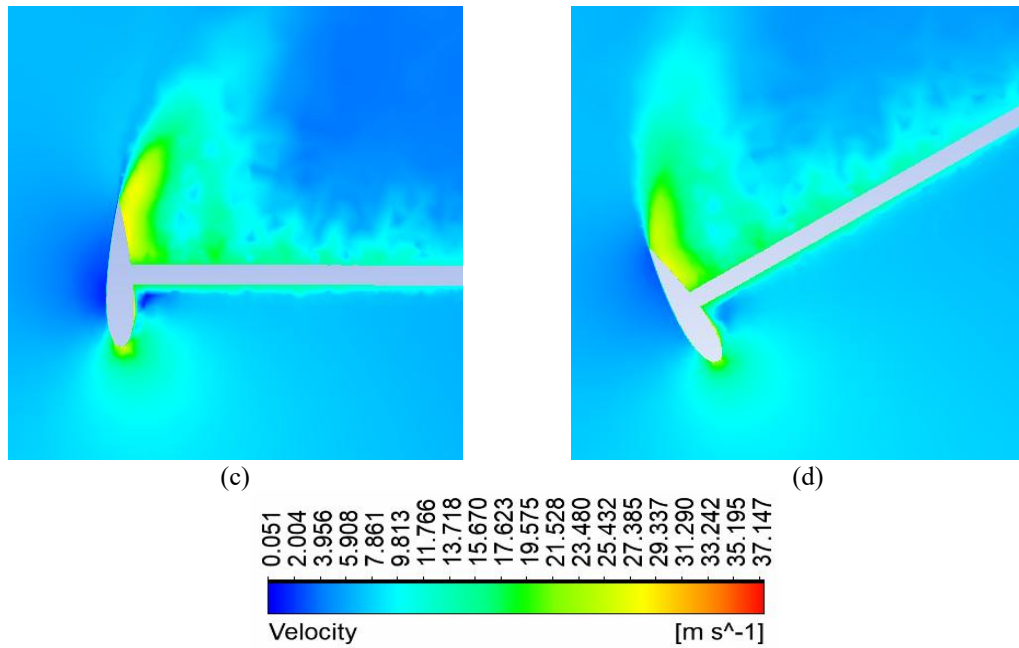
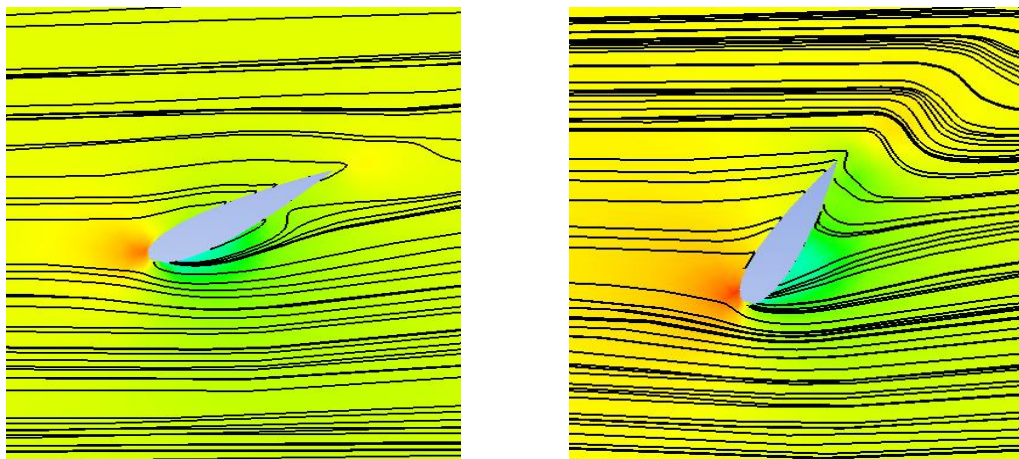


Fig 4.14. Velocity contour of the flow physics for TSR 2.5 of the full turbine with no support-arms at azimuthal angles (a) 30°, (b) 60°, (c) 90° and (d) 120°.

4.4.4 Pressure contour and streamlines analysis

Similar to the velocity contour, the same plane was used as reference for the pressure contour. Fig 4.15 illustrated the velocity at azimuth angles 30°, 60°, 90°, and 120° of the baseline turbines with no support-arms. It is observed that, from the streamlines in Fig 4.15(a), Fig 4.15(b), and Fig 4.15(c), as the turbine rotated from 30° to 90° azimuth angle, high pressure concentrated more on the top side of the turbine blade at the leading edge with the lower surface of the turbine blade experiencing much higher negative pressure. Streamlines in Fig 4.15(d) showed flow concentrated more on the inner surface of the blade.



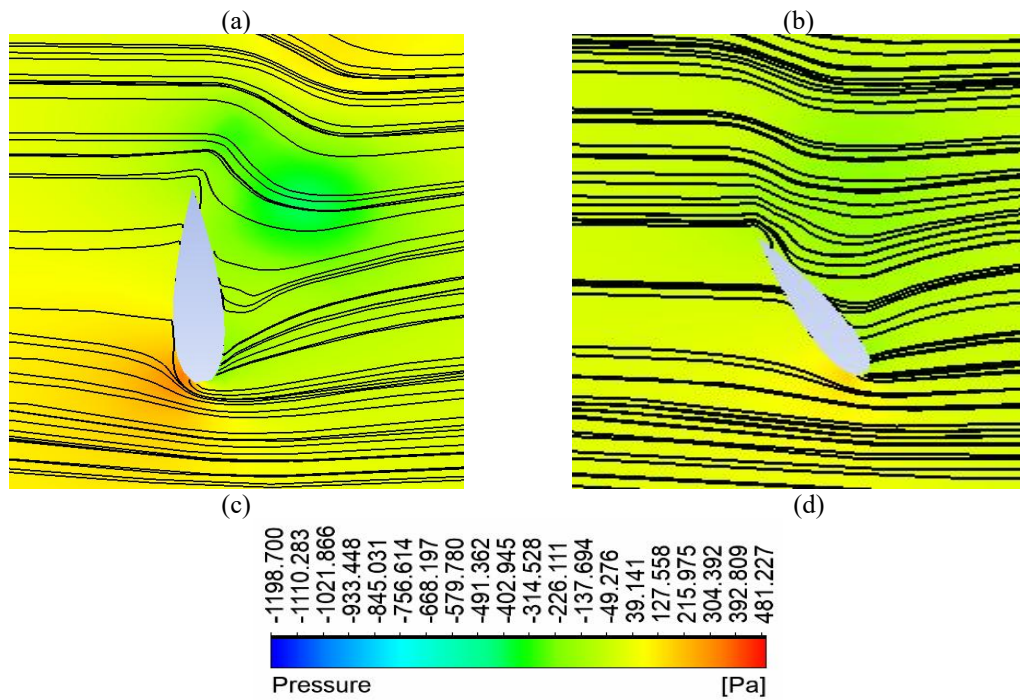


Fig 4.15. Pressure contour of the flow physics with streamlines for the TSR 2.5 of the baseline turbine at azimuthal angles (a) 30°, (b) 60°, (c) 90° and (d) 120°.

For the full turbine configuration, the general trend mirrors previously discussed above in the velocity contour. In Fig 4.16(a), higher negative pressure concentrated at the bottom surface of the turbine blade but also along the span of the support-arms. The streamline also showed a circular movement of flow indicating vortex forming caused by the support-arm. Higher positive pressure concentrated on the leading edge at the outer surface of the turbine blade. From azimuthal angles 60° to 90° in Fig 4.16(b) and Fig 4.16(c), the pressure values increased, and the streamline flow starts to concentrate at the front of the turbine blade and arms. This was the point of maximum lift achieved by the support-arms. As it passed through and started to exit the upwind region, from Fig 4.16(d) at azimuthal angle 120°, the streamlines showed maximum concentration at the front of the turbine blade with lower pressure concentration acting on both turbine blade and support-arm structure. Minimum drag coefficient was observed from this point onwards which was within the leeward region.

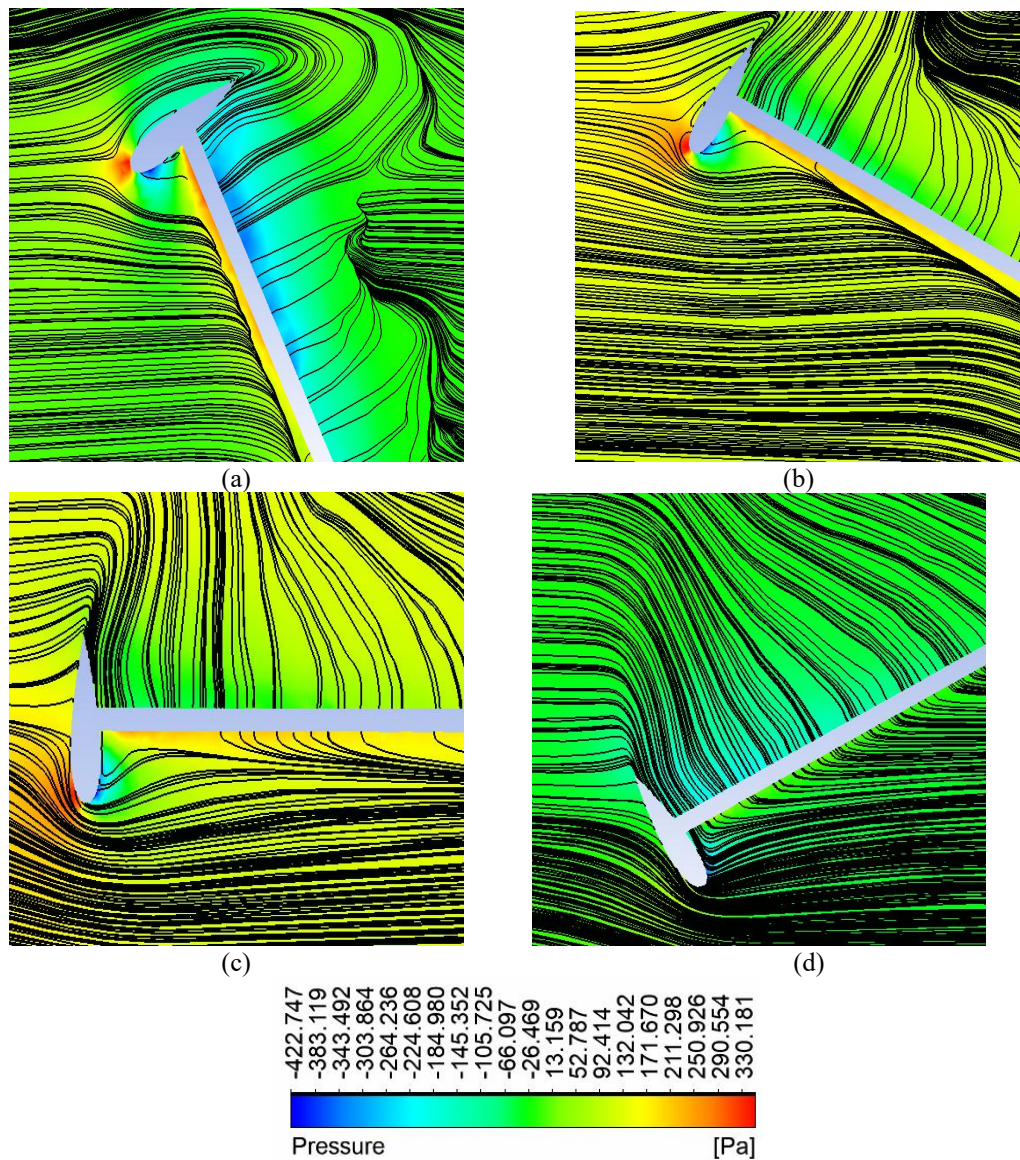


Fig 4.16. Pressure contour of the flow physics with streamlines for the TSR 2.5 of the full turbine configuration at azimuthal angles (a) 30°, (b) 60°, (c) 90° and (d) 120°.

4.4.5 NACA0021 - Summary

In conclusion, the wind turbine support-arm has a significant effect on the performance prediction of the VAWT. To summarize the findings in this study, the following are conclusions that can be drawn:

- Comparisons of the full turbine configuration against the baseline turbine with only turbine blades indicates that taking the turbine support-arm in numerical simulation and predictions results in a power coefficient loss by 37.6% at TSR 2.5.

- The additional consideration of double support-arms in numerical simulation introduces significant drag effects and, therefore, has a negative consequence on the power coefficient.
- In terms of lift acting on the support-arms, it was found that positive lift was obtained within the upwind region whereas negative lift predominately occurs within the downwind region.
- In the drag coefficient analysis, the effects of drag were most prominent between the azimuthal angles of 0° - 120° and 240° - 360° which is the transitional phase as the blade moves from the downwind to the windward region.
- When comparing velocity contours, the flow physics of the full turbine configuration showed significantly more regions of high velocity which suggest more turbulence during operation.
- The effects of the support-arms on the flow around the turbine are quite pronounced as wake generated are much larger which affects the next blade passing through.
- Lastly, a critical location where high wind flow on the trailing edge of the blade nearer to the blade and support-arm connection suggest that this is a possible location which experiences the most significant amount of drag.

Hence, a baseline understanding of the H-VAWT has been established. A significant portion of the lift and therefore torque generation was on the turbine blades. However, the support-arm geometry also has a quantifiable effect on the turbine performance. The support-arm is an aerodynamic feature of the turbine that warrants improvements to its aerodynamic characteristics to enhance the turbines performance. Hence, in the next chapter, an optimization scheme of a symmetrical NACA0018 blade utilizing the adjoint solver was developed, tested, and verified to generate a novel and original shape with enhance aerodynamic performance to maximise the power production of the turbine. This new shape can be applied to both the turbine blade and support-arm. The following sections explored the effect of turbine parameters on the optimization scheme and discussions on the resulting candidate blades in 2D and 3D numerical simulations.

4.5 A Novel Aerodynamic Shape Optimization Scheme on a NACA0018 VAWT for Improved Turbine Performance Using the Adjoint Method

In this study, aerodynamic shape optimization of a NACA0018 blade was conducted using the adjoint method, together with the gradient-based optimizer available in FLUENT, at low operating TSR in pseudo-steady state conditions. Since the turbine blade of a straight bladed VAWT is uniform throughout its span length, the optimization was conducted in 2D to reduce mesh and geometric complexity and therefore result in a smoother mesh morphing operation. The effect of tip speed ratio and effect of flow conditions on the optimization scheme was studied. The objective function was set to maximize blade moment. The optimization was then conducted with constant blade thickness and free form morphing with no constraints placed on the mesh morpher. The results produced several different airfoil geometries which were later analysed. The candidate blade optimized at TSR 2 produced the largest increase in single blade moment by 30.48% which also yielded the highest power coefficient when compared in a full turbine configuration against the NACA0018 turbine. The selected candidate blade showed the largest overall performance increase of 28.77%. This study provides an optimization framework for the use of the adjoint method for blade optimization of the VAWT.

4.5.1 Moment Optimization at TSR 1

4.5.1.1 TSR 1 single blade analysis

Single blade optimization using the adjoint solver and gradient-based optimizer on the NACA0018 was conducted. The angles selected were between 0° and 120° , all within the windward and upwind region as these are the locations known to have the most significant moment during rotation. When comparing the results of the blade moment optimization, the highest average single blade moment was found to be the candidate blade optimized at 90° with an improvement of 7.79%. The second highest moment coefficient increase was 20° with a 5.45% increase. Optimization conducted at 0° , 50° , 100° , 110° and 120° showed a reduction in performance over the baseline NACA0018 whereas the remaining azimuthal angles showed minimal improvements of around 2%. Table 4.4 summarizes the results of the optimization at TSR 1.

Table 4.4. Summary of the torque optimization at TSR 1 at various incremental azimuth angle.

Azimuthal angle	Average moment, C_m	Difference, %
10	0.0682	2.50
20	0.0669	5.45
30	0.0685	0.61
40	0.0663	2.88
50	0.0663	-0.34
60	0.0675	1.48
70	0.0681	2.35
80	0.0681	2.35
90	0.0719	7.79
100	0.0556	-17.94
110	0.0333	-66.52
120	0.0646	-2.97

Fig 4.17 shows the moment coefficient comparison of two best case candidate blades optimized at azimuthal angles 90° and 20° against the NACA0018 blade. The candidate blades were labeled 90D – TSR 1 and 20D – TSR 1 respectively. Both candidate blades showed very similar curve characteristics over a single rotation with several differences noted at various points. The moment coefficient curves for both candidate blades showed slightly higher values than the NACA0018 during the upwind phase between the azimuthal angles of 60° to about 120° , particularly most obvious at the peak of the curve at about 65° . As the blade moves through the downwind region, however, it was observed that, again, the candidate blades extracted better moment coefficient compared to the NACA0018 blade. This shows both candidate blades have improved moment efficiency over the NACA0018 blade with the 90D – TSR 1 being marginally better than the 20D – TSR 1 over the whole single blade rotation.

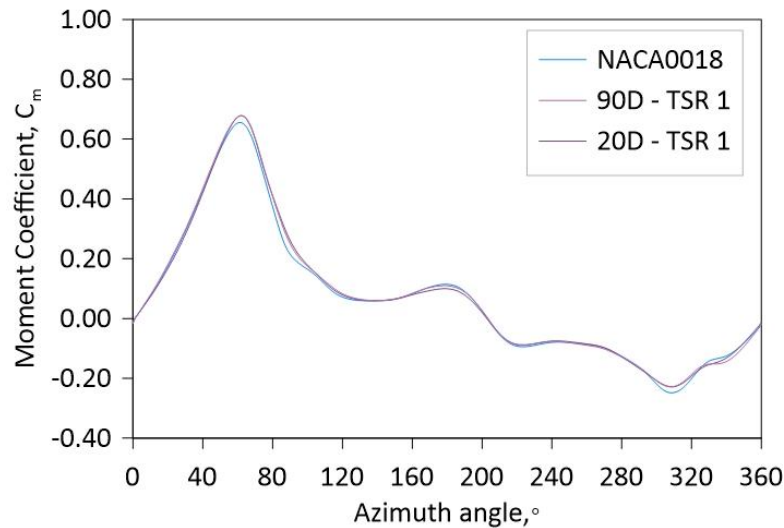


Fig 4.17. Single blade moment coefficient comparison between candidate blades optimized at the selected angles with respect to moment and NACA0018 at TSR 1.

4.5.1.2 Full turbine performance analysis and comparison

Building upon the results from the single blade optimization, the geometries of the 90D – TSR 1 and 20D – TSR 1 blades were extracted and redesigned into a dual bladed turbine. Each candidate turbine was then compared against the baseline NACA0018. From Fig 4.18, the 90D – TSR 1 turbine showed a similar curve to the NACA0018 turbine but at slightly higher power coefficient at the lower TSR ranges before experiencing a significant decrease in power coefficient starting from TSR 1.5 onwards. This indicated that the candidate 90D – TSR 1 blade was optimized for lower TSR but not at higher TSR. The candidate blade 20D – TSR 1, however, showed much better power coefficient curve than both the 90D – TSR 1 and the NACA0018 turbines at almost all instances of TSR with a significant performance uplift at TSR 0.5 of about 32.57% and maximum power coefficient at TSR 1.75 also increased by 1.72%. The overall average power coefficient improvement by the 20D – TSR 1 over the NACA0018 was 6.8%. Therefore, the 20D – TSR 1 was picked as the chosen blade for the TSR 1 optimization.

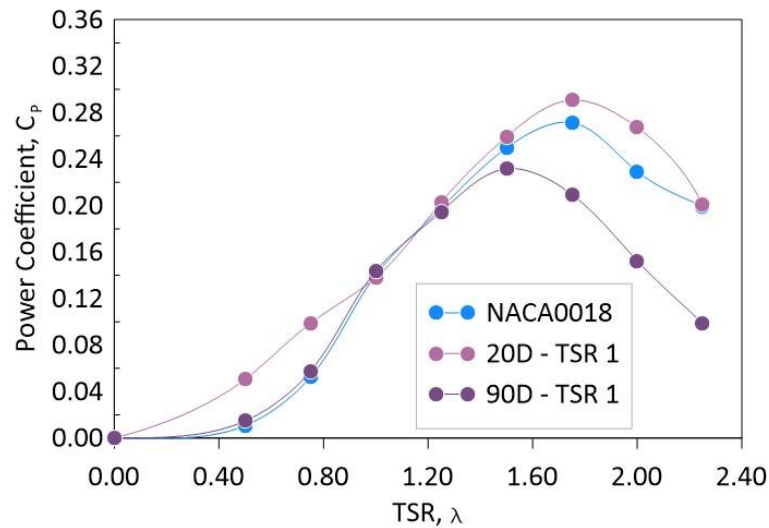


Fig 4.18. Power coefficient comparison between VAWT turbines of candidate blades 20D – TSR 1 and 90D – TSR 1 against the baseline NACA0018.

4.5.1.3 20D – TSR 1 blade profile

Fig 4.19 shows a geometric comparison of the selected 20D – TSR 1 airfoil and the NACA0018 airfoil. As expected, the mesh morphing process produced a cambered design based on improving the blade moment force at each iteration by 5%. The 20D – TSR 1 has a slight indent at around $0.2c$ from the leading edge. The trailing edge scopes slightly outwards at $0.7c$ and then inwards at $0.92c$. The mesh morpher was able to maintain the blade thickness of the 20D – TSR 1 to a similar degree to the NACA0018 blade.

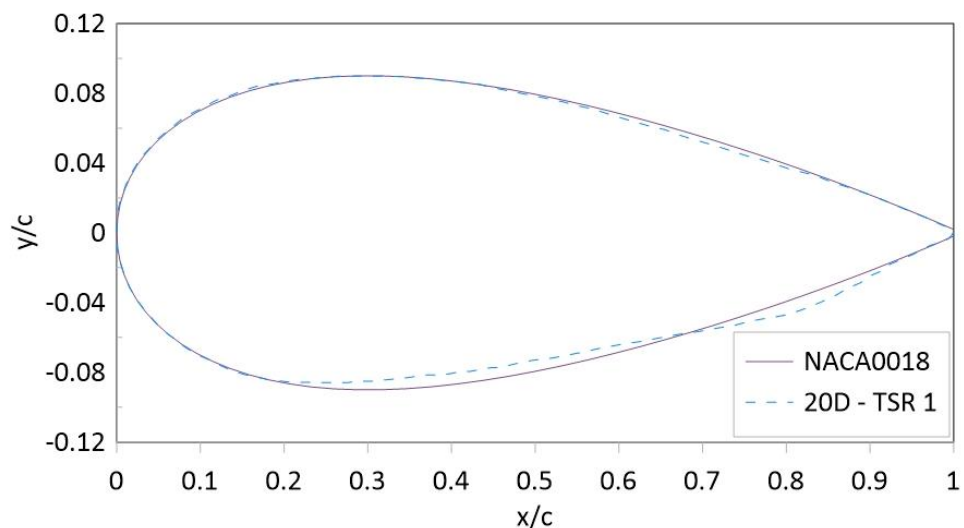
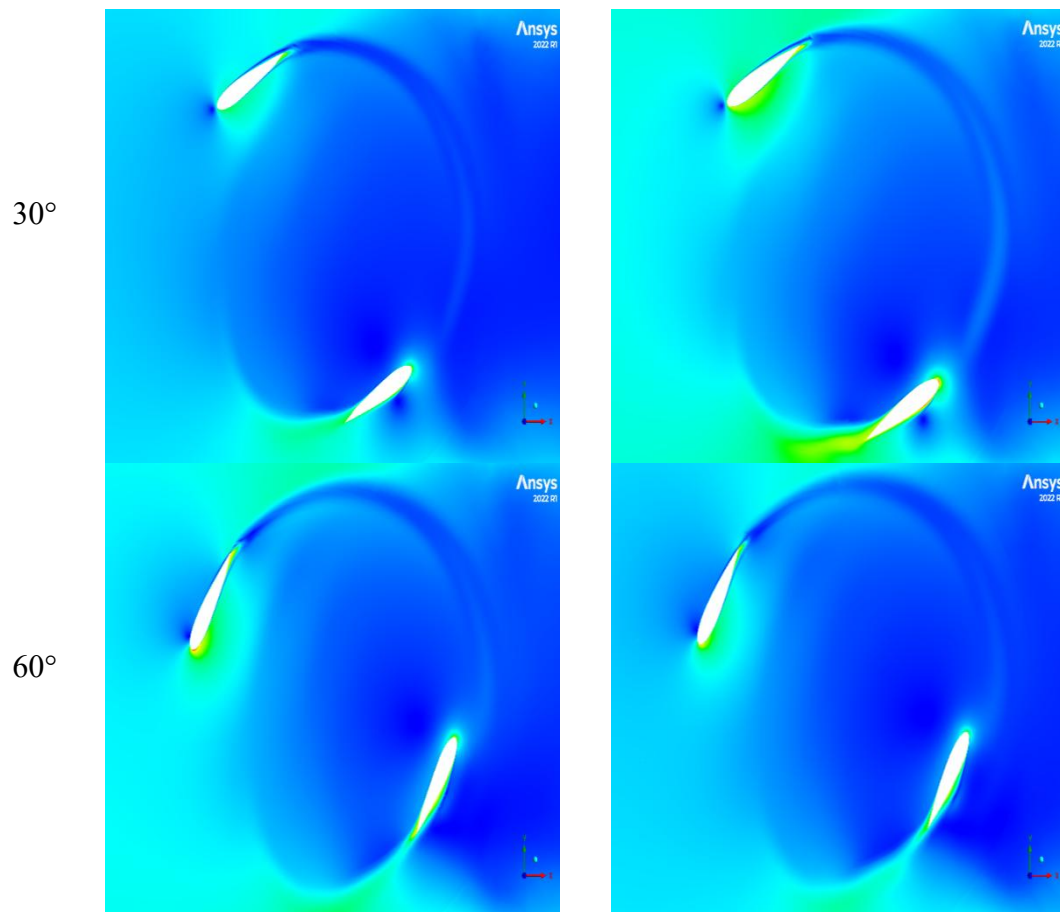


Fig 4.19. Geometric comparison between the selected candidate blade 20D – TSR 1 and NACA0018.

4.5.1.4 Velocity flow contour

Fig 4.20 shows the velocity flow comparison between the 20D – TSR 1 and NACA0018 turbine. At 30° , the flow velocity showed a larger velocity contour around both blades of the NACA0018 compared to the 20D – TSR 1. The 20D – TSR 1 experienced more streamline flow by contrast. The leading edge of the 20D – TSR 1 shows concentrated higher velocity at 60° compared to the NACA0018 turbine. The velocity flow contour showed minimal difference thereafter. In all other instances except for 30° , the second blades during the downwind phase of the rotation for both 20D – TSR 1 and NACA0018 show similar flow profile. This is consistent with the findings from Fig 4.18 where the single blade moment coefficient curves of the 20D – TSR 1 were similar to the NACA0018 blade.



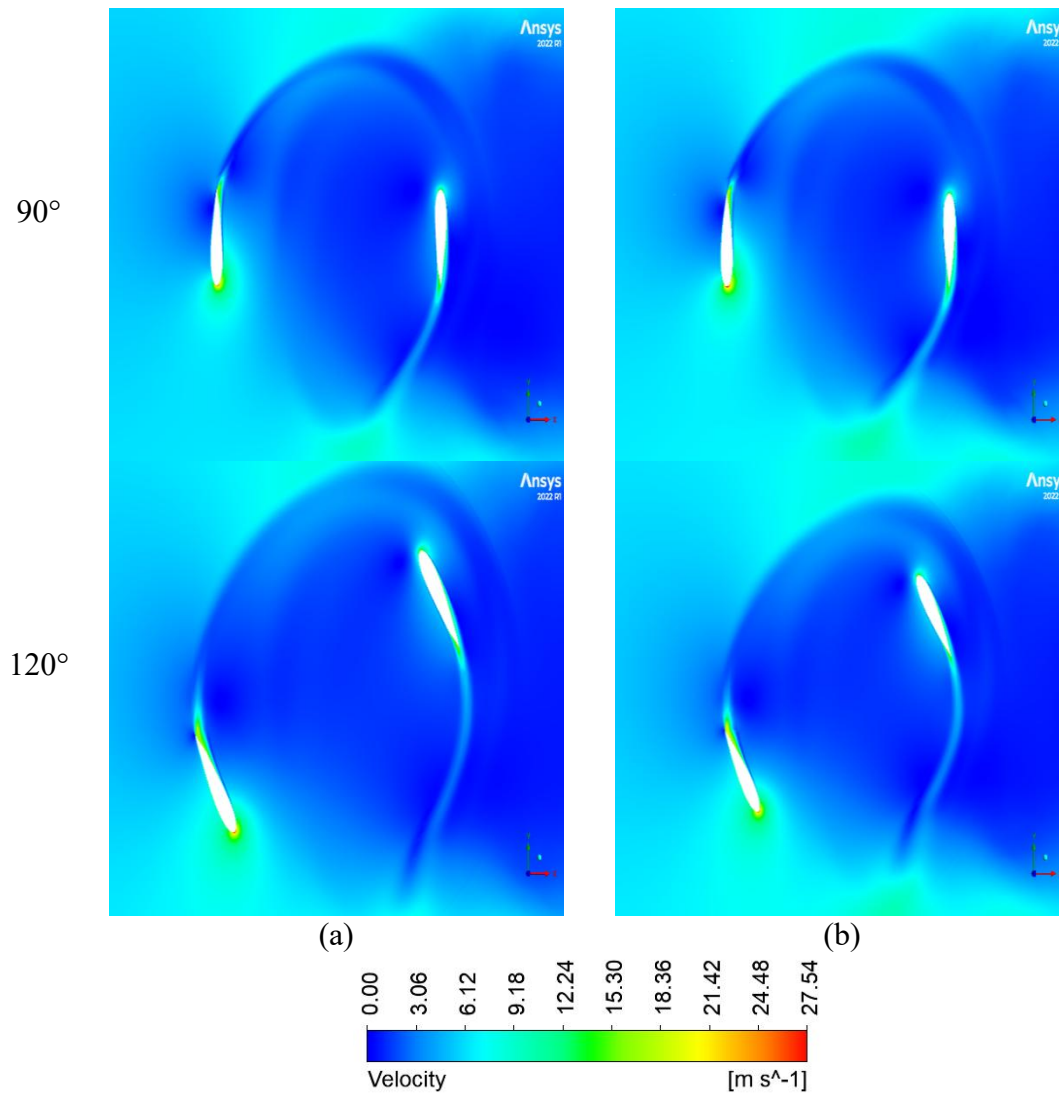
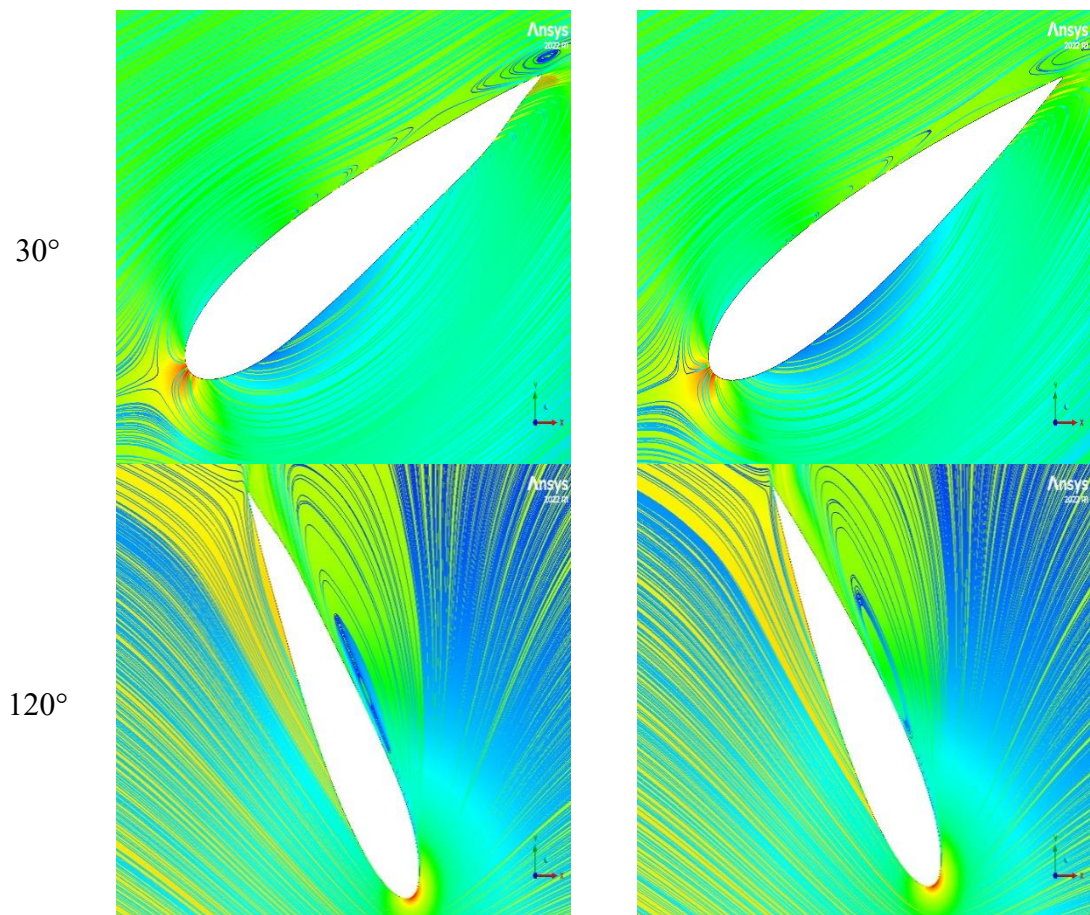


Fig 4.20. Velocity flow contour comparison in full turbine configuration between the (a) candidate torque optimized blade at 20° and the (b) NACA0018 blade at TSR 2.

4.5.1.5 Streamline and pressure contour

Fig 4.21 shows the streamline imposed on the pressure contour comparison between the 20D – TSR 1 and NACA0018 turbine taken at TSR 2. Previous performance analysis showed several locations of interest with differences in power coefficient performance. Hence, to highlight these observations, snapshots of the airfoil were taken at various azimuth angles as the turbine enters and exits different phases during the turbine rotation. At 30° , the pressure side is stronger on the NACA0018 at the leading-edge lower surface. The 20D – TSR 1 however has a stronger vortex forming at the trailing edge of the blade. This may be due to the 20D – TSR 1 having a more cambered profile leading towards the trailing edge which gives a stronger rotational momentum towards the blade's back flow as it entered the upwind region. At 120° ,

the streamline shows a denser pressure side on the 20D – TSR 1 compared to the NACA0018 blade. Both the second blades of the NACA0018 and 20D – TSR 1 show similar pressure contours at 210° with the former showing thicker streamlines at the outer surface which indicates the blade experiencing stronger pressure on the outer surface. The streamline in the 20D – TSR 1, however, is slightly denser on the pressure side compared to the NACA0018 blade while the NACA0018 blade shows stronger rotational vortex on the suction side the blade as they enter the downwind region. The corresponding second blade at 300° shows similar pressure contour and streamline shape as the blades pass the downwind region and enter the upwind phase of the turbine rotation which indicates similar behaviour between both blades.



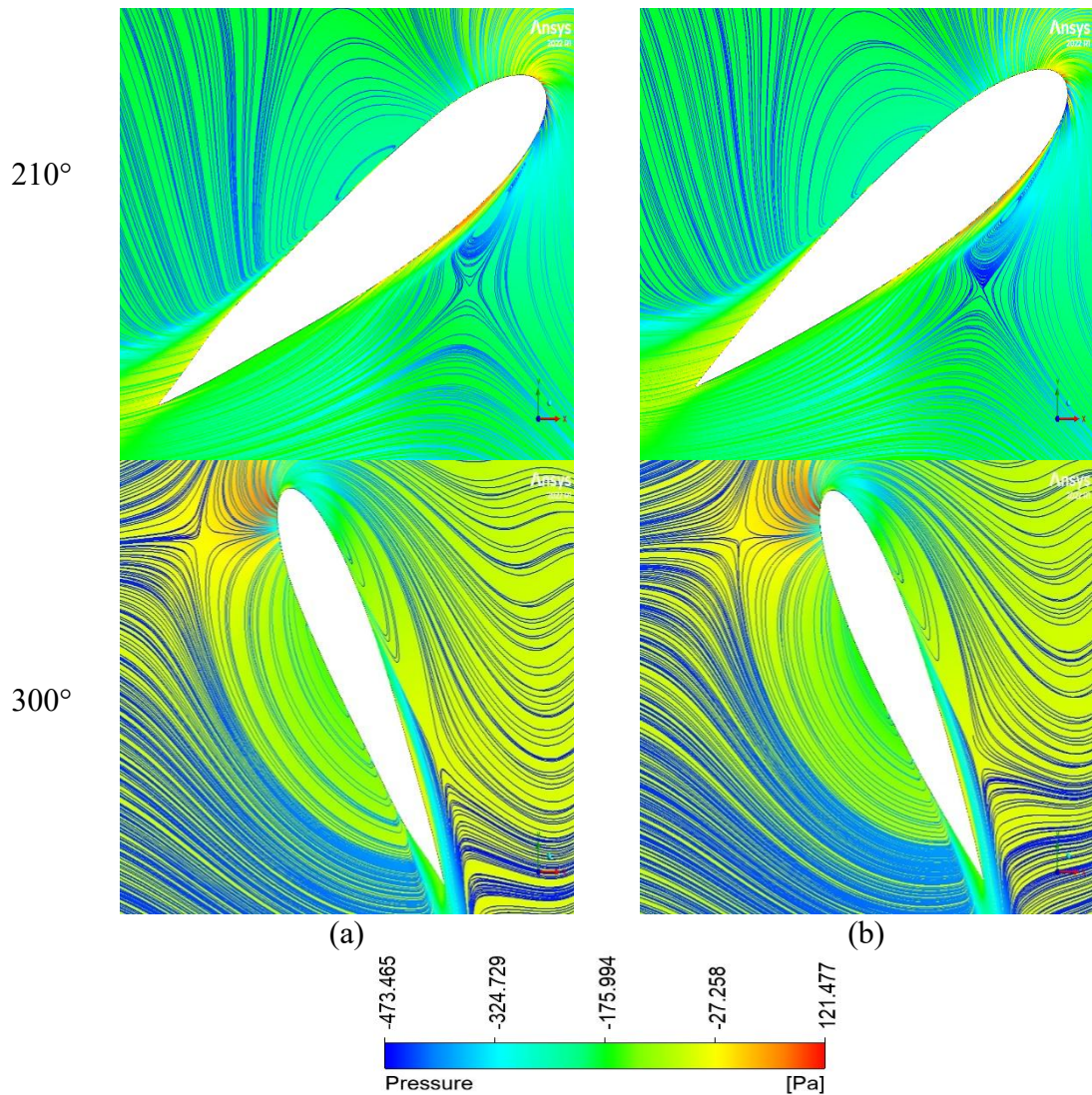


Fig 4.21. Streamline flow contour comparison between the (a) candidate torque optimized blade at 20° and the (b) NACA0018 blade at TSR 2. Streamline contour imposed onto the pressure contour.

4.5.2 Moment Optimization at TSR 2

4.5.2.1 TSR 2 single blade analysis

In this section, optimization of the single blade NACA0018 was conducted at a higher TSR 2. Similar conditions to the optimization at TSR 1 were imposed here with the operating TSR the only difference. Table 4.5 summarizes the optimization results. Compared to optimization at TSR 1, there was, generally, a higher average increase with respect to single blade moment. Several cases were noted. Between 40° to 60° , at 80° and 120° , the optimization difference compared to the baseline NACA0018 turbine saw double digit increases in percentage. These results were all achieved within the upwind phase of the turbine rotation. The two highest percentage increases were found at 60° and 120° with 20.28% and 30.48% increase over the

baseline respectively. Therefore, similar to the previous optimization at TSR 1, the best two results were selected for further analysis.

Table 4.5 Summary of the moment optimization at TSR 2 at various incremental azimuth angle.

Azimuth angle, °	Average torque, Cm	Difference, %
10	0.119	0.684
20	0.118	-0.10
30	0.129	9.00
40	0.142	18.30
50	0.135	13.57
60	0.145	20.28
70	0.122	2.72
80	0.137	14.97
90	0.105	-12.07
100	0.115	-2.63
110	0.115	-3.08
120	0.161	30.48

Fig 4.22 shows the single blade comparison of NACA0018 against candidate turbine blades optimized at 60° and 120°. It was observed that the candidate blade optimized at 60°, designated as 60D – TSR 2, has a higher moment during the first quarter of the turbine rotation, peaking at about 92° azimuthal angle. The maximum moment of the second candidate blade optimized at 120°, designated as 120D – TSR 2, however was found to be the lowest of the 3 tested blades. It was also observed that the maximum coefficient of both candidate blades was shifted forward slightly to 92° azimuth angle as opposed to the NACA0018 blade which peaked at 90°. Later in the rotation, within the leeward region, both the 60D – TSR 2 and 120D – TSR 2 showed higher torque values between 130° up to 200°. From that point onwards, the 60D – TSR 2 showed similar curve characteristics with the NACA0018 baseline with slight difference at 320° when the blade entered the windward region. A significant difference between the NACA0018 and 60D – TSR 2 blades against the 120D – TSR 2 blade can be observed between 240° and 360° azimuth angle, which encompasses the downwind region into the windward region. The 120D – TSR 2 experienced much higher moment coefficient values as well as a consistent positive moment

during this phase before dipping into the negative region at about 310° azimuth angle. This is in stark contrast to the NACA0018 and 60D – TSR 2 with both dipping into negative moment values from 160° azimuthal angle and dropped even lower during this cycle of the turbine rotation. This indicated that the 120D – TSR 2 blade was more optimal during the downwind cycle of the rotation compared to the other two blades. Unlike the results at TSR 1, these observations indicated a more dramatic improvement in performance which also showed a significant shift in the blade characteristics when the optimization was conducted at a higher TSR.

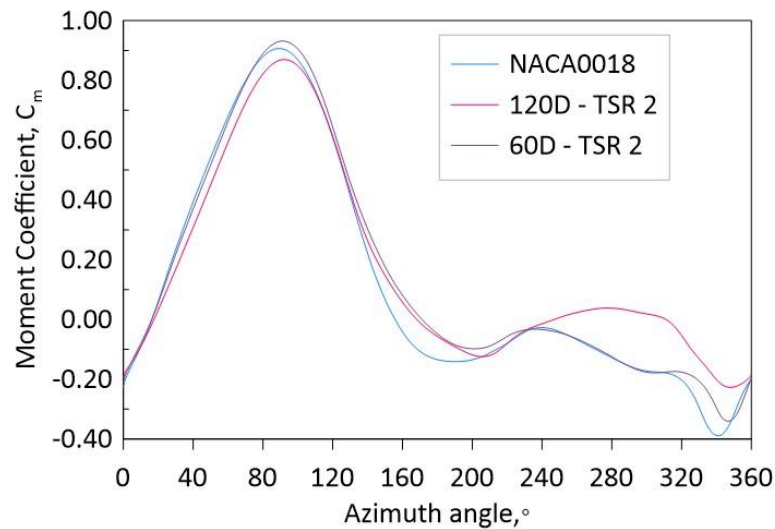


Fig 4.22. Single blade moment coefficient comparison of the selected candidate blades with respect.

4.5.2.2 TSR 2 full turbine performance analysis and comparison

The candidate blades, 60D – TSR 2 and 120D – TSR 2, were compared against the baseline NACA0018 blade in a two-bladed turbine. Fig 4.23 shows the power coefficient comparison between the candidate turbines and the baseline NACA0018 turbine. At a glance, it was observed that the 120D – TSR 2 turbine produced higher efficiency among the compared blades. The maximum power coefficient peaked at TSR 1.5 at C_p 0.34 whereas the NACA0018 turbine peaked at TSR 1.75 with a C_p value of 0.27. This is an increase of 21.39% in maximum power coefficient for the 120D – TSR 2 blade over the NACA0018 blade. The overall power coefficient increase was found to be 28.77% over the range of tested TSR. In the second test case of the 60D – TSR 2, the overall curve shows a similar trend to the baseline NACA0018. At higher TSR, the 60D – TSR 2 extracted higher power coefficient than the NACA0018. The best overall performance, however, was the 120D – TSR 2

candidate blade which had a significant improvement over a range of TSR as well as having the highest percentage increase in maximum power coefficient.

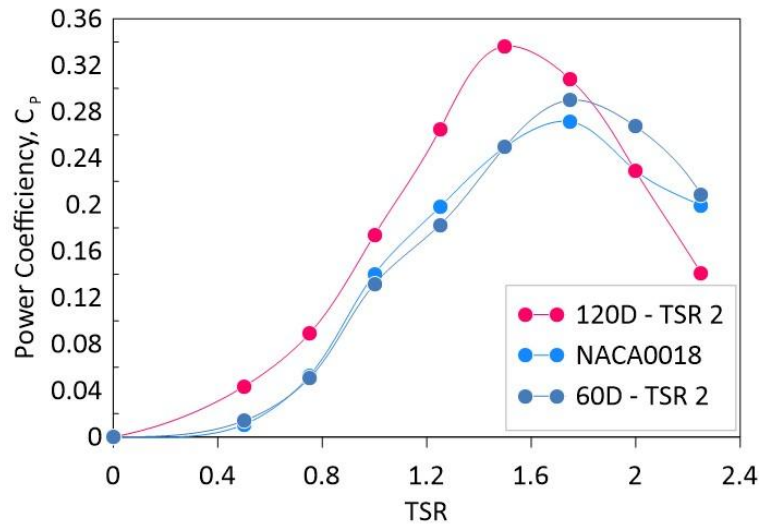


Fig 4.23. Power coefficient comparison between candidate blades optimized at the selected angles with respect to torque and NACA0018.

4.5.2.3 120D - TSR 2 blade profile

Fig 4.24 shows the geometric comparison of the selected 120D – TSR 2 profile against the baseline NACA0018 airfoil. Unlike the previous 20D – TSR 1, the 120D – TSR 2 saw an increase in turbine thickness of about 7.14% which was measured at each blades' thickest point. The mesh morphing produced a geometry which scoped upwards when compared to the NACA0018 profile. The leading edge has a similar curve to the NACA0018 airfoil but a noticeable bump on the upper portion of the blade was noted at about 0.23c. A camber was also observed from 0.11c which extended up to 0.75c.

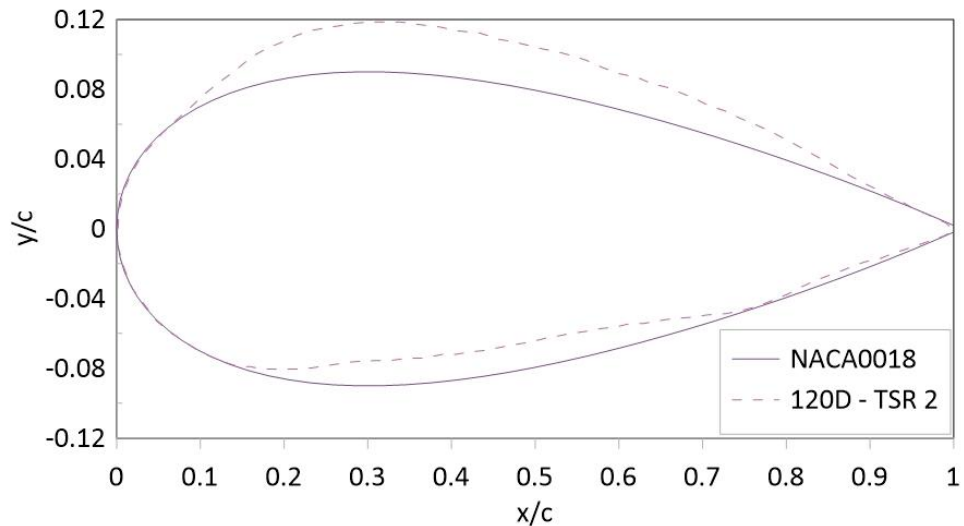


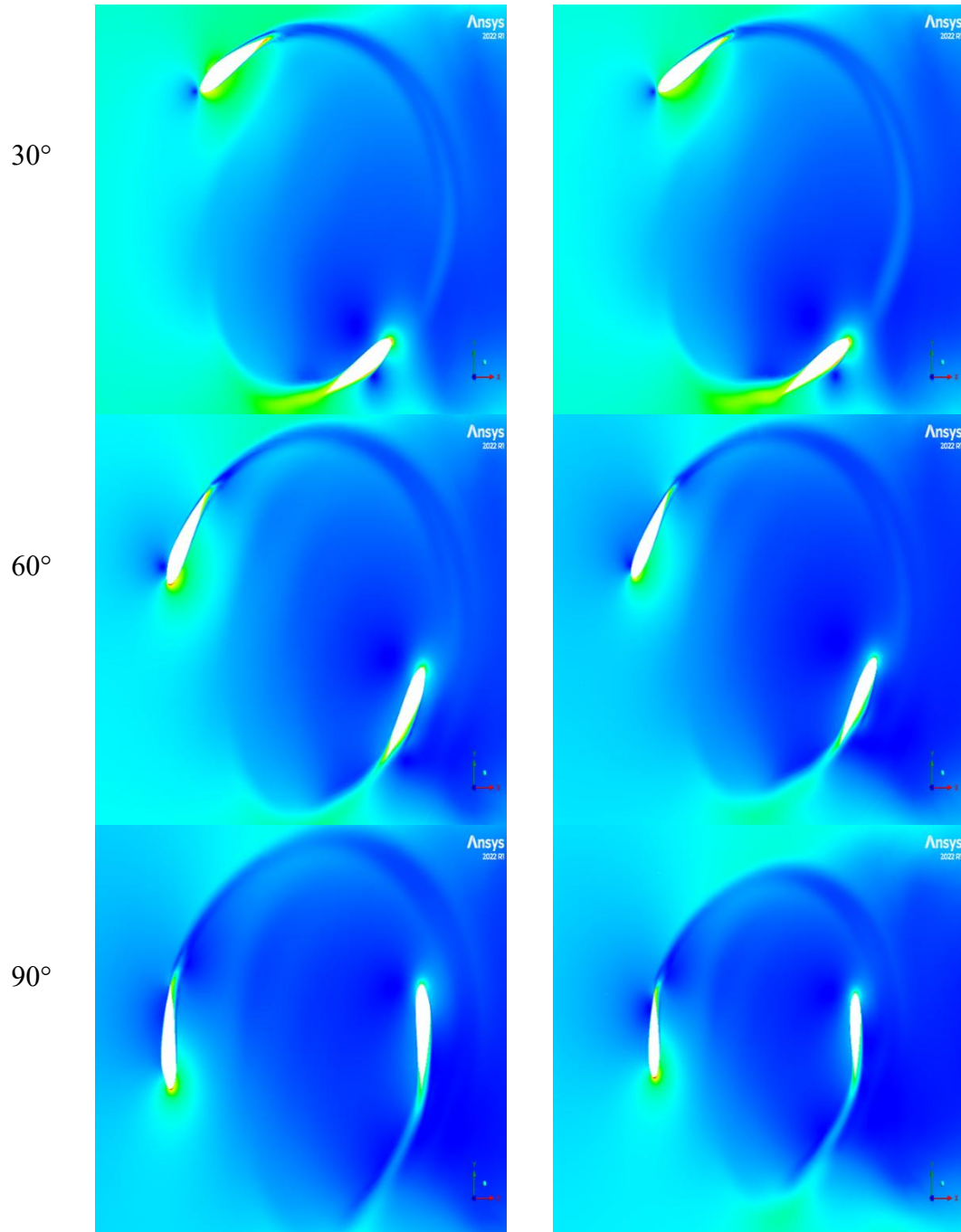
Fig 4.24. Geometric comparison between the selected candidate blade optimized at 120° 120D and NACA0018.

4.5.2.4 Velocity flow contour analysis

Fig 4.25 shows the velocity flow comparison between the candidate turbine 120D – TSR 2 and NACA0018 turbine. It was observed that the NACA0018 turbine showed a much more streamlined flow compared to the candidate turbine with the later being slightly more turbulent. Comparing the baseline NACA0018 turbine and the candidate 120D – TSR 2 turbine, it was observed that the turbine overall velocity flow contour was more turbulent in the 120D – TSR 2 turbine. Between 30° and 60°, the 120D – TSR 2 first blade experienced large velocity concentrated at the inner surface of leading edge of the blade. The velocity intensity grew towards the leading edge of the blade at 60°. At 90°, the upper surface of the 120D – TSR 2 blade suffered lower fluid velocity compared to the NACA0018 blade. At 120°, both blades within the leeward region showed similar streamlined flow. These observations may explain how the 120D – TSR 2 blade yielded the lowest peak of the compared turbine blades in the previous Fig showing the single blade moment coefficient comparison during this stage of the turbine rotation.

With respect to the second blade during each stage, taking the first and second in Fig 4.25 labelled 30° and 60°, the 120D – TSR 2 blade showed a similar velocity contour to the NACA0018 blade as it starts to exit the leeward region and enters the downwind region. Thereafter, the 120D – TSR 2 blade showed more streamlined flow compared to the NACA0018 blade. Referring to Fig 4.22, these

observations may explain how, at 210° and 240° azimuth angles, the turbine moment coefficient curves were similar. Thereafter, at 270° and 310° azimuth angles, the more streamlined flow of the 120D – TSR 2 blade resulted in a higher moment coefficient.



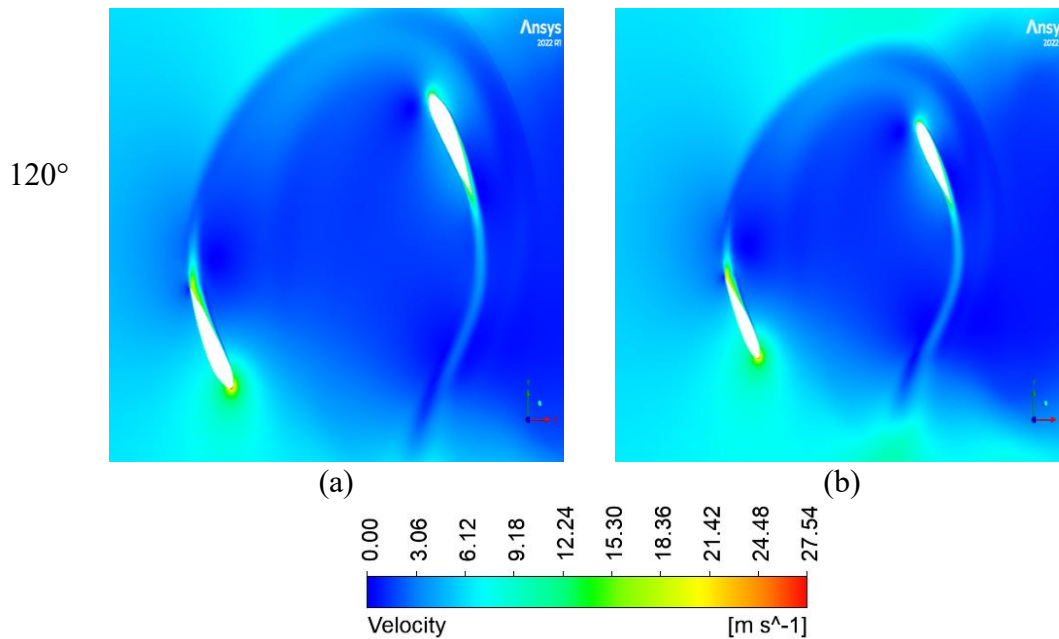
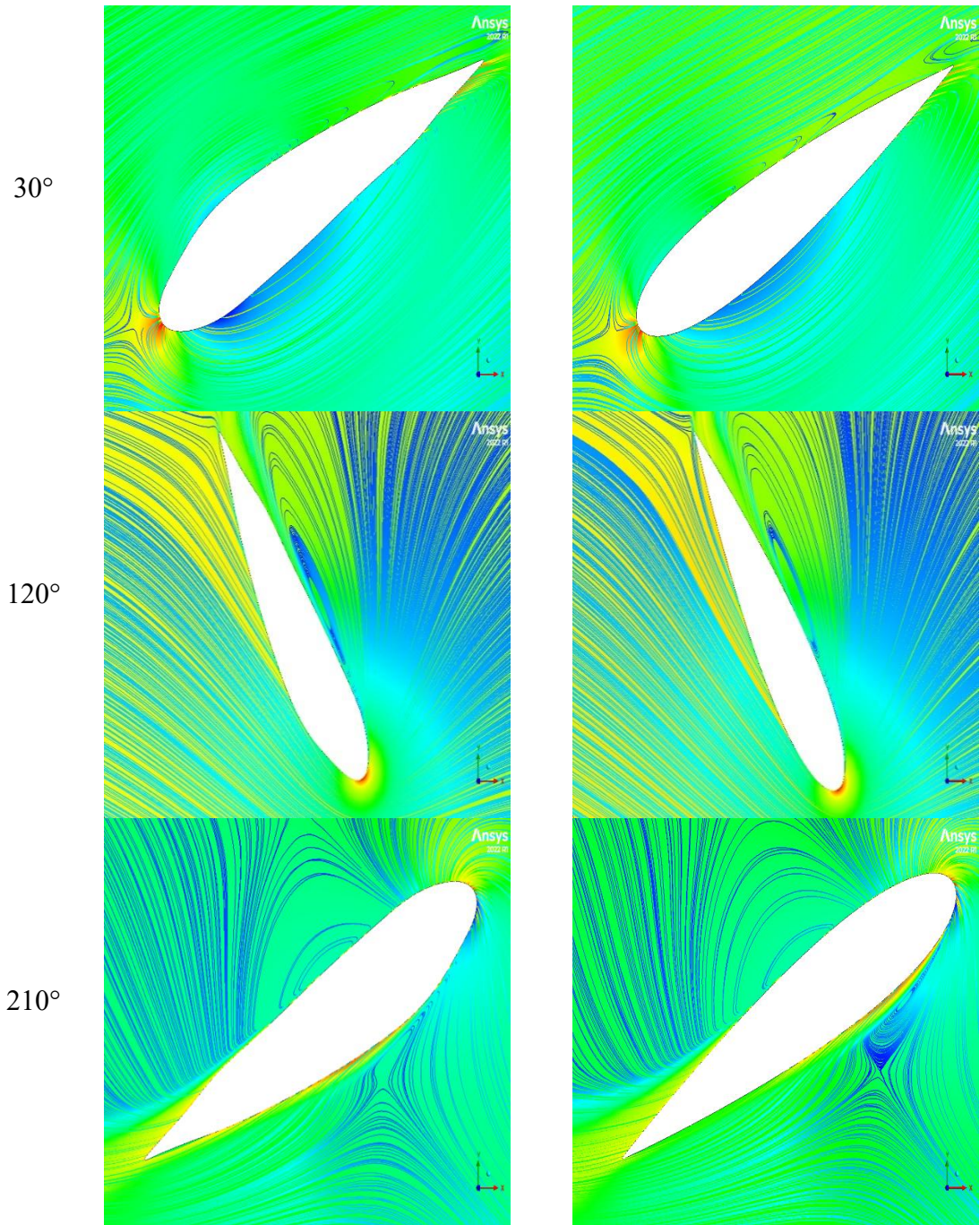


Fig 4.25. Velocity flow contour comparison between the (a) candidate blade 120D optimized at 120° and the (b) NACA0018 blade at TSR 2.

4.5.2.5 Streamline and pressure contour

Fig 4.26 shows the streamline imposed on the pressure contour comparison between the 120D – TSR 2 and NACA0018 turbine. Here, the azimuthal angles comparisons were similar to the previous 20D – TSR 1 from Fig 4.21. At 30°, the NACA0018 experienced a vortex forming at the trailing edge which was indicated by the swirling streamlines. This was not observed with the 120D – TSR 2 blade, which experienced a noticeably lower pressure compared to the NACA0018 on the pressure side of the blade. At 120°, the pressure side of the 120D – TSR 2 experienced denser rotational streamlines which indicated lower pressure. At 210°, the NACA0018 blade showed a denser streamline at the suction side compared to the 120D – TSR 2 which indicated lower pressure compared to the inner surface of the blade. The pressure side also showed denser streamlines in 120D – TSR 2 at 300°. Recalling Fig 4.22, this would explain how the 120D – TSR 2 performed better than the NACA0018 between azimuthal angles 240° and 360°. The pressure difference between the inner side and outer side in the 120D encouraged better lift which, then, translated to better moment production and power efficiency during the leeward and downwind region.



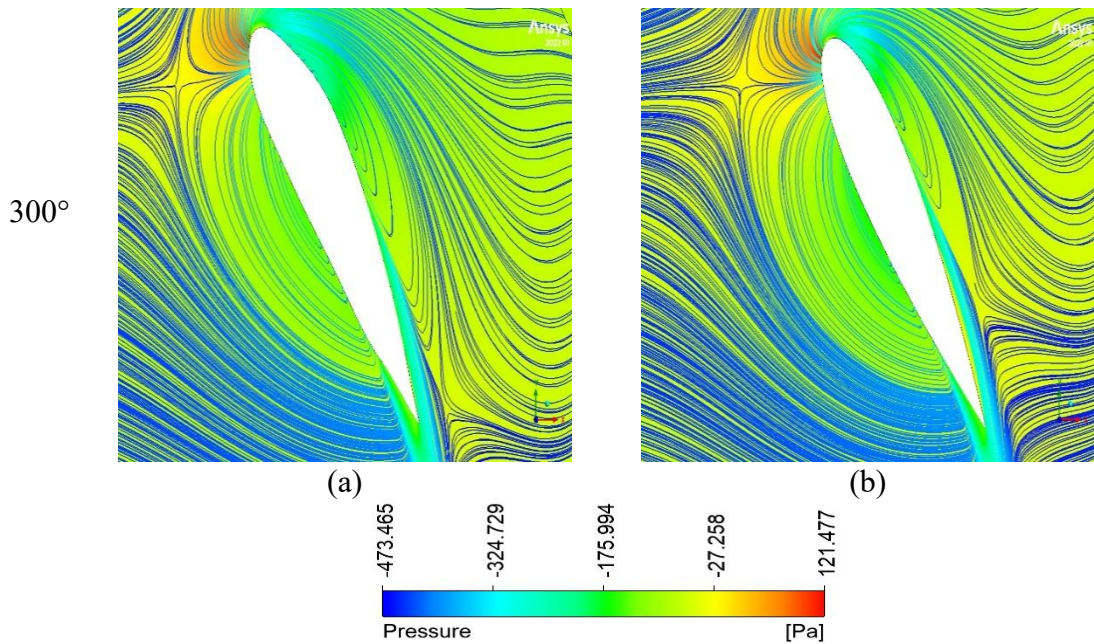


Fig 4.26. Streamline contour comparison between the (a) candidate torque optimized blade at 120° and the (b) NACA0018 blade at TSR 2. Streamline contour imposed onto pressure contour.

4.5.3 Lift Coefficient

Fig 4.27 compares the lift coefficient of each candidate blade against the NACA0018 baseline at TSR 2. In Fig 4.27(a), it was observed that the 20D – TSR 1 blade achieved a higher lift than the NACA0018 blade over the whole turbine rotation. The overall characteristic and shape of the curves were similar between the two blades with the 20D – TSR 1 experiencing higher peaks at 130° and 340° . This indicated a performance improvement in lift as the blade exited the upwind and entered the leeward phase and as the blade exited the downwind and entered the windward region. This showed how the performance of the 20D – TSR 1 blade was higher than the NACA0018 blade.

From Fig 4.27(b), a comparison between the 120D – TSR 2 blade and the NACA0018 blade was shown. Unlike the previous comparison with the 20D – TSR 1 blade, the overall curve is markedly different in the 120D – TSR 2 blade. At 50° , as the blade entered the upwind phase, the 120D blade experienced a much higher lift compared to the baseline NACA0018 blade. At 130° , a slight reduction of lift was observed as the blade entered the leeward region. Thereafter, the 120D – TSR 2 blade experienced higher lift from 260° onwards. This indicated that the 120D – TSR 2 blade performed much better than both the NACA0018 and 20D – TSR 1 blade during the downwind and windward phase.

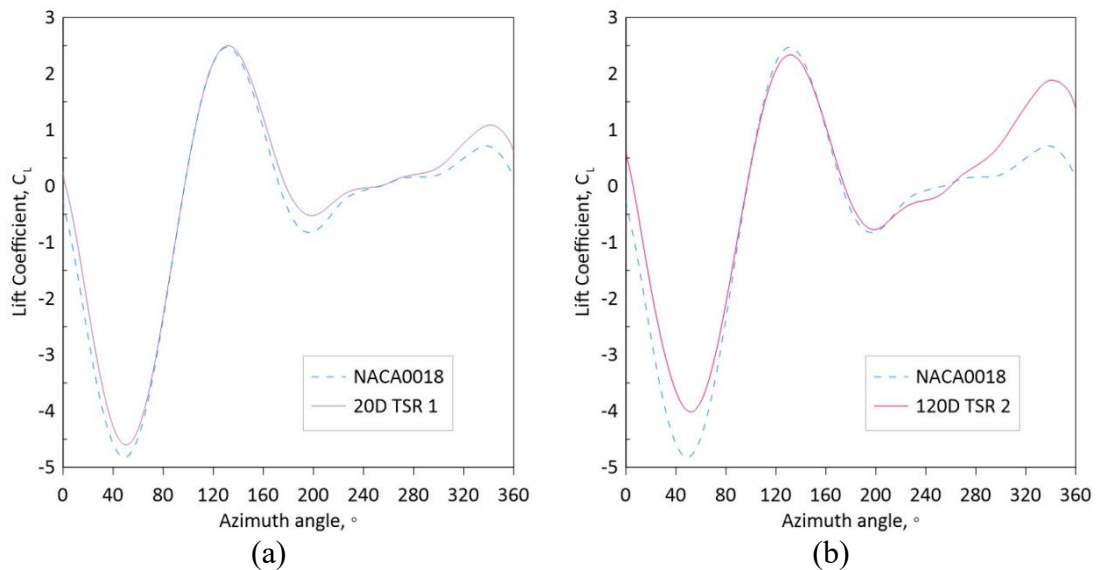


Fig 4.27. Lift coefficient comparison between (a) 20D at TSR 1 and the (b) 120D at TSR 2 against the baseline NACA0018 blade. Analysis conducted at TSR 2.

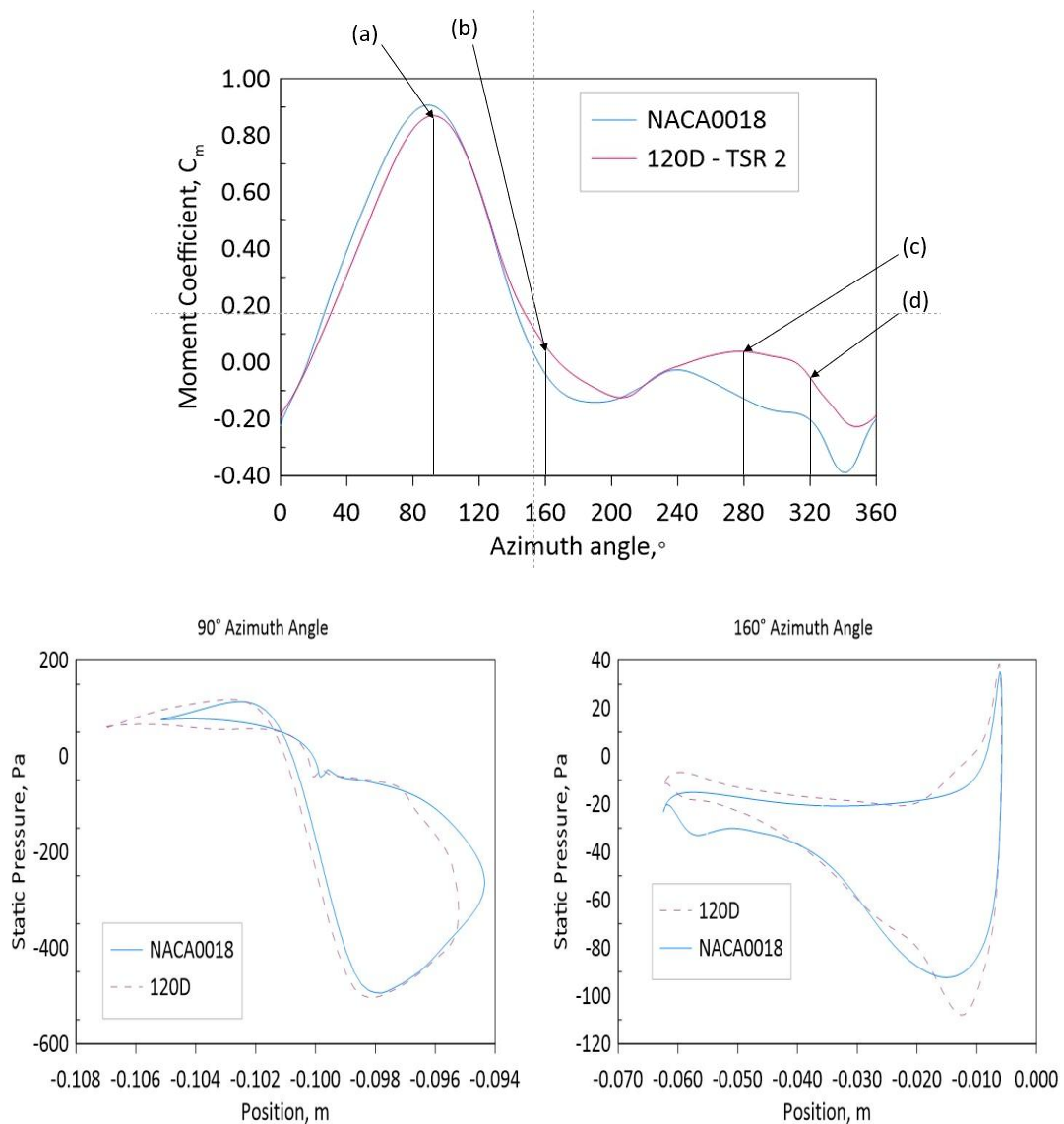
4.5.4 Blade Surface Pressure Distribution

Fig 4.22 showed important differences in curve characteristics where the 120D – TSR 2 blade improved performance during the turbine rotation. Hence, in this section, the static pressure analysis was conducted comparing just the NACA0018 and 120D – TSR 2 blade. The Y – axis represents the blade static pressure and the X – axis shows the position of the blade relative to the centre of the turbine. At 90° , from Fig 4.28(a), the 120D blade showed a smaller curve compared to the NACA0018 blade. This would explain how the moment coefficient curve would be slightly lower during this turbine phase. From Fig 4.28 (b), the 120D – TSR 2 curve saw a shift upwards on the left-hand side of the blade. However, the right-hand side of the curve showed a significant drop in negative pressure at -0.01m while at the same time an seeing increase in positive pressure. This increase in pressure difference between the pressure and suction sides also coincides with an increase in moment coefficient.

In Fig 4.28(c), there is a significant shift towards the right side of the airfoil at 280° . This indicates a shift towards the trailing edge of the blade whereby both the upper and lower surface of the blade experienced higher suction pressure. The higher-pressure difference of the 120D – TSR 2 at the right-hand side also indicates that the blade experienced better lift and therefore generated better moment compared to the NACA0018 blade. In Fig 4.28(d), at 320° between 0.05m and

0.065m, the pressure difference between the upper and lower surface of the 120D – TSR 2 blade was larger compared to the NACA0018 blade. It was also noted that the intersection point, where no pressure difference exists and therefore no lift generated, of the 120D – TSR 2 also shifted significantly towards the right compared to the NACA0018 which was more towards the left side of the loop.

These observations illustrated the role of the upper surface hump which increased and shifted the higher-pressure difference towards to the centre of the blade. This was especially highlighted at the downwind towards windward phase where the pressure higher pressure difference was concentrated more towards the trailing edge. This resulted in higher lift and therefore increased torque during this phase of the turbine rotation.



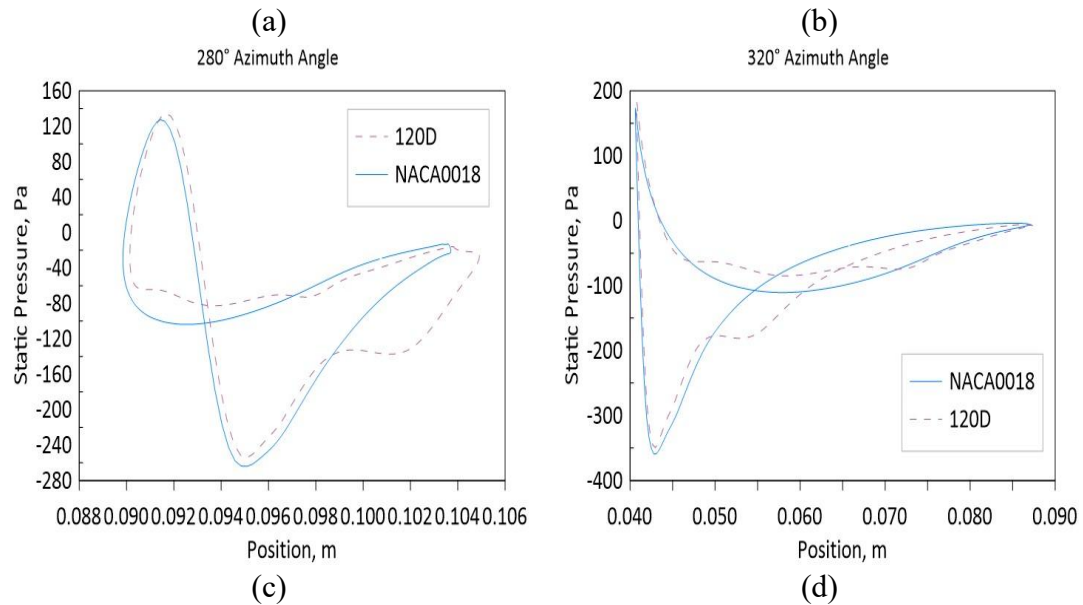


Fig 4.28. Static pressure distribution comparison between NACA0018 and the 120D at (a) 90°, (b) 160°, (c) 280°, and (d) 320°. Data taken at TSR 2.

4.5.5 Adjoint Observables

In this section, the observable changes in the adjoint optimization were analyzed. Fig 4.29(a) illustrated the observable changes with respect to blade moment for the 20D – TSR 1. The optimization started at about 0.105 Nm and ended at 0.121 Nm. Comparing the observable values and the expected change curve, this shows an increase of 14.16% in moment force. Although the curve showed a potential increase in moment if the iteration number was increased, the optimization was limited to 10 iterations due to time constraints and to limit geometric changes to an acceptable profile.

The observable changes for 120D – TSR 2 were shown in Fig 4.29(b). Here, the observable started at 0.018 Nm which then dropped significantly after the first iteration and gradually increased and peaked at 0.019 Nm. This was a 5.99% increase in moment after 10 iterations from the start of the optimization. Although this resulted in a more moderate increase compared to the 20D, the optimization scheme still saw a significant performance improvement over the baseline NACA0018 turbine.

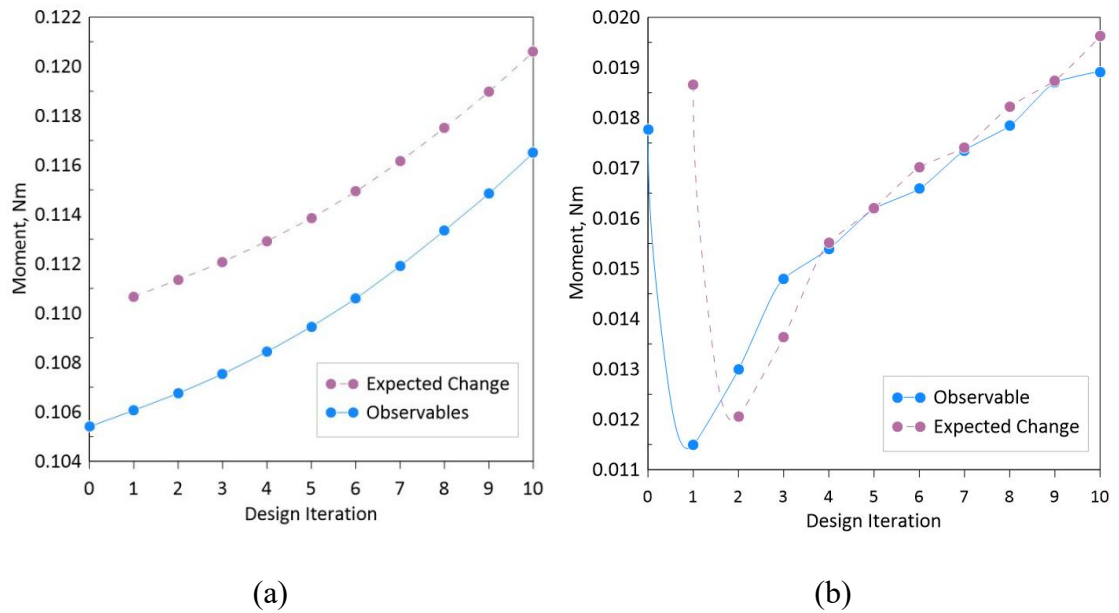


Fig 4.29. Changes in adjoint observables over 10 design iterations (a) 20D – TSR 1 and (b) 120D – TSR 2.

4.5.6 2D Aerodynamic Optimization - Summary

The shape optimization process of a NACA0018 airfoil has been described. Two optimized geometries were selected from a set of optimization results and were then compared against the baseline NACA0018 turbine. The adjoint optimization scheme was conducted at 2 different TSRs which produced interesting sets of data. Although optimized at similar azimuthal angles, the difference between the optimization results overall clearly pointed to the higher operating TSR as the more effective and optimal condition for optimization in terms of the power coefficient increases. The improved single blade moment coefficients were, on average, higher when optimized at TSR 2 compared to TSR 1. Summarizing this finding, Fig 4.30 illustrates the comparison between 20D – TSR 1 and 120D – TSR 2 against the baseline NACA0018 turbine.

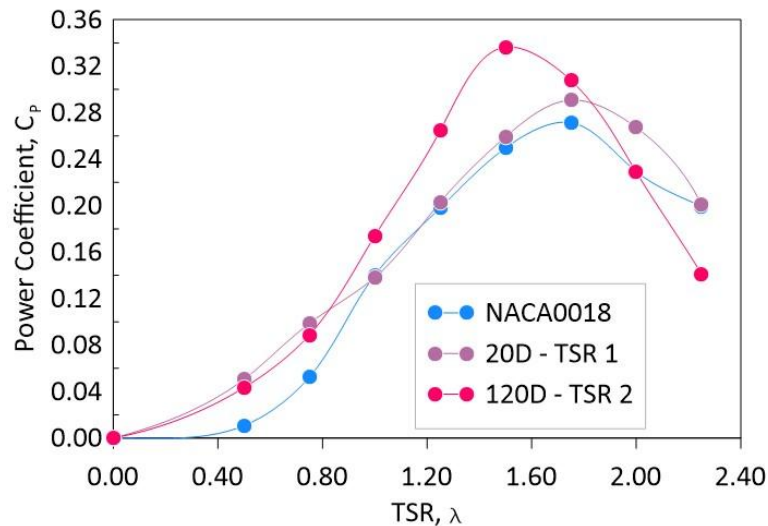


Fig 4.30. Summary of the two selected candidate blades, 20D – TSR 1 and 120D – TSR 2, against the baseline NACA0018 blade.

The results proved the adjoint optimization has successfully optimized the turbine blade, with the 120D – TSR 2 showing the most promise for better turbine efficiency. Summarizing the findings from this study, the following points were highlighted:

- The adjoint optimization scheme successfully improved the turbine performance of a NACA0018 VAWT. It was shown that the operating TSR has a significant effect on the optimization scheme, which produced very different sets of results in terms of airfoil geometries at different azimuthal angles.
- Adjoint optimization at TSR 1 yielded the best result with the 20D – TSR 1 proving the most efficient of all the compared optimized blades with a performance uplift of 6.8%.
- Adjoint optimization at TSR 2 yielded the largest maximum power coefficient increase, at 21.39%, as well as the highest overall performance increase of 28.77% over the whole tested TSR.
- Comparing the selected optimized blades at each TSR, it was observed that the 120D – TSR 2 was optimized for the downwind region of the turbine rotation as the blade shows a remarkably higher torque during this phase of the rotation.

- The 120D – TSR 2 showed, overall, a better lift coefficient curve among the compared blades with notably increased lift between the downwind and windward region.

The results in this study showed the ability of the adjoint method to optimize a symmetrical airfoil to obtain a cambered blade based on the given optimization parameters through mesh morphing. The mesh morphing results in several optimized cambered blade designs and eventually the 120D – TSR 2 was deemed the most optimal among the tested blades. This study demonstrated the ability of the adjoint method together with the gradient-based optimizer to direct the mesh morpher and produce various novel shape designs and could therefore lead to superior blades based on the inputs of the user. With the parameters described above having established good results with respect to the optimization of a symmetrical uncambered blade, the following section explored applying the adjoint solver with the optimal parameters set above on a cambered starting shape of S1046 airfoil.

4.6 Adjoint Method Shape Optimization of a Vertical Axis Wind Turbine blade: S1046 Blade Starting Shape

In the previous section, it was established that a higher TSR value yielded more optimal candidate blades. It was also shown that varying the turbine azimuthal angle, which also means the varying of the angle of attack, yields different blade shapes and geometries with each flow field at the tested TSRs having different effects on the blades adjoint shape sensitivity. It was also established that, starting with a symmetrical, non-cambered blade predictably yielded cambered blades performing better than the baseline symmetrical blade. Therefore, taking into account the observations and results of the previous section on the adjoint shape optimization scheme applied on the symmetrical NACA0018 blade, a further analysis was conducted by changing the starting blade for the optimization. A similar optimization scheme used in the NACA0018 optimization was applied here with the only difference being the TSR was set to TSR 2, which yielded the better results of the two tested TSR values in the previous section. The azimuthal angle was also done between 10° - 120° and the results were taken, quantified, and discussed.

In this study, aerodynamic shape optimization of a S1046 blade was conducted using the adjoint method, together with the gradient-based optimizer available in FLUENT, at low operating TSR in pseudo-steady state conditions. The optimization was conducted on a single S1046 blade and optimized at different azimuthal angle to observe the effects of the flow field on the candidate blade. The largest percentage in the average single blade moment was obtained at 30° . The performance improvement was mostly concentrated during the upwind region most obvious at 90° with a significant increase in maximum torque. Further 2D simulation in a 2 bladed setup found an average increase of 9.5% over the tested TSR range. The flow field analysis identified various interesting characteristics of the candidate blade which enhanced its performance over the baseline S1046 blade. This study confirmed the validity of the adjoint solver to optimize the S1046 blade for further improvement.

4.6.1 Single Blade Optimization Analysis

Table 4.6 shows the optimization results conducted at the range of azimuthal angles of the turbine. It was observed that the positive optimization cases were found during the later part of the windward region as the blade nears the upwind region with the rest of the test cases yielding negative results with a single exception at 120° . The best results were obtained at 30° and 40° azimuthal angles showing a 9.2% increase and 6.3% increase respectively. Both candidate blades were selected for extraction and designed into a 2-turbine blade configuration for further turbine comparisons. For the following results, the test cases were assigned the names S1046 – 30D and S1046 – 40D respectively to differentiate from the previous sections.

Fig 4.31 shows the comparison of the two largest percentage increases in moment coefficient from the optimization results. The moment coefficient curve does not change significantly at any stage of the rotation. This indicated an improvement on the turbine blade that maintains the overall characteristics of the starting baseline blade. The optimization scheme improved two locations in particular; the first observation was found between 120° and 200° and the second between 250° and 340° azimuthal angles. The optimization scheme improved torque production during the initial phase of the leeward region and later phase of the downwind region. However, the overall differences observed were minimal. This may be due to the single blade condition with no blade interactions occurring.

Table 4.6 Summary of the moment optimization at TSR 2 at various incremental azimuth angle

Azimuthal angle, °	Average torque, Cm	Difference, %
10	0.167	-0.251
20	0.174	3.997
30	0.183	9.182
40	0.178	6.301
50	0.168	0.172
60	0.164	-1.868
70	0.164	-1.771
80	0.163	-2.594
90	0.164	-1.904
100	0.167	-0.216
110	0.169	0.812
120	0.170	1.417

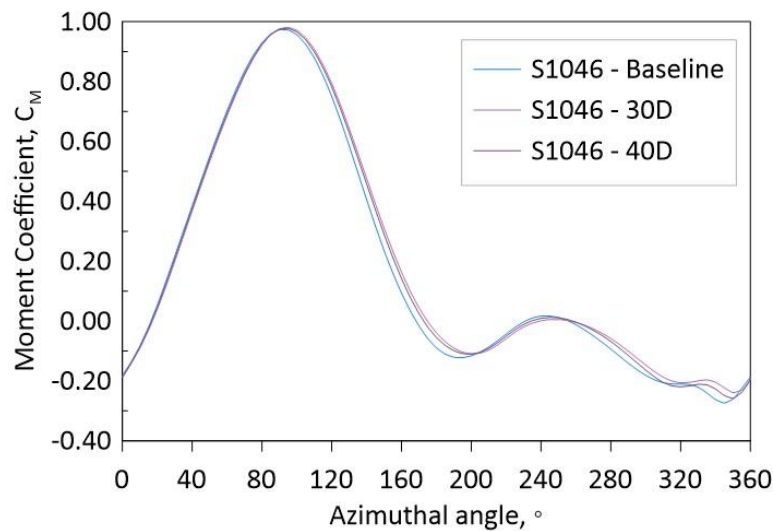


Fig 4.31. Instantaneous of moment coefficient comparison in single blade configuration.

4.6.2 Turbine Performance Analysis

Fig 4.32 shows the single blade instantaneous power coefficient curves of the blade. The results in a two bladed turbine operation which were subject to normal turbine rotations and flow effects. It was observed that, of the 3 turbine blades, the S1046 – 30D produced the highest peak at 90°. The S1046 - 30D blade showed highest efficiency during the windward and upwind phase of the rotation. The performance

curve showed a slight dip around 200° and thereafter showed negligible differences compared to the baseline S1046.

The S1046 - 40D curve saw a phase shift forward and peaked later at 95° which also means this candidate blade showed better efficiency during the latter half of the upwind region. There was, however, a noticeable dip in performance around 180° which is at the peak of the leeward phase. Overall, the adjoint optimization procedure increased the maximum performance of the turbine during the upwind phase whereas the previous optimization on the symmetrical blades yielded improvements in downwind phase.

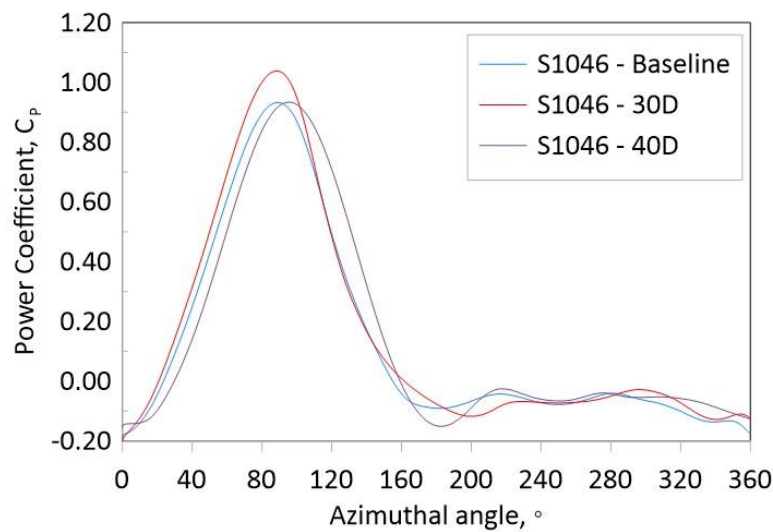


Fig 4.32. Power coefficient comparison of the cambered candidate turbines against the baseline S1046 in turbine configuration.

Fig 4.33 shows the comparison of the two S1046 optimized candidate turbines against the baseline. It was observed that all three turbines performed similarly during the initial phase of the turbine rotation at the lower TSR range. Thereafter, both candidate turbines performed better than the baseline S1046 turbine. The largest percentage increase in power coefficient was found at TSR 1.5 with a 15.1% increase in performance between the baseline and the S1046 – 30D. As expected, however, the S1046 – 30D blade showed the most optimal performance over the tested TSR range. The average performance uplift of the S1046-30D over the baseline turbine was 9.5%. Hence, the S1046 – 30D candidate blade was selected for further analysis in the following sections.

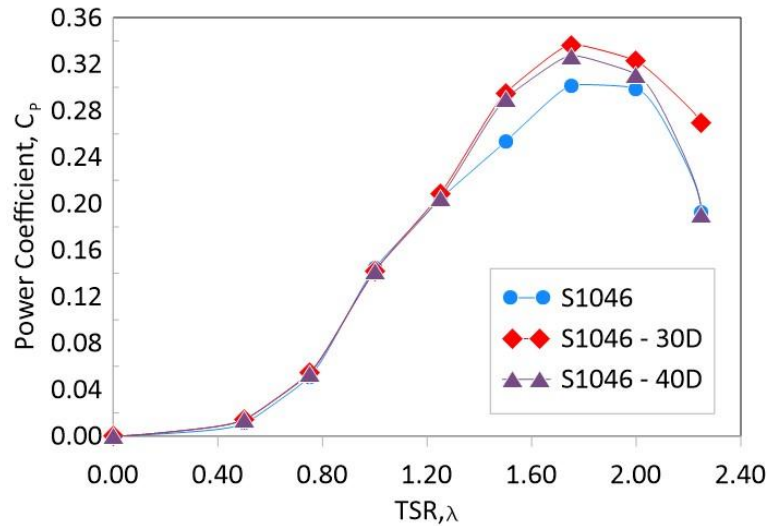


Fig 4.33. Instantaneous power coefficient comparisons of single turbine blades of the candidate turbines during turbine operation at TSR 1.5.

The S1046 – 30D geometry was illustrated in Fig 4.34. The leading upper surface of the blade showed no changes. The upper surface of the trailing edge, however, morphed inwards. The inner surface of the blade showed an inward and upward morphing direction that started at $0.15c$ and went up to about $0.75c$. Thereafter, the morphing changed in the opposite direction outwards and downwards up to $0.9c$. Overall, the mesh morphing of the blade showed morphing that slightly reduced the area of the blade cross section.

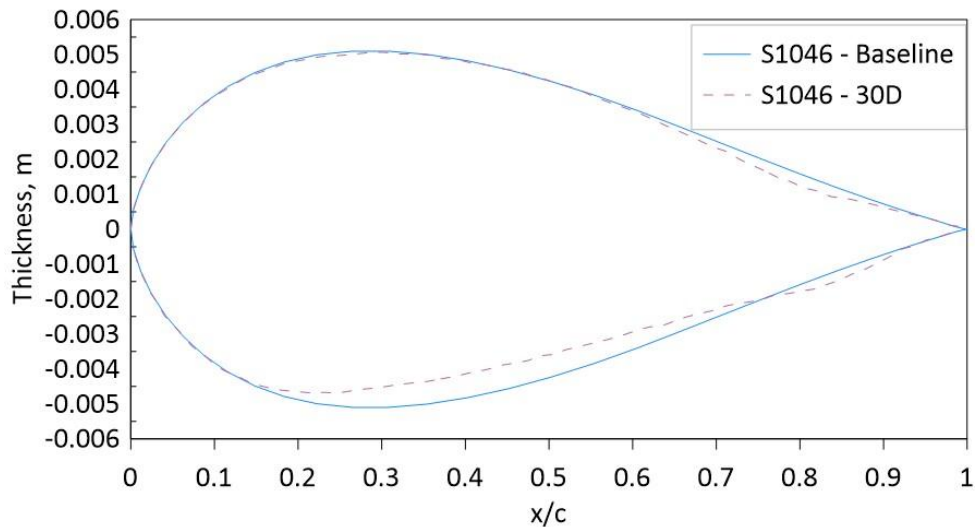
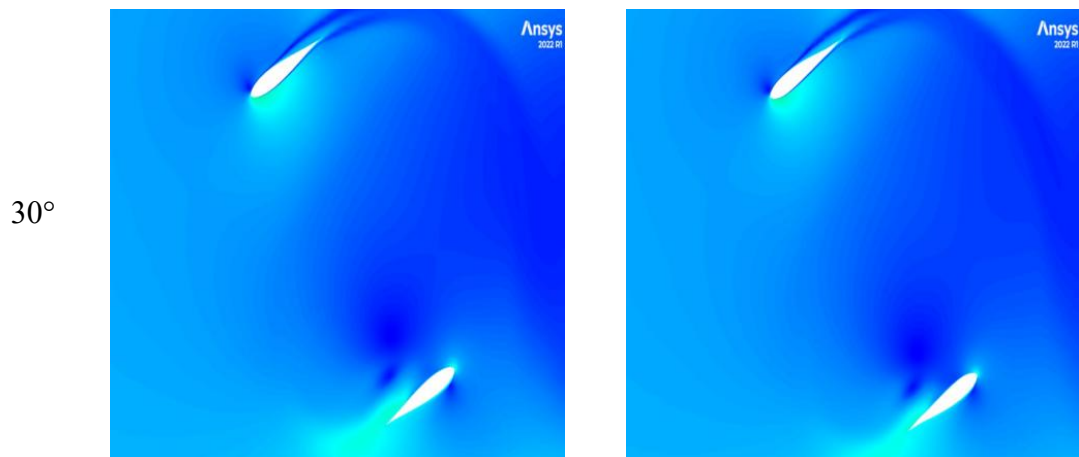


Fig 4.34. Shape comparison of the candidate blade S1046 – 30D and the S1046 baseline blade.

4.6.3 Velocity Contour Comparisons – S1046 Optimization

From the previous Fig 4.32, a significant point of difference between the baseline S1046 blade and the candidate blade S1046 - 30D was during the upwind phase. Hence, this section examined the velocity flow contour during this stage of the turbine rotation. Fig 4.35 shows the velocity contour comparisons between both turbines at instances between 30° to 120° . In the following Fig 4.35(a) and Fig 4.35(b), both turbines showed similar velocity contours with differing magnitudes of flow speed. At 30° , as the first blade enters the upwind region, the inner surface of the S1046 blade showed a slightly larger formation of high velocity flow. At 60° , the velocity flow magnitude is slightly higher at the leading edge of the candidate blade compared to the S1046 baseline. The S1046 - 30D second blade in the downwind region experienced less intensity of flow turbulence compared to the baseline. At 90° , as the blade enters the peak upwind phase, the leading edge of the S1046 - 30D showed slightly higher velocity speed. Thereafter, as the blade enters the leeward region shown at 120° , the velocity contour of both turbines shows similar characteristics. The leading edge of the S1046 - 30D however does show slightly higher velocity at the inner surface.



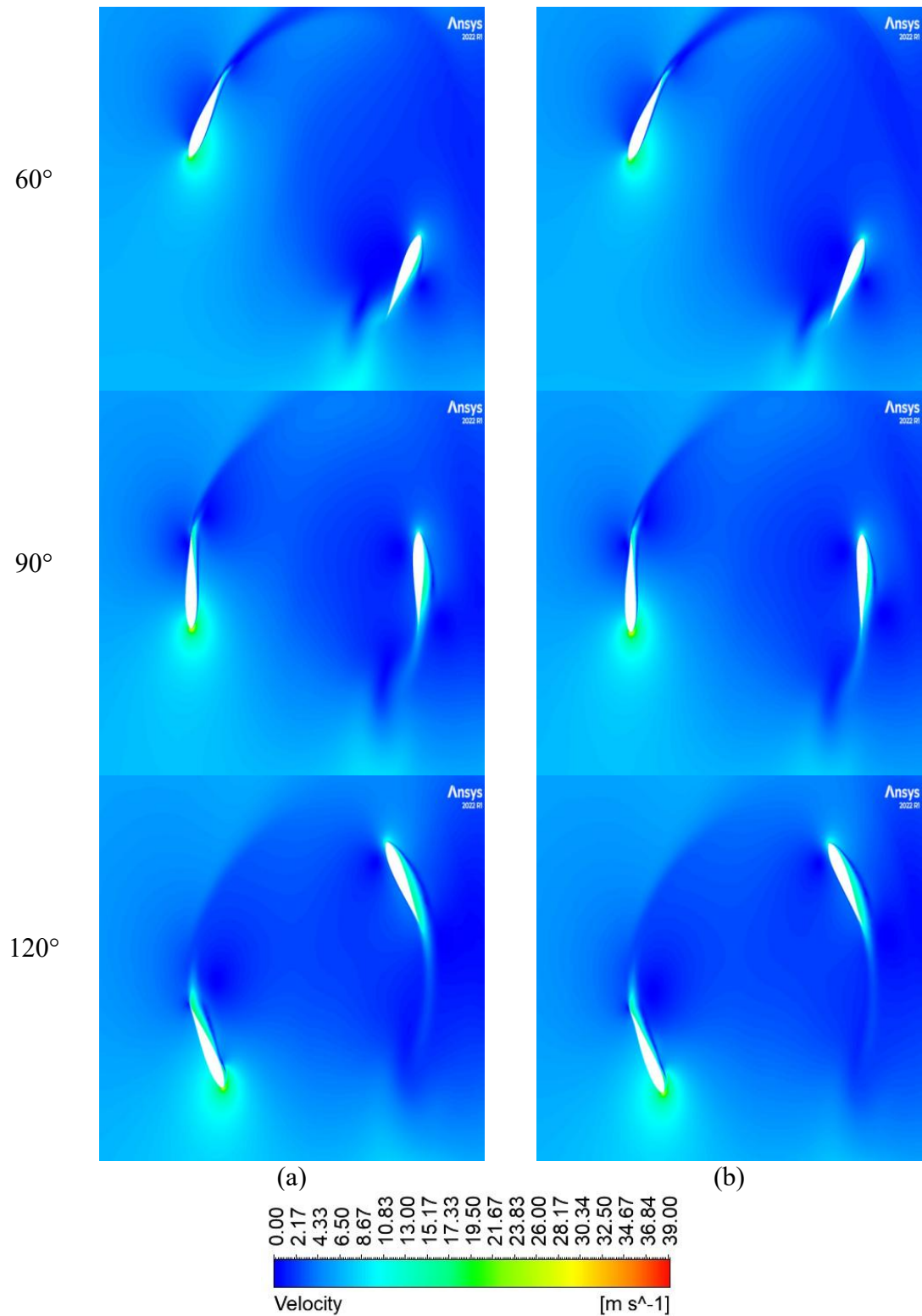


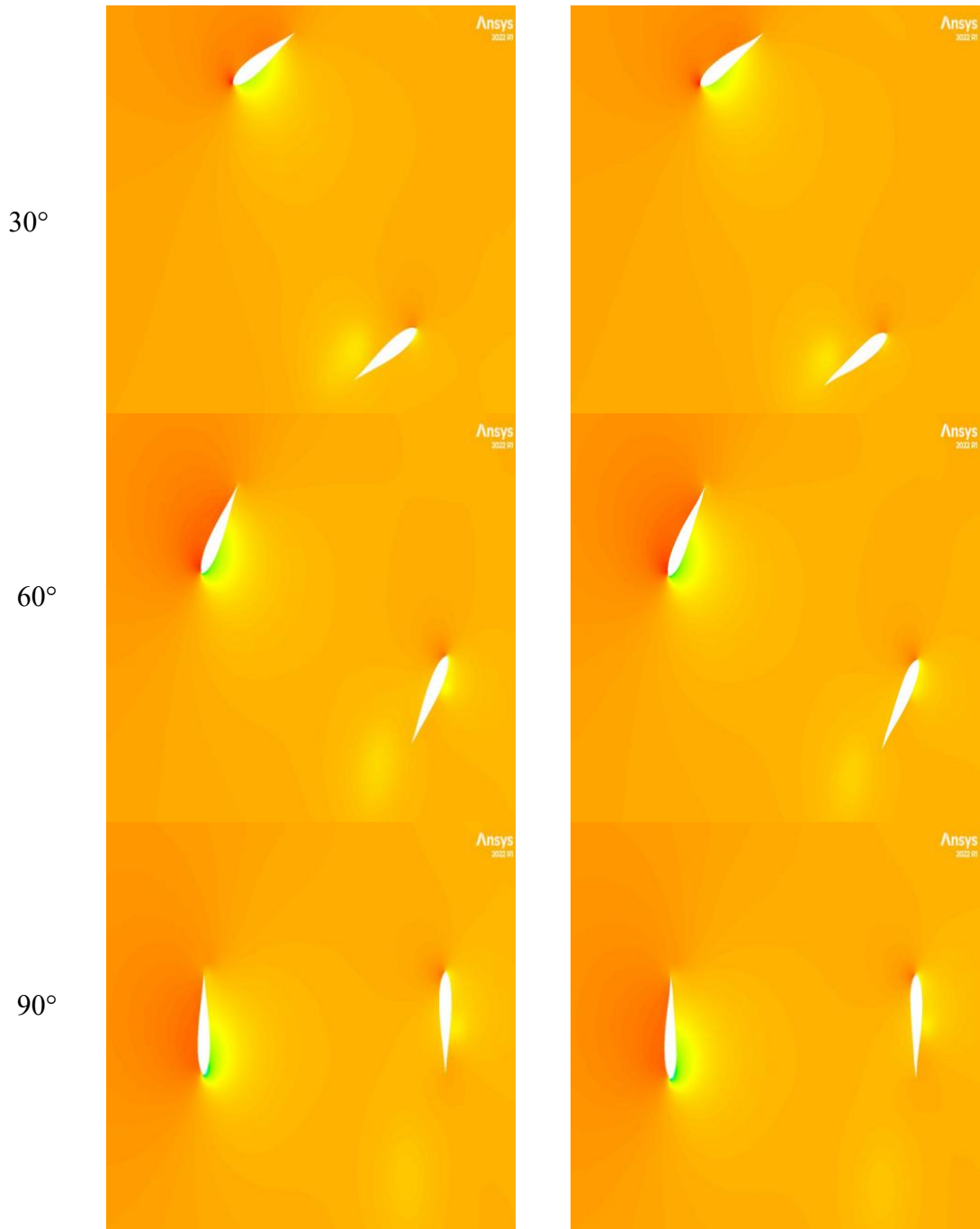
Fig 4.35. Velocity contour comparison for (a) S1046 and (b) S1046 – 30D taken at TSR 1.5.

4.6.4 Pressure and streamline contour analysis – S1046 Optimization

Fig 4.36 compares the pressure contour between the baseline S1046 and the candidate blade S1046 - 30D. The contours were taken in the upwind phase between

30° to 120° azimuthal angle. It was observed that, although the overall Fig shows similar contours between both blades, slight differences were observed with respect to pressure magnitude due to the optimized geometry of the S1046 - 30D. At 30°, the pressure difference between the upper surface and inner surface was similar between the two turbine blades. Between 60° to 90°, during the peak of the upwind phase of the rotation experienced by the first blade, it was observed that the pressure difference experienced by the S1046 - 30D blade was higher compared to the baseline S1046. This larger pressure difference led to an increase in lift force during this phase and therefore increased power extraction. At 120°, the negative suction pressure on the inner surface of the S1046 - 30D was more pronounced at the midpoint of the blade surface whereas the S1046 blade was more evenly distributed along its inner surface. These observations were in line with the performance curves presented in the previous section.

Fig 4.37 discussed the streamline flow field comparisons between the baseline and the selected S1046 – 30D. The analysis was conducted similar to the previous section between 30° and 120°. At 30°, both blades showed similar flow patterns with a small difference observed at the leading edge of the upper surface. The flow circulation at 60° was also observed to be similar. However, the streamlines showed more concentrated flow experience by the S1046 baseline at the upper surface. At 90°, the flow circulation at the inner surface of the S1046 – 30D blade showed a smaller and more concentrated swirl as the blade reached the peak of the upwind phase. This allows the fluid flow to curve easily as the blade passes and increased lift and torque during this phase of the rotation. The concentration of swirling flow in the inner surface of the blade was also observed at 120°. The circulation of flow by the S1046 shifts towards the trailing edge slightly compared to the S1046 – 30D blade. This may indicate an imminent flow detachment from the trailing edge of the S1046 and that the optimized geometry of the S1046 – 30D delayed this phenomenon as the blade entered the leeward region. These observations, highlighting the difference in flow, explains why the S1046 blade was more optimal during the upwind phase of the flow.



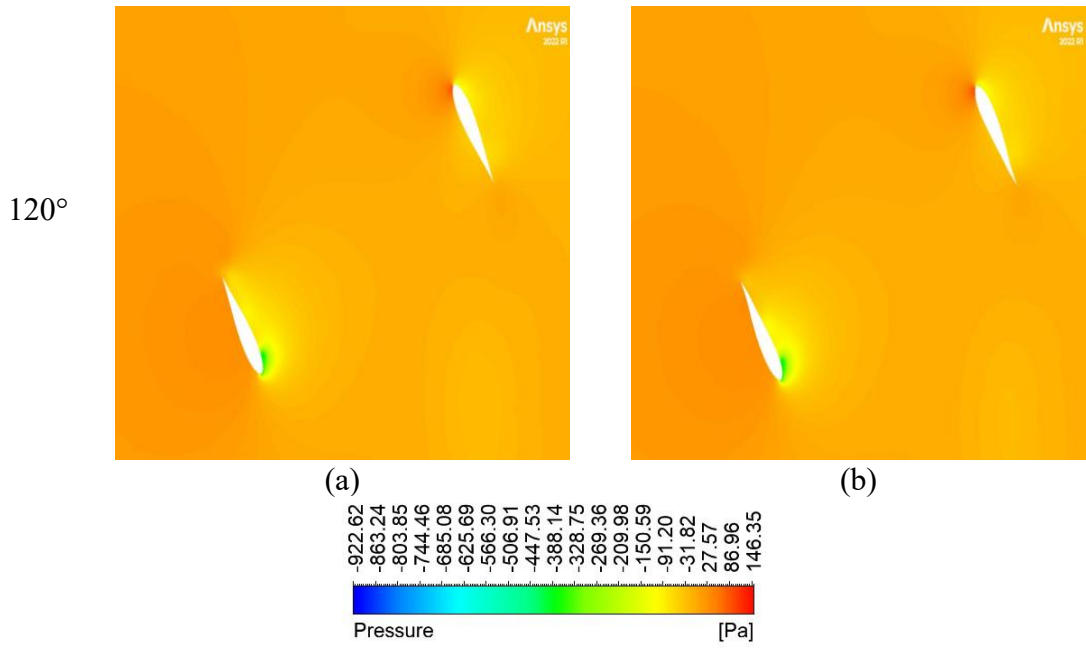
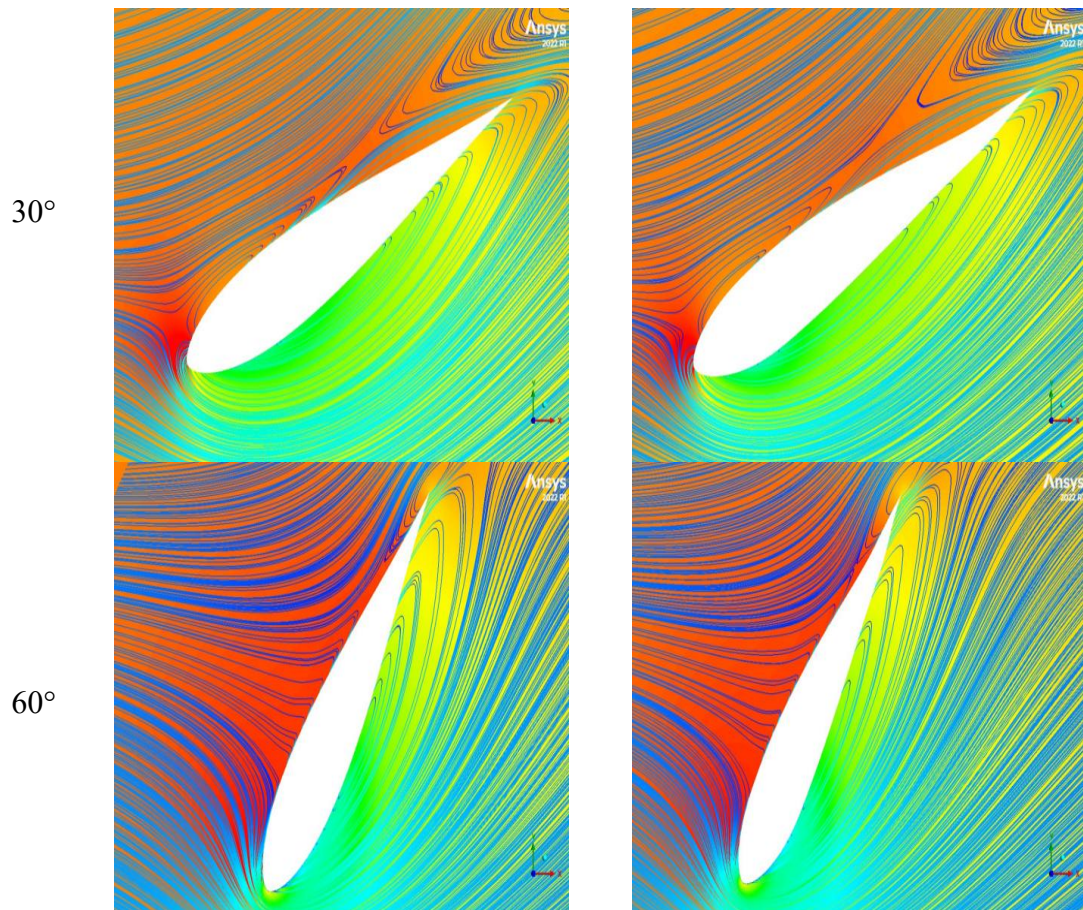


Fig 4.36. Pressure contour comparison between (a) S1046 and (b) S1046 – 30D. Data taken at TSR 1.5.



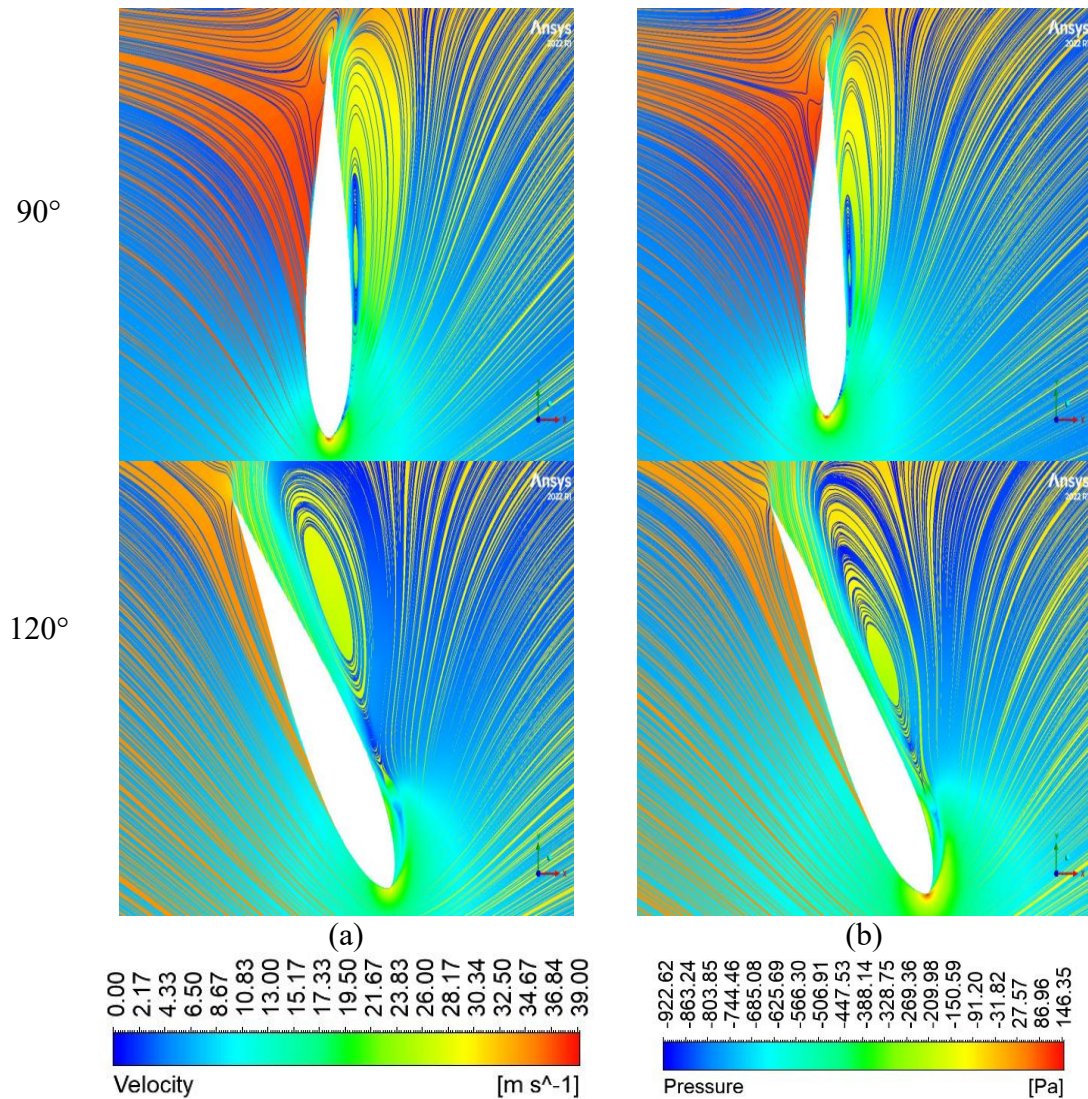


Fig 4.37. Streamline contour comparisons coloured by velocity of the baseline (a) S1046 against the (b) S1046 – 30D taken at TSR 1.5. Streamline imposed on the pressure contour from previous Fig.

4.6.5 Lift Coefficient Analysis – S1046 Optimization

In this section, the lift coefficient curve over a single turbine rotation was analyzed. Two of the best performing candidate blades were compared against the baseline S1046 blade. From Fig 4.38(a), the S1046 – 30D blade has a higher overall lift coefficient during the exit stage of the windward region between 0° to 40°. Thereafter, no significant difference was observed until the blade entered the leeward region. The S1046 - 30D lift coefficient curve peaked at 140° and later showed higher values than the S1046 up to 220°. A similar trend was also noted during the later stage of downwind phase and the initial stage of the windward phase which is between 280° and 360°. These observations were consistent with the previous sections showing minimal difference in pressure contour during certain phases of the

turbine rotation. In the case of the S1046 – 40D, shown in Fig 4.38(b), the overall curve showed slight increases in lift coefficient mainly concentrated at transitional regions such as at 40° (windward to upwind), 160° (upwind to leeward), and 280° (downwind to windward). The peak lift coefficient values, however, although higher than the baseline S1046, were notably lesser than the S1046 - 30D blade. This observation indicated as to how the S1046 – 40D performed better than the baseline S1046 blade but fell short against the S1046 – 30D blade.

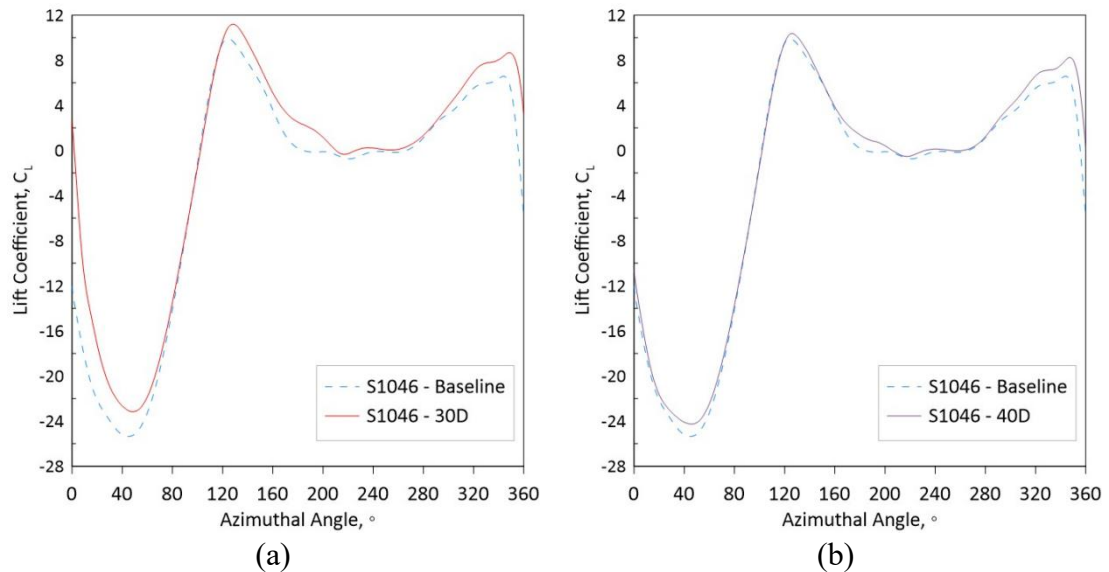


Fig 4.38. Lift coefficient comparison between (a) 20D at TSR 1 and the (b) 120D at TSR 2 against the baseline NACA0018 blade. Analysis conducted at TSR 1.5.

4.6.6 Blade Surface Pressure Comparison – S1046 Optimization

Further analysis was conducted to compare the performance improvement gained from the adjoint solver by quantifying the blade surface pressure distribution and how it differs from the baseline. For the blade surface pressure, comparisons were made azimuthal angles 30° and 90° . The data was taken with respect to the blade X direction. From Fig 4.39(a), it was observed that the overall area of the S1046 – 30D curve was smaller than the baseline S1046. Significant improvement was observed between -0.07m to -0.04m . This indicated an increase in suction pressure on the blade at these locations. For the S1046 – 40D curve, from Fig 4.39(b), the main difference was seen between -0.07m and -0.06m , showing a larger area compared to the S1046 - 30D. At 90° , both candidate blades show similar overall curve with the most noticeable difference observed at the trailing edge of the blade. From Fig 4.39(c), the trailing edge of the S1046 – 30D showed an inward curl of the static

pressure curve compared to the baseline. A similar observation, albeit to a lesser degree, was also seen from Fig 4.39(d) with the S1046 – 40D blade. This was the crucial location where the geometry of the blades differs from the optimization scheme. With respect to the S1046 – 30D, the increased static pressure and tighter curve shown here contributed to the significant increase moment coefficient observed previously from Fig 4.32.

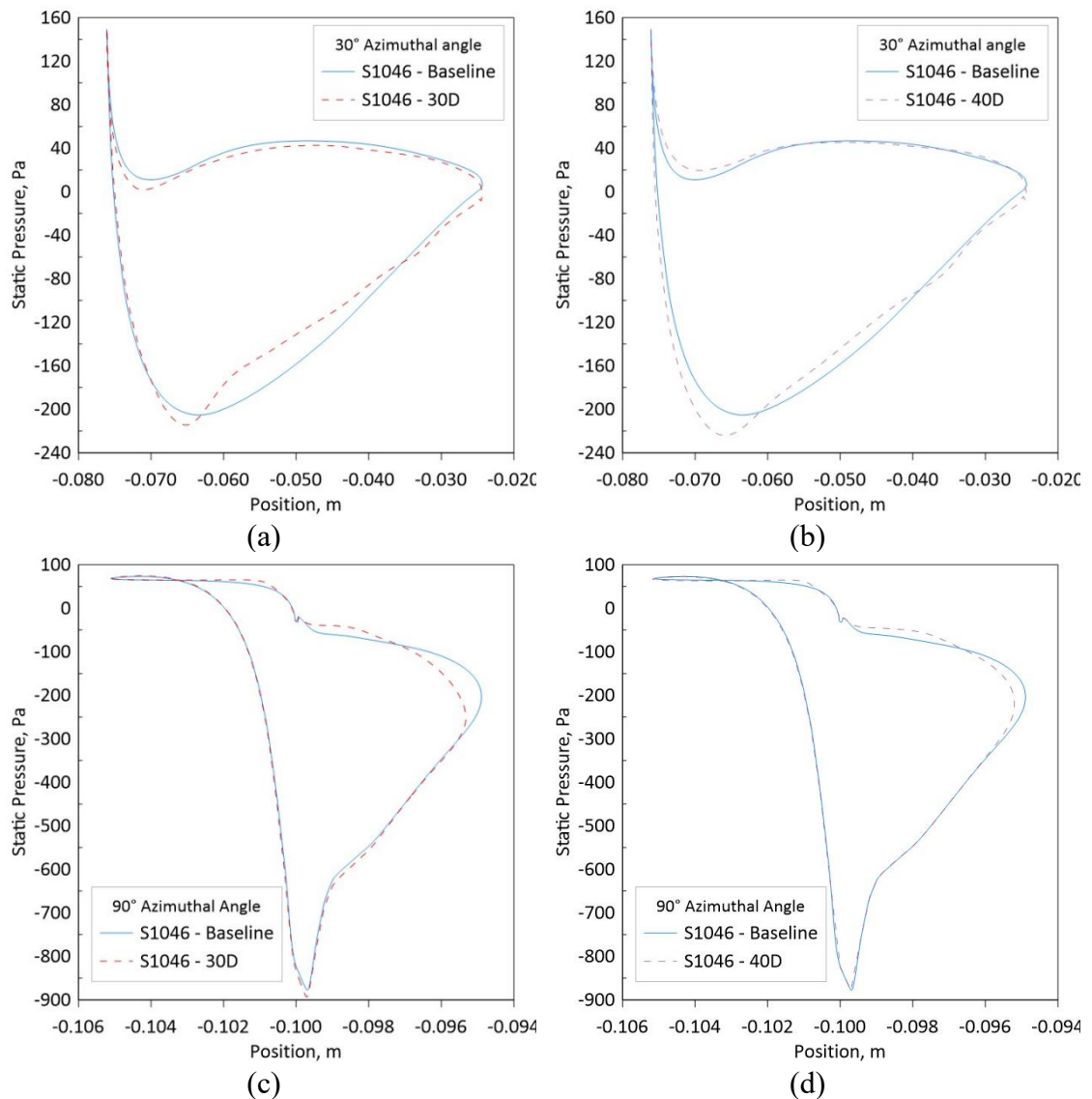


Fig 4.39. Pressure distribution analysis and comparisons at 30° and 90° azimuthal angles. Data taken at TSR 1.5.

4.6.7 Adjoint Observables – S1046 Optimization

As was previously mentioned, the adjoint solver was used together with the gradient based optimizer to optimize the S1046 iteratively over 10 iterations. The optimization scheme can be monitored by the change in observables against the

expected change. Each iteration was done to increase the blade moment at a set percentage of increase of 5%. The gradient solver then runs based on the initial adjoint feedback of the sensitivity gradient. From Fig 4.40(a), the S1046 – 30D optimization starts from a steady state blade moment of 0.061 Nm. The final iteration yielded a blade moment of 0.0745 Nm which is a significant overall increase of 20.8%. Fig 4.40(b) shows the adjoint observable changes of the S1046 – 40D candidate blade. The S1046 – 40D blade started at 0.0744 Nm and reached the final iteration moment value of 0.0887 Nm. The overall increase was 17.5% over the baseline. Both Figs indicated that the optimization can be continued further beyond the 10th iteration. However, the optimization was not continued to reduce the aggressiveness of the solver to yield more realistic geometry expectations.

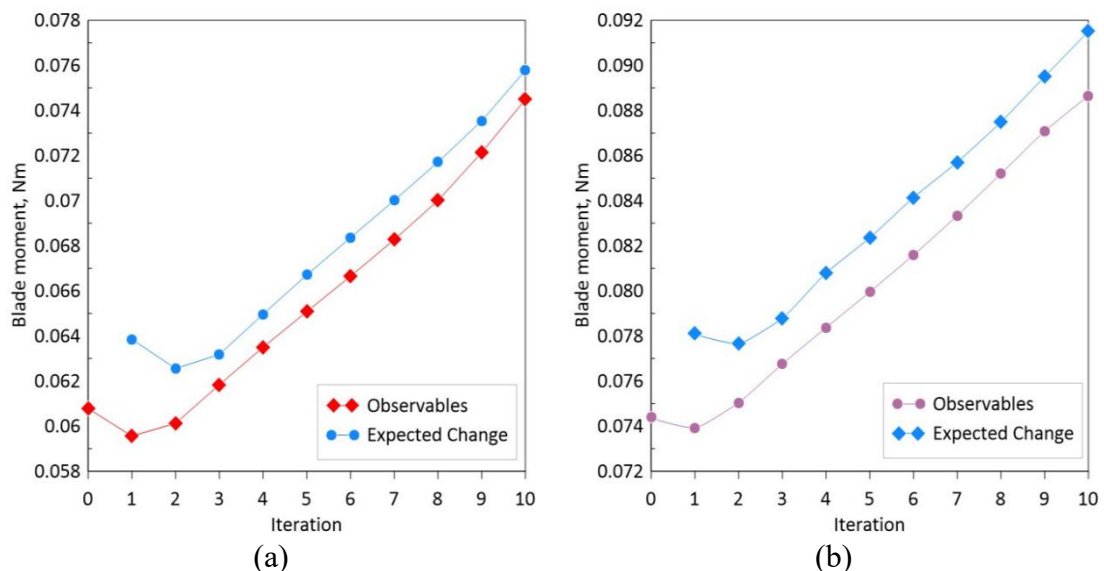


Fig 4.40. Changes in observables for (a) S1046 – 30D and (b) S1046 - 40D.

4.6.8 S1046 Optimization - Summary

The study has successfully conducted an adjoint-based shape optimization on a S1046 blade with significant improvement in terms of power coefficient. The candidate blade S1046 – 30D performed better than the baseline S1046 blade with increased power coefficient most noticeable within the upwind region. Summarizing the findings from this study, the following points were highlighted:

- Applying the optimization scheme on a the cambered S1046 blade, the best result was obtained at 30° azimuthal angle with a 9.2% increase over the baseline S1046 blade.

- A 2 bladed numerical analysis showed a 9.5% increase in average performance over the test TSR range.
- The optimized S1046 – 30D blade showed positive improvement in the windward and early phase of the upwind region with significant increase of the blade maximum torque at 90°.
- Further analysis of the lift coefficient changes showed remarkable increase concentrated at the transitional regions such as when the blade moves between the windward and upwind and as the blade exits the downwind and rotates into the windward region. This observation was also recorded with the second candidate blade S1046 - 40D but to a lesser degree.

The results showed the adjoint method was able to yield an optimal candidate blade based on the S1046 shape. It was also observed that, when comparing the morphing pattern of the S1046, the results above can also be used to verify the results from the NACA0018 optimization in that further cambering of the blade, guided by the adjoint method and affected by the flow field at different azimuth angle, increased moment and therefore power coefficient further. However, the starting shape of NACA0018 yielded a higher percentage increase in power coefficient with a distinctly different shape from the original starting blade compared to the resulting blade from the S1046 optimization which showed similar characteristics to its starting blade. In the following section, 3D analysis of the candidate blade from the NACA0018 optimization was conducted.

4.7 Adjoint Method Shape Optimization of a Vertical Axis Wind Turbine: 3D Analysis and Characterization of the candidate 120D blade

This study demonstrated the efficacy of the adjoint method to optimize a VAWT blade. The optimization of the symmetrical uncambered blade NACA0018 produced a strong candidate blade which improves the average single blade moment coefficient by over 30%. A 3D analysis was then conducted to study, compare, and characterize the performance of the candidate 120D blade from the NACA0018 optimization. This was done to include 3D effects in the numerical simulation such as blade tip losses and 3D production of wake and vortices across the blade span length since 2D numerical simulation does not consider blade depth. The candidate

blade was compared against the baseline NACA0018 blade and S1046 blade. The results showed the candidate blade performed much better than the NACA0018 blade by 20.42% as well as the S1046 blade by 15.18%. These results indicate the adjoint method is a suitable optimization code to aerodynamically optimize and improve the VAWT turbine blade.

4.7.1 3D Blade Comparisons

The candidate blade obtained from the 2D optimization scheme was then exported and redesigned into a 3D dual blade turbine. 3D numerical simulation was then conducted with the performance coefficients between the NACA0018 and 120D. Fig 4.41(a) shows the power coefficient comparison between the NACA0018 turbine and candidate 120D turbine. It was observed that 120D performed better than NACA0018 turbine by 29.02% over the range of TSR. The largest difference was found at TSR1.75 and TSR 1.5 with a power coefficient difference of 45.0.8% and 32.55% respectively. For added comparison, the cambered blade S1046 was also compared. However, the 120D was also found to outperform the S1046 blade. The average difference over the range of tested TSR against the NACA0018 was 20.42% whereas the average performance uplift over the S1046 was 15.18%. Further comparative analysis between all three blades was conducted in the later sections. A short analysis was conducted at low wind speed of 3m/s shown in Fig 4.41(b). The 120D curve show poor performance which was expected at such a low wind speed.

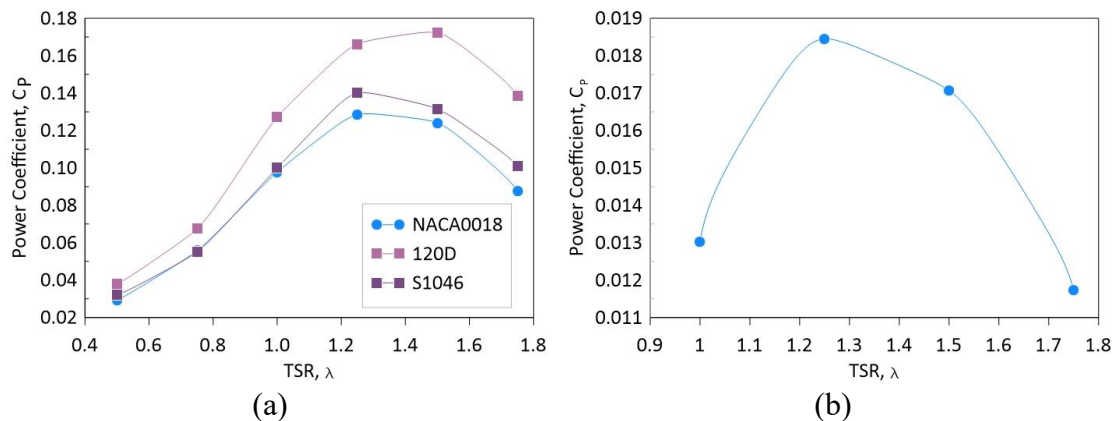


Fig 4.41. (a) Power coefficient comparison between the candidate turbine against the NACA0018 and S1046 and (b) power coefficient curve at low wind speed of 3m/s.

Fig 4.42 compares the single blade instantaneous moment coefficient curve between the NACA0018 and the 120D taken at TSR 1. During the first half of the turbine rotation, it was observed that both blades performed similarly between 0° to

90°. This shows that there was little difference in terms of power performance between the blades during the latter half of the windward phase and the early phase of the upwind. However, the 120D blade showed better performance during the latter half of the upwind phase and into the early phase of the leeward region. A slight performance dip was observed thereafter. During the downwind phase of the rotation, the candidate blade showed better overall efficiency leading into the windward region, as illustrated in Fig 4.43. The NACA0018 curve shows a smoother downward trending line whereas the 120D blade shows slight oscillation between 200° and 320° albeit with higher efficiency. This indicates that the shape of the unsymmetrical 120D blade is more optimized for the downwind region and is better at extracting power in a more turbulent flow generated from the passing blade.

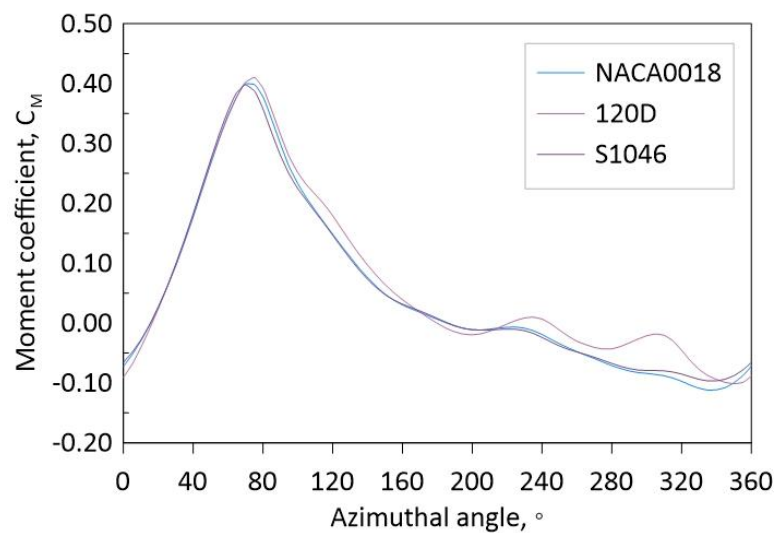


Fig 4.42. Instantaneous coefficient comparison single blade between baseline NACA0018 and candidate turbine 120D at TSR 1.

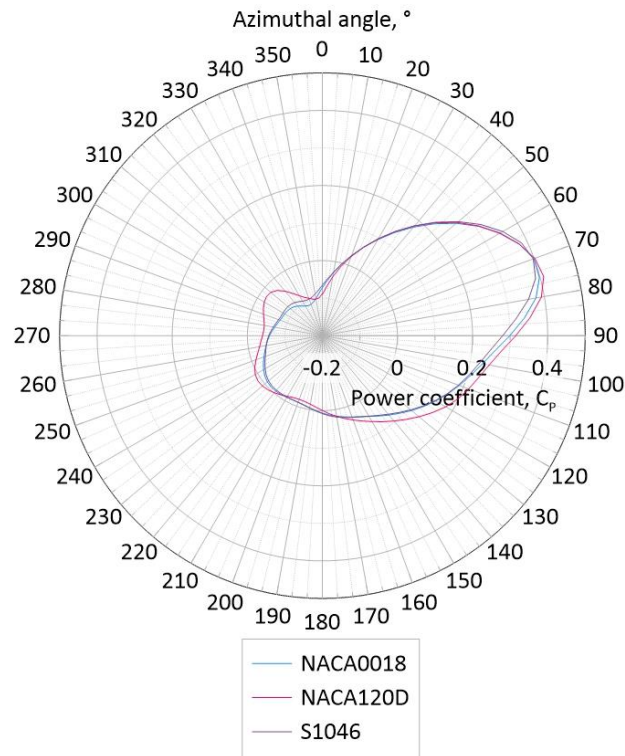


Fig 4.43. Polar plot of the instantaneous power coefficient comparison between the candidate 120D blade against the common symmetrical blades. Data taken at TSR 1.

4.7.2 Lift comparison – 3D Analysis

Fig 4.44 shows the lift coefficient comparison between all 3 blades. It was observed that the overall 120D shows higher lift between 0° to 80° . The S1046 blade showed highest lift coefficient at 120° . Thereafter, from 200° azimuthal angle onwards, the 120D blade showed the largest lift coefficient of the compared during the latter half of the leeward region, the downwind region and into the windward phase of the rotation. During the later stage of the downwind rotation, the 120D blade experienced higher lift, which peaked at 320° .

The Fig indicates the 120D blade showed more similar lift characteristics with the NACA0018 between latter half of the upwind and initial stages of the leeward region. During the first half of the rotation, the 120D blade showed better lift during the upwind region whereas the S1046 performed better during the leeward region. The 120D blade showed better lift thereafter during the downwind region with a noticeably large peak at the transition region as the blade exits the downwind and enters the windward region. Most importantly, a cambered blade tends to perform better during the downwind phase of the turbine rotation and, in the case of

the 120D candidate blade, the adjoint-optimized blade performed better than the compared S1046 blade. A blade pressure analysis was conducted in a later subsection with regards to the observations made in this Fig.

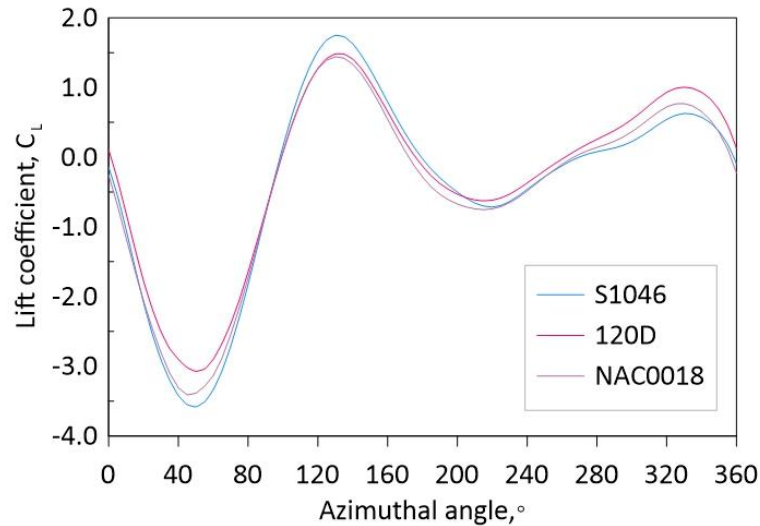


Fig 4.44. Lift coefficient comparison. Data taken at TSR 1.5.

4.7.3 Flow Contour Comparisons

In the previous section, various performance coefficients of the candidate 120D turbine were compared against the baseline NACA0018 turbine and S1046 turbine. The following section discusses the flow contour with respect to velocity, pressure, and streamline contour comparisons of the 120D against the baseline NACA0018 turbine and the cambered S1046 turbine.

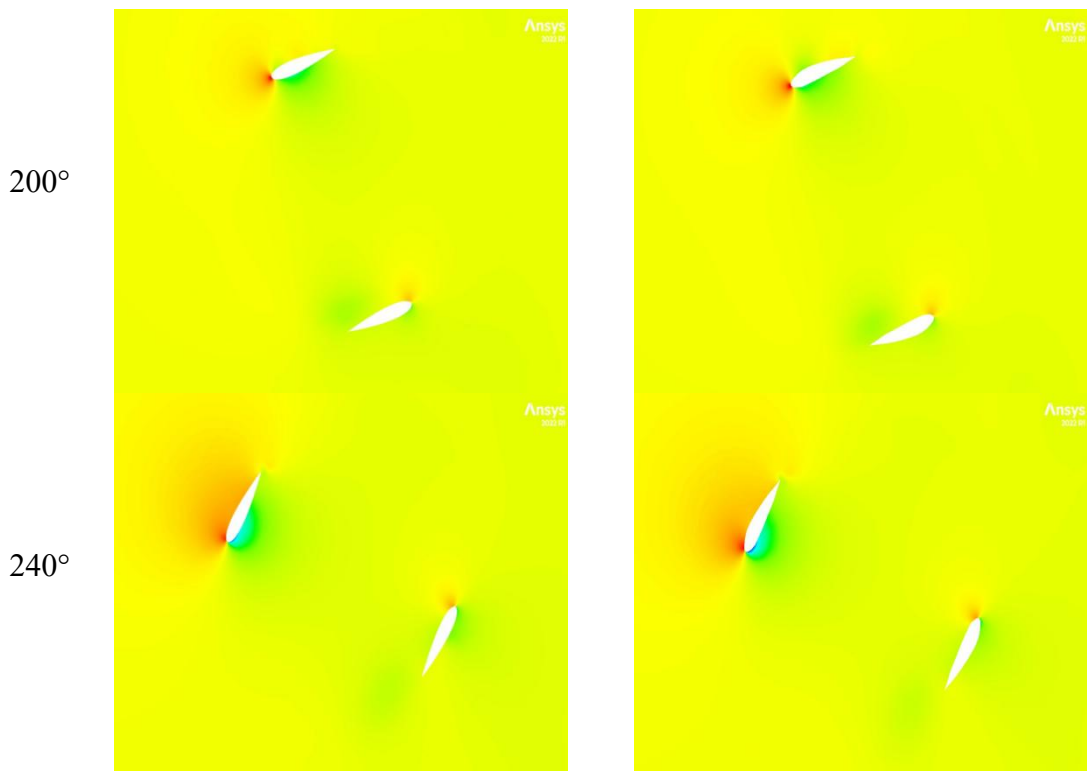
4.7.3.1 Pressure contour comparisons – NACA0018 and 120D

Fig 4.45 shows the pressure contour comparison between the NACA0018 and 120D turbines. As was previously discussed, a significant point of difference between the turbines is mainly seen in the downwind region where the 120D performed better with respect to turbine power production. In this section, snapshots of the pressure contour were taken at 200°, 240°, 280°, and 320°. The azimuth angle designation was named in reference to the position of the first turbine blade during the downwind phase of the rotation.

At 200°, from Fig 4.45(a), it was observed that both NACA0018 and 120D turbines showed similar pressure contour with little pressure difference as the blade exits the leeward region and enters the downwind region. The first blade, at 40°

azimuth angle, a difference can be observed at the upper surface of the blades. The upper surface of the upper blade shows lower pressure similar to the inner surface. Compared to the NACA0018 blade, this indicates a lower pressure difference between the upper and lower surface of the blade which would explain the previous observation of reduced performance during the upwind region.

At 240°, the overall contour shows similar characteristics. However, when looking closer, it can be observed that the pressure magnitude experienced by the 120D blade in the downwind region is higher than the NACA0018 which is more conducive for higher lift and more efficient power production. The blades in the upwind region however show significant difference observed at the leading edge. The 120D blade shows more pressure difference than the NACA0018 blade. Similar observations can be seen at the 280° instance. As the blade exits the downwind region and enters the windward phase at 320°, it can be observed that the negative suction pressure is more evenly distributed on the NACA0018 blade surface. However, this suction pressure is higher in magnitude and more concentrated on the leading edge of the 120D. These observations show how the 120D performs better during this stage of the rotation which was reported in the previous sections.



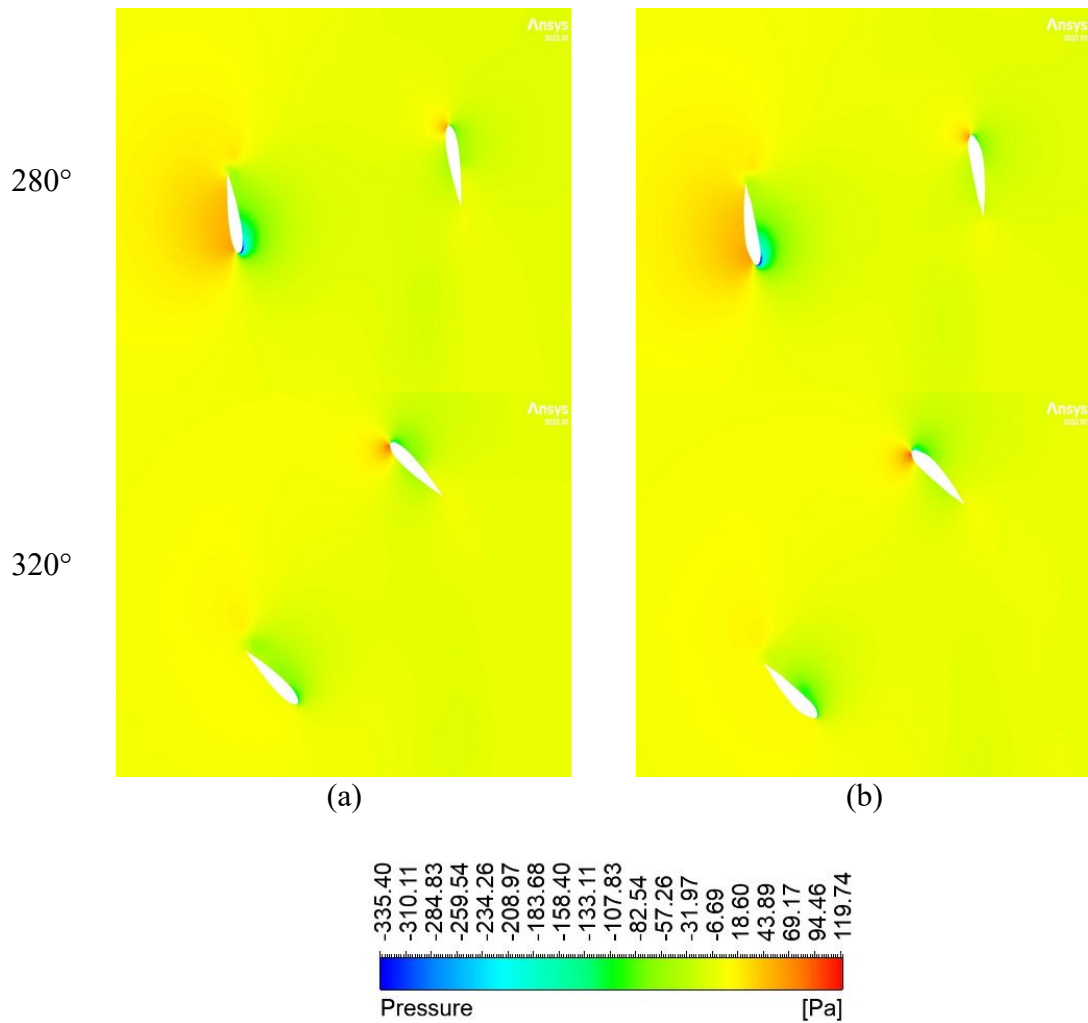


Fig 4.45. Instantaneous coefficient comparison single blade between (a) NACA0018 and (b) candidate turbine 120D at TSR 1.5.

4.7.3.2 Streamline comparisons – NACA0018 vs 120D

As was shown in the previous section, a significant difference between the NACA0018 and 120D blade was between the 200° and 320° azimuth angle or as the blade exits the leeward region, enters the downwind phase, and later exits into the windward region. Hence, in this analysis, a comparison was made of the 120D blade against the NACA0018 blade during the downwind phase of the turbine rotation.

Fig 4.46 shows the streamline contour comparison of the baseline NACA0018 and the candidate turbine 120D. At 200°, as the blade starts to exit the leeward region and enter the downwind region, a larger concentration of swirling or fluid circulation was observed at the inner surface of the 120D blade, indicating larger vortices forming at the lower surface of the 120D blade. Referring to Fig 4.42, this may have resulted in a loss of lift force as the resulting effect of this was shown

to have a reduction in moment coefficient during this phase of rotation. At 240° , from Fig 4.46(a) the outer surface of the NACA0018 blade showed a swirling streamlines indicating vortices forming at the outer surface of the blade. In Fig 4.46(b), the 120D, however, showed slight circulation towards the trailing edge of the outer surface. The inner surface of the NACA0018 blade showed thicker concentration of swirl compared to the 120D blade which indicates stronger vortex forming at the inner blade of NACA0018. At 280° , it was observed that a large swirl at the outer surface of the NACA0018 blade starts to detach from the surface of the blade. The 120D blade, however, showed two smaller swirling vortices at the outer surface. At 320° , the streamline pattern between the two blades were similar but the NACA0018 blade showed a larger swirl and therefore higher vortex intensity. Comparatively, although similar, the 120D blade showed slightly more streamlining of the flow as the blade exits the downwind region and enters the windward phase. This indicates a loss in vortex intensity of the first swirl seen previously during the 280° azimuth angle. The second vortex formed towards the trailing edge of the blade during the previous azimuth angle showed a disconnect from the first swirl which indicates shedding of the vortex.

Overall, the front hump of the 120D shifts the vortices forming at the outer of the blade backwards towards the trailing edge of the blade as was observed at 240° and 280° azimuth angles. This indicates a delay in flow separation and therefore better lift compared to the baseline NACA0018 blade during this phase of the turbine rotation. This effect showed a positive impact on the turbine moment coefficient during the downwind region. These observations were recorded in the previous section whereby the 120D performed better than the NACA0018 especially at 240° and about 300°

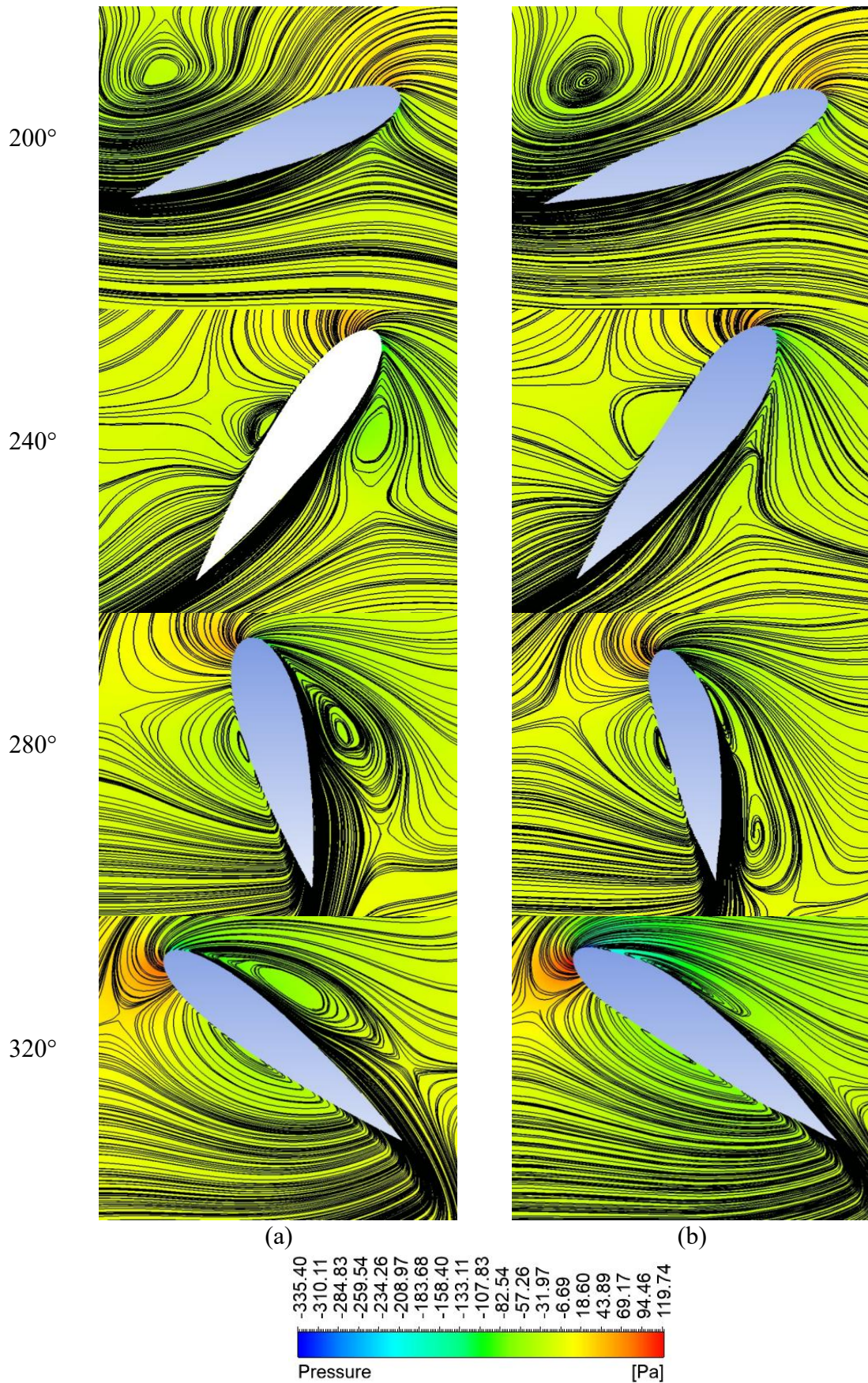
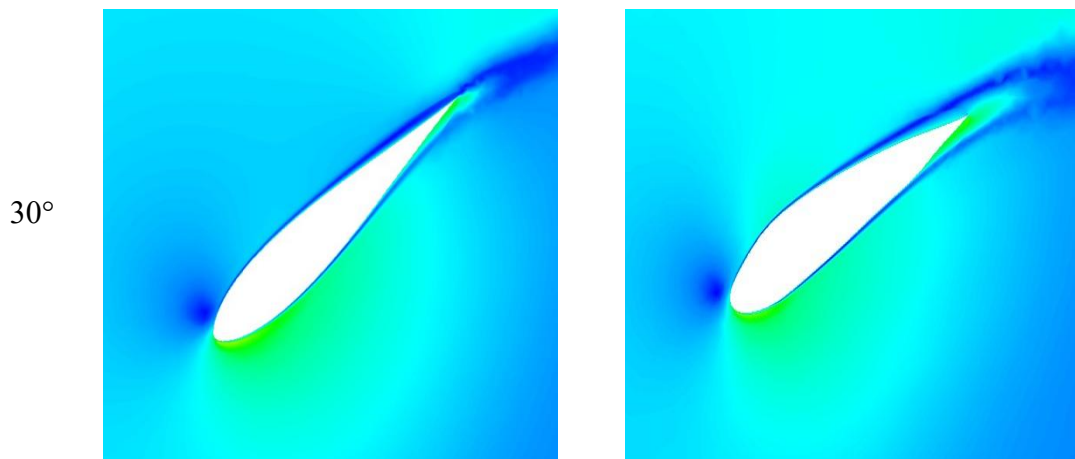


Fig 4.46. Streamline and pressure contour comparison between the (a) NACA0018 blade and the (b)120D blade at TSR 1.5.

4.7.3.3 Velocity flow contour comparisons – S1046 vs 120D

Fig 4.47 compares the velocity flow contour between the S1046 and 120D within the upwind region. At 30° , both the S1046, in Fig 4.47(a), and 120D, in Fig 4.47(b), blades showed similar overall flow contour. However, the upper surface contour of the 120D blade experienced a slightly higher velocity as evidenced in the Fig. At 60° , the leading edge of both blades displayed similar contour patterns with the 120D marginally higher in intensity. The boundary layer of the S1046 was more attached to the blade towards the trailing edge but the upward morphing of the lower surface caused the 120D blade to have a less attached boundary layer and, therefore, a more pronounced wake at the trailing edge. At 90° , the same observation was made with regards to the boundary layer of the 120D. Due to the straightened nature of the inner surface, the boundary layer separation occurred closer to the leading edge as opposed to the S1046 which occurred closer towards the centre of the blade. Again, this results in a more significant wake and vortex shedding from the trailing edge of the 120D blade. At 120° , the overall contours of both blades were identical as was expected since performance differences between the two blades in the previous moment analysis was also similar at this stage of the turbine rotation.



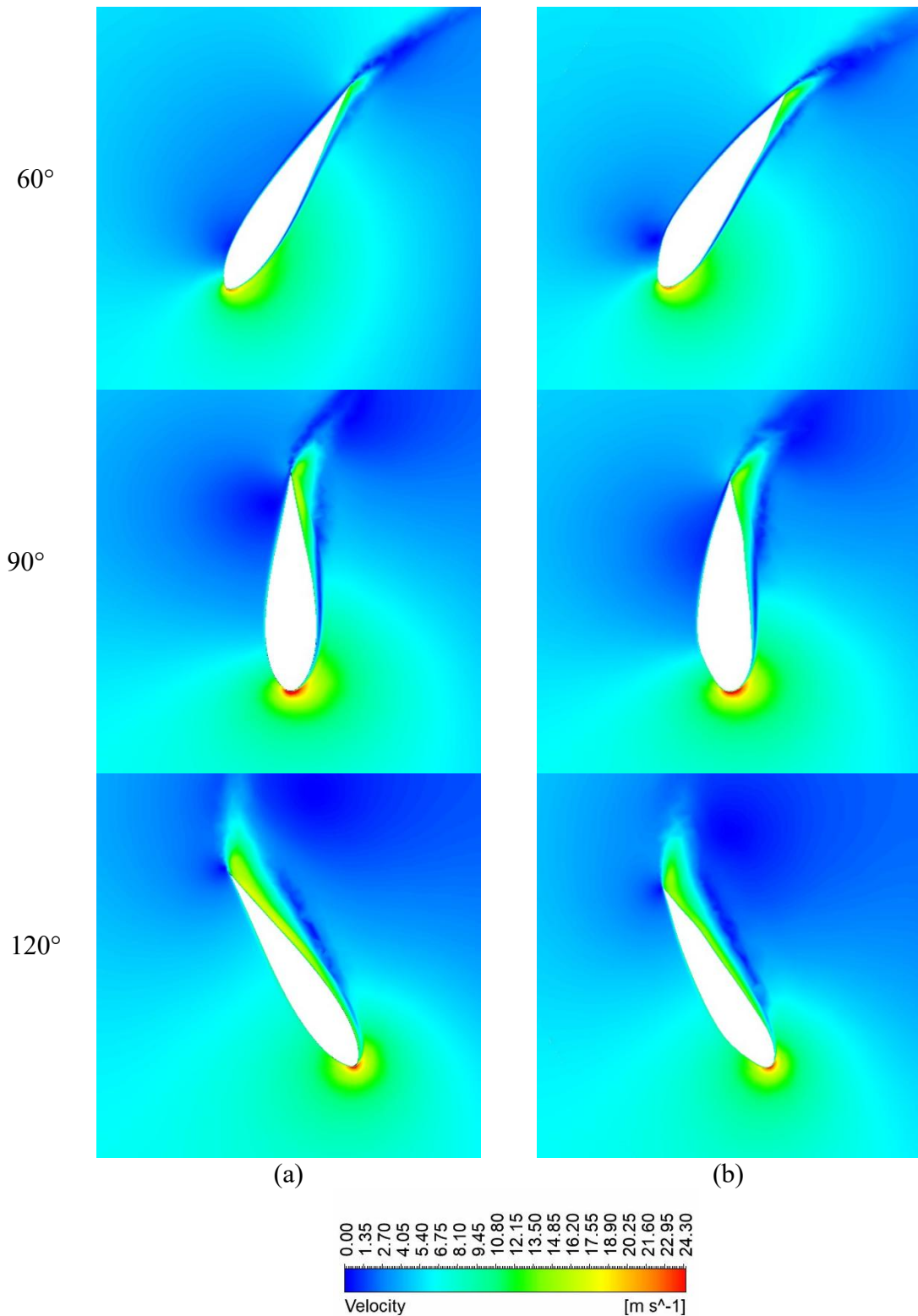


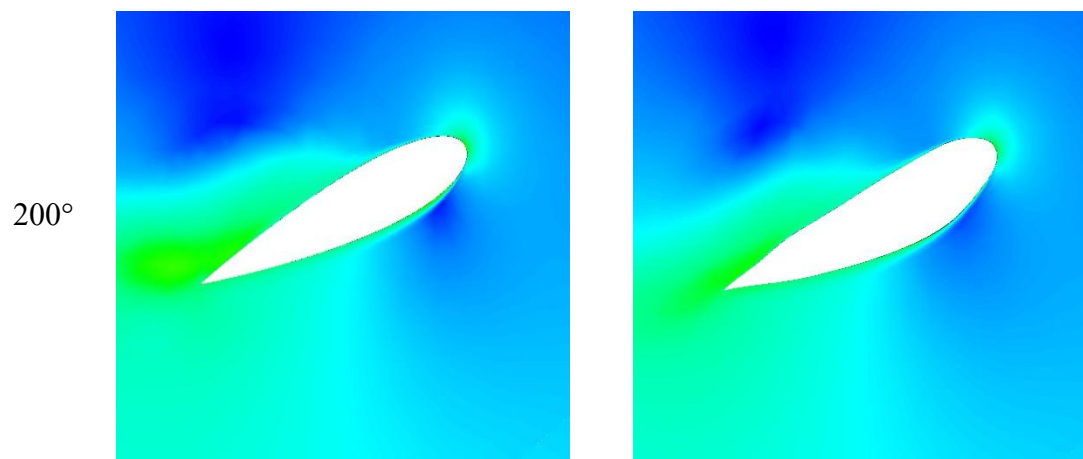
Fig 4.47. Velocity flow comparisons between the (a) S1046 and (b) candidate turbine 120D at TSR 1.5.

4.7.3.4 Velocity flow contour comparisons – NACA0018 vs 120D

From the previous moment coefficient and lift coefficient figures, it was observed that the 120D blade performed the most optimal during the downwind and windward

phase of the turbine rotation. Hence, a flow analysis was conducted for this turbine rotation phase shown in Fig 4.48. At 200° , the flow contour showed similar patterns enveloping both turbine blades with the NACA0018 blade showing slightly higher intensity at the trailing edge. This would match both the moment and lift coefficient curve showing negligible differences between the two blades at this stage of the rotation. At 240° , as the blade enters the downwind phase, the leading edge of the NACA0018 blade showed noticeably more chaotic flow than the 120D blade. At 280° and 320° , the previous observations were repeated. The 120D blade showed a more streamlined flow at the leading edge whereas the NACA0018 showed slightly more erratic contour.

These observations indicated an imminent flow detachment from the leading edge of the NACA0018 whereas the flow is more attached in the 120D blade. The 120D blade, with the slight hump at the leading edge, was able to reduce the flow detachment and therefore minimize dynamic stall during this phase of the rotation. This would, in turn, reduce the turbulent flow within the turbine which would lessen the flow impacting the incoming blade. With a flow more attached, lift was better maintained and therefore resulted in better moment production which was previously seen in Fig 4.42 and Fig 4.43.



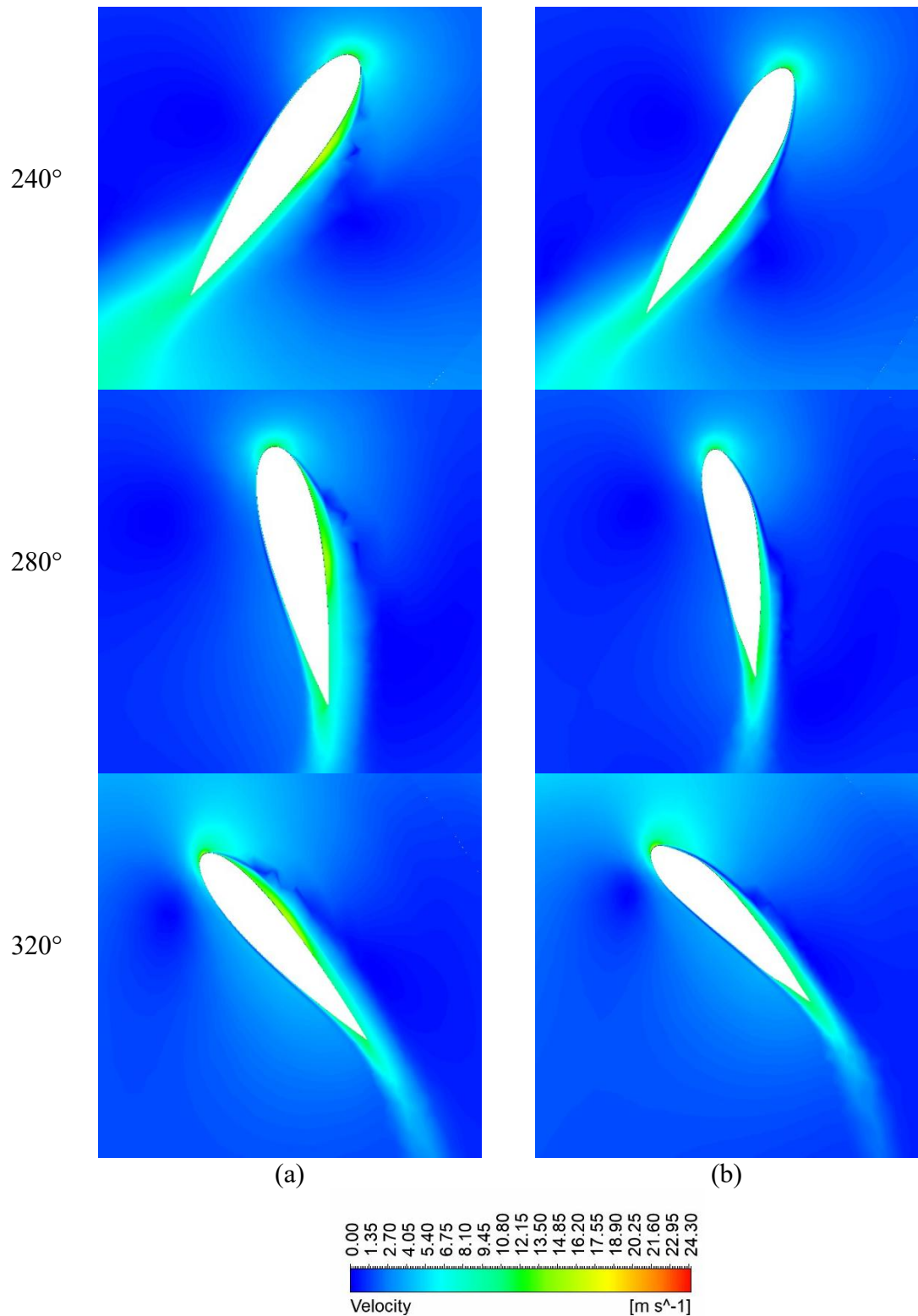


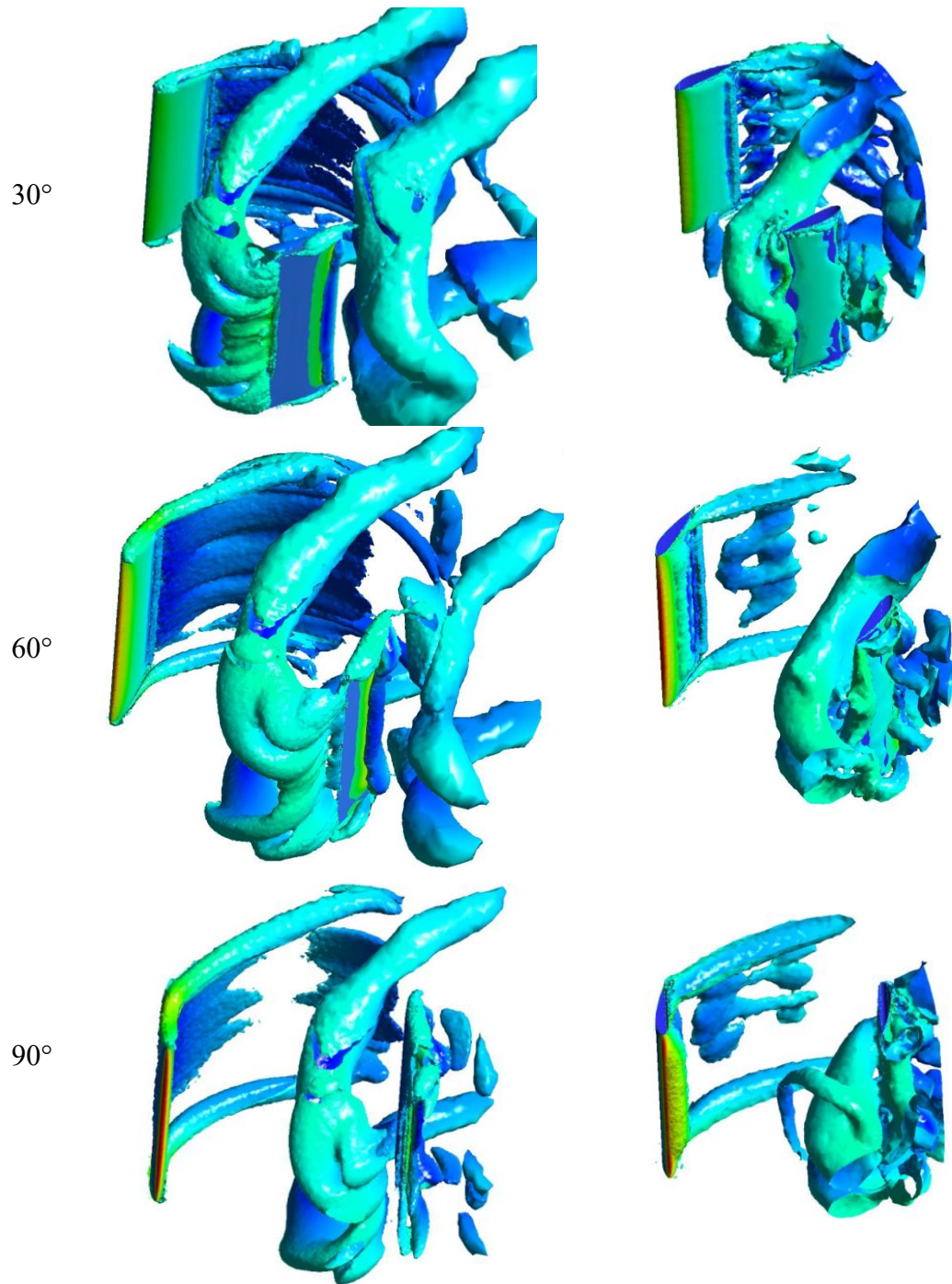
Fig 4.48. Velocity flow comparisons between the (a) NACA0018 and (b) candidate turbine 120D at TSR 1.5.

4.7.4 Vortex Q-Criterion comparison - S1046 vs 120D

The following section describes the flow of the turbine blades at different instances of turbine rotation. The azimuth angle designation was relative to the position of the

first turbine blade. The comparisons were taken at TSR 1.5. As shown in Fig 4.49, at 30°, the S1046 turbine produced larger vortical structures at the trailing edge of both blades. During this initial upwind phase, it was seen that the 120D blades produced lesser vortex compared to the S1046 blade in the same phase. Similar observations were made at 60°. The S1046 blade in the upwind region showed strong vortices at the trailing edge. However, the 120D blade in the same region showed a detachment of the vortices and mostly were concentrated at the blade tips of both ends. The second blade in the downwind region showed vortices enveloping the blade but of lower magnitude compared to the S1046 blade in the same rotational phase. At 90°, similar vortical structures and patterns were observed in both turbines with the S1046 showing larger structures at the trailing edge of the second blade within the downwind region. At 120°, both first S1046 and 120D first blades in upwind region entering leeward region showed concentrated vortices at the blade tips with the 120D blade showing slight vortex shedding along the blade span. Both turbines' second blade in the downwind phase before entering the windward region showed strong vortices shed mainly from the trailing edge. The S1046 blade, however, showed significantly larger vortical structures especially prominent from the blade tips.

Overall, the S1046 turbine blades produced more vortices during the turbine rotation which left a significant trailing edge wake. This, in turn, affected the next incoming blade and therefore resulted in higher effects of drag. Contrary to this, the 120D blade not only has an increased lift performance due to its optimized shape, but when looking at the turbine 3D performance, the 120D blade was found to also have lesser vortex shedding and therefore lesser negative drag effects for the incoming second blade. This result confirmed the improvement of the turbine flow field made by the 120D blade.



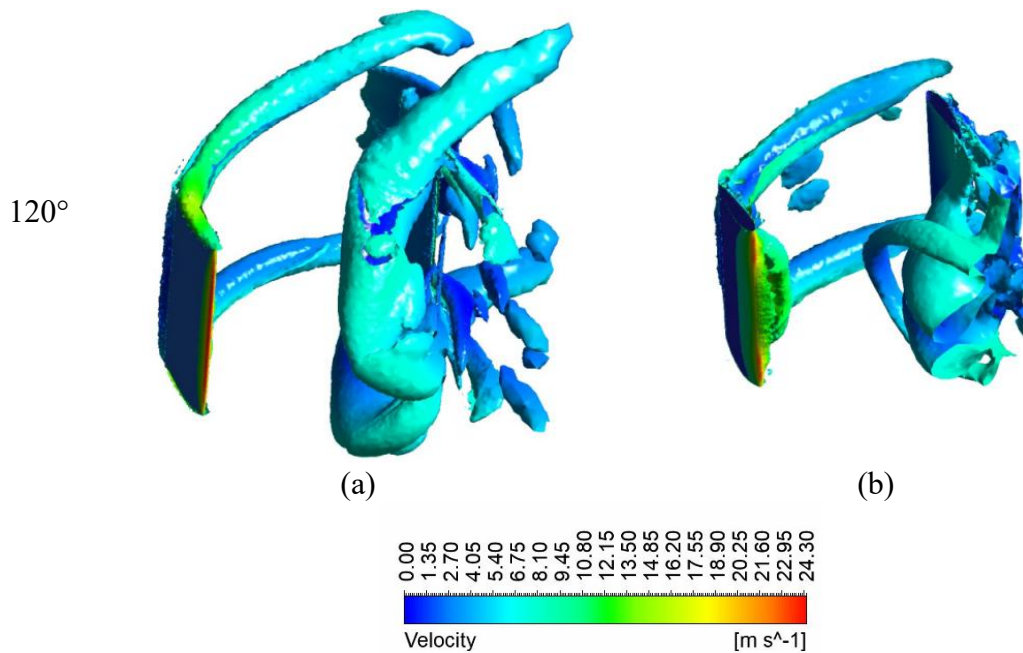


Fig 4.49. Q-criterion comparisons between the (a) S1046 and (b) candidate turbine 120D at TSR 1.5.

4.7.5 Blade surface comparison

Fig 4.50 compares the blade surface comparison between the three turbine blades. The comparisons were made at 40° and 320° where the 120D blade showed significant increase in lift coefficient against the NACA0018 and S1046 blades referenced from Fig 4.44. From Fig 4.50(a), at 40° , the 120D blade showed much lower negative pressure at -0.08m compared to both the NACA0018 and S1046. The loop towards the right side of the blade also showed a smaller area compared to the two baseline blades. At 320° , shown in Fig 4.50(b), whereby the lift coefficient also showed a higher curve compared to the baseline blades, the 120D blade much lower negative values on the left side of the curve as well as a larger loop area between 0.05 and 0.06m . This is consistent with the observations made in the 2D section at the same location. In this analysis, however, it can be conclusively shown that the increase in moment coefficient during this stage was also the results of increased lift during the initial stage of the windward region. While the observations here is similar to the ones made in the 2D section comparing the 120D blade with the NACA0018 blade, this 3D analysis of the blade surface pressure distribution also showed a better curve with larger area and therefore higher lift generated by the 120D blade against the S1046 blade. It was also noted that the intersection point, on the right – hand side of the curve, of the 120D blade was located between the NACA0018 and S1046.

This indicates a cambering or inward curving of the surface of the blade shifts the zero-pressure difference region towards the trailing edge of the blade.

The observations above explains how the 120D blade performed better during the initial upwind and windward phase of the rotation. The blade surface pressure analysis indicates that curve characteristics of the 120D blade showed a larger pressure difference between the upper and lower surface of the blade, indicated by the area of the pressure curve, which therefore promotes higher lift.

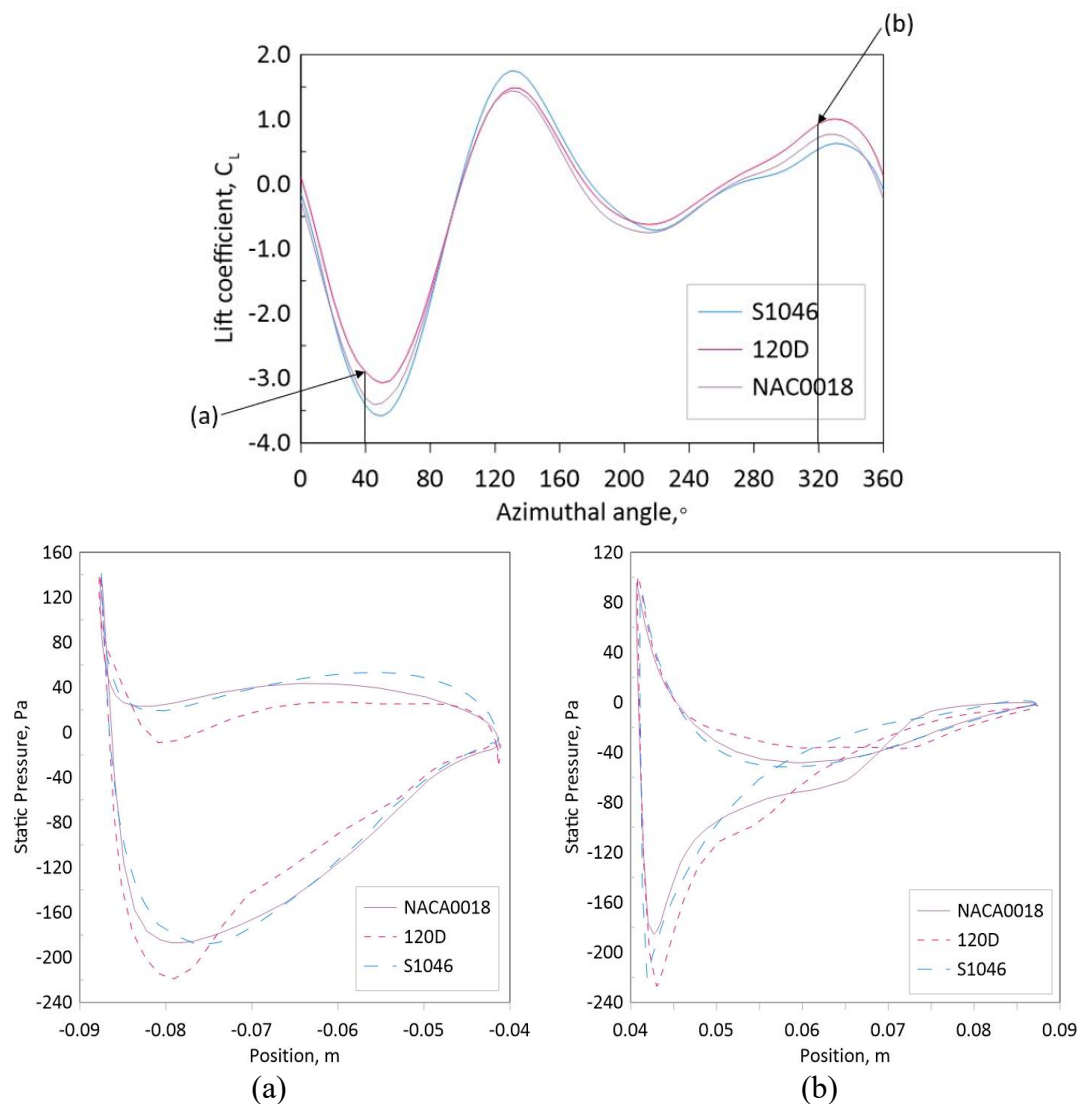


Fig 4.50. Pressure distribution analysis and comparisons at 40° and 320° azimuthal angles. Data taken at TSR 1.5.

4.7.6 3D Turbine Blade Analysis - Summary

The single blade optimization of the symmetrical blade NACA0018 using the adjoint method together with the gradient-based optimizer produced a candidate blade, 120D,

that has shown to be more efficient in power production compared to the baseline symmetrical blade. Comparisons of the 120D to the unsymmetrical S1046 turbine were also conducted and showed significantly better performance. From this study, the following conclusions were made:

- The 120D turbine was found to have a significant 20.42% and 15.18% increase in performance over the NACA0018 and S1046 turbines respectively.
- The main improvement of the 120D was observed during the downwind portion of the turbine rotation, showing significantly higher power production between 200° and 340° azimuth angles.
- Pressure contours showed the 120D generated less vortices and therefore experienced less drag effects during the downwind phase of the turbine rotation.
- 3D visualization of the Q-criterion showed large formations vortices around the S1046 blade which indicated higher drag effects affecting the turbine blades during rotation. The 120D however showed the opposite with less vortices and therefore more aerodynamically efficient to produce power.
- Hence, the 120D has been shown to be optimized.

This study demonstrated the optimized blade 120D against two known symmetrical blades: uncambered NACA0018 and cambered blade S1046. The results above have shown that, when 3D effects were considered in the numerical simulation, the 120D blade still showed higher performance over the two baseline blades. However, the study only showed the performance of the turbine blades without any support structures in place. In the subsequent section, a full turbine configuration, together with support-arms analysis, was performed.

4.8 Adjoint Method Shape Optimization of a Vertical Axis Wind Turbine: 3D Analysis and Characterization of The Full Turbine Configuration with Turbine support-arms

An extension of the previous section, this study now focuses on the full turbine configuration performance comparing both the conventional turbine with both NACA0018 blade and support-arms against the 120D with the candidate geometry

120D also applied to the turbine blade and support-arms. The results showed a significant average improvement of 12.5% increase over the baseline turbine over the range of tested TSR. Applying the same 120D blade geometry onto the turbine support-arms yielded better results with respect to aerodynamic forces and power production of the turbine. The results showed promising use of the adjoint method for VAWT optimization that may be applied to other VAWT blades in different configurations or under different turbine conditions.

4.8.1 3D Full Turbine Comparisons

The following section compares the 3D CFD results between the NACA0018 turbine and 120D turbine. Fig 4.51 shows the results of the 3D turbine comparison between the candidate 120D turbine and the NACA0018 turbine. It was observed that the 120D turbine is more optimized than the NACA0018 turbine. As the turbine starts at the lower TSR range, the NACA0018 turbine was marginally better. However, there was an incremental increase in difference favouring the 120D turbine starting from 4.30% at TSR 1 and 50.76% TSR1.75 with respect to the power coefficient. The maximum power coefficient was also found to have shifted between the two turbines. The maximum power coefficient for the NACA0018 turbine was found at TSR 1.25 whereas the 120D turbine was shifted up to TSR 1.5. The average increased power coefficient uplift of the 120D over the baseline NACA0018 turbine over the simulated range of TSR was 12.5%.

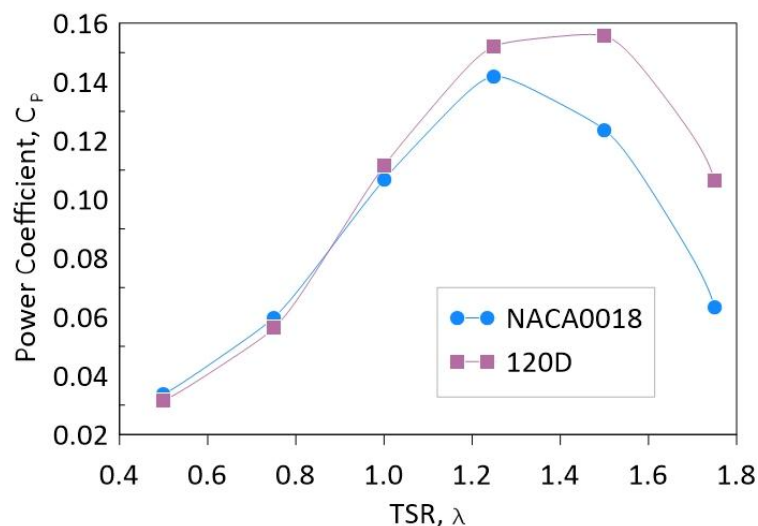


Fig 4.51. Power coefficient comparison between baseline NACA0018 and candidate turbine 120D.

Fig 4.52 compares the instantaneous single blade support-arm moment coefficient full turbine configuration between the NACA0018 and the 120D taken at TSR 1. The NACA0018 blade combination has a higher maximum peak at 80° whereas the maximum peak of the 120D was found to be slightly before that at 75° . Thereafter, the moment coefficient curve was similar between the two as the blade passes from the upwind region into the leeward phase of the rotation. From 200° onwards, as the blade started to exit the leeward region and enter the downward phase, the difference in moment coefficient was found to be more pronounced as the 120D experiences a higher increase in moment coefficient compared to the NACA0018 blade combination. This trend was consistent throughout the rotation from the downwind phase and into the early phase of the windward region. The NACA0018 blade combination was also found to have a smoother curve after 240° compared to the 120D which experiences more erratic peaks and troughs particularly between 280° and 320° where a large bump in moment efficiency was observed. This indicated that the optimization scheme was able to reduce aerodynamic losses within the downwind area.

Although, by design, the VAWT usually extracts most power during the upwind phase of the rotation, the optimized candidate blade was found to also minimize the effects of power coefficient losses during other phases of the turbine rotation. The blade camber, resulting from the optimization, was found to increase in the blade efficiency in the downwind region which then has a positive effect on the overall turbine performance, maximizing power extraction not only within the traditionally upwind region but also within the downwind region. This observation is consistent with the findings of Castelli et al (Castelli et al. 2012) whereby the authors also found cambering a NACA0021 blade improves the power coefficient in the downwind phase but slight poorer efficiency in the upwind region.

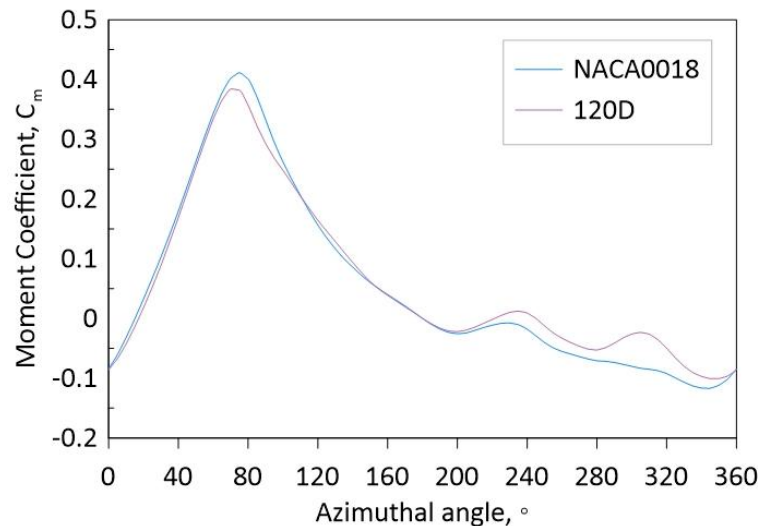


Fig 4.52. Instantaneous coefficient comparison single blade and support-arm between baseline NACA0018 and candidate turbine 120D at TSR 1.

4.8.2 Lift And Drag Coefficient Comparisons of Main Turbine Blade

The symmetrical blade of the NACA0018 has been generally well known. The novel shape of the 120D blade, however, is a newly generated blade shape with a different aerodynamic characteristic compared to the baseline blade. Fig 4.53 shows the lift and drag coefficients of the 120D blade compared to the NACA0018 turbine blade. The comparisons were made at $Re\ 30 \times 10^3$. Fig 4.53(a) instantiates the lift coefficient comparisons between the two blades. As expected, the 120D blade showed significantly higher lift coefficient during the positive angle of attack and lower lift coefficient during the negative angle of attack. The unsymmetrical profile of the blade allows a pressure difference that favours lift even at 0° angle of attack. While both blades have a stall angle of attack of 8° , the lift coefficient was found to continue increasing in the case of the 120D blade. The drag coefficient comparison was shown in Fig 4.53(b). The overall curve showed significantly higher drag effects experienced by the 120D blade compared to the NACA0018 blade. The symmetrical shape of the NACA0018 was expected to experience lower drag effects at lower angles of attack. In the case of the 120D, however, the front hump of the blade design means an increase in the frontal area of the blade and therefore larger drag coefficient. Both lift and drag figure comparisons showed the unsymmetrical blade shape of the 120D not only yielded a significantly higher lift coefficient, but also experienced higher drag effects as the blade angle of attack increased.

Comparing the lift to drag ratio between the two blades in Fig 4.53(c), it was shown that, at positive angles of attack, the symmetrical NACA0018 showed marginally higher ratio up to 8° , which then reduces significantly due to the drop of lift towards 0° as the angle of attack increased. The 120D showed a lesser drop at similar angles of attack. The differences showed that the significant gain in lift of the 120D reduces the impact of the increased drag coefficient. Hence, even at higher angles of attack, the ratio shows the lift generation is still stronger than the drag effects. At negative angles of attack, the 120D showed higher lift to drag ratio.

Lastly, comparing the lift vs drag curve of both the blades in Fig 4.53(d), the NACA0018 expectedly showed a tighter curve. The 120D however showed a significantly larger curve than the NACA0018 blade. The curve characteristics of the 120D indicated that the lift effects of the blade were more dominant even as the drag coefficient increased. This was shown at C_D value of 0.5 to 0.75 whereby the increase in drag coefficient was also followed by the increase in lift coefficient.

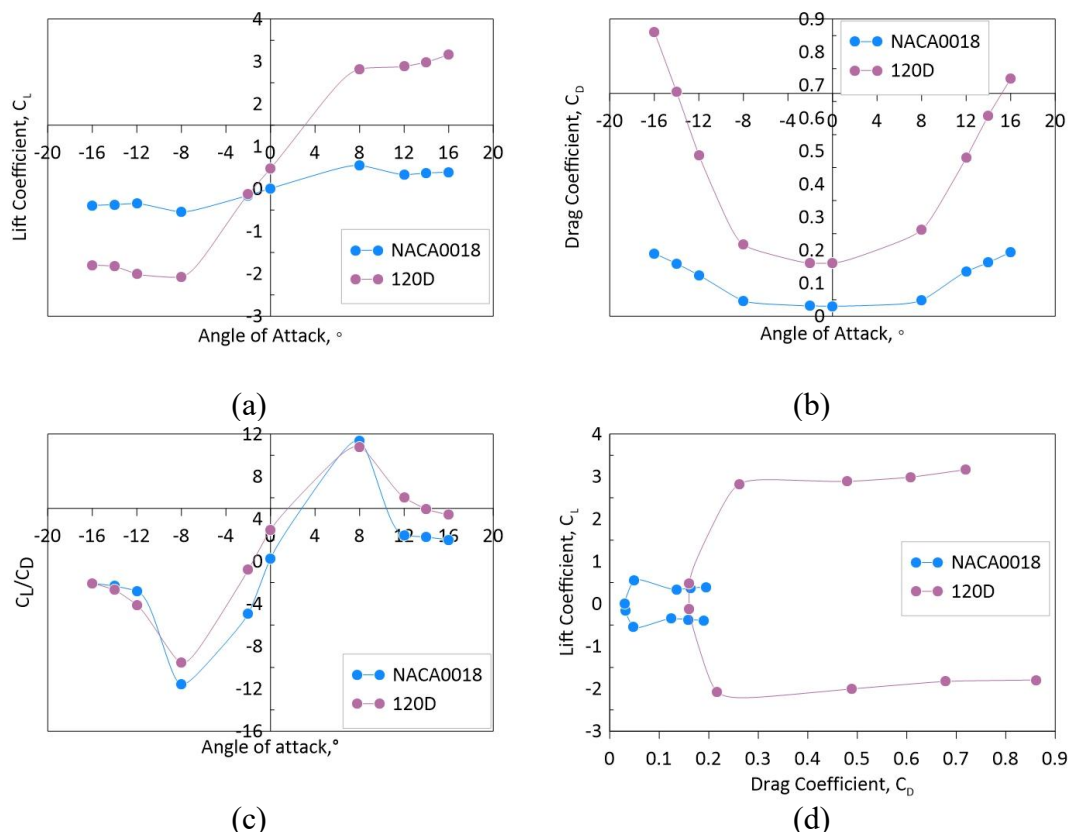


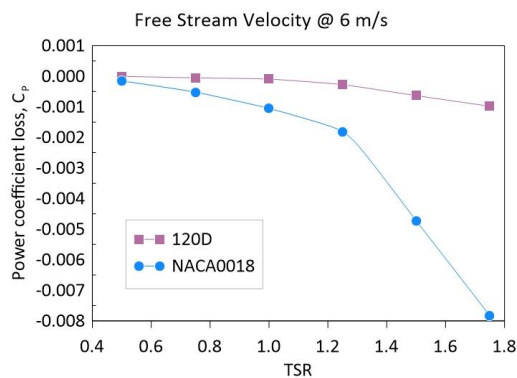
Fig 4.53 (a) Lift coefficient vs angle of attack, (b) drag coefficient vs angle of attack, (c) lift to drag ratio vs angle of attack, and (d) lift coefficient vs drag coefficient.

4.8.3 Turbine support-arm performance

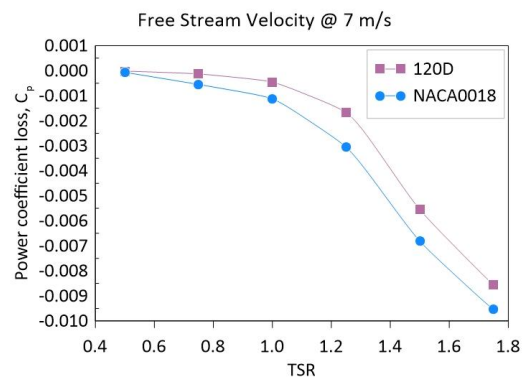
In the previous sections, the overall turbine performance was analysed and discussed. Next, a thorough performance analysis and evaluation of the support-arm geometry was conducted. Comparisons of power production as well as aerodynamic forces such as lift and drag characteristics were presented between the NACA0018 and 120D geometry.

4.8.3.1 Support-arm performance comparisons

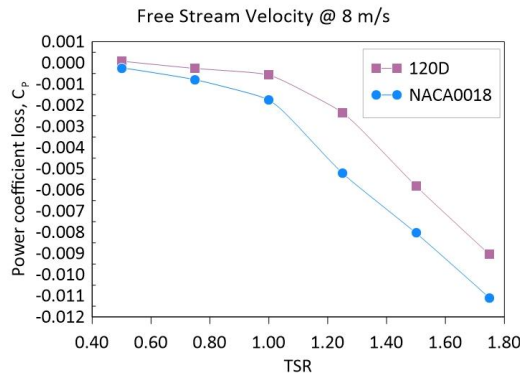
Both turbine configurations featured similar blade geometry to its turbine blade geometry. In this section, the support-arm effects on the turbine power coefficient were measured and quantified. The analysis was conducted at 3 different inlet wind speeds as shown in Fig 4.54. In all wind speed cases, the NACA0018 geometry showed higher percentage losses than the 120D. The test case at 6m/s, shown in Fig 4.54(a), the difference in average power coefficient loss between the two arm geometries was 174.75%. In Fig 4.54(b), the percentage difference at 7m/s was the lowest of the velocities compared at 65.72%. The percentage difference at 8m/s, shown in Fig 4.54(c) was 119.43%. In all wind speed test cases, it was observed that the percentage difference between the NACA0018 and 120D support-arm was larger at the lower TSRs but reduced as the TSR value increased. This indicated that, as the TSR value increased, both blades show similar characteristics in terms power coefficient losses.



(a)



(b)



(c)

Fig 4.54. Power coefficient losses comparisons at (a) 6m/s, (b) 7m/s, and (c) 8m/s.

Fig 4.55 shows the percentage power coefficient loss comparison between the 120D and NACA0018 support-arm. It was observed that as the TSR increases, the power coefficient loss due to both support-arm structures increased. This showed that as the turbine rotation increased, the power coefficient losses increased more with the NACA0018 support-arm than the 120D. However, the 120D experienced much lower percentage losses over the tested TSR range compared to the NACA0018 support-arm. On average, the percentage difference between the two arm geometries was 65.72% in favour of the 120D. This observation could be scaled further for different or bigger turbine sizes.

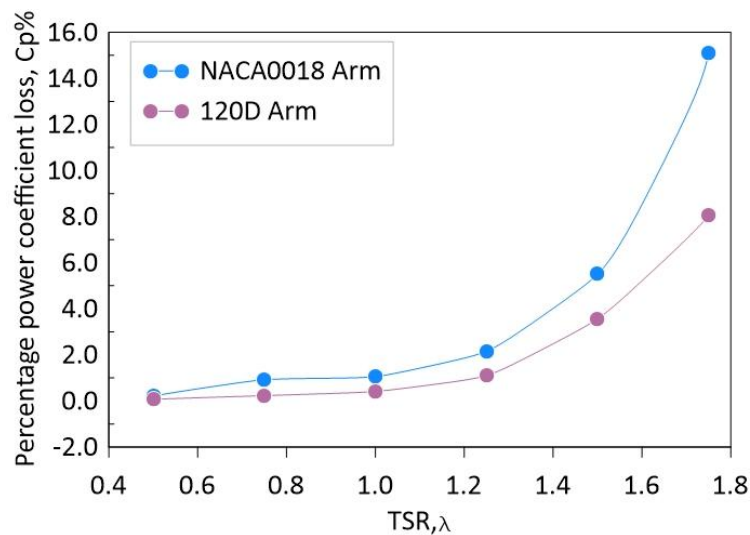
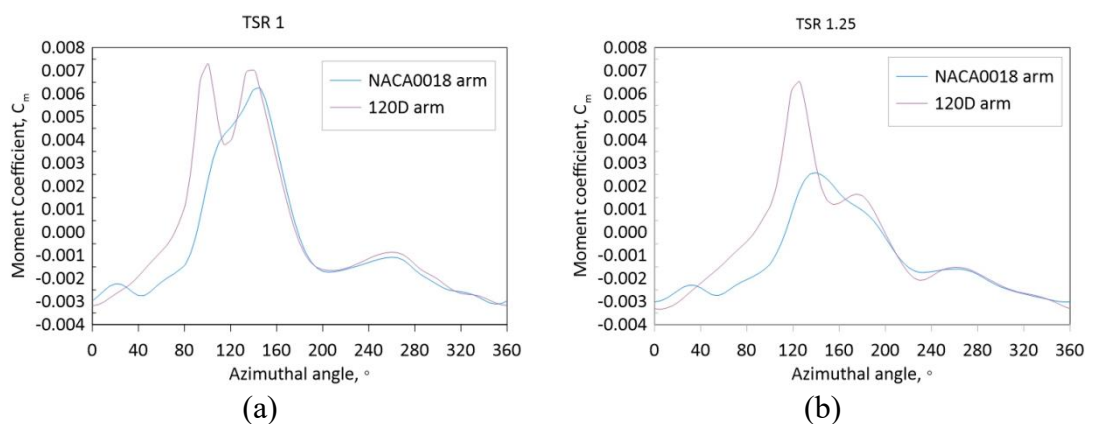


Fig 4.55. Percentage power coefficient loss comparison between baseline NACA0018 arm and candidate turbine 120D.

Fig 4.56 shows the instantaneous moment coefficient comparison of a single support-arm at multiple TSR ranges. From Fig 4.56(a), at TSR 1, a dual peak at 90° and 140° was observed. This would indicate a sudden shift in fluid flow conditions

which may have caused flow separation or detachment at the first higher peak (90°), then a reattachment at 120° which later peaks at 140° . At TSR 1.25, from Fig 4.55(b), the dual peak was shifted to 120° and 180° azimuthal angle. The first higher peak occurred at the end of the upwind region and the second occurring at the beginning of the leeward phase. At TSR 1.5, from Fig 4.56(c), the 120D moment coefficient peak was again shifted forward to 140° which is within the leeward region. Lastly, at TSR 1.75 from Fig 4.56(d), the maximum 120D moment efficiency was extended from 80° to 160° before dropping lower than the NACA0018 support-arm.

At all instances, it was observed that the NACA0018 curve characteristics did not vary much and consistently peaked at the initial stage of the leeward rotation phase. It was also observed that the NACA0018 arm tended to perform better during the windward phase between 0° to 30° . However, the curve characteristics of the 120D arm varied significantly from one TSR to the next. A common characteristic of all the 120D curve in all TSR cases, however, is that the 120D blade consistently showed higher moment efficiency throughout the upwind phase and into the initial stage of the leeward region. Overall, in all the cases presented, the biggest performance increase was observed in the upwind region. The Figs showed that, at all TSR ranges, the 120D arm yielded better performance with respect to moment coefficient compared to the NACA0018 support-arm particularly within the upwind region. The cambered nature of the blade may have played a part in the higher peaks than the symmetrical NACA0018 blade which would produce different flow characteristics that are more conducive for better moment production seen in the previous Fig 4.54.



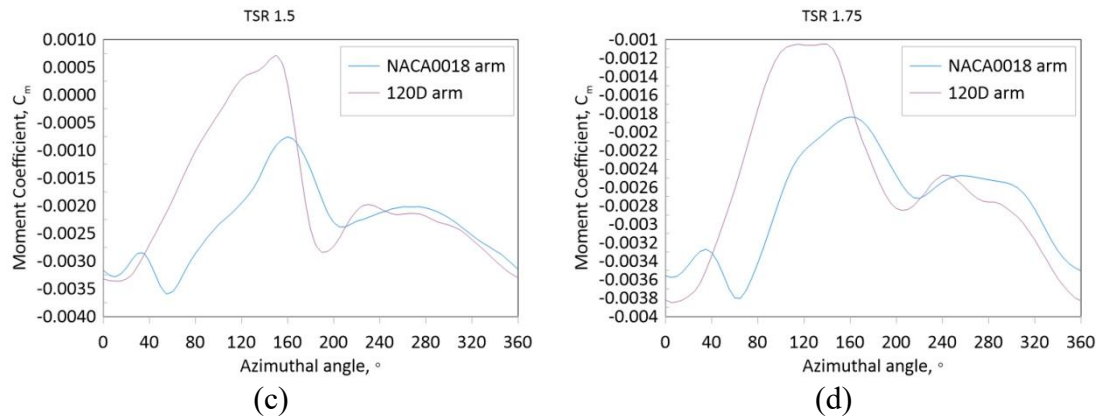


Fig 4.56. Instantaneous moment coefficient comparison single arm between baseline NACA0018 and candidate turbine 120D at (a) TSR 1, (b) TSR 1.25, (c) TSR1.5, and (d) TSR1.75.

Fig 4.57 shows the power coefficient curve over a single turbine rotation comparison between the NACA0018 support-arm and the 120D arm. It was observed that the 120D has much higher peaks between 40° to 160° and 220° to 350° and much lower troughs 0° to 40° and 170° to 220° compared to the NACA0018 blade. This would indicate the cambered shape of the 120D was able to optimally perform better within the upwind and downwind region but performs poorer during the windward and leeward region compared to the NACA0018 arm. It was also observed that there was a phase shift in that the 120D increases in power coefficient and peaked sooner compared to the NACA0018 arm. The NACA0018 blade showed unsteady oscillations between 0° to 80° and 180° to 260°. This is in stark contrast to the 120D arm, however, which showed a significant increase in power coefficient during these stages of the rotation. The observations made here explain how the 120D geometry has a better and more positive effect on the power coefficient losses compared to the NACA0018 arm. Also shown is the average power coefficient of each support-arm geometry with the 120D showing a 20.39% performance uplift over the NACA0018 arm.

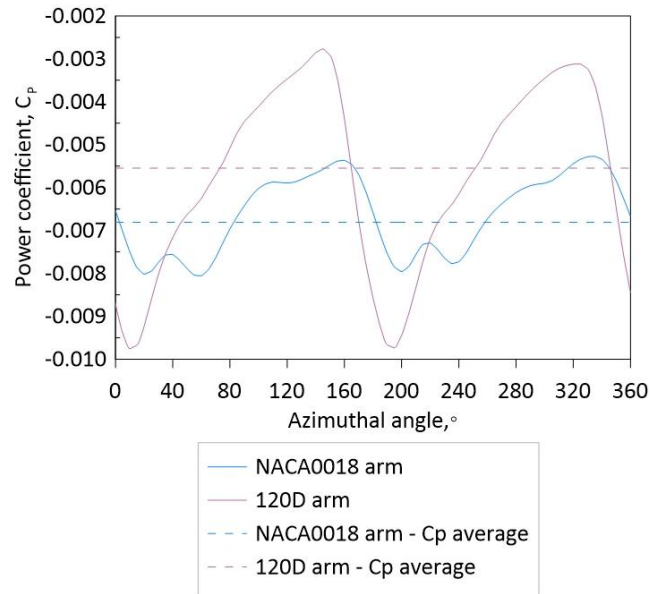


Fig 4.57. Power coefficient curve comparison between the NACA0018 support-arm and 120D support-arm over a single turbine rotation.

Fig 4.58 shows the power coefficient comparisons between the NACA0018 support-arm and the 120D support-arm. The NACA0018 showed higher efficiency during the windward phase of the rotation between 350° and 30° and the leeward region between 170° to 220° . However, the 120D curve showed significantly higher power coefficients during the upwind and downwind region, indicating that the cambered arm geometry has less parasitic effect towards power production of the turbine during these stages of the rotation.

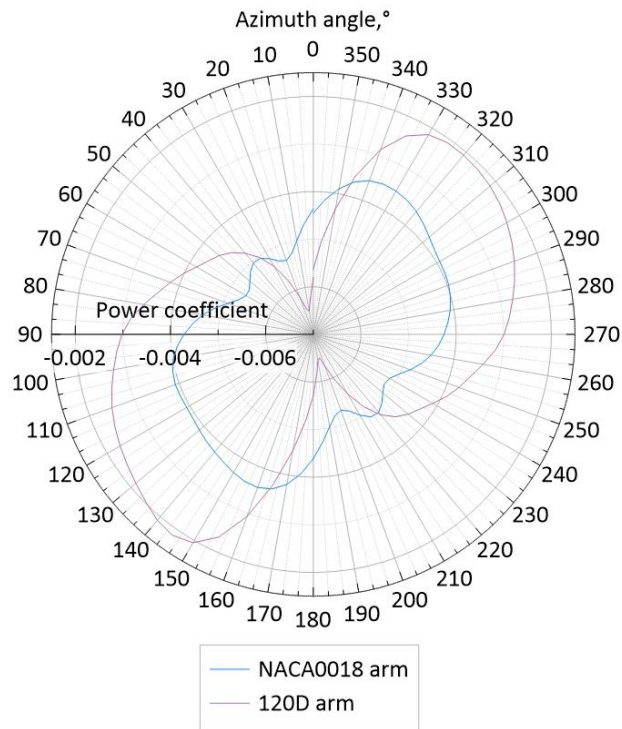


Fig 4.58. Polar plot of power coefficient curve comparison over a single turbine rotation taken at TSR 1.5.

4.8.3.2 Support-arm aerodynamic characteristics

The following section discusses the lift and drag performance coefficients with respect to lift and drag. Fig 4.59 shows the lift coefficient curve comparisons between the candidate blade and the baseline NACA0018 blade. Fig 4.59(a) illustrated the algebraic sum of turbine support-arms comparison. It was observed that the 120D blade peaked lower than the NACA0018 blade. The overall curve was also much lower, mostly within the negative region. The lift coefficient of 120D was the lowest at 120° and 300° . Referring to the previous section, these locations coincide with the power coefficient peaks during the transition phase from upwind into the leeward region and the downwind into the windward region. The 120D blade also peaked earlier at 40° and about 220° azimuthal angles whereas the NACA0018 support-arm blade, in both similar instances, peaked 40° later. Fig 4.59(b) shows the single blade curve comparison with respect to the lift coefficient. Similar observations were made whereby the NACA0018 blade peaked later than the 120D by about 40° . This showed that the NACA0018 support-arm peaked within the centre of the upwind phase whereas the 120D support-arm peaked earlier just as the blade entered the upwind region. A small peak was observed at 180° azimuthal angle. The

overall lift coefficient curve showed a much lower overall lift experienced by the 120D blade compared to the NACA0018 blade.

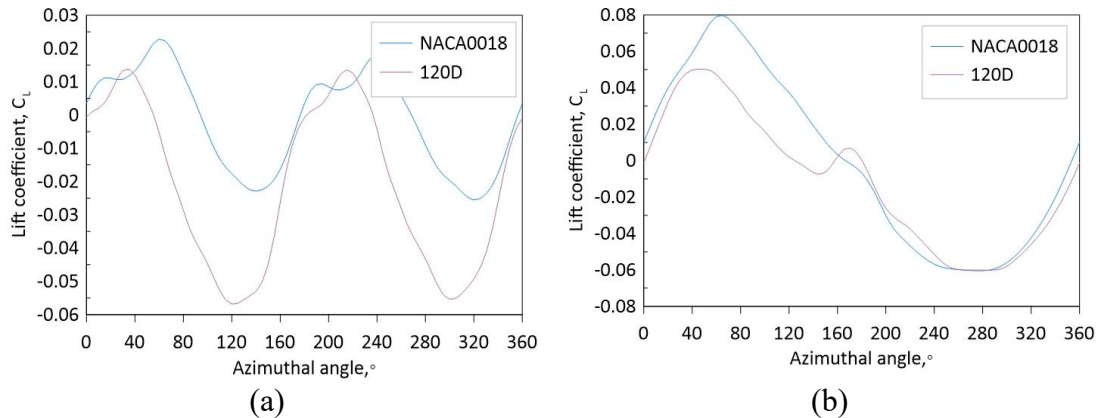


Fig 4.59. Lift coefficient curve comparison (a) algebraic sum of arms (b) single support-arm over a single turbine rotation taken at TSR 1.5.

Fig 4.60 shows the drag coefficient curves. From Fig 4.60(a), it was observed that the algebraic sum of both 120D support-arms has a higher peak than the NACA0018 arm. Like the previous observations of the lift coefficients, it was also observed that there was a phase lag between the two blades with the 120D peaking earlier at 140° and 320° whereas the NACA0018 support-arm peaked at 180° and 340° . The drag curves showed higher values of 120D than the NACA0018 blade between 80° and 160° as well as between 270° to 340° . This indicated that the 120D support-arm experienced higher levels of drag during the upwind and downwind region. Fig 4.60(b) shows the single blade curve comparison between the candidate turbine and the NACA0018 turbine with respect to the blade drag coefficient. The 120D showed a higher peak at 140° and lower trough at 180° . It was also observed that there was a distinct overall shift in drag at 180° with the 120D exhibiting higher drag than the NACA0018 in the first half of the rotation but the NACA0018 arm showing higher drag in the later half. This showed that the 120D experienced higher drag during the upwind phase whereas the NACA0018 blade experienced higher drag during the downwind phase.

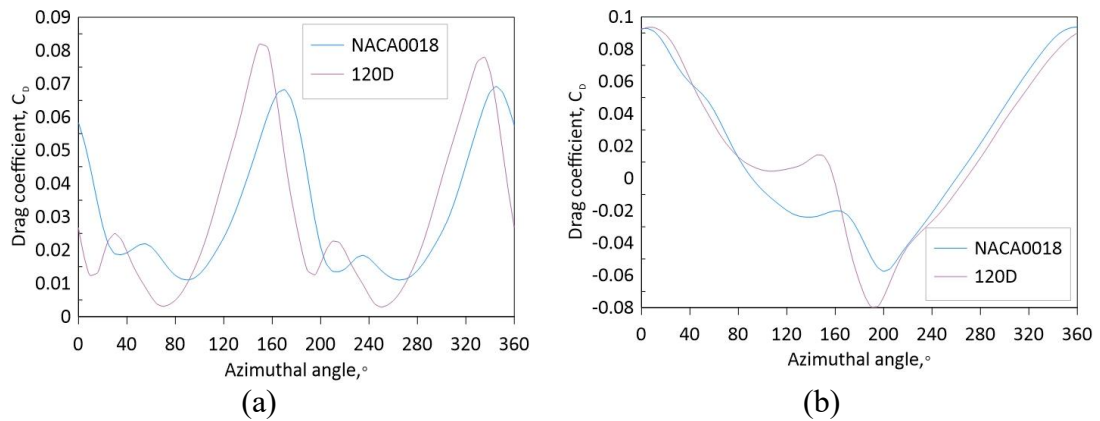


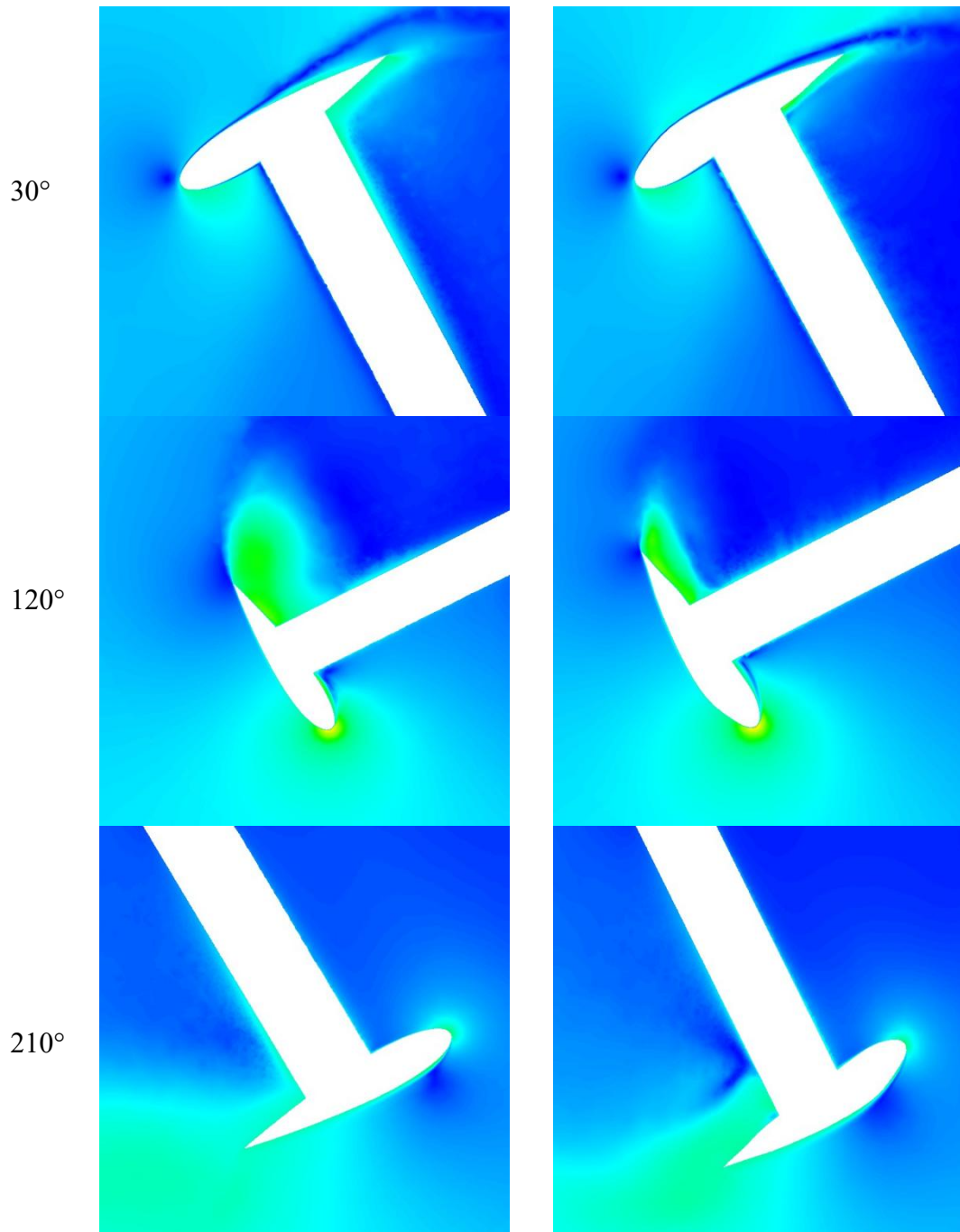
Fig 4.60. Drag coefficient curve comparison (a) algebraic sum of arms (b) single support-arm over a single turbine rotation taken at TSR 1.5.

4.8.4 Velocity Flow Contour - Full Turbine Configuration

Fig 4.61 shows the velocity flow contour comparison between the two blades. Unlike the analysis in the previous section 4.7, here, the effects of the turbine blade support-arms on the flow physics were considered. At 30° , the leading edge of the NACA0018 showed vortex shedding at the on the upper surface. This phenomenon was not observed with the 120D blade which showed a much more streamlined flow at the same location. The trailing edge of the NACA0018 also showed higher intensity of high velocity indicating higher shedding compared to the 120D. At 120° , large shedding was observed at the trailing edge of the NACA0018 blade. The blade – arm connection showed this. The 120D blade, however, showed smaller flow at the trailing edge. At 210° , the trailing edge of the 120D blade showed a larger formation of high velocity vortices. The blade – arm connection region showed a noticeably larger formation of high velocity vortices compared to the NACA0018 blade arm combination. At 300° , the leading edge of the NACA0018 showed a more erratic flow indicating turbulence. The leading edge of the 120D was more streamlined.

These observations and differences in flow field around the blade of each turbine at different turbine phases of the rotation indicated as to how the 120D performed better during the downwind phase compared to the NACA0018 blade. The overall flow visualizations showed the unsymmetrical design performed better due to its efficiency in deflecting flow onto the upper and lower surface of the airfoil in a way that benefits the lift force generated by the airfoil and therefore has a positive impact on the turbine power generation. This was especially true in the downwind

region as the optimal shape increases the power generation in this phase of the rotation when usually it suffers.



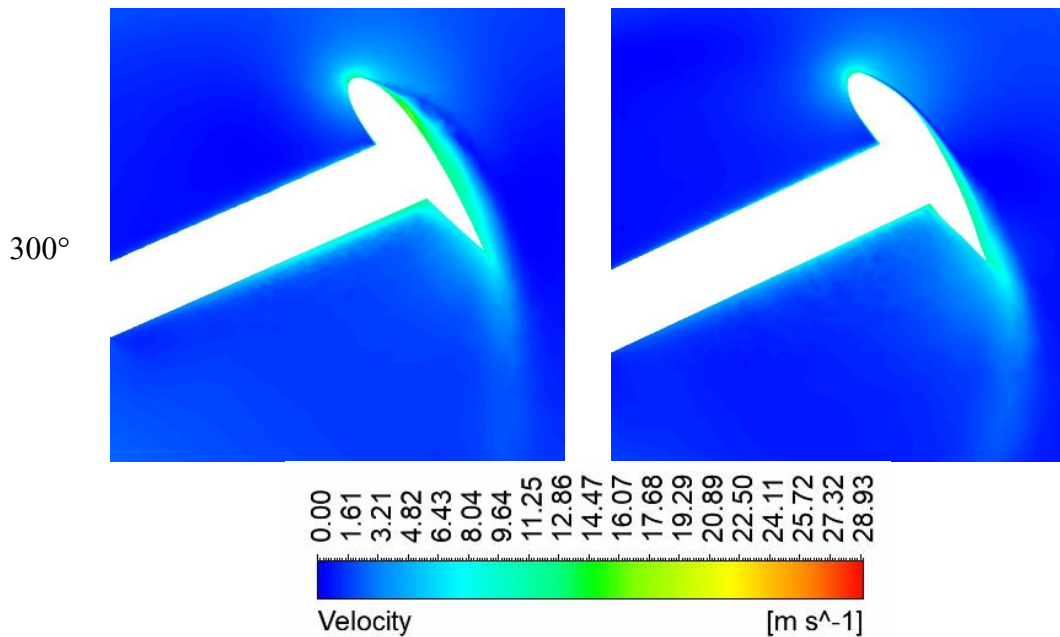
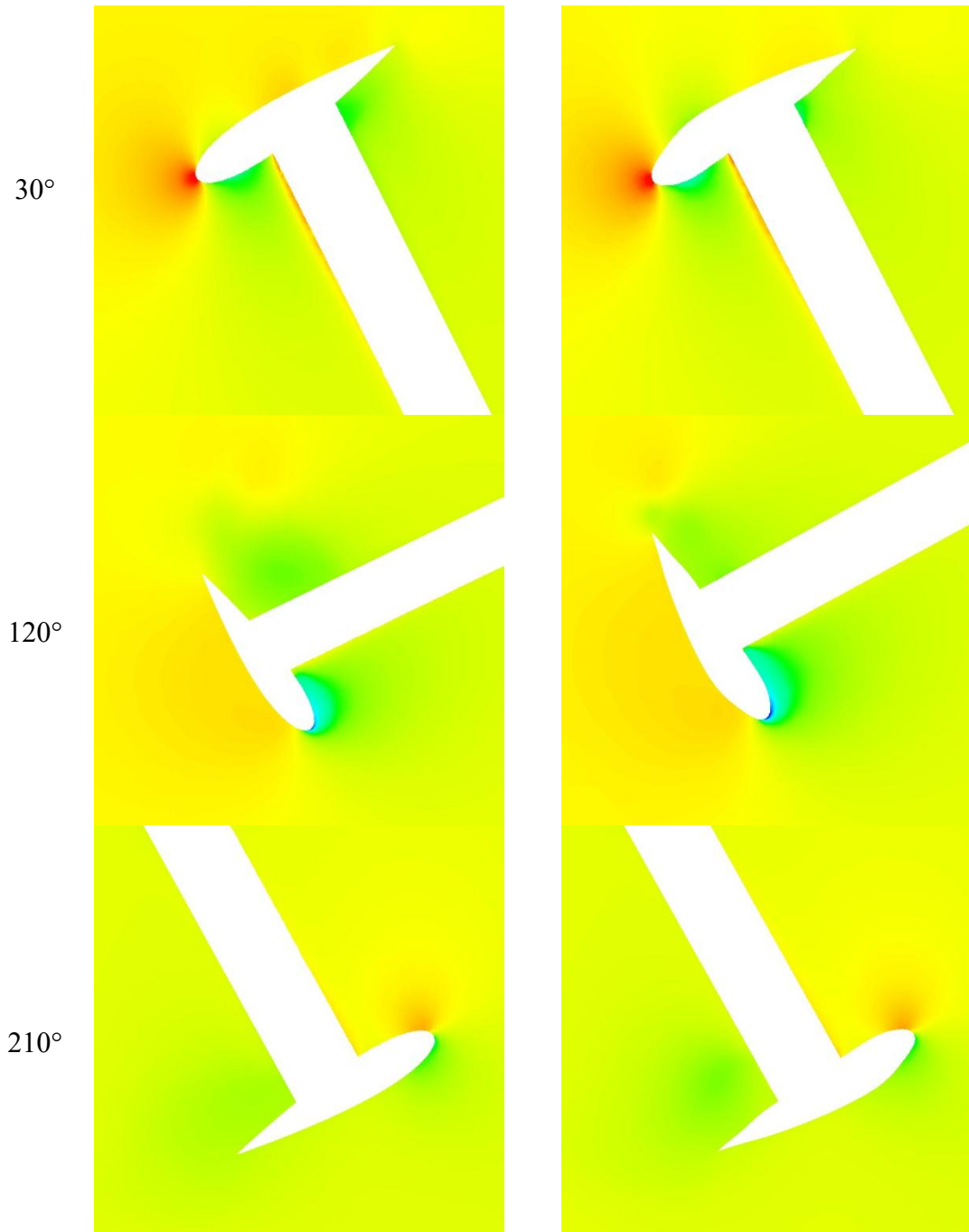


Fig 4.61. Velocity flow contour between the (a) NACA0018 and (b) 120D

4.8.5 Pressure contour - full turbine configuration

Fig 4.62 shows the pressure contour comparison between the NACA0018, from Fig 4.62(a), and 120D blade, shown in Fig 4.62(b). At 30° , the upper surface of the 120D leading edge showed a slightly lower pressure compared to the NACA0018. The lower pressure indicates higher flow velocity and is consistent with the previous velocity section and therefore resulted in a more streamlined flow. Both 120D and NACA0018 support-arms showed higher pressure on the leading edge concentrated towards the blade – arm connection during this phase. At 120° , both leading edges of the blade experienced low negative pressure. However, the suction pressure on the 120D leading edge showed higher intensity compared to the NACA0018 blade. At 210° , both blades showed minimal differences in pressure contour indicating similar flow conditions during the leeward phase of the rotation. At 300° , the leading edge of the upper surface of the NACA0018 blade showed a more distributed contour of low negative pressure whereas the negative pressure was more concentrated towards the leading edge of the 120D blade. The leading edge of the NACA0018 support-arm showed slightly higher pressure compared to the 120D support-arm.



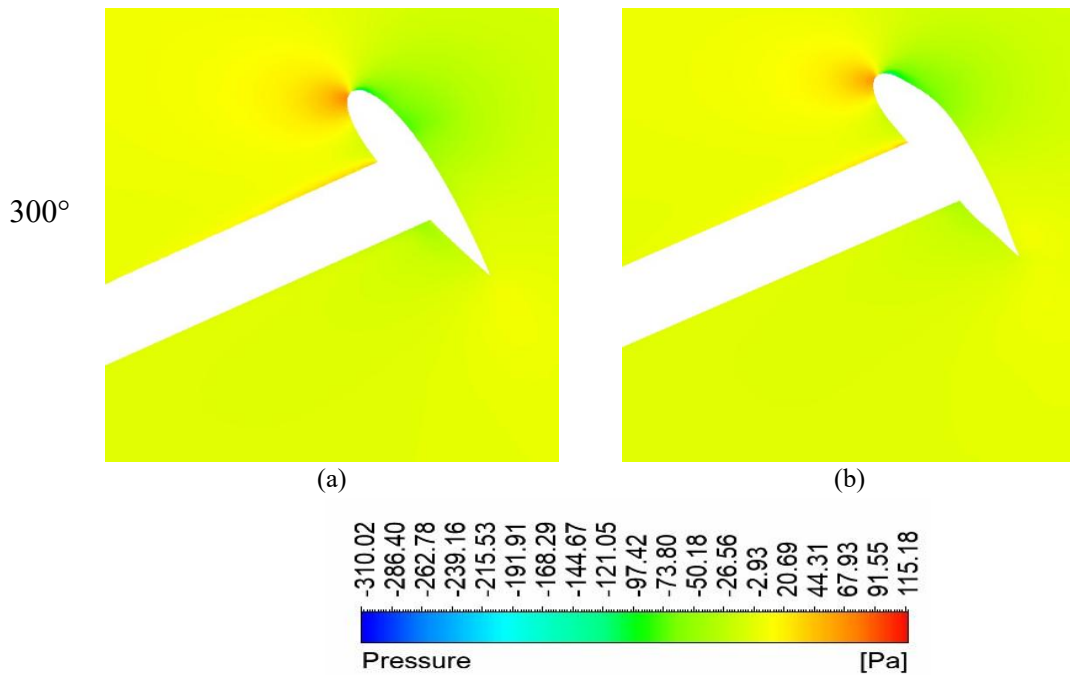
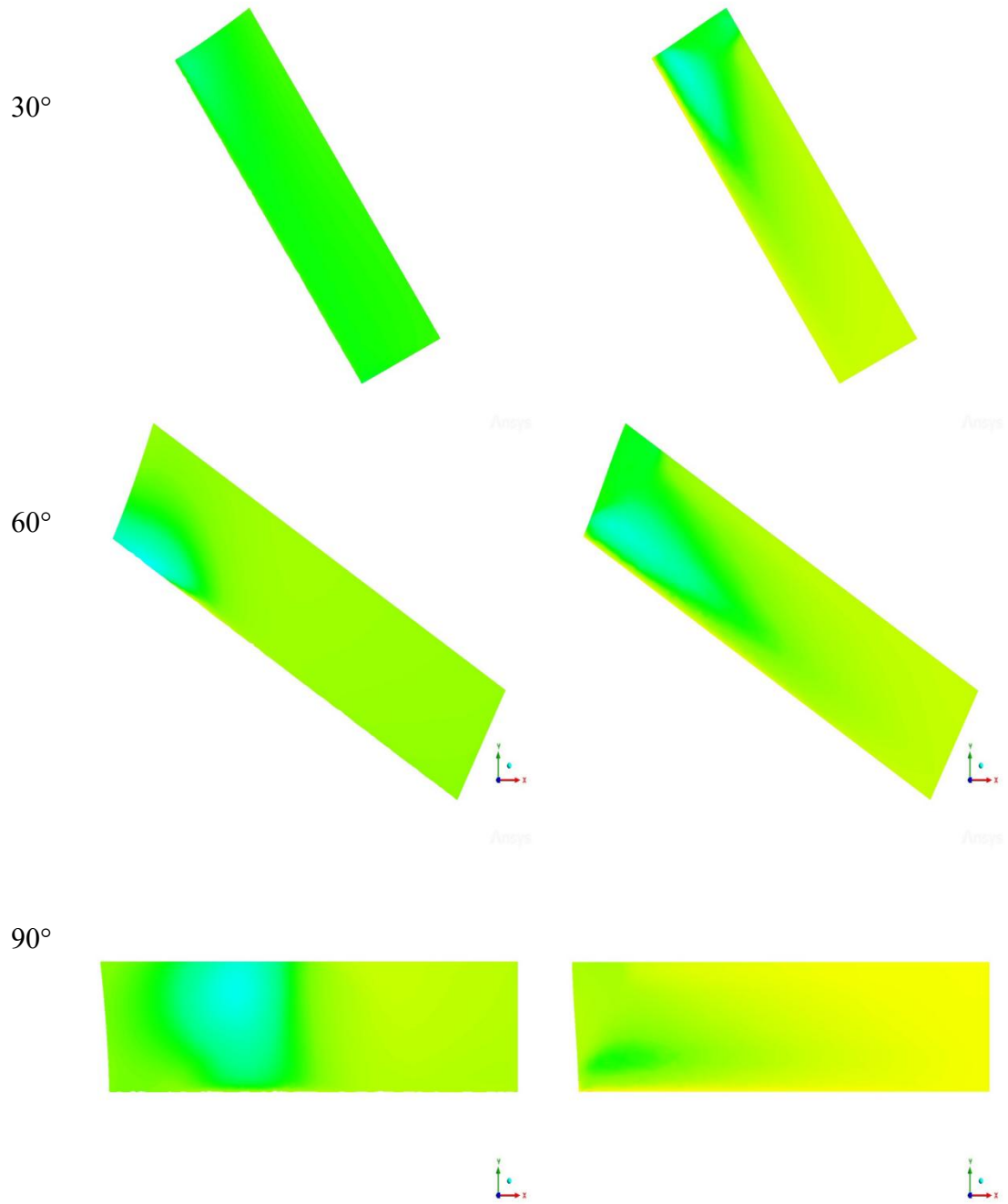


Fig 4.62. Pressure contour between the (a) NACA0018 and (b) 120D.

4.8.6 Further support-arm analysis

The following chapter discusses the pressure contour comparisons experienced by the support-arm. Fig 4.63 shows the upper surface of the support-arm of the (a) NACA0018 and (b) 120D blade. From Fig 4.63(a), at 30°, the NACA0018 experienced constant negative pressure throughout the span length on the support-arm. From Fig 4.63(b), the blade-arm connection of the 120D shows a patch of lower pressure towards the leading edge of the turbine. As the turbine continues to rotate to 60°, this lower suction pressure starts to extend further along the support-arm span length. A similar formation of lower pressure also starts to form at the leading edge near the blade-arm connection of the NACA0018 arm. At 90°, the NACA0018 support-arm shows large negative pressure over the span of the blade chord close to the arm blade connection. The negative pressure exerted on the 120D support-arm, however, decreases in intensity at 90° as well as minimal pressure difference across the span length of the blade except for a small patch at the leading edge of the blade. At 120°, the negative pressure on the 120D support-arm concentrates only at the blade-arm connection while the span length of the support-arm experiences a large positive pressure difference towards the centre of the rotor. This coincides with an increase in drag coefficient and power coefficient during this stage of the turbine rotation. The NACA0018 support-arm shows lower negative pressure at the trailing edge.



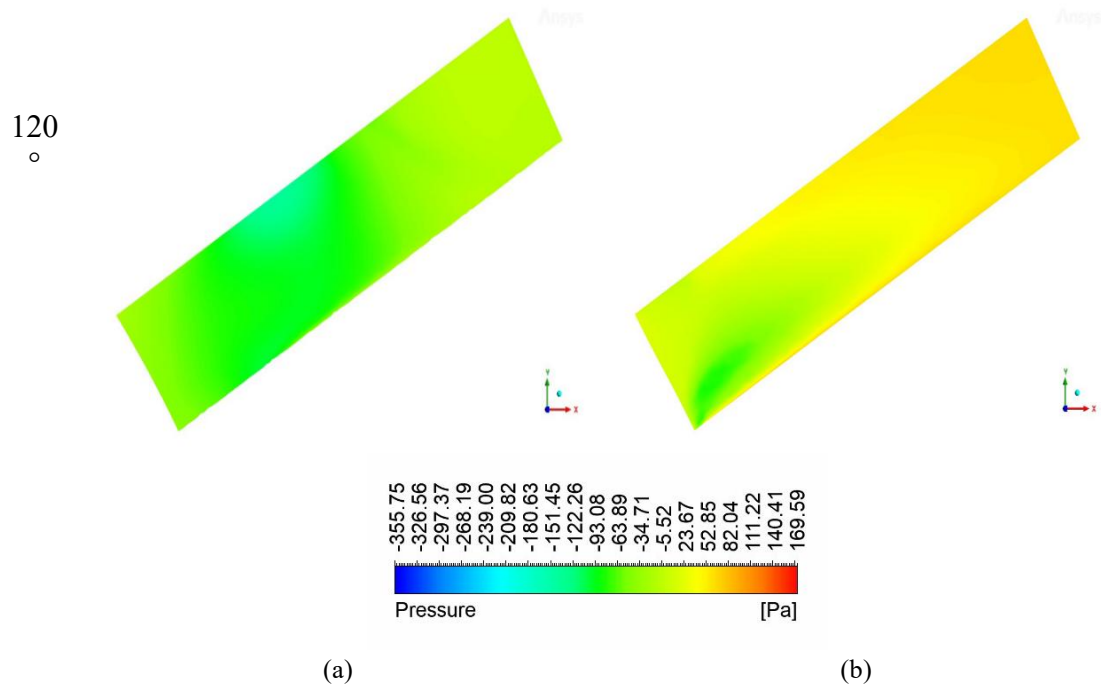
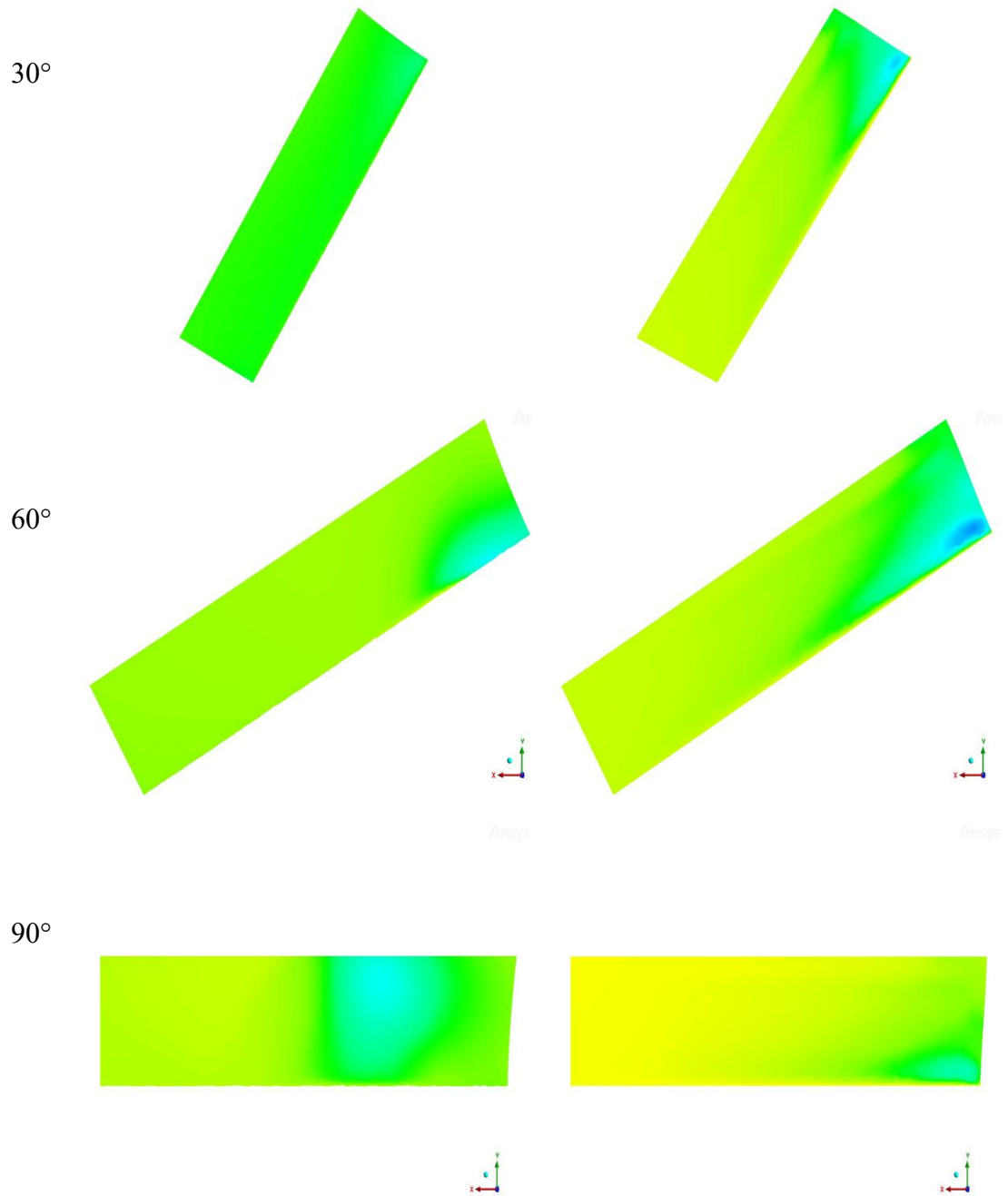


Fig 4.63. Upper surface arm pressure contour comparison between the (a) NACA0018 and (b) 120D.

Fig 4.64 shows the lower side of the turbine blade. Instantly, due to the symmetrical shape of the NACA0018 blade, the lower arm pressure contour showed an identical contour pattern to the upper surface previously seen. With regards to the 120D arm however, although there were some notable differences, the general trend of the pressure contour was similar to the previous sections. At 30° , the blade-end of the support-arm showed a strong concentration of low pressure compared to previously observed at the upper surface. The same observation and pattern were noted at 60° and 90° which showed the concentration of negative pressure towards the blade-arm connection increasing in magnitude. This indicated stronger suction pressure compared to the NACA0018 arm experienced near the blade-end or blade-arm connection as the blade moves through the upwind phase. At 120° , the positive pressure contour moving towards the turbine rotor and negative suction pressure was also observed like the upper surface. Overall, the negative pressure magnitude on the blade lower side was higher in all instances compared to the upper surface.

Based on the lift and drag coefficient analysis from the previous section, these observations indicated as to how the 120D experienced lower lift coefficients throughout the turbine rotation. Although the moment or torque loss was observed to be lesser than the NACA0018 blade, this may be due to the moment generated by the support-arm itself because of the drag effects on the support-arm. These observations

were corroborated based on the findings made in Fig 4.57 and Fig 4.58 whereby the overall moment coefficient generated by the 120D was higher compared to the NACA0018 support-arm.



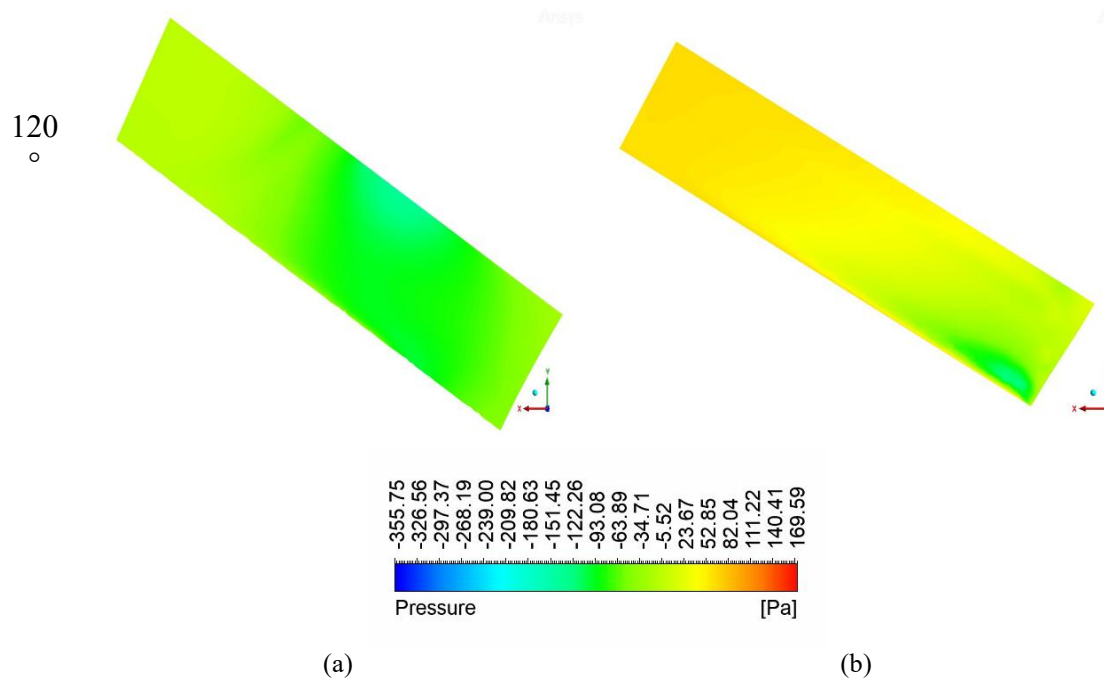


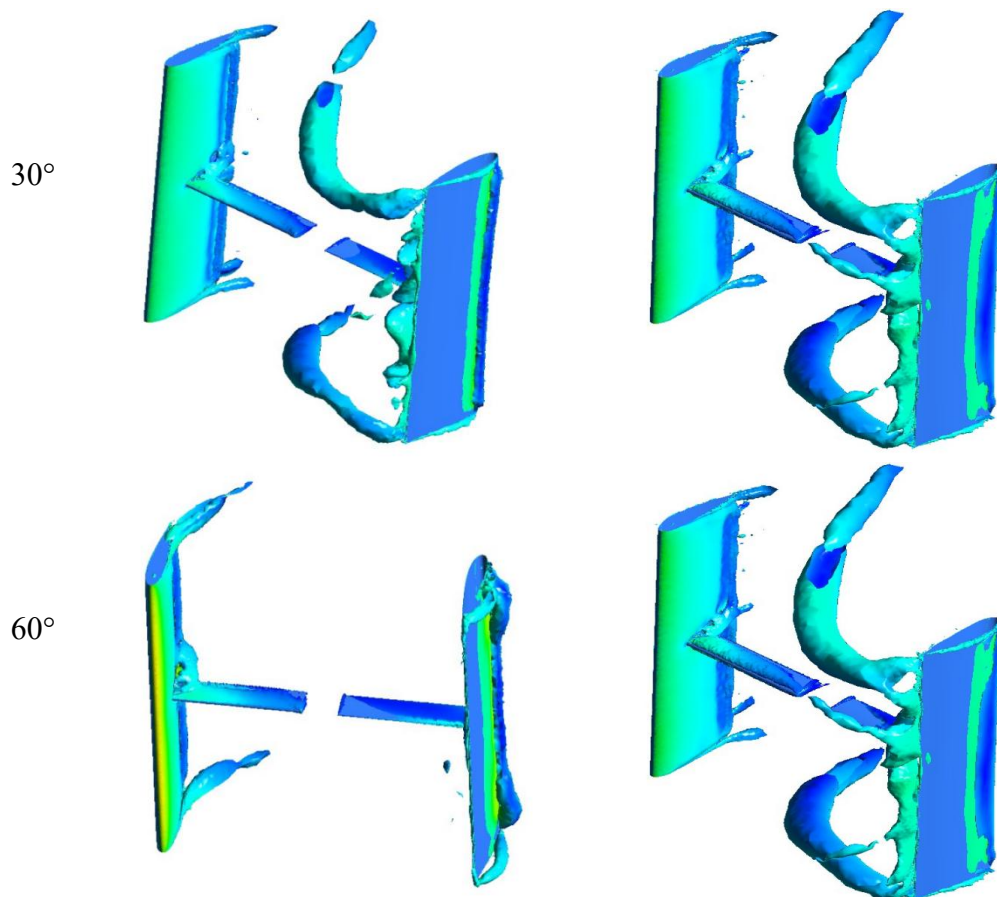
Fig 4.64. Lower arm pressure contour comparison between the (a) NACA0018 and (b) 120D.

4.8.7 Q – Criterion Flow Visualization

Fig 4.65 shows the Q-Criterion comparisons between the two turbines. When comparing the two turbines at 30°, it was observed that larger vortical structures were present at the trailing edge of the 120D turbine blade which indicated significant vortex shedding at the blade edges of the 120D. The blade support-arm connection point also showed significant vortex shedding compared to the NACA0018 turbine. At 60°, shedding of the trailing edge vortices was observed with the NACA0018 blade showing more prominent shedding compared to the 120D. The arm blade connection of the NACA0018 turbine also showed significant shedding on the upper surface of the support-arm blade. This was not observed with the 120D blade. The second blade entering the downwind region of both turbines experienced significant vortex shedding at the leading edge of the blade. It was also observed that during these two instances of the rotation, shedding occurred towards the blade tips which is more prominent at the NACA0018 blade compared to the 120D. At 90°, the trailing edge of the second blade observed a rotational flow in the NACA0018 blade. The 120D turbine, however, showed minimal shedding. This would suggest as to how the 120D experienced minimal aerodynamic losses in the downwind region compared to the NACA0018 blade. The observation was also exemplified at 120° with the vortex shedding more significantly seen in the NACA0018 turbine from the leading edge of

the second blade in the downwind region. The 120D arm blade connection also showed minimal shedding compared to the NACA0018 blade.

Overall, the Q-Criterion visualization indicated the 120D experienced less vortex shedding compared to the NACA0018 blade. The vortex shedding not only resulted in loss of lift force and therefore dynamic stall during these occurrences but also caused more turbulent flow within the inner rotor region. A more turbulent flow within the turbine inner region would severely impact the next incoming blade as the blade would have to pass through the more chaotic flow which gave rise to an increase in drag effects towards the second blade. The visualization of the vorticity magnitude below indicates that the morphing of the 120D blade negates and reduces this effect which resulted in a significant increased in performance seen in the downwind region where the vorticity was lower.



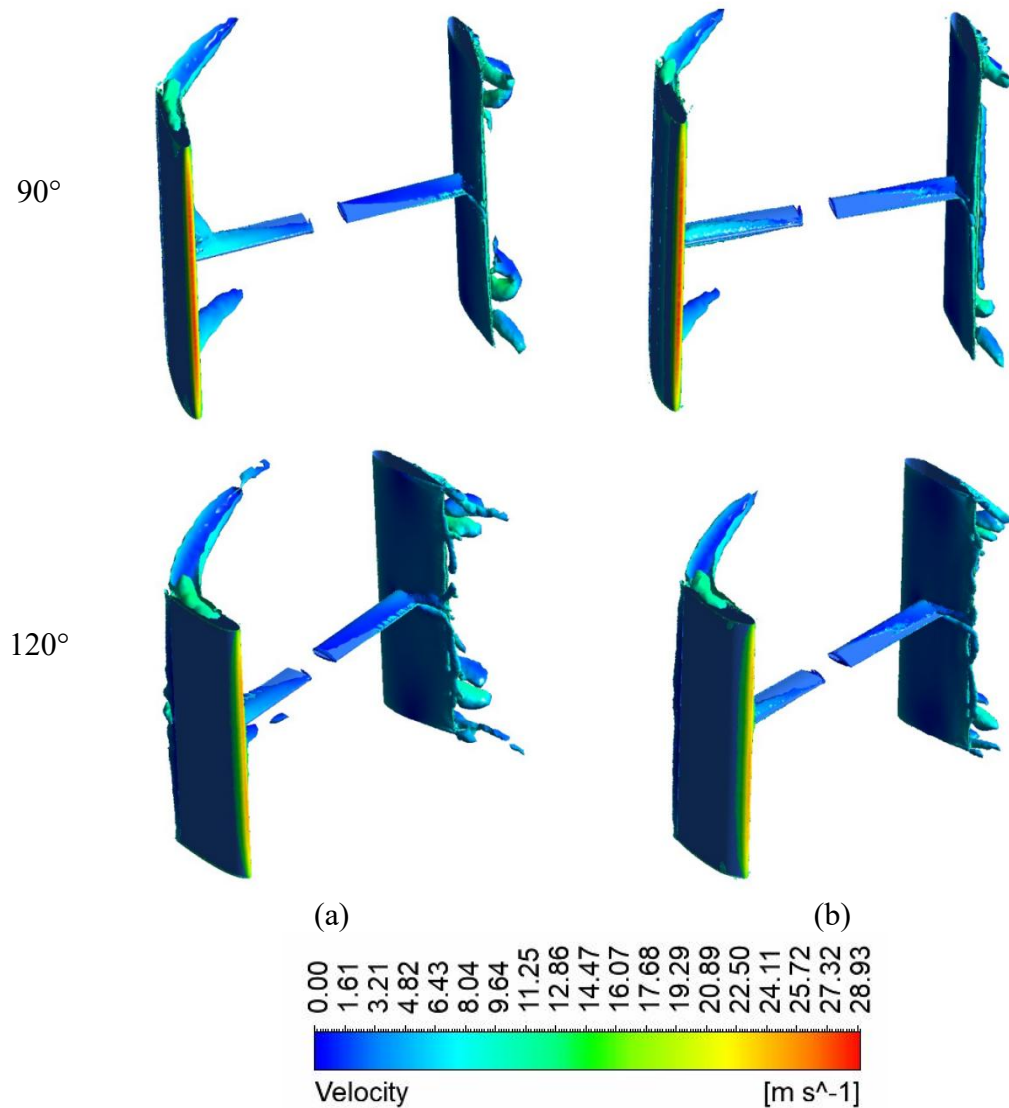


Fig 4.65. Q criterion visualization contour of (a) NACA0018 turbine and (b) 120D turbine.

4.8.8 3D Full Turbine Configuration - Summary

In this study, the numerical aerodynamic optimization of the NACA0018 blade was conducted. Several conclusions can be drawn from this study:

- The 2D optimization scheme performed at various snapshots of azimuthal angles at TSR 2 produced a candidate blade with a significant increase in average single blade moment coefficient of 30.48%.
- The 3D numerical analysis comparing the candidate blade 120D blade and support-arm combination against the initial baseline geometry NACA0018 also showed a significant increase in performance.

- The largest increase was found at TSR 1.75 with an increase of 50.76%. The average performance uplift over the range of tested TSR was 12.5%.
- An analysis and comparison of the 120D geometry applied to the turbine support-arm shows a significantly higher 20.39% improvement in terms of power coefficient compared to the NACA0018 geometry.
- The support-arm comparisons showed the unsymmetrical blade has a more positive impact on the turbine performance with lesser power coefficient losses compared to the symmetrical blade NACA0018 support-arm. The average power coefficient loss difference was 65.7%.
- Although the observed effects were conducted and performed on a small-scale turbine, the results indicate, as turbine size and operating TSR range increases, the same effects could also be achieved at a larger scale.

The results above concluded the numerical work of the optimization of the VAWT blade. The chosen 120D candidate blade was found to be the most optimal as both a turbine blade and a support-arm in a VAWT configuration. However, an experimental validation of the numerical results above would need to be conducted to verify that the adjoint optimized 120D blade can be translated into real world use as well as being more optimal than the NACA0018. Other turbine characterisations such as solidity and aspect ratio were also discussed in the experimental section.

4.9 Experimental Performance Analysis, Characterization, and Validation

After numerical analysis was conducted, the results above with the 120D blade were then analyzed in an experimental study with the wind tunnel. The turbine components such as the blades and turbine support-arms were all 3D printed and the experiment was conducted at varying low wind speed. This was due to the plastic nature of the turbine components which were susceptible to breakage and sudden explosive breakage due to the force when operated at high wind speed. Hence, the chosen wind speed varied between 5m/s to 6.5m/s. The experiments were conducted as per the turbine arrangement mentioned in section 4.8. This means the NACA0018 turbine blade was paired with the NACA0018 support-arm while the 120D blade profile was applied to both the turbine blade and turbine arm geometry.

4.9.1 Rotational speed

Fig 4.66 shows the rotational speed of the turbine at various loads. This was done by applying and varying the rope brake dynamometer attached to the spring balance. It was observed that, at all tested wind speeds, the 120D turbine showed much higher. From Fig 4.65(a), at 5m/s, the maximum speed of the 120D turbine reached 835RPM compared to the NACA0018 of 580RPM. This was a significant 33.10% increase in maximum RPM. Shown in Fig 4.65(b), the 5.6m/s test case saw the largest increase in rotational speed at 42.35% over the baseline NACA0018.

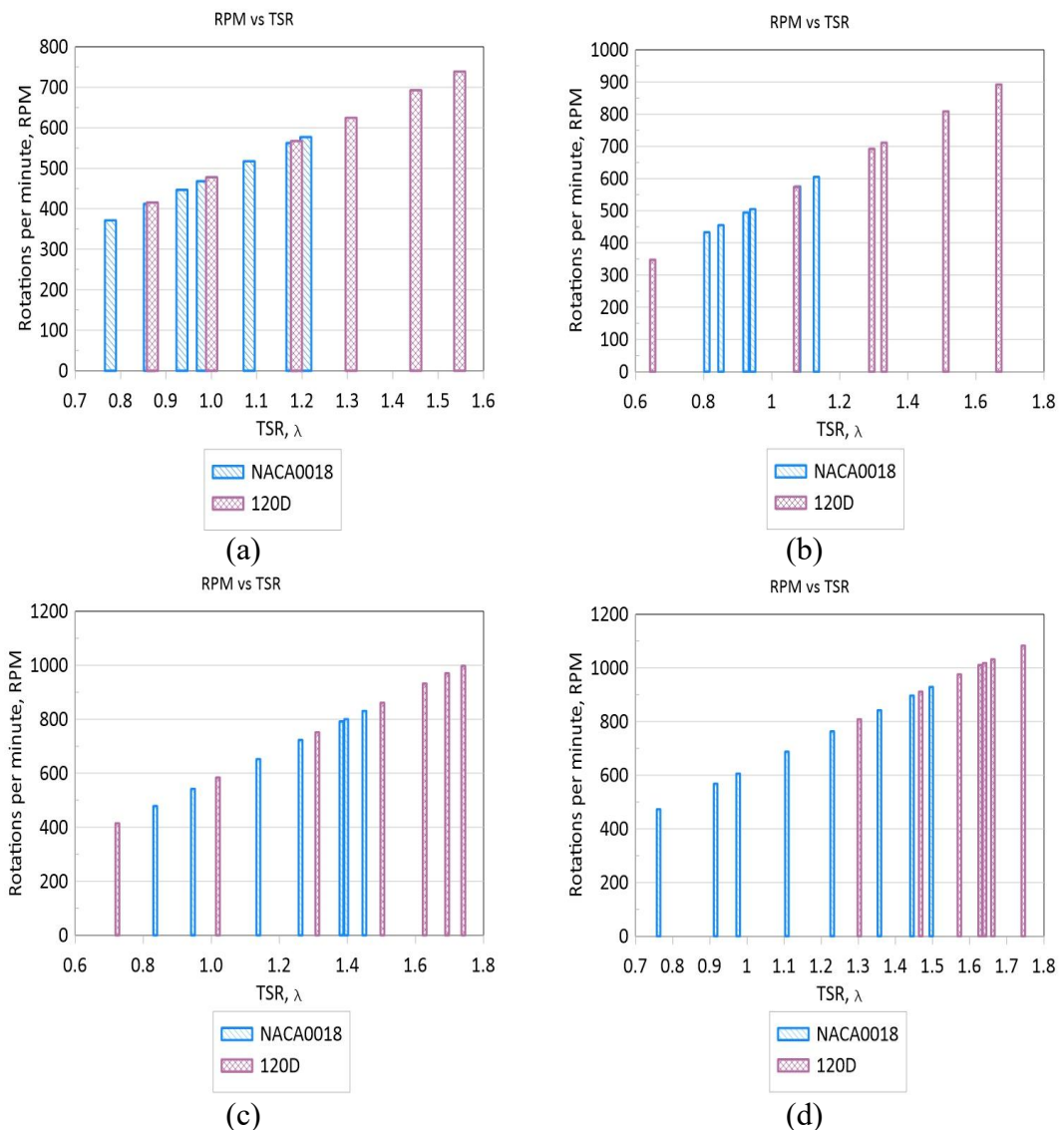


Fig 4.66. Turbine rotational speed comparisons at (a) 5m/s, (b) 5.6m/s, (c) 6m/s and (d) 6.5m/s

The maximum RPM of the 120D turbine at 6m/s, Fig 4.65(c), reached 1000RPM compared to the maximum NACA0018 wind speed of 835RPM. This was a 29.55% increase in maximum RPM. At inlet velocity of 6.5m/s, Fig 4.65(d), the

increase in rotational speed saw the least difference between the two turbines with an uplift of 15.38%. The average increase in maximum RPM in all tested inlet velocity speed was 30.10%. The higher rotational speed resulted in higher TSR and therefore a wider operational range of the turbine.

4.9.2 Power performance analysis

In this section, the power performance of the turbine blades was compared. Fig 4.67 below shows the power performance comparisons of the two turbines at different inlet wind speeds. Immediately, it was clear that, in all test cases, it was observed that the higher RPM of the 120D turbine resulted in a wider range of operational TSR which then resulted in a general increase in power production. From Fig 4.67(a), at 5m/s inlet velocity, the 120D turbine saw a maximum power extraction uplift by 7.96%. When the wind speed was increased to 5.6m/s, Fig 4.67(b), the 120D turbine was able to operate at a much higher TSR. This time, the maximum power was increased by 21.76%. Increasing the wind speed further up to 6m/s, shown in Fig 4.67(c), the percentage increase of maximum power production of the 120D turbine against the baseline NACA0018 turbine was significant at 29.43%. At 6.5m/s, illustrated in Fig 4.67(d), the maximum power was increased by a very large margin of 30.02%. Hence, the power production difference between the two turbines increased as the wind speed increased.

The main factor in the increase of the power production of the 120D turbine over the NACA0018 turbine was its much higher operating speed. Due to the morphing of the blade which changed the nature of the blade profile in the 120D turbine, the Figs showed very different curve characteristics. Hence, this study has shown that, both in numerical predictions and experimental testing, the 120D blade was proven to be much more optimal for this small turbine performance. Since the candidate blade 120D has been experimentally validated to be an improvement over the NACA0018 blade, a further analysis was conducted on the solidity and aspect ratio of the 120D turbine.

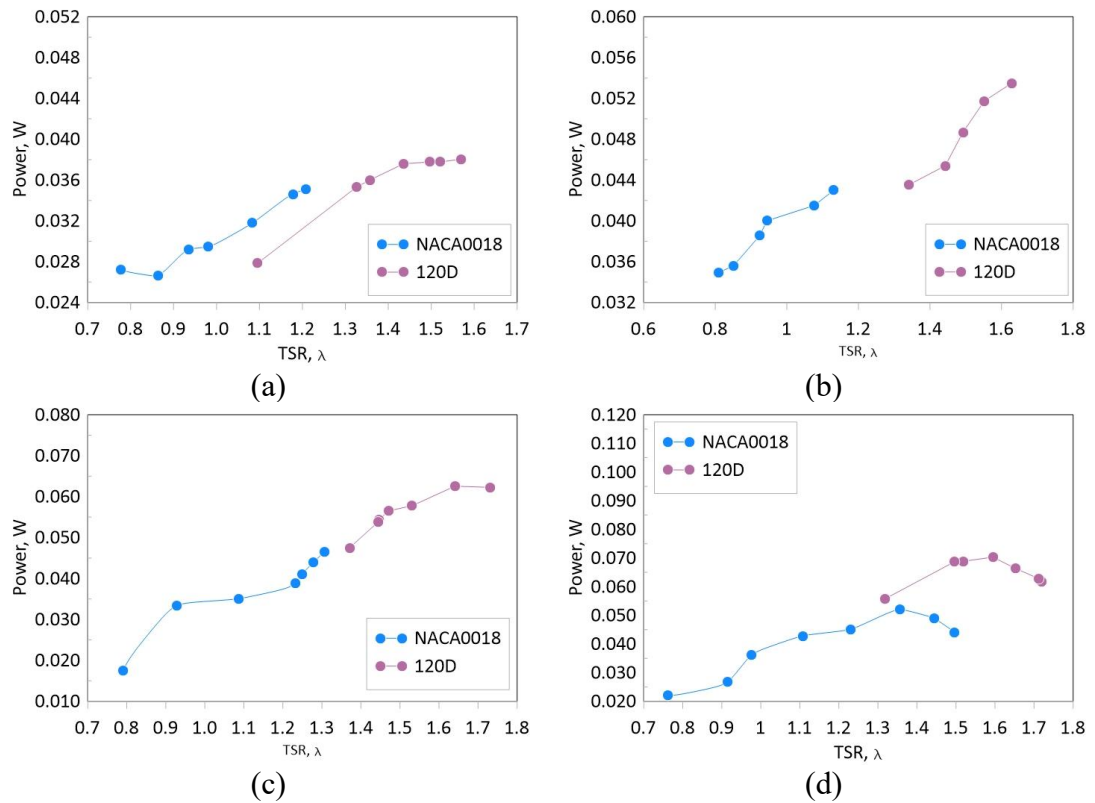


Fig 4.67. Power performance comparison between the candidate 120D turbine and baseline NACA0018 turbine at (a) 5m/s, (b) 5.6m/s, (c) 6m/s and (d) 6.5m/s.

4.9.3 Effect of Optimized Blade on Turbine Solidity

In the 2D numerical optimization study, the blade chord was kept at 60mm. The turbine was also rotated at various angles with a turbine diameter of 200mm. However, as was previously discussed in the literature section of this thesis, the blade chord and turbine diameter are significant factors affecting the turbine solidity. The previous numerical sections investigated the turbines' performances with these two parameters in mind. Therefore, it can be deduced that the adjoint optimization was conducted with optimizing the turbine blade with these two factors considered. Hence, in this section, an experimental study was conducted to investigate the performance of the candidate turbine blade and support-arms with 120D geometry while varying the number of blades. The analysis was conducted at inlet velocity 5m/s and 5.6m/s. Parameters for this study were summarized in Table 4.7.

Table 4.7 Parameters of the turbine solidity study.

Parameter	Turbine 1	Turbine 2	Turbine 3
Number of blades	2	3	4
Solidity	0.19	0.28	0.38
Chord	0.06	0.06	0.06
Height, H	0.2	0.2	0.2

From Fig 4.68(a), it was observed that the higher the number of blades extracted better power at lower TSR. The two bladed turbine extracted power over a wider range of TSR. The 3 bladed turbine peaked at TSR 1.35 whereas the 4 bladed turbine peaked at TSR 1.1. At 5.6m/s, in Fig 4.68(b), the 2 bladed turbine also showed the widest operating TSR. However, the 4 bladed turbine showed the highest peak despite showing a much narrower operating TSR range. The increased solidity of the turbine was able to improve maximum power production of the turbine but at the cost of a much lower operating TSR range.

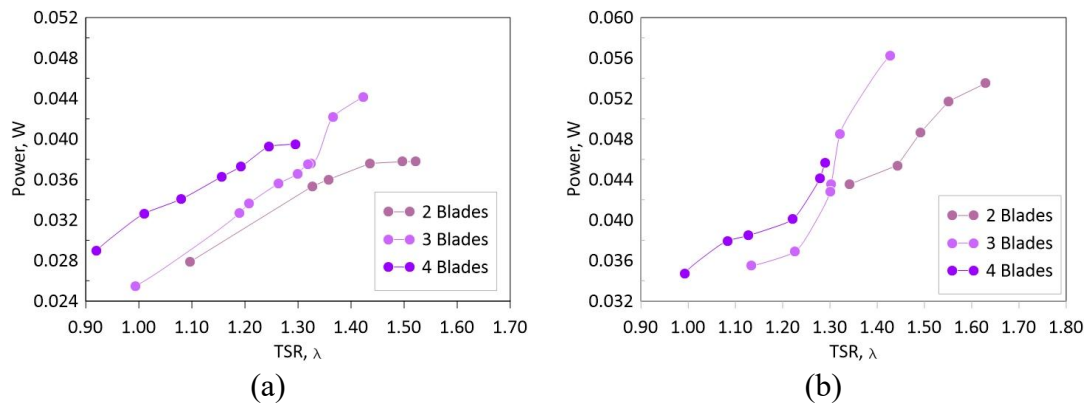


Fig 4.68. Power performance comparison of the different turbine solidity at (a) 5m/s, and (b) 5.6m/s inlet velocity.

The results showed that the 2 bladed setup showed the widest operational TSR range as well as good power production capability of the three tested turbine setups differing blade number and solidity. Increasing the number of blades was also found to be a viable option as increasing the turbine blade number increased the power production of the turbine. The observations made were consistent with the reported literature whereby a lower solidity extracted power at a wider TSR range whereas a higher solidity turbine or number of blades has a higher power production (Brusca, Lanzafame, and Messina 2014, Ahmadi-Baloutaki, Carriveau, and Ting 2014). For

this study, the two bladed turbine can be safely recommended and is consistent with (Hand and Cashman 2017).

4.9.4 Effect of Optimized Blade on Turbine Aspect Ratio

The aspect ratio of the turbine is affected by the turbine diameter and turbine height. In the optimization section of this study, the azimuth angle, in which the candidate blade 120D was obtained through optimization, was varied with a turbine diameter of 200mm in mind. Hence, similar to the case of the turbine solidity, the optimized 120D blade geometry was the result of the aforementioned turbine diameter. Therefore, in this section, the characteristic of the 120D on the aspect ratio of the turbine blade was investigated. The number of blades were kept constant at 2 blades and the turbine diameter and turbine blade height was varied. The inlet velocity for this study was conducted at 6m/s and 6.5m/s. The parameters for this study were summarized in Table 4.8.

Table 4.8 Parameters of the aspect ratio study.

Parameter	Turbine 1	Turbine 2	Turbine 3
Height, H	0.16	0.20	0.20
Diameter	0.20	0.20	0.16
Aspect ratio	0.8	1	1.25
Number of blades, H	2	2	2

Fig 4.69 shows the results of the compared aspect ratio. In Fig 4.69(a), at inlet velocity of 6m/s, all three aspect ratios show similar performances between TSR 1.1 and TSR 1.6. However, it was noticed that the higher turbine aspect ratio of 1.25 performed slightly poorer of the 3 turbines. Turbine 2, with aspect ratio of 1, showed the best performance with higher maximum power production and wider operational TSR range. When the inlet speed was increased to 6.5m/s, from Fig 4.69(b), the lower power production of the Turbine 3, with an aspect ratio of 1.25, was more noticeable of the compared turbines. Turbine 1, aspect ratio of 0.8, showed better performance of the 3 tested turbines with Turbine 2 performing better than Turbine 3 but was poorer than Turbine 1 as the TSR increased. In all cases, an aspect ratio of 1 was determined to be the most optimal for the 120D blade with aspect ratio of 0.8 also recommendable.

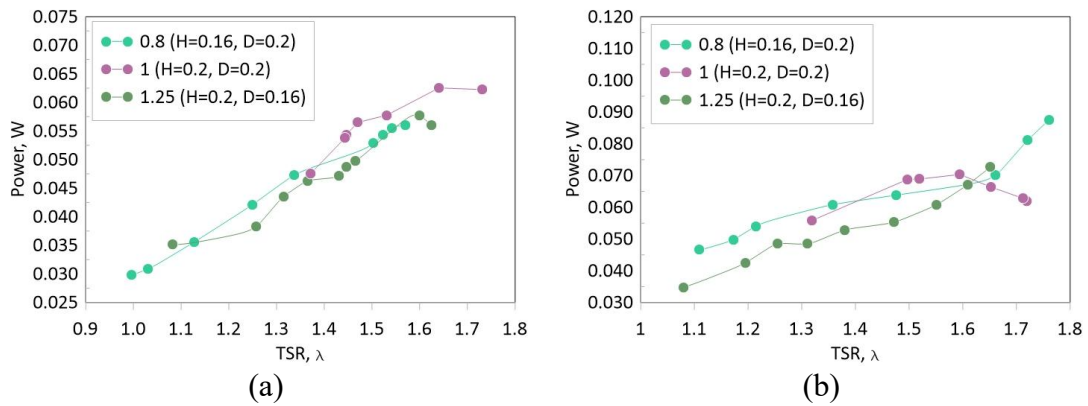


Fig 4.69. Comparisons of different turbine aspect ratio at (a) 6m/s, and (b) 6.5m/s inlet velocity.

4.9.5 Experimental Summary

As was expected, the experimental results showed the 120D candidate turbine outperformed the NACA0018 turbine. The following are the points made from the experiment:

- The 120D turbine was able to extract higher power as well as operate at a higher TSR and RPM.
- At all tested inlet velocity cases, the largest increase in maximum power production was observed at 6.5m/s with an increase of 30.02%.
- The 120D turbine has a 24.11% increase in RPM across all tested inlet velocity.
- Solidity and aspect ratio studies were also performed which illustrated the performance characteristics of the 120D blade in different turbine configurations. This showed that, in real world application, the adjoint optimized blade has a significant performance improvement and therefore validates the optimization scheme using the adjoint method and gradient-based optimizer.

4.10 Results - Summary

Hence, the results and discussion section has been concluded. 2D optimization produced multiple different candidate blades with the 120D blade optimized at TSR 2 showing the most improvement. 3D analysis confirmed the improvements made over the baseline NACA0018 blade with respect to various performance coefficients. Visualization of the flow physics showed significant improvements within the downwind region which validated and proved the

hypothesis correct. Finally, experimental wind tunnel test showed the increased performance was due to the higher gains in RPM which not only increased the maximum power production, but also an increased range of operational TSR. Therefore, it can be conclusively summarized that the optimization scheme proposed in this study has been proven by the design on a novel 120D with significantly increased performance.

Based on the numerical and experiment results of this study, the following table summarizes the recommend dimensions, parameters and operating conditions for the optimized small-scale turbine based on the 120D turbine blade design.

Table 4.9 Recommended parameter for the 120D turbine.

Parameter	Unit	Value
Number of blades	-	3
Chord Length, c	m	0.06
Solidity	-	0.28
Aspect Ratio	-	1
Operating TSR range, λ	-	0 - 2

Chapter 5

Conclusions

5.1 Concluding Remarks

In conclusion, the research questions and objectives have been successfully achieved. A new H-type vertical axis geometry obtained from the adjoint method optimization was developed. To summarize the findings of this study, the following conclusions were found:

Research Question 1: What are the aerodynamic force contributions of the wind turbine blade and support-arm during turbine operations?

- In the preliminary study, the aerodynamic force contributions of the support-arms were established. The lift and drag effects were discussed as well as their impact on the performance predictions on in a 3D numerical study.
- The presence, or considerations, of turbine support-arm results in a significant reduction in performance prediction in numerical simulation by up to **55.5%**.
- Later, an analysis was conducted on the NACA0018 compared against the 120D blade. Blade characteristics such as lift, drag, and blade surface pressure of the baseline NACA0018 and improvement by the 120D blade was presented.
- Hence, the aerodynamic forces of the turbine blade and support-arms were identified and objective 1 was fulfilled.

Research Question 2: What is the flow physics around the wind turbine blade and arms and what are its aerodynamic contributions during turbine operation?

- In the velocity flow contours, the maximum velocity around the turbine were found to be lower in both full turbine configurations compared to the baseline turbines.
- Large structures resembling turbulence could be seen around the support-arm – blade connection region as observed from the velocity contours and Q – criterion visualization.

- Later, the NACA0018 turbine blade paired with the NACA0018 support-arms were studied as well.
- For the aerodynamic contributions, the support-arm was proven to have a parasitic effect on the turbine performance.
- Hence, the flow physics of the NACA0018 turbine blade as well as circular and NACA0018 support-arm has been described and objective 2 has been achieved.

Research Question 3: Can a shape optimization scheme be applied to a transient wind turbine problem to enhance the turbine blade and support-arm performance?

- The candidate blade from each tested TSR of TSR 1 and TSR 2 showed promise in that both blades show better performance than the NACA0018. However, further comparisons showed the candidate blade and turbine optimized at TSR 2 to be better. The 120D blade was found to be most optimal when compared against the NACA0018 and candidate blade optimized at TSR 1 with higher maximum power coefficient as well as higher average power coefficient over the range of tested TSR **28.77%**.
- Therefore, from the proposed 2D optimization scheme, it was found that the tip speed ratio (TSR) played a significant role in the optimization. A higher TSR consideration was found to obtain a more optimized blade shape.
- Applying the optimization scheme on the S1046 blade, the best result was obtained at 30° azimuth angle with a **9.2%** increase over the baseline S1046 blade. Further turbine analysis shows **9.5%** increase in power coefficient.
- Therefore, a shape optimization scheme utilizing the adjoint method paired with the gradient-based optimizer has been described with positive results. Objective 3 has been achieved.

Research Question 4: What will be the new optimized turbine blade and support-arm geometry?

- From the 2D optimization, while taking into account the S1046 results, the NACA0018 optimization which produced the 120D candidate blade was selected as the most ideal and promising blade and therefore merits further analysis.

- An inward morphing or cambering of the mesh produced a more straightened lower side as well as a hump like shape on the upper surface of the blade which resulted a pressure difference positive effects during the downwind phase of the rotation.
- Expanding further in a 3D numerical study, it was observed that with 3D effects added, the 120D turbine was found **to have a significant 20.42% and 15.18% increase in performance** over the NACA0018 and S1046 turbines respectively.
- The improved performance was mainly due to the **120D blade performing better during the downwind phase** of the turbine rotation.
- Hence, the new optimized turbine blade and support-arm geometry was decided on and objective 4 was answered.

Research Question 5: What is the flow physics like around the new turbine blade and support-arm and how does it compare against current symmetrical and unsymmetrical blade designs?

- The power coefficient curves show the 120D candidate turbine performed better as the TSR increased. **The average power coefficient uplift over the baseline NACA0018 blade was 12.5%**. Although the 120D blade extracted slightly less than the NACA0018 blade in traditionally considered a region whereby most power is extracted, this was offset due to the 120D blade performing better during the downwind phase of the rotation.
- The flow visuals showed that the upper surface hump produced by the optimization scheme improved flow during the downwind phase by delaying flow separation and dynamic stall which enabled the blade to extract better power during this phase.
- The flow physics showed that the 120D blade was able to retain longer flow attachment and as well as lesser turbulence and vortex formulation. This means the blades passing through the wake of the previous blade do not encounter large vortices and therefore experienced lesser drag than the NACA0018 and S1046.
- Q-criterion visualization indicated that the 120D experienced significantly less vortex shedding compared to the NACA0018 blade.
- Hence, the effect of the new optimized full turbine blade and support-arm on the turbine flow characteristics were presented and the final has been achieved.

The findings of this study, in line with the research questions and objectives outlined at the start of the thesis, have been successfully summarized above. By addressing the research questions and meeting the objectives, the thesis has ultimately resulted in the creation of a turbine blade prototype known as the 120D blade. However, while this prototype is significant, the true value of the thesis lies in its exploration of the adjoint method as an optimization tool and the developed procedures to maximize its potential for enhancing wind turbine performance. This research has highlighted the capability of the adjoint method in improving small-scale wind turbines under specified conditions. The demonstrated optimization procedure based on the adjoint method and gradient-based optimizer opens up a plethora of possibilities for optimizing various parameters and refining turbine designs. The ideas presented in this thesis offer endless opportunities for implementing and further developing turbine optimization strategies.

5.2 Future work

Although the objectives of this research study have been achieved and a new optimized candidate turbine was demonstrated, there are still further studies worth pursuing in relation to the turbine optimization utilizing the adjoint method. Other parameters as well as optimization techniques could be studied to further improve the aerodynamic performance of the turbine. However, due to the limitations imposed on this study with respect to time as well as resources, other possible modifications can be made to the ring. Therefore, the following research topics were suggested for possible future work to further optimize the VAWT:

1. Study the effects of turbine solidity and aspect ratio as the optimization parameter.
2. Implementation of the adjoint method on other VAWT blade of different geometry and thickness.
3. Implementation of the optimized shape on the support-arm geometry yielded significantly better aerodynamics conducive to increased turbine performance. Optimization of the support-arm based on its span length can be further investigated.
4. Blades can be fabricated with different materials to increase power to weight ratio and reduce surface roughness.

References

- (IRENA), The International Renewable Energy Agency. 2021. *Renewable Energy Statistics 2021*.
- Abdolahifar, Abolfazl, and S. M. H. Karimian. 2022. "A comprehensive three-dimensional study on Darrieus vertical axis wind turbine with slotted blade to reduce flow separation." *Energy* 248:123632. doi: <https://doi.org/10.1016/j.energy.2022.123632>.
- Ahmadi-Baloutaki, Mojtaba, Rupp Carriveau, and David S-K Ting. 2014. "Straight-bladed vertical axis wind turbine rotor design guide based on aerodynamic performance and loading analysis." *Proceedings of the Institution of Mechanical Engineers, Part A: Journal of Power and Energy* 228 (7):742-759. doi: 10.1177/0957650914538631.
- Al-Obaidi, ASM, and Ganesh Madivaanan. 2022. "Investigation of the blockage correction to improve the accuracy of Taylor's low-speed wind tunnel." *Journal of Physics: Conference Series*.
- Alaimo, Andrea, Antonio Esposito, Antonio Messineo, Calogero Orlando, and Davide %J Energies Tumino. 2015. "3D CFD analysis of a vertical axis wind turbine." 8 (4):3013-3033.
- Almohammadi, K. M., D. B. Ingham, L. Ma, and M. Pourkashanian. 2015. "Modeling dynamic stall of a straight blade vertical axis wind turbine." *Journal of Fluids and Structures* 57:144-158. doi: <https://doi.org/10.1016/j.jfluidstructs.2015.06.003>.
- Bachant, Pete, and Martin Wosnik. 2015. "Characterising the near-wake of a cross-flow turbine." *Journal of Turbulence* 16:392-410. doi: 10.1080/14685248.2014.1001852.
- Bachant, Peter, and M. Wosnik. 2016a. "Effects of Reynolds Number on the Energy Conversion and Near-Wake Dynamics of a High Solidity Vertical-Axis Cross-Flow Turbine."
- Bachant, Peter, and Martin Wosnik. 2016b. "Modeling the near-wake of a vertical-axis cross-flow turbine with 2-D and 3-D RANS." *Journal of Renewable and Sustainable Energy* 8 (5):053311. doi: 10.1063/1.4966161.
- Baghdadi, M., S. Elkoush, B. Akle, and M. Elkhoury. 2020. "Dynamic shape optimization of a vertical-axis wind turbine via blade morphing technique." *Renewable Energy* 154:239-251. doi: <https://doi.org/10.1016/j.renene.2020.03.015>.
- Bangga, Galih, Go Hutomo, Raditya Wiranegara, Herman %J Journal of Mechanical Science Sasongko, and Technology. 2017. "Numerical study on a single bladed vertical axis wind turbine under dynamic stall." 31 (1):261-267. doi: 10.1007/s12206-016-1228-9.
- Barnes, Andrew, Daniel Marshall-Cross, Ben Richard %J Journal of Ocean Engineering Hughes, and Marine Energy. 2021. "Validation and comparison of turbulence models for predicting wakes of vertical axis wind turbines." 7 (4):339-362.
- Bausas, Michael D., and Louis Angelo M. Danao. 2015. "The aerodynamics of a camber-bladed vertical axis wind turbine in unsteady wind." *Energy* 93:1155-1164. doi: <https://doi.org/10.1016/j.energy.2015.09.120>.
- Belabes, Belkacem, and Marius Paraschivoiu. 2021. "Numerical study of the effect of turbulence intensity on VAWT performance." *Energy* 233:121139. doi: <https://doi.org/10.1016/j.energy.2021.121139>.
- Bianchini, Alessandro, Francesco Balduzzi, Peter Bachant, Giovanni Ferrara, and Lorenzo Ferrari. 2017. "Effectiveness of two-dimensional CFD simulations for Darrieus VAWTs: a combined numerical and experimental assessment." *Energy Conversion and Management* 136:318-328. doi: <https://doi.org/10.1016/j.enconman.2017.01.026>.

- Bilgili, Mehmet, Abdulkadir Yasar, and Erdogan Simsek. 2011. "Offshore wind power development in Europe and its comparison with onshore counterpart." *Renewable and Sustainable Energy Reviews* 15 (2):905-915. doi: <https://doi.org/10.1016/j.rser.2010.11.006>.
- Bravo, R., S. Tullis, and S. Ziada. 2007. "Performance Testing of a Small Vertical-Axis Wind Turbine." *Proceedings of the 21st Canadian Congress of Applied Mechanics (CANCAM07)*.
- Brusca, S., R. Lanzafame, and M. Messina. 2014. "Design of a vertical-axis wind turbine: how the aspect ratio affects the turbine's performance." *International Journal of Energy and Environmental Engineering* 5 (4):333-340. doi: 10.1007/s40095-014-0129-x.
- Campobasso, M. S., A. Zanon, E. Minisci, and A. Bonfiglioli. 2009. "Wake-tracking and turbulence modelling in computational aerodynamics of wind turbine aerofoils." *Proceedings of the Institution of Mechanical Engineers, Part A: Journal of Power and Energy* 223 (8):939-951. doi: 10.1243/09576509JPE778.
- Carbó Molina, Andreu, Tim De Troyer, Tommaso Massai, Antoine Vergaerde, Mark C. Runacres, and Gianni Bartoli. 2019. "Effect of turbulence on the performance of VAWTs: An experimental study in two different wind tunnels." *Journal of Wind Engineering and Industrial Aerodynamics* 193:103969. doi: <https://doi.org/10.1016/j.jweia.2019.103969>.
- Carrigan, Travis J, Brian H Dennis, Zhen X Han, and Bo P %J International Scholarly Research Notices Wang. 2012. "Aerodynamic shape optimization of a vertical-axis wind turbine using differential evolution." 2012.
- Castelli, Guido Ardizzon, Lorenzo Battisti, Ernesto Benini, and Giorgio Pavesi. 2010. *Modeling Strategy and Numerical Validation for a Darrieus Vertical Axis Micro-Wind Turbine*. Vol. 7.
- Castelli, Giulia Simioni, Ernesto %J International Journal of Aerospace Benini, and Mechanical Engineering. 2012. "Numerical analysis of the influence of airfoil asymmetry on VAWT performance." 6 (1):75-84.
- Celik, Yunus, Lin Ma, Derek Ingham, and Mohamed Pourkashanian. 2020. "Aerodynamic investigation of the start-up process of H-type vertical axis wind turbines using CFD." *Journal of Wind Engineering and Industrial Aerodynamics* 204:104252. doi: <https://doi.org/10.1016/j.jweia.2020.104252>.
- Chakroun, Yosra, and Galih %J Sustainability Bangga. 2021. "Aerodynamic characteristics of airfoil and vertical axis wind turbine employed with Gurney flaps." 13 (8):4284.
- Chen, and Cheng-Hsiung Kuo. 2013. "Effects of pitch angle and blade camber on flow characteristics and performance of small-size Darrieus VAWT." *Journal of Visualization* 16. doi: 10.1007/s12650-012-0146-x.
- Chen, Jian, Liu Chen, Hongtao Xu, Hongxing Yang, Changwen Ye, and Di Liu. 2016. "Performance improvement of a vertical axis wind turbine by comprehensive assessment of an airfoil family." *Energy* 114:318-331. doi: <https://doi.org/10.1016/j.energy.2016.08.005>.
- Chen, Jian, Hongxing Yang, Mo Yang, and Hongtao Xu. 2015. "The effect of the opening ratio and location on the performance of a novel vertical axis Darrieus turbine." *Energy* 89:819-834. doi: <https://doi.org/10.1016/j.energy.2015.05.136>.
- Cimbala, Yunus A. Cengel. John M. 2009. *Fluid Mechanics: Fundamentals and Applications*. 2nd edition ed: McGraw-Hill Education - Europe.
- Coton, F N, R A McD Galbraith, and D Jiang. 1996. "The Influence of Detailed Blade Design on the Aerodynamic Performance of Straight-Bladed Vertical Axis Wind Turbines."

- Proceedings of the Institution of Mechanical Engineers, Part A: Journal of Power and Energy* 210 (1):65-74. doi: 10.1243/pime_proc_1996_210_009_02.
- Danao, Louis Angelo, Ning Qin, and Robert Howell. 2012. "A numerical study of blade thickness and camber effects on vertical axis wind turbines." *Proceedings of the Institution of Mechanical Engineers, Part A: Journal of Power and Energy* 226 (7):867-881. doi: 10.1177/0957650912454403.
- Daróczy, László, Gábor Janiga, Klaus Petrasch, Michael Webner, and Dominique Thévenin. 2015. "Comparative analysis of turbulence models for the aerodynamic simulation of H-Darrieus rotors." *Energy* 90:680-690. doi: <https://doi.org/10.1016/j.energy.2015.07.102>.
- Daróczy, László, Gábor Janiga, and Dominique Thévenin. 2018. "Computational fluid dynamics based shape optimization of airfoil geometry for an H-rotor using a genetic algorithm." *Engineering Optimization* 50 (9):1483-1499. doi: 10.1080/0305215X.2017.1409350.
- Day, Harry, Derek Ingham, Lin Ma, and Mohamed Pourkashanian. 2021. "Adjoint based optimisation for efficient VAWT blade aerodynamics using CFD." *Journal of Wind Engineering and Industrial Aerodynamics* 208:104431. doi: <https://doi.org/10.1016/j.jweia.2020.104431>.
- De Lellis, Marcelo, Romeu Reginatto, Ramiro Saraiva, and Alexandre Trofino. 2018. "The Betz limit applied to Airborne Wind Energy." *Renewable Energy* 127:32-40. doi: <https://doi.org/10.1016/j.renene.2018.04.034>.
- De Marco, Agostino, Domenico P. Coiro, Domenico Cucco, and Fabrizio Nicolosi. 2014. "A Numerical Study on a Vertical-Axis Wind Turbine with Inclined Arms %J International Journal of Aerospace Engineering." 2014:14. doi: 10.1155/2014/180498.
- De Tavernier, Delphine, Carlos Ferreira, and Gerard %J Wind Energy van Bussel. 2019. "Airfoil optimisation for vertical-axis wind turbines with variable pitch." 22 (4):547-562.
- Delafin, P. L., T. Nishino, L. Wang, and A. Kolios. 2016. "Effect of the number of blades and solidity on the performance of a vertical axis wind turbine." *Journal of Physics: Conference Series* 753:022033. doi: 10.1088/1742-6596/753/2/022033.
- Dhert, Tristan, Turaj Ashuri, and Joaquim Martins. 2017. "Aerodynamic Shape Optimization of Wind Turbine Blades Using a Reynolds-Averaged Navier--Stokes Model and an Adjoint Method." *Wind Energy* 20:909-926. doi: 10.1002/we.2070.
- Difuntorum, John Keithley, and Louis Angelo M Danao. 2019. "Improving VAWT performance through parametric studies of rotor design configurations using computational fluid dynamics." *Proceedings of the Institution of Mechanical Engineers, Part A: Journal of Power and Energy* 233 (4):489-509. doi: 10.1177/0957650918790671.
- Dominy, R., P. Lunt, A. Bickerdyke, and J. Dominy. 2007. "Self-starting capability of a Darrieus turbine." *Proceedings of the Institution of Mechanical Engineers, Part A: Journal of Power and Energy* 221 (1):111-120. doi: 10.1243/09576509JPE340.
- Durrani, Naveed, Haris Mian, Hammad Rahman, and Sajid Chaudhry. 2011. *A Detailed Aerodynamic Design and Analysis of a 2-D Vertical Axis Wind Turbine Using Sliding Mesh in CFD*.
- Eboibi, Okeoghene, Louis Angelo M Danao, and Robert J %J Renewable Energy Howell. 2016. "Experimental investigation of the influence of solidity on the performance and flow field aerodynamics of vertical axis wind turbines at low Reynolds numbers." 92:474-483.

- El-Samanoudy, M., A. A. E. Ghorab, and Sh Z. Youssef. 2010. "Effect of some design parameters on the performance of a Giromill vertical axis wind turbine." *Ain Shams Engineering Journal* 1 (1):85-95. doi: <https://doi.org/10.1016/j.asej.2010.09.012>.
- El Bassam, Nasir, Preben Maegaard, and Marcia Lawton Schlichting. 2013. "Chapter Eight - Wind Energy." In *Distributed Renewable Energies for Off-Grid Communities*, edited by Nasir El Bassam, Preben Maegaard and Marcia Lawton Schlichting, 111-123. Elsevier.
- Elsakka, Mohamed Mohamed, Derek B Ingham, Lin Ma, Mohamed Pourkashanian, Gamal Hafez Moustafa, and Yasser %J Energy Reports Elhenawy. 2022. "Response Surface Optimisation of Vertical Axis Wind Turbine at low wind speeds." *Energy Reports* 8:10868-10880.
- Fiedler, Andrzej J., and Stephen Tullis. 2009. "Blade Offset and Pitch Effects on a High Solidity Vertical Axis Wind Turbine." *Wind Engineering* 33 (3):237-246. doi: 10.1260/030952409789140955.
- Fleischli, B, A Del Rio, E Casartelli, L Mangani, BF Mullins, C Devals, and M Melot. 2021. "Application of a General Discrete Adjoint Method for Draft Tube Optimization." IOP Conference Series: Earth and Environmental Science.
- García Auyanet, Antonio, Rangga E. Santoso, Hrishikesh Mohan, Sanvay S. Rathore, Debapriya Chakraborty, and Patrick G. Verdin. 2022. "CFD-Based J-Shaped Blade Design Improvement for Vertical Axis Wind Turbines." 14 (22):15343.
- Gipe, P. 1995. "Wind-Works: Éole Darrieus VAWT." accessed [accessed 15/03/2020. <http://www.wind-works.org/cms/index.php?id=506>.
- Gosselin, Rémi, Guy Dumas, and Matthieu Boudreau. 2013. "Parametric study of H-Darrieus vertical-axis turbines using uRANS simulations." 21st Annual Conference of the CFD Society of Canada (CFDSC), Sherbrooke, QC, Canada, May.
- Greenblatt, David, Magen Schulman, and Amos %J Renewable Energy Ben-Harav. 2012. "Vertical axis wind turbine performance enhancement using plasma actuators." 37 (1):345-354.
- Gudmundsson, Snorri. 2014. "Chapter 8 - The Anatomy of the Airfoil." In *General Aviation Aircraft Design*, edited by Snorri Gudmundsson, 235-297. Boston: Butterworth-Heinemann.
- Gupta, Rajat, Sukanta Roy, and Agnimitra Biswas. 2010. "Computational fluid dynamics analysis of a twisted airfoil shaped two-bladed H-Darrieus rotor made from fibreglass reinforced plastic (FRP)." *International Journal of Energy and Environment* 1.
- Hand, Brian, and Andrew Cashman. 2017. "Conceptual design of a large-scale floating offshore vertical axis wind turbine." *Energy Procedia* 142:83-88. doi: <https://doi.org/10.1016/j.egypro.2017.12.014>.
- Hand, Brian, and Andrew Cashman. 2020. "A review on the historical development of the lift-type vertical axis wind turbine: From onshore to offshore floating application." *Sustainable Energy Technologies and Assessments* 38:100646. doi: <https://doi.org/10.1016/j.seta.2020.100646>.
- Hand, Brian, Andrew Cashman, and Gerard Kelly. 2019. "Aerodynamic Analysis of a 5 MW Stall-Regulated Offshore Vertical Axis Wind Turbine Using Computational Fluid Dynamics: Energy and Geotechnics." In, edited by Proceedings of the 1st Vietnam Symposium on Advances in Offshore Engineering., 485-491.
- Hara, Yutaka, Naoki Horita, Shigeo Yoshida, Hiromichi Akimoto, and Takahiro Sumi. 2019. "Numerical Analysis of Effects of Arms with Different Cross-Sections on Straight-Bladed Vertical Axis Wind Turbine." *Energies* 12:2106. doi: 10.3390/en12112106.

- Hashem, I., and M. H. Mohamed. 2018. "Aerodynamic performance enhancements of H-rotor Darrieus wind turbine." *Energy* 142:531-545. doi: <https://doi.org/10.1016/j.energy.2017.10.036>.
- He, Jiao, Xin Jin, Shuangyi Xie, Le Cao, Yaming Wang, Yifan Lin, and Ning Wang. 2020. "CFD modeling of varying complexity for aerodynamic analysis of H-vertical axis wind turbines." *Renewable Energy* 145:2658-2670. doi: <https://doi.org/10.1016/j.renene.2019.07.132>.
- Hill, N., R. Dominy, G. Ingram, and J. Dominy. 2008. "Darrieus turbines: The physics of self-starting." *Proceedings of the Institution of Mechanical Engineers, Part A: Journal of Power and Energy* 223 (1):21-29. doi: 10.1243/09576509JPE615.
- Howell, Robert, Ning Qin, Jonathan Edwards, and Naveed Durrani. 2010. "Wind tunnel and numerical study of a small vertical axis wind turbine." *Renewable Energy* 35 (2):412-422. doi: <https://doi.org/10.1016/j.renene.2009.07.025>.
- Huang, Huilan, Jiabin Luo, and Gang Li. 2023. "Study on the optimal design of vertical axis wind turbine with novel variable solidity type for self-starting capability and aerodynamic performance." *Energy* 271:127031. doi: <https://doi.org/10.1016/j.energy.2023.127031>.
- IRENA. 2019. Renewable Energy Statistics 2019. International Renewable Energy Agency (IRENA).
- Islam, M. R., S. Mekhilef, and R. Saidur. 2013. "Progress and recent trends of wind energy technology." *Renewable and Sustainable Energy Reviews* 21:456-468. doi: <https://doi.org/10.1016/j.rser.2013.01.007>.
- Islam, Syed M., Chem V. Nayar, Ahmed Abu-Siada, and Md Mubashwar Hasan. 2018. "25 - Power Electronics for Renewable Energy Sources." In *Power Electronics Handbook (Fourth Edition)*, edited by Muhammad H. Rashid, 783-827. Butterworth-Heinemann.
- Ismail, Md Farhad, and Krishna Vijayaraghavan. 2015. "The effects of aerofoil profile modification on a vertical axis wind turbine performance." *Energy* 80:20-31. doi: <https://doi.org/10.1016/j.energy.2014.11.034>.
- Jacob, Joe, and Dhiman Chatterjee. 2019. "Design methodology of hybrid turbine towards better extraction of wind energy." *Renewable Energy* 131:625-643. doi: <https://doi.org/10.1016/j.renene.2018.07.064>.
- Jin, Guoqing, Zhi Zong, Yichen Jiang, and Li %J Ocean Engineering Zou. 2020. "Aerodynamic analysis of side-by-side placed twin vertical-axis wind turbines." 209:107296.
- Joo, Sungjun, Heungsoap Choi, and Juhee Lee. 2015. "Aerodynamic characteristics of two-bladed H-Darrieus at various solidities and rotating speeds." *Energy* 90:439-451. doi: <https://doi.org/10.1016/j.energy.2015.07.051>.
- Kanyako, Franklyn, and Isam Janajreh. 2014. "Numerical Investigation of Four Commonly Used Airfoils for Vertical Axis Wind Turbine." Cham.
- Kjellin, J., F. Bülow, S. Eriksson, P. Deglaire, M. Leijon, and H. Bernhoff. 2011. "Power coefficient measurement on a 12 kW straight bladed vertical axis wind turbine." *Renewable Energy* 36 (11):3050-3053. doi: <https://doi.org/10.1016/j.renene.2011.03.031>.
- Láin, Santiago, Manuel Taborda, and Omar %J Energies López. 2018. "Numerical study of the effect of winglets on the performance of a straight blade Darrieus water turbine." *Energies* 11 (2):297.
- Lång, Marcus. 2019. CFD-Method for 3D Aerodynamic Adjoint Simulations: For External Automotive Aerodynamics.

- Lanzafame, Rosario, Stefano Mauro, and Michele Messina. 2014. "2D CFD Modeling of H-Darrieus Wind Turbines Using a Transition Turbulence Model." *Energy Procedia* 45:131-140. doi: <https://doi.org/10.1016/j.egypro.2014.01.015>.
- Lauder, B. E., and D. B. Spalding. 1974. "The numerical computation of turbulent flows." *Computer Methods in Applied Mechanics and Engineering* 3 (2):269-289. doi: [https://doi.org/10.1016/0045-7825\(74\)90029-2](https://doi.org/10.1016/0045-7825(74)90029-2).
- Lee, Young-Tae, and Hee-Chang Lim. 2015. "Numerical study of the aerodynamic performance of a 500 W Darrieus-type vertical-axis wind turbine." *Renewable Energy* 83:407-415. doi: <https://doi.org/10.1016/j.renene.2015.04.043>.
- Lei, Hang, Dai Zhou, Yan Bao, Caiyong Chen, Ning Ma, and Zhaolong Han. 2017. "Numerical simulations of the unsteady aerodynamics of a floating vertical axis wind turbine in surge motion." *Energy* 127:1-17. doi: <https://doi.org/10.1016/j.energy.2017.03.087>.
- Li, Chao, Songye Zhu, You-lin Xu, and Yiqing Xiao. 2013. "2.5D large eddy simulation of vertical axis wind turbine in consideration of high angle of attack flow." *Renewable Energy* 51:317-330. doi: <https://doi.org/10.1016/j.renene.2012.09.011>.
- Li, Qing'an, Takao Maeda, Yasunari Kamada, Junsuke Murata, Kazuma Furukawa, and Masayuki Yamamoto. 2015. "Effect of number of blades on aerodynamic forces on a straight-bladed Vertical Axis Wind Turbine." *Energy* 90:784-795. doi: <https://doi.org/10.1016/j.energy.2015.07.115>.
- Li, Qing'an, Takao Maeda, Yasunari Kamada, Junsuke Murata, Toshiaki Kawabata, Kento Shimizu, Tatsuhiko Ogasawara, Alisa Nakai, and Takuji Kasuya. 2016a. "Wind tunnel and numerical study of a straight-bladed vertical axis wind turbine in three-dimensional analysis (Part I: For predicting aerodynamic loads and performance)." *Energy* 106:443-452. doi: <https://doi.org/10.1016/j.energy.2016.03.089>.
- Li, Qing'an, Takao Maeda, Yasunari Kamada, Junsuke Murata, Toshiaki Kawabata, Kento Shimizu, Tatsuhiko Ogasawara, Alisa Nakai, and Takuji Kasuya. 2016b. "Wind tunnel and numerical study of a straight-bladed Vertical Axis Wind Turbine in three-dimensional analysis (Part II: For predicting flow field and performance)." *Energy* 104:295-307. doi: <https://doi.org/10.1016/j.energy.2016.03.129>.
- Li, Qing'an, Takao Maeda, Yasunari Kamada, Tatsuhiko Ogasawara, Alisa Nakai, and Takuji Kasuya. 2017. "Investigation of power performance and wake on a straight-bladed vertical axis wind turbine with field experiments." *Energy* 141:1113-1123. doi: <https://doi.org/10.1016/j.energy.2017.10.009>.
- Li, Qing'an, Takao Maeda, Yasunari Kamada, Kento Shimizu, Tatsuhiko Ogasawara, Alisa Nakai, and Takuji Kasuya. 2017. "Effect of rotor aspect ratio and solidity on a straight-bladed vertical axis wind turbine in three-dimensional analysis by the panel method." *Energy* 121:1-9. doi: <https://doi.org/10.1016/j.energy.2016.12.112>.
- Li, Qing'an, Takao Maeda, Yasunari Kamada, Junsuke Murata, Kento Shimizu, Tatsuhiko Ogasawara, Alisa Nakai, and Takuji Kasuya. 2016. "Effect of solidity on aerodynamic forces around straight-bladed vertical axis wind turbine by wind tunnel experiments (depending on number of blades)." *Renewable Energy* 96:928-939. doi: <https://doi.org/10.1016/j.renene.2016.05.054>.
- Li, Yan, Shouyang Zhao, Chunming Qu, Guoqiang Tong, Fang Feng, Bin Zhao, and Tagawa Kotaro. 2019. "Aerodynamic characteristics of Straight-bladed Vertical Axis Wind Turbine with a curved-outline wind gathering device." *Energy Conversion and Management*:112249. doi: <https://doi.org/10.1016/j.enconman.2019.112249>.

- Li, Ye, and Sander M. Calisal. 2010. "Three-dimensional effects and arm effects on modeling a vertical axis tidal current turbine." *Renewable Energy* 35 (10):2325-2334. doi: <https://doi.org/10.1016/j.renene.2010.03.002>.
- Lin, Yang-You Lin, Chi-Jeng Bai, and Wei-Cheng Wang. 2016. "Performance analysis of vertical-axis-wind-turbine blade with modified trailing edge through computational fluid dynamics." *Renewable Energy* 99:654-662. doi: <https://doi.org/10.1016/j.renene.2016.07.050>.
- Lin, Jinghua, Leo K. K. Leung, You-Lin Xu, Sheng Zhan, and Songye Zhu. 2018. "Field measurement, model updating, and response prediction of a large-scale straight-bladed vertical axis wind turbine structure." *Measurement* 130:57-70. doi: <https://doi.org/10.1016/j.measurement.2018.07.057>.
- Liu, Qingsong, Weipao Miao, Chun Li, Winxing Hao, Haitian Zhu, and Yunhe Deng. 2019. "Effects of trailing-edge movable flap on aerodynamic performance and noise characteristics of VAWT." *Energy* 189:116271. doi: <https://doi.org/10.1016/j.energy.2019.116271>.
- Lositaño, Ian Carlo M., and Louis Angelo M. Danao. 2019. "Steady wind performance of a 5 kW three-bladed H-rotor Darrieus Vertical Axis Wind Turbine (VAWT) with cambered tubercle leading edge (TLE) blades." *Energy* 175:278-291. doi: <https://doi.org/10.1016/j.energy.2019.03.033>.
- Ma, Ning, Hang Lei, Zhaolong Han, Dai Zhou, Yan Bao, Kai Zhang, Lei Zhou, and Caiyong Chen. 2018. "Airfoil optimization to improve power performance of a high-solidity vertical axis wind turbine at a moderate tip speed ratio." *Energy* 150:236-252. doi: <https://doi.org/10.1016/j.energy.2018.02.115>.
- Maalouly, M, M Souaiby, A ElCheikh, JS Issa, and M %J Energy Reports Elkhoury. 2022. "Transient analysis of H-type vertical axis wind turbines using CFD." 8:4570-4588.
- Manickam, Thanesh A. L., and Sukanta Roy. 2020. "Aerodynamic Analysis of Active Trailing-Edge Flaps and Passive Surface Roughness on NACA 4412 Airfoil." *IOP Conference Series: Materials Science and Engineering* 943 (1):012036. doi: 10.1088/1757-899x/943/1/012036.
- Marie, Darrieus Georges Jean. 1931. Turbine having its rotating shaft transverse to the flow of the current. Google Patents.
- Marinić-Kragić, Ivo, Damir Vučina, and Zoran %J Energy Milas. 2019. "Concept of flexible vertical-axis wind turbine with numerical simulation and shape optimization." *Energy* 167:841-852.
- Marinić-Kragić, Ivo, Damir Vučina, and Zoran %J Energy Milas. 2022. "Global optimization of Savonius-type vertical axis wind turbine with multiple circular-arc blades using validated 3D CFD model." *Energy* 241:122841.
- Marinić-Kragić, Ivo, Damir Vučina, and Zoran %J Renewable energy Milas. 2018. "Numerical workflow for 3D shape optimization and synthesis of vertical-axis wind turbines for specified operating regimes." *Renewable Energy* 115:113-127.
- Marsh, Philip, Dev Ranmuthugala, Irene Penesis, and Giles Thomas. 2015. "Numerical investigation of the influence of blade helicity on the performance characteristics of vertical axis tidal turbines." *Renewable Energy* 81:926-935. doi: <https://doi.org/10.1016/j.renene.2015.03.083>.
- McLaren, Kevin W. 2011. "A numerical and experimental study of unsteady loading of high solidity vertical axis wind turbines."
- Menter, F. R. 1994. "Two-equation eddy-viscosity turbulence models for engineering applications." 32 (8):1598-1605. doi: 10.2514/3.12149.

- Menter, Florian R, Martin Kuntz, Robin %J Turbulence Langtry, heat, and mass transfer. 2003. "Ten years of industrial experience with the SST turbulence model." 4 (1):625-632.
- Miao, Weipao, Qingsong Liu, Qiang Zhang, Zifei Xu, Chun Li, Minnan Yue, Wanfu Zhang, and Zhou Ye. 2023. "Recommendation for strut designs of vertical axis wind turbines: Effects of strut profiles and connecting configurations on the aerodynamic performance." *Energy Conversion and Management* 276:116436. doi: <https://doi.org/10.1016/j.enconman.2022.116436>.
- Mohamed, M. H. 2012. "Performance investigation of H-rotor Darrieus turbine with new airfoil shapes." *Energy* 47 (1):522-530. doi: <https://doi.org/10.1016/j.energy.2012.08.044>.
- Molina, A. Carbó, T. Massai, F. Balduzzi, A. Bianchini, G. Ferrara, T. De Troyer, and G. Bartoli. 2018. "Combined experimental and numerical study on the near wake of a Darrieus VAWT under turbulent flows." *Journal of Physics: Conference Series* 1037:072052. doi: 10.1088/1742-6596/1037/7/072052.
- Naseem, Ammar, Emad Uddin, Zaib Ali, Jawad Aslam, Samiur Rehman Shah, Muhammad Sajid, Ali Abbas Zaidi, Adeel Javed, and Muhammad Yamin Younis. 2020. "Effect of vortices on power output of vertical axis wind turbine (VAWT)." *Sustainable Energy Technologies and Assessments* 37:100586. doi: <https://doi.org/10.1016/j.seta.2019.100586>.
- Nini, Michele, Valentina Motta, Giampiero Bindolino, and Alberto Guardone. 2014. "Three-dimensional simulation of a complete Vertical Axis Wind Turbine using overlapping grids." *Journal of Computational and Applied Mathematics* 270:78-87. doi: <https://doi.org/10.1016/j.cam.2014.02.020>.
- Parakkal, Jabir Ubaid, Khadije El Kadi, Ameen El-Sinawi, Sherine Elagroudy, and Isam Janajreh. 2019. "Numerical analysis of VAWT wind turbines: Joukowski vs classical NACA rotor's blades." *Energy Procedia* 158:1194-1201. doi: <https://doi.org/10.1016/j.egypro.2019.01.306>.
- Paraschivoiu, Ion. 2002. "Wind turbine design with emphasis on Darrieus concept [ressource électronique] / Ion Paraschivoiu."
- Qin, Ning, Robert Howell, Naveed Durrani, Kenichi Hamada, and Tomos %J Wind Engineering Smith. 2011. "Unsteady flow simulation and dynamic stall behaviour of vertical axis wind turbine blades." *Wind Engineering* 35 (4):511-527.
- REN 21, 2021. 2021. *Renewables 2021 Global Status Report*. Edited by REN21 Secretariat.
- Rezaeiha, Abdolrahim, Ivo Kalkman, and Bert Blocken. 2017a. "CFD simulation of a vertical axis wind turbine operating at a moderate tip speed ratio: Guidelines for minimum domain size and azimuthal increment." *Renewable Energy* 107:373-385. doi: <https://doi.org/10.1016/j.renene.2017.02.006>.
- Rezaeiha, Abdolrahim, Ivo Kalkman, and Bert Blocken. 2017b. "Effect of pitch angle on power performance and aerodynamics of a vertical axis wind turbine." *Applied Energy* 197:132-150. doi: <https://doi.org/10.1016/j.apenergy.2017.03.128>.
- Roy, Sukanta, and Ujjwal K Saha. 2013a. "Review of experimental investigations into the design, performance and optimization of the Savonius rotor." 227 (4):528-542. doi: 10.1177/0957650913480992.
- Roy, Sukanta, and Ujjwal K. Saha. 2013b. "Review on the numerical investigations into the design and development of Savonius wind rotors." *Renewable and Sustainable Energy Reviews* 24:73-83. doi: <https://doi.org/10.1016/j.rser.2013.03.060>.
- Sanei, Maryam, and Reza Razaghi. 2018. "Numerical investigation of three turbulence simulation models for S809 wind turbine airfoil." *Proceedings of the Institution of*

- Mechanical Engineers, Part A: Journal of Power and Energy* 232 (8):1037-1048. doi: 10.1177/0957650918767301.
- Santos, Gabriel B., Aluisio V. Pantaleão, and Leandro O. Salviano. 2023. "Using deep generative adversarial network to explore novel airfoil designs for vertical-axis wind turbines." *Energy Conversion and Management* 282:116849. doi: <https://doi.org/10.1016/j.enconman.2023.116849>.
- Scheurich, F, T M Fletcher, and R E Brown. 2011. "Effect of blade geometry on the aerodynamic loads produced by vertical-axis wind turbines." *Proceedings of the Institution of Mechanical Engineers, Part A: Journal of Power and Energy* 225 (3):327-341. doi: 10.1177/2041296710394248.
- Scheurich, Frank, Timothy Fletcher, and Richard Brown. 2010. *The Influence of Blade Curvature and Helical Blade Twist on the Performance of a Vertical-Axis Wind Turbine*.
- Sengupta, A. R., A. Biswas, and R. Gupta. 2016. "Studies of some high solidity symmetrical and unsymmetrical blade H-Darrieus rotors with respect to starting characteristics, dynamic performances and flow physics in low wind streams." *Renewable Energy* 93:536-547. doi: <https://doi.org/10.1016/j.renene.2016.03.029>.
- Shamsoddin, Sina, and Fernando Porté-Agel. 2020. "Effect of aspect ratio on vertical-axis wind turbine wakes." *Journal of Fluid Mechanics* 889:R1. doi: 10.1017/jfm.2020.93.
- Shen, Xin, Jinge Chen, Ping Hu, Xiaocheng Zhu, and Zhaohui Du. 2018. "Study of the unsteady aerodynamics of floating wind turbines." *Energy* 145:793-809. doi: <https://doi.org/10.1016/j.energy.2017.12.100>.
- Siddiqui, M. Salman, Naveed Durrani, and Imran Akhtar. 2015. "Quantification of the effects of geometric approximations on the performance of a vertical axis wind turbine." *Renewable Energy* 74:661-670. doi: <https://doi.org/10.1016/j.renene.2014.08.068>.
- Siddiqui, M. Salman, Naveed Durrani, and Akhtar Imran. 2013. "Numerical Study to Quantify the Effects of Struts and Central Hub on the Performance of a Three Dimensional Vertical Axis Wind Turbine Using Sliding Mesh." *Proceedings of the ASME 2013 Power Conference* 2. doi: 10.1115/POWER2013-98300.
- Singh, A. Biswas, and R. D. Misra. 2015. "Investigation of self-starting and high rotor solidity on the performance of a three S1210 blade H-type Darrieus rotor." *Renewable Energy* 76:381-387. doi: <https://doi.org/10.1016/j.renene.2014.11.027>.
- Singh, Enderaaj, Sukanta Roy, Yam Ke San, and Law Ming Chiat. 2022. "Optimisation of H-Darrieus VAWT Solidity for Energy Extraction in Cooling Tower Exhaust Systems." *Journal of Advanced Research in Fluid Mechanics and Thermal Sciences* 91 (2):51-61.
- Singh, Enderaaj, Sukanta Roy, Ke San Yam, and Ming Chiat Law. 2023. "Numerical analysis of H-Darrieus vertical axis wind turbines with varying aspect ratios for exhaust energy extractions." *Energy* 277:127739. doi: <https://doi.org/10.1016/j.energy.2023.127739>.
- Song, Chenguang, Guoqing Wu, Weinan Zhu, and Xudong Zhang. 2019. "Study on Aerodynamic Characteristics of Darrieus Vertical Axis Wind Turbines with Different Airfoil Maximum Thicknesses Through Computational Fluid Dynamics." *Arabian Journal for Science and Engineering*. doi: 10.1007/s13369-019-04127-8.
- Souaissa, Khaled, Moncef Ghiss, Mouldi Chrigui, Hatem Bentaher, and Aref Maalej. 2018. "A comprehensive analysis of aerodynamic flow around H-Darrieus rotor with camber-bladed profile." *Wind Engineering* 43 (5):459-475. doi: 10.1177/0309524X18791390.

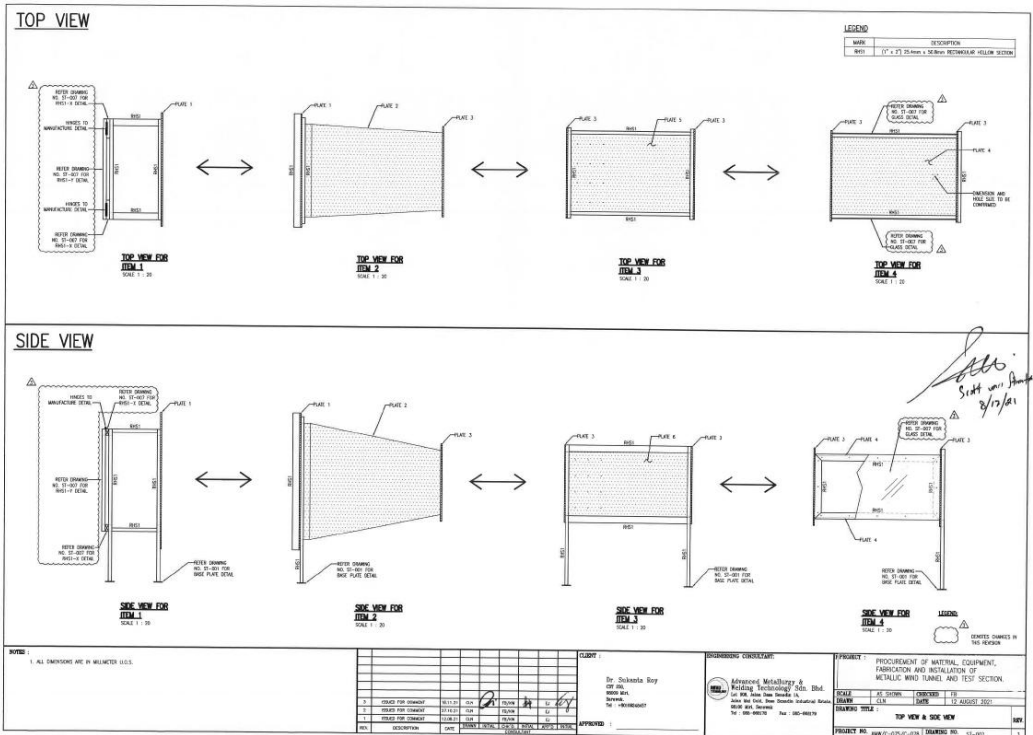
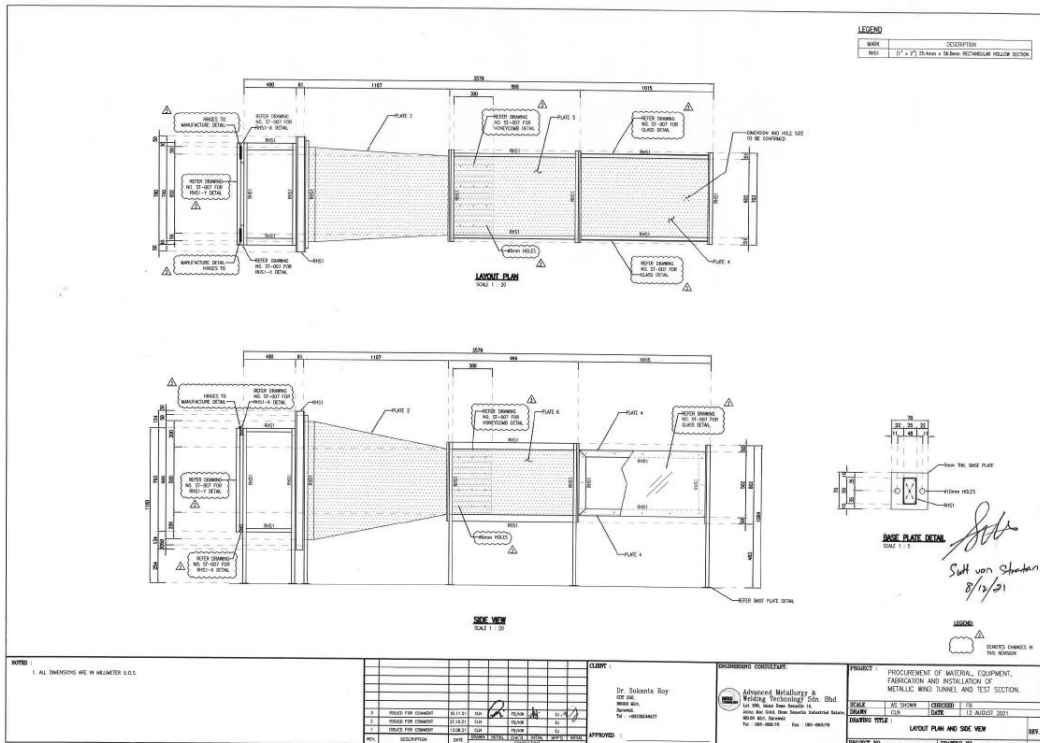
- su, Liu, and Isam Janajreh. 2012. "Wind energy assessment: Masdar City case study." *2012 8th International Symposium on Mechatronics and its Applications, ISMA 2012*. doi: 10.1109/ISMA.2012.6215162.
- Subramanian, Abhishek, S. Arun Yogesh, Hrishikesh Sivanandan, Abhijit Giri, Madhavan Vasudevan, Vivek Mugundhan, and Ratna Kishore Velamati. 2017. "Effect of airfoil and solidity on performance of small scale vertical axis wind turbine using three dimensional CFD model." *Energy* 133:179-190. doi: <https://doi.org/10.1016/j.energy.2017.05.118>.
- Tahani, Mojtaba, Narek Babayan, Seyedmajid Mehrnia, and Mehran Shadmehri. 2016. "A novel heuristic method for optimization of straight blade vertical axis wind turbine." *Energy Conversion and Management* 127:461-476. doi: <https://doi.org/10.1016/j.enconman.2016.08.094>.
- Tirandaz, M. Rasoul, and Abdolrahim Rezaeiha. 2021. "Effect of airfoil shape on power performance of vertical axis wind turbines in dynamic stall: Symmetric Airfoils." *Renewable Energy* 173:422-441. doi: <https://doi.org/10.1016/j.renene.2021.03.142>.
- Tong, Guoqiang, Yan Li, Kotaro Tagawa, and Fang Feng. 2023. "Effects of blade airfoil chord length and rotor diameter on aerodynamic performance of straight-bladed vertical axis wind turbines by numerical simulation." *Energy* 265:126325. doi: <https://doi.org/10.1016/j.energy.2022.126325>.
- Tsai, Hsieh-Chen, and Tim Colonius. 2016. "Numerical Investigation of Self-Starting Capability of Vertical-Axis Wind Turbines at Low Reynolds Numbers." 34th AIAA Applied Aerodynamics Conference.
- Tzanakis, Athanasios. 2014. "Duct optimization using CFD software ANSYS Fluent Adjoint Solver'."
- Vennell, Ross. 2013. "Exceeding the Betz limit with tidal turbines." *Renewable Energy* 55:277-285. doi: <https://doi.org/10.1016/j.renene.2012.12.016>.
- Vergaerde, Antoine, Tim De Troyer, Lieven Standaert, Joanna Kluczewska-Bordier, Denis Pitance, Alexandre Immas, Frédéric Silvert, and Mark C. Runacres. 2020. "Experimental validation of the power enhancement of a pair of vertical-axis wind turbines." *Renewable Energy* 146:181-187. doi: <https://doi.org/10.1016/j.renene.2019.06.115>.
- Wang, Sheng Shen, Gaohui Li, Diangui Huang, and Zhongquan Zheng. 2018. "Investigation on aerodynamic performance of vertical axis wind turbine with different series airfoil shapes." *Renewable Energy* 126:801-818. doi: <https://doi.org/10.1016/j.renene.2018.02.095>.
- Wang, Yuchen Wang, and Mei Zhuang. 2018. "Improvement of the aerodynamic performance of vertical axis wind turbines with leading-edge serrations and helical blades using CFD and Taguchi method." *Energy Conversion and Management* 177:107-121. doi: <https://doi.org/10.1016/j.enconman.2018.09.028>.
- Wang, Quan, Boyang Liu, Cong Hu, Fengyun Wang, and Shuyi %J International Journal of Low-Carbon Technologies Yang. 2022. "Aerodynamic shape optimization of H-VAWT blade airfoils considering a wide range of angles of attack." 17:147-159.
- Wang, S., Y. Zhou, M. M. Alam, and H. X. Yang. 2014. "Turbulent Intensity Effect on Low Reynolds Number Airfoil Wake." Berlin, Heidelberg.
- Wang, Xuefei, Xiangwu Zeng, Jiale Li, Xu Yang, and Haijun Wang. 2018. "A review on recent advancements of substructures for offshore wind turbines." *Energy Conversion and Management* 158:103-119. doi: <https://doi.org/10.1016/j.enconman.2017.12.061>.
- Wang, Ying, Xiaojing Sun, Xiaohua Dong, Bing Zhu, Diangui Huang, and Zhongquan Zheng. 2016. "Numerical investigation on aerodynamic performance of a novel vertical axis

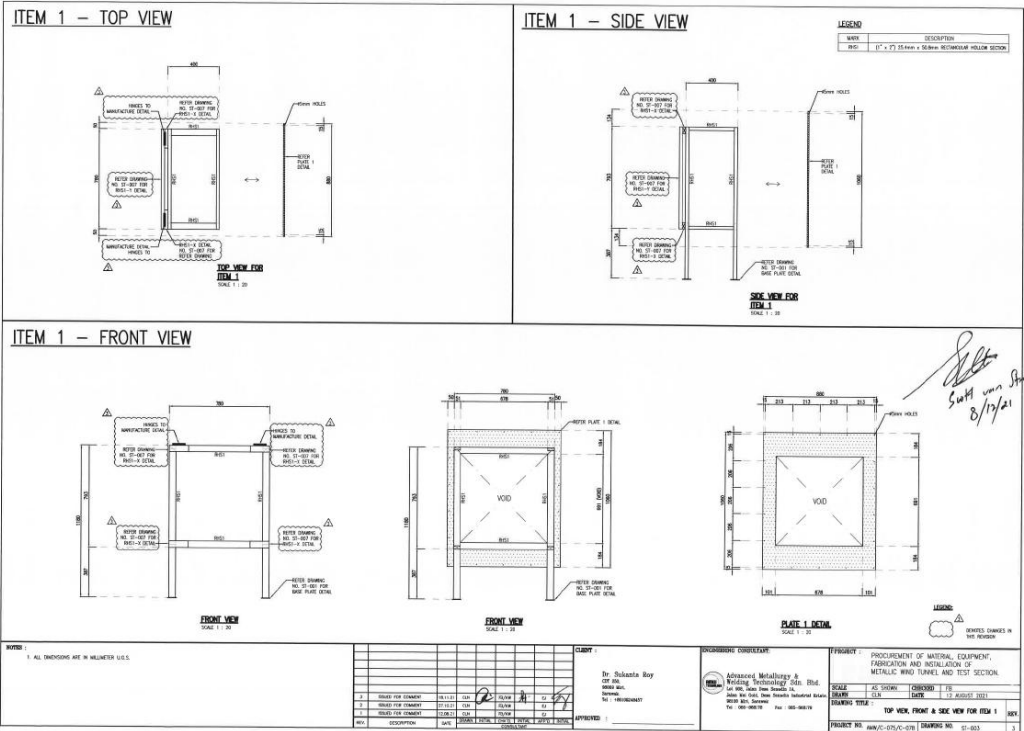
- wind turbine with adaptive blades." *Energy Conversion and Management* 108:275-286. doi: <https://doi.org/10.1016/j.enconman.2015.11.003>.
- Wekesa, David Wafula, Churchill Otieno Saoko, and Joseph Ngugi Kamau. 2020. "An experimental investigation into performance characteristics of H-shaped and Savonius-type VAWT rotors." *Scientific African* 10:e00603. doi: <https://doi.org/10.1016/j.sciaf.2020.e00603>.
- White, Frank M. 2009. *Fluid Mechanics*. 7th Edition ed: McGraw-Hill.
- Wilcox, David C. 2008a. "Formulation of the k-w Turbulence Model Revisited." 46 (11):2823-2838. doi: 10.2514/1.36541.
- Wilcox, David C. 2008b. "Formulation of the k-w Turbulence Model Revisited." *AIAA Journal* 46 (11):2823-2838. doi: 10.2514/1.36541.
- WindEurope. 2019. Wind Energy in Europe in 2018. In *Trends and Statistics: Wind Europe*.
- WindEurope. 2020a. Offshore Wind in Europe. In *Key Trends and Statistics 2019: Wind Europe*.
- WindEurope. 2020b. Wind Energy in Europe 2019. In *Trends and Statistics: Wind Europe*.
- Wolfe, Walter, Stuart Ochs, Walter Wolfe, and Stuart Ochs. 1997. "CFD calculations of S809 aerodynamic characteristics." 35th Aerospace Sciences Meeting and Exhibit.
- Worasinchai, S., G. Ingram, and R. Dominy. 2011. "A low-Reynolds-number, high-angle-of-attack investigation of wind turbine aerofoils." *Proceedings of the Institution of Mechanical Engineers, Part A: Journal of Power and Energy* 225 (6):748-763. doi: 10.1177/0957650911405411.
- Wu, Zhenlong, and Yihua Cao. 2018. "Investigation of vertical axis wind turbine airfoil performance in rain." 232 (2):181-194. doi: 10.1177/0957650917721776.
- Xu, You-Lin, Yi-Xin Peng, and Sheng Zhan. 2019. "Optimal blade pitch function and control device for high-solidity straight-bladed vertical axis wind turbines." *Applied Energy* 242:1613-1625. doi: <https://doi.org/10.1016/j.apenergy.2019.03.151>.
- Yan, Yan, Eldad Avital, John Williams, and Jiahuan Cui. 2021. "Aerodynamic performance improvements of a vertical axis wind turbine by leading-edge protuberance." *Journal of Wind Engineering and Industrial Aerodynamics* 211:104535. doi: <https://doi.org/10.1016/j.jweia.2021.104535>.
- Yang, Yang, Chun Li, Wanfu Zhang, Xueyan Guo, and Quanyong Yuan. 2017. "Investigation on aerodynamics and active flow control of a vertical axis wind turbine with flapped airfoil." *Journal of Mechanical Science and Technology* 31 (4):1645-1655. doi: 10.1007/s12206-017-0312-0.
- Youngblood, K., and S. Roy. 2021. "Performance Analysis of Multi Rotating Savonius Turbines for Exhaust Air Energy Recovery Through CFD Simulations." *Journal of Physics: Conference Series* 2051 (1):012007. doi: 10.1088/1742-6596/2051/1/012007.
- Zhang, Lijun, Jiawei Gu, Kuoliang Hu, Huaibao Zhu, Junjie Miao, Xiang Li, Dongchen Ma, Yuxia Mi, and Zhiwei Wang. 2021. "Influences of trailing edge split flap on the aerodynamic performance of vertical axis wind turbine." *Energy Science and Engineering* 9 (1):101-115. doi: <https://doi.org/10.1002/ese3.818>.
- Zhang, Yanfeng, Zhiping Guo, Xinyu Zhu, Yuan Li, Xiaowen Song, Chang Cai, Yasunari Kamada, Takao Maeda, and Qing'an Li. 2022. "Investigation of aerodynamic forces and flow field of an H-type vertical axis wind turbine based on bionic airfoil." *Energy* 242:122999. doi: <https://doi.org/10.1016/j.energy.2021.122999>.
- Zhong, Junwei, Jingyin Li, Penghua Guo, and Yu Wang. 2019. "Dynamic stall control on a vertical axis wind turbine aerofoil using leading-edge rod." *Energy* 174:246-260. doi: <https://doi.org/10.1016/j.energy.2019.02.176>.

- Zhu, Haitian, Wenxing Hao, Chun Li, and Qinwei Ding. 2019. "Numerical study of effect of solidity on vertical axis wind turbine with Gurney flap." *Journal of Wind Engineering and Industrial Aerodynamics* 186:17-31. doi: <https://doi.org/10.1016/j.jweia.2018.12.016>.
- Zhu, Haitian, Wenxing Hao, Chun Li, Shuai Luo, Qingsong Liu, and Chuang Gao. 2021. "Effect of geometric parameters of Gurney flap on performance enhancement of straight-bladed vertical axis wind turbine." *Renewable Energy* 165:464-480. doi: <https://doi.org/10.1016/j.renene.2020.11.027>.

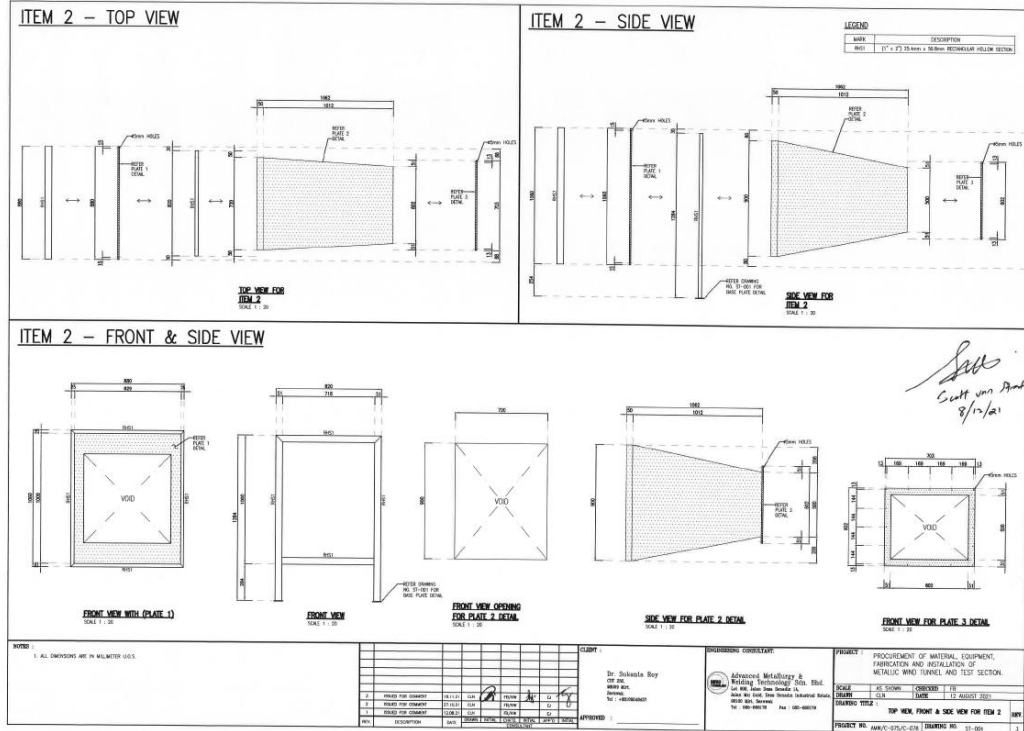
“Every reasonable effort has been made to acknowledge the owners of copyright material presented in this thesis. I would be pleased to hear from any copyright owner who has been omitted or incorrectly acknowledged.”

Appendix A – Wind Tunnel Drawings

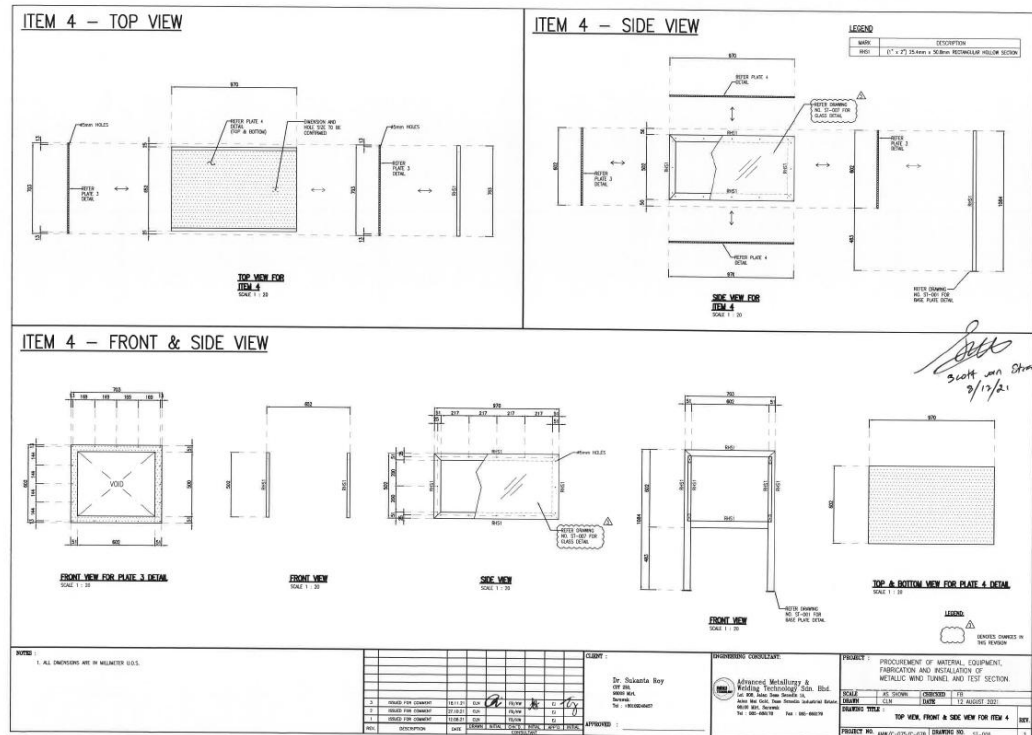
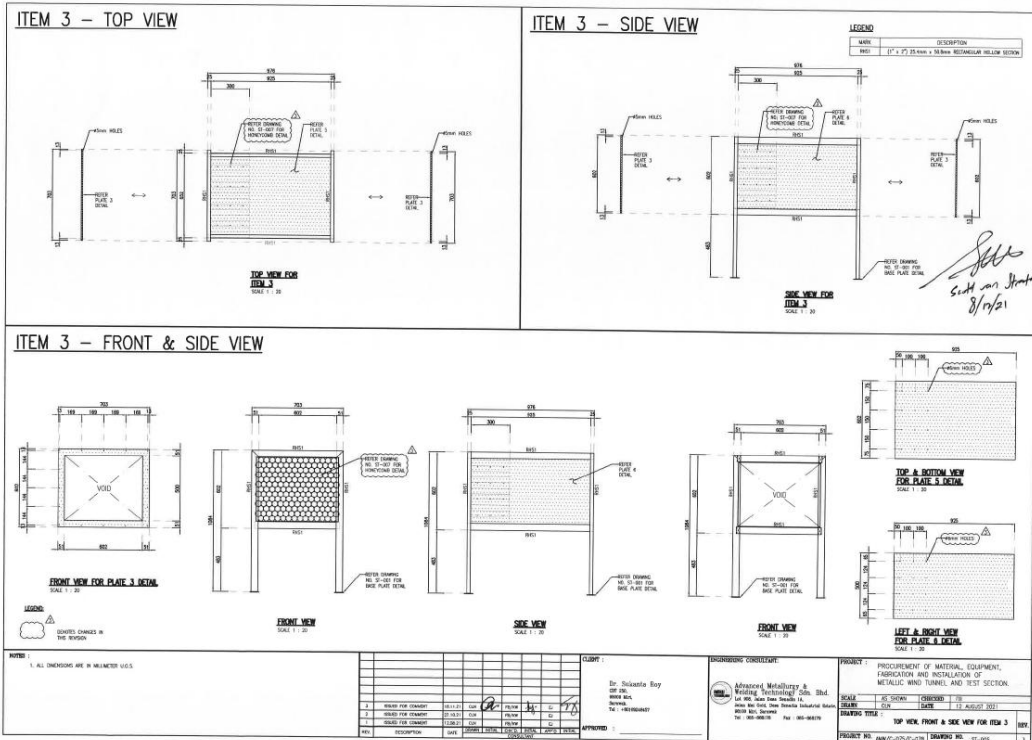


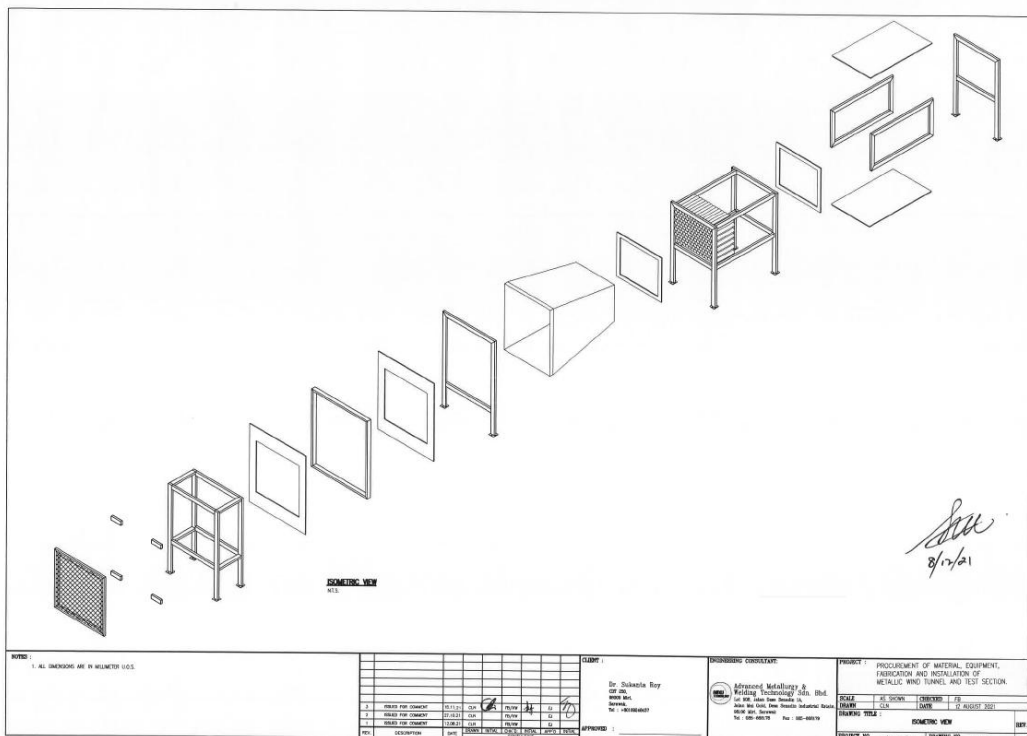
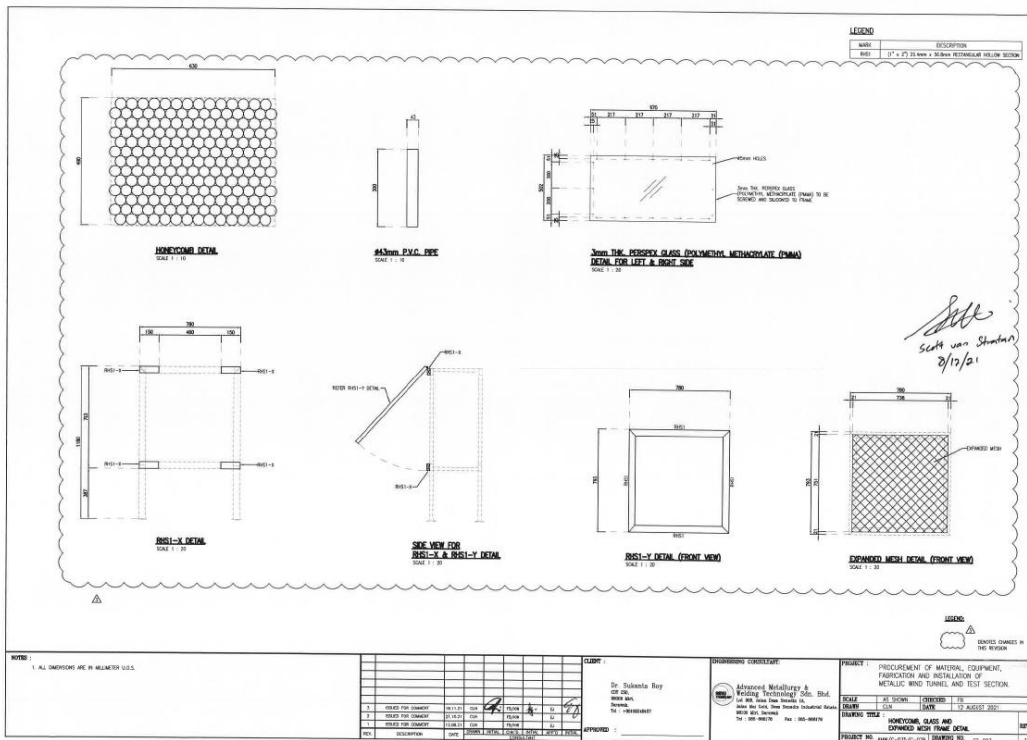


Suff van Arden
8/12/21



Suff van Arden
8/12/21





Appendix B – Experimental sensors and equipment



Torque sensor used in the experimental study.



Velocity sensor Testo 420 for the wind tunnel experiment.